

DEVELOPMENTS IN FULLERENE SCIENCE

Periodic Nanostructures

Mircea V. Diudea and Csaba L. Nagy

 Springer

Periodic Nanostructures

Developments in Fullerene Science

Volume 7

Series Editor:

Tibor Braun, *Institute of Inorganic and Analytical Chemistry, L. Eötvös University,
Budapest, Hungary*

The titles published in this series are listed at the end of this volume.

Periodic Nanostructures

by

Mircea V. Diudea

*Babes-Bolyai University,
Cluj, Romania*

and

Csaba L. Nagy

*Babes-Bolyai University,
Cluj, Romania*



Springer

A C.I.P. Catalogue record for this book is available from the Library of Congress.

ISBN 978-1-4020-6019-9 (HB)

ISBN 978-1-4020-6020-5 (e-book)

Published by Springer,

P.O. Box 17, 3300 AA Dordrecht, The Netherlands.

www.springer.com

Printed on acid-free paper

All Rights Reserved

© 2007 Springer

No part of this work may be reproduced, stored in a retrieval system, or transmitted in any form or by any means, electronic, mechanical, photocopying, microfilming, recording or otherwise, without written permission from the Publisher, with the exception of any material supplied specifically for the purpose of being entered and executed on a computer system, for exclusive use by the purchaser of the work.

Table of Contents

Foreword	ix
Chapter 1. Periodic Fullerenes by Coalescence Reactions	1
1.1 Fullerene Fusion via Stone-Wales Transformation	1
1.1.1 Fullerene Dimers and Their Derivatives	1
1.1.2 Theoretical Considerations About Fullerene Fusion	5
1.1.3 Coalescence in Peapods	8
1.2 Results and Discussion	9
1.2.1 The sp^3 Adducts: C_{120} , $C_{120}O$ and $C_{120}O_2$	10
1.2.2 Coalescence by Stone-Wales Bond Flipping	12
1.2.3 Pathway to C_{114} Tubulene	16
1.3 Closed Nanotubes Viewed as Coalescence Products	19
1.3.1 Finite-Length Carbon Nanotubes Related to C_{60} ..	19
1.3.2 Simple Hückel Theory	21
1.3.3 Leapfrog Transformation and Leapfrog Structures	22
1.3.4 Construction and Classification of Nanotube Caps	22
1.4 Armchair and Zig-Zag Closed Nanotubes	23
1.4.1 Construction of Nanotube Caps	23
1.4.2 Construction of Capped Armchair Nanotubes	25
1.4.3 Construction of Capped Zig-Zag Nanotubes	26
1.5 Energetics of Capped Nanotubes	28
1.5.1 Methods	28
1.5.2 Stability of Capped Armchair Nanotubes	28
1.5.3 Stability of Capped Zig-Zag Nanotubes	31

Conclusions.....	33
References.....	33
Chapter 2. Polyhex Tori	35
2.1 Introduction.....	35
2.2 Construction of Polyhex Tori from Square Tiled Tori	36
2.3 Topology of Polyhex Tori.....	39
2.4 Strain Energy Calculation	41
2.5 π -Electronic Structure of Polyhex Tori.....	43
2.6 Identical Polyhex Toroidal Graphs	45
2.7 Resonance Energy in Polyhex Tori	46
Conclusions.....	47
References.....	48
Chapter 3. New Classes of Toroidal Structures	51
3.1 Distinct Walled Tori.....	51
3.1.1 DWNT as DWT Precursors.....	51
3.1.2 Perfect Clar DWTs.....	57
3.2 Conetori	60
3.2.1 Conetori with: Internal H/Z-Tube, External V/A-Tube	61
3.2.2 Conetori with: Internal H/Z-Tube, External Cone (Without Tube).....	63
3.2.3 Conetori with: Internal V/A-Tube, External Cone (Without Tube).....	64
3.3 Diameter Doubling of SWNT.....	65
Conclusions.....	67
References.....	67
Chapter 4. Counting Polynomials of Nanostructures	69
4.1 Graph Theory Background.....	69
4.2 Counting Polynomials	77
4.3 Layer/Shell Matrices and Polynomial Coefficients.....	78
4.4 Cluj Polynomials	82
4.5 Properties of the Cluj Polynomials	83
4.6 Omega-type Polynomials	86
4.7 Hosoya Polynomial in Toroidal Nanostructures.....	89
4.7.1 Polyhex (6,3) Covering.....	89
4.7.2 Twisted T(6,3)HV _t [c, n] Tori.....	92
4.7.3 Covering ((4,8)3)S	94
4.8 Omega Polynomial in Tubular Nanostructures	98
4.8.1 Polyhex (6,3) Covering.....	98
4.8.2 Covering ((4,8)3)	104

4.9	QSPR Studies by Omega-derived Descriptors.	107
	Conclusions.....	111
	References.....	112
Chapter 5.	Operations on Maps	115
5.1	Introduction.....	115
5.2	Simple Operations on Maps.....	116
5.2.1	Dualization Du	116
5.2.2	Medial Me	116
5.2.3	Truncation Tr	117
5.2.4	Polygonal P_n Capping.....	117
5.2.5	Snub Sn	118
5.3	Composite Operations	119
5.3.1	Leapfrog Le.....	119
5.3.2	Quadrupling Q.....	120
5.3.3	Septupling Operations.....	121
5.3.4	Molecular Realization of Septupling Operations ..	126
5.4	Generalized Operations	128
5.5	Isomerization Routes on Tubular Nanostructures	130
5.5.1	Isomerizations on (6,3) Net	132
5.5.2	Isomerizations on ((4,8)3) Net.....	133
	Conclusions.....	135
	References.....	135
Chapter 6.	Aromaticity of Nanostructures	137
6.1	Introduction.....	137
6.2	Aromaticity of Nanostructures	138
6.3	Corannulenic Cages.....	140
6.4	Corazulenic Cages.....	145
6.4.1	Covering by $[n : (7(5c))_n]$ Fw Patterns	146
6.4.2	Covering by $[n : (7(5d))_n]$ Fw, 3	149
6.5	Retro Endo-Kroto Reaction.....	161
	Conclusions.....	163
	References.....	163
Chapter 7.	Triply Periodic Nanostructures	167
7.1	Introduction.....	167
7.2	Background on Surface Curvature.....	168
7.3	Carbon Lattices Embedded in TPMSs.....	170
7.4	Nanotube Junctions	172
7.4.1	Digonal Junctions.....	173
7.4.2	Planar Junctions	173
7.4.3	Tetrahedral Junctions	175

7.4.4	Octahedral Junctions	177
7.4.5	Icosahedral Junctions	178
7.4.6	Structures of High Genera	179
7.5	Periodic Schwarzites	180
7.5.1	D- and FRD-Type Schwarzites.....	180
7.5.2	P-Type Schwarzites.....	187
	Conclusions.....	188
	References.....	189
	Gallery of Carbon Nano Junctions and Derived Infinite Lattices	193
	Index	205

Foreword

Some twenty years ago, an article in *Nature* (London) announced the synthesis of the first fullerene. This fullerene was named C_{60} , and is also commonly known as *Buckminsterfullerene*. C_{60} was isolated *via* the self-assembled products of graphite heated by plasma. Later, the synthesis of nanotubes by the laser vaporization of graphite, led to a further increase in the family of nanostructures and heralded unprecedented perspectives for a new science and technology to impact humanity.

The coalescence reactions (illustrated by electronic microscopy) have shown that the nanoworld is continuous, giving rise to zero- (fullerenes), one- (tubules), two-(graphite) and three-(diamond, spongy carbon) dimensional carbon allotropes. Peapods are nanotubes doped with fullerenes (zero-dimensional cages) or longer capsules, formed inside the tube by coalescence of spherical units. Hetero-atomic nanostructures, containing boron, nitrogen, germanium, selenium, etc. have also been synthesized and studied.

Foam-like carbon structures, related to ‘schwarzites’, have been well documented and represent infinite periodic minimal surfaces of negative curvature. They contain polygons with dimensions larger than hexagons (w.r.t. to the graphite), that induce the negative curvature. Units of such structures appear as nanotube junctions, produced in an electron beam, with wide potential applications in molecular electronics. Self-assembling supra-molecular structures, of various tessellation, and diamond architectures, have also been recently proposed. The periodicity of close repeat units of such structures is more evident in these structures, but is also present in all the carbon allotropes.

Depending on the lattice tessellation, heteroatom type, and/or doping, metal nanostructures (nanotubes in particular) can be metallic or semiconductors. Therefore their properties can be changed by chemical functionalization. This has led to the improved performance of Li-ion batteries, capacitors, and field electron emitters in displays. Their use as tips in scanning tunneling microscopy (STM)

and atomic force microscopy (AFM) has introduced a new generation of nanoscale biological/chemical/physical devices.

This book is organized as follows.

Chapter 1 introduces the reader to the realm of periodic fullerenes, obtainable by coalescence reactions. It presents literature data and the authors own results on nanostructure building, and semiempirical and strain energy calculations. Novel dimeric and oligomeric structures predicted to appear via the coalescence of C_{60} molecules and the cages that could result by loss of carbon atoms from the starting molecules are the main subjects discussed herein.

Chapter 2 presents one of the most intensively studied carbon allotropes (entirely covered by a benzenoid lattice) namely the polyhex torus. Original methods of construction and tiling modification, nomenclature and correspondence to other nomenclatures are presented. Criteria for metallic and aromatic character properties are tabulated. Rules to identify identical polyhex toroidal graphs within families of chiral embedding isomers (furnished by the authors building method) are formulated in terms of the net dimensions. Resonance energy of polyhex tori is evaluated in the context of a generalized Clar theory of aromaticity.

Chapter 3 introduces a new class of toroidal structures, named Distinct Walled Tori (DWT), so called to indicate the varying number of atoms on the inner and outer walls, respectively. The energetics and aromaticity for various types of DWTs derived from armchair nanotubes or conical domains are presented. Diameter doubling of single-walled carbon nanotubes and zigzag nanotubes are also discussed.

Chapter 4 begins with a background on Graph Theory followed by defining some of the most discussed counting polynomials and the more recently proposed Omega and Cluj polynomials. Some theorems in the two latter named polynomials are discussed and demonstrated. Hosoya, Cluj, and Omega polynomials are detailed and used in the topological characterization and stability prediction of nanostructures: spherical, tubular, and toroidal. A *factorization* procedure, for describing the chiral polyhex tori in terms of Omega polynomial is presented.

Chapter 5 deals with the study of planar and 3D surfaces by various polygonal faces. Operations on maps and geometrical-topological transformation of a parent covering, are systematically introduced, from the simplest, through to composites, and up to generalized operations, which enable the embedding of various coverings in any surface. General analytical relations among the parameters of transformed and parent maps are presented. Molecular realizations of the proposed operations or sequences of operations are illustrated. Stone-Wales edge-rotations (related to map operations) are presented as possible routes of isomerization, enabling changes in the nanostructure tessellation.

Chapter 6 offers a detailed discussion on the aromatic character of fullerenes, with classical and non-classical covering. It is shown that aromatic character is a multi-conditional molecular property which can be dependent upon energetics, electronic structure, magnetic response, geometric characteristics, or chemical behaviour.^{16–18} It is shown that having a varied aromaticity criteria results in a random ordering of molecules. Generalized perfect Clar structures, with the 2-

factor designed as corannulenic or corazulenic disjoint flowers have been proven. Sequences of classical or single generalized map operations were used to obtain these coverings (also given as π -electron partitions within Kekulé valence structures). As a structural/geometric parameter of aromaticity, the HOMA index enabled an evaluation of local aromatic character of the featured supra-faces and thus generated evidence for several dominant Kekulé valence structures. The described operations and structures are believed to be helpful in the process of molecular structure elucidation and in guiding researchers in finding novel nanostructured materials.

Chapter 7 discusses triply periodic nanostructures and associated units which, by a self-assembly process, provide architectures of negative curvature, also known as schwarzites (or spongy structures). A short introduction to the theory of triply periodic minimal surfaces is offered. Unit blocks built up by opening map operations could model the junctions of carbon nanotubes; these can be synthesized by “nanowelding”, that is, crossing tubes in an electron beam. Junctions are rationalized according to the building operation. A gallery of junctions and triply periodic architectures is offered in the appendices. This book is aimed at scientists working in the field of nanoscience and nanotechnology, Ph.D. and MSc. degree students, and others interested in amazing nanoarchitectures, which could inspire the cities of the future.

* * *

Although each author contributed to the entire book, Chapters 1 and 3 were written by C. L. N. and Chapters 2, 4 to 7 by M. V. D. Each author takes responsibility only for the materials outlined in the chapters written by himself. The authors acknowledge the help of Dr. Aniela Vizitiu (contributing with objects and calculations to the sections: 3.2 and 7.4.3 to 7.4.6) and Dr. Katalin Nagy (with contributions to the Gallery). Many thanks are addressed to Prof. Tibor Braun, Hungarian Academy of Sciences, for his valuable advice and encouragement during the editing of this book.

Cluj, Winter, 2006

Mircea V. Diudea

Csaba L. Nagy

Chapter 1

Periodic Fullerenes by Coalescence Reactions

Short closed nanotubes are generated inside a SWNT by heating or irradiating “C₆₀ peapods”, where the C₆₀ molecules are encapsulated in the SWNT. According to transmission electron microscopy observations, the tubes capped with fullerene hemispheres have lengths of 13.7 and 21.2 Å when they consist of three and four C₆₀ molecules in size. End-cap effects as well as finite-size effects should play an important role in determining their electronic and geometrical properties. The study of reaction pathways in fullerene fusion is of high interest as it may reveal the isomeric population of isolated substances. Capped nanotubes represent yet isolated nanostructures and represent the final products of fullerene coalescence.

1.1. Fullerene Fusion via Stone-Wales Transformation

1.1.1. Fullerene Dimers and Their Derivatives

The first dimeric fullerene C₁₂₀ was synthesized by using light irradiation. Applying visible or ultraviolet light to a film of solid C₆₀ resulted in a polymer. The X-ray study of the photo-transformed film has shown a contraction in the fullerene lattice, found less than two van der Waals radii between the C₆₀ cages. It was supposed that a covalently bonded [2 + 2] cycloadduct (involving *sp*³ hybridized carbon atoms in the junction) of two *quasi*-spherical molecules is formed.¹ Later, by simultaneous application of high pressure and temperature, C₆₀ was converted into two different structures: a face-centered-cubic structure (300–400°C and 5GPa) and a rhombohedral structure (500–800°C and 5GPa). Further theoretical and experimental studies proved that the dimeric C₁₂₀ has a structure in which the two fullerene cages are connected through a four-fold ring, closed by a cycloaddition over two *h*-bonds.² We call an *h*-bond the one shared by two hexagons and a *p*-bond that shared by pentagon-hexagon.

A synthesis of C_{120} , using KCN as a catalyst, has been described³ and the resulting structure was assigned by X-ray analysis and ^{13}C NMR spectroscopy. It was suggested that C_{120} can be taken as a subunit of the C_{60} polymers.

Since KCN is a highly toxic substance, a different preparation method was elaborated, with the catalyst being Li powder. Small amounts of LiOH or Li_2CO_3 increased considerably the yields. Using the same method for polymerization of C_{70} failed, proving that C_{70} is not as easily polymerized as C_{60} . Raman spectra of C_{120} exhibit similar patterns with the dimeric oxides $C_{120}O$ and $C_{120}O_2$.⁴

Among the 1812 topologically possible structures of C_{60} , the most stable is that in which all p edges are formally single bonds and all h edges are double. That is why, in C_{120} dimer, the bridge formation is favored when it originates in a formal double bond, leaving the rest of the Kekulé valence structure unaltered. It was stressed that, the experimental factor deciding the preferable dimeric isomer is the mutual orientation of the two parent molecules, rather than the dimer stability.⁵

Keeping in mind the two types of bonds involved, the cycloaddition of C_{60} will result in four different (sp^3 -joined) isomers (Figure 1-1): (i) hh ; (ii) hp ; (iii) $pp-c$ and (iv) $pp-t$. In the last two isomers, the two pentagons lie on the same side (*cis*) or they are opposite (*trans*), with respect to the junction ring.

Fullerene derivatives have attracted great attention of synthesists. Oxygen derivatives represent an important class of functionalized fullerenes, with particular applications (*e.g.*, precursors of odd-numbered fullerenes, production of singlet oxygen, *etc.*).

The first observed fullerene oxide was $C_{70}O$, an epoxide of $D_{5h}C_{70}$. The decay of $C_{70}O$ into C_{70} suggested that the oxygen is located on the external surface of the cage. ^{13}C NMR data suggested a structure of C_{2v} symmetry, with the epoxy group across an h double bond. Synthesis of $C_{60}O$ was performed by the ozonolysis of C_{60} solution in CS_2 ; its structure is analogous to that of $C_{70}O$ (Figure 1-2a,b).

The dimeric monoxide $C_{120}O$ was prepared, in solid phase, by heating a $C_{60}/C_{60}O$ mixture, at 200°C. This synthesis was also performed in solution, but the

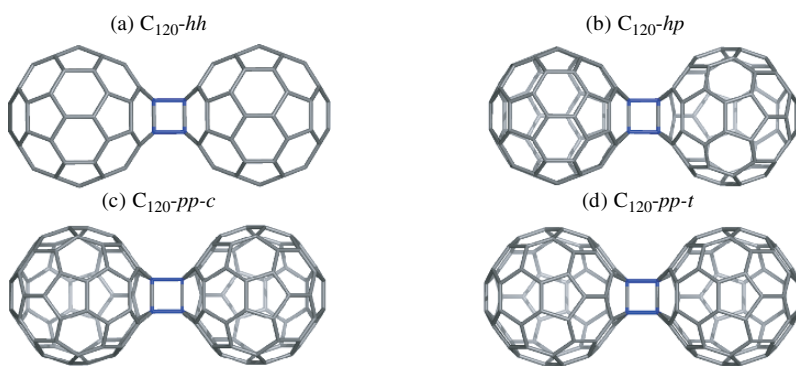


Figure 1-1. The four possible C_{120} sp^3 dimers resulted by (2+2) cycloaddition.

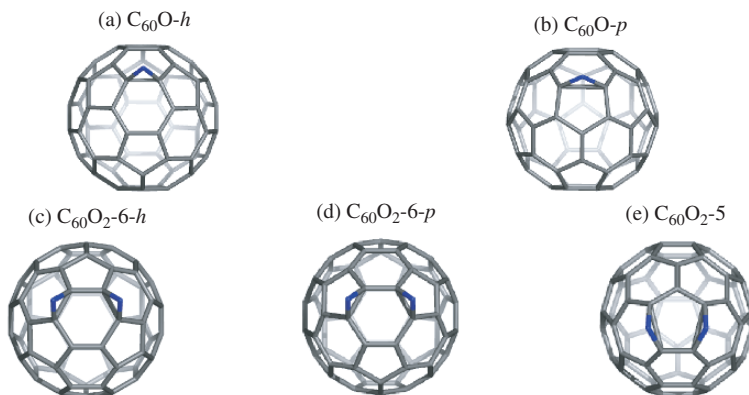


Figure 1-2. $C_{60}O$ and $C_{60}O_2$ fullerene epoxides.

yields were much lower. Similarly, the ozonolysis of a C_{60} solution, led to a mixture of $C_{60}O$ and higher oxides $C_{60}O_n$ ($n > 1$, Figures 1-2,c-1-2,e), next separated by the HPLC method. The reaction products were analyzed and characterized by UV-VIS, FT-IR and MALDI-TOF MS. In the mass spectrum of the isolated product, the peak of $C_{120}O$ appeared (together with the peaks of C_{60} and $C_{60}O$, eventually resulted by the fragmentation of $C_{120}O$).⁶

The structure assignment for $C_{120}O$ was analogous to that for the dimer C_{120} ; actually, a furan like bridge is formed between two h bonds of each cage (Figure 1-3a). For this, a [3+2] cycloaddition mechanism was proposed. CO and CO_2 were also detected, by heating the product over $400^\circ C$, and the peak of C_{119} appeared in the mass spectrum as well. It was proposed that $C_{120}O$ is the precursor of the odd-numbered fullerene C_{119} .

The thermolysis of solid $C_{120}O$, in argon atmosphere at $400^\circ C$ and normal pressure, led to the dimeric dioxide $C_{120}O_2$, along with other oligomeric oxides $(C_{60})_nO_m$ ($n = 3-5$, $m = 3-9$). $C_{120}O_2$ was separated by HPLC and characterized by MALDI-TOF MS, UV-VIS, and FTIR. The mass spectrum of $C_{120}O_2$ evidenced C_{60} and $C_{60}O$ as major fragmentation ions. The ^{13}C NMR spectra suggested a structure of C_{2v} symmetry.⁷

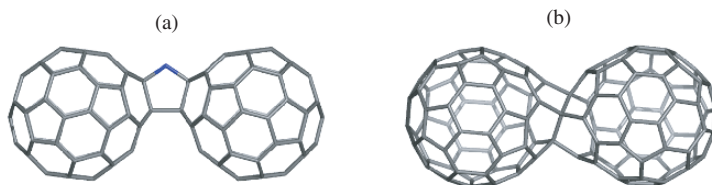


Figure 1-3. $C_{120}O$ (a) and the corresponding odd-numbered fullerene C_{119} (b) resulted by the loss of CO or CO_2 .

Two different structures, having the two cages bis-linked by adjacent furanoid rings, have been proposed. In the first case, the furanoid bridges are attached at the sites of neighboring *h* bonds in each parent cage (Figures 1-4a,b), while in the second one, *p* junctions are involved in the linkage (in this last case the carbon frame is that of C_{120-hh}).

Another method for preparing $C_{120}O_2$ is the thermal transformation of a $C_{60}/C_{60}O/C_{60}O_2$ system, in solid state.⁸ $C_{60}O_2$ was prepared as a mixture of regio-isomers during ozonolysis of C_{60} . The mixture was heated at 200°C under argon, resulting, beside $C_{120}O$ and $C_{120}O_2$, a trimeric product, $C_{180}O_2$. The ^{13}C NMR analysis detected two isomers of $C_{120}O_2$, with C_1 symmetry, in 4:1 ratio, different from the one above discussed. Spectroscopic data suggested these isomers are closely related to $C_{120}O$, probably one of its epoxides. Again, the dimeric $C_{120}O_2$ can result by two ways: (i) the cycloaddition of one $C_{60}O$ molecule across a *h* double bond of another $C_{60}O$ one, or (ii) the cycloaddition of $C_{60}O_2$ to C_{60} via one of the two epoxy groups. Regio-isomers of $C_{60}O_2$ and $C_{120}O_2$ have been modeled and the lowest energy isomers were found to have the epoxy group in the proximity of the furanoid bridge (Figures 1-4c,d). The *cis*-1 *anti* structure (nomenclature according to ref.⁹) can rearrange by opening the epoxy cycle to the proximal *h* bond of the other cage, resulting the bis-linked structure ($C_{2v}C_{120}O_2$). The other possible regio-isomers of $C_{120}O_2$ can easily react with molecules of C_{60} to form $C_{180}O_2$, since the epoxy group is sterically accessible.

Similar to $C_{120}O_2$, the first sulfur containing dimeric fullerene, $C_{120}OS$, was prepared. The synthesis was performed either by the thermal reaction of a 1:1 mixture of solid $C_{120}O$ and elemental sulfur at 230°C under argon, or by heating of $C_{60}/C_{60}O$ system with sulfur.¹⁰

The mass spectra of the reaction product also revealed C_{60} , $C_{60}O$ and $C_{60}S$. Molecular modeling has shown that the lowest energy structure is that having an oxygen atom in one of the furanoid rings in $C_{2v}C_{120}O_2$ replaced by sulfur. This can

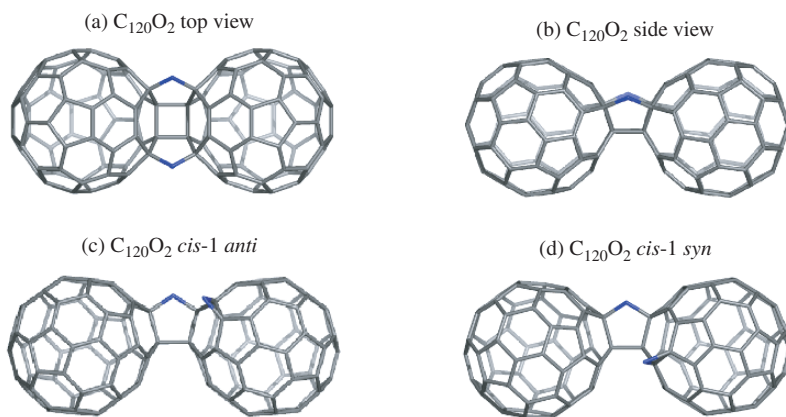


Figure 1-4. C_{60} cages connected by furanoid ring(s) attached to *h* junctions in each cage.

result from $C_{120}O$ by addition of a sulfur atom to the h double bond next to the furanoid ring, followed by thiophene bridge formation.

As mentioned above, signals for odd numbered fullerenes (C_{119} , C_{129} and C_{139}) were observed in the mass spectra of fullerene oxides. These species correspond to dimers of C_{60} , C_{60}/C_{70} and C_{70} , respectively, less one carbon atom. Since the loss of a carbon atom in the reaction of two cages would be thermodynamically expensive, it was supposed that oxygen is involved, because loss of CO or CO_2 could be the driving force of the reaction. For this, fullerene solution was exposed to ozone; the experiments have confirmed the above hypothesis.¹¹

On the ground of semiempirical calculations, a peanut structure of C_2 symmetry, where two equivalent C_{58} cages are connected by a bridge of three four-connected carbons, was proposed. Later, calculated Raman spectra for a series of C_{119} fullerenes with C_2 symmetry were compared with the experimentally obtained spectra. The conclusion was, the prepared isomer is indeed the thermodynamically most stable one, as proposed earlier (Figure 1-4b).¹²

1.1.2. Theoretical Considerations About Fullerene Fusion

At the pioneering age of fullerene science, it seemed impossible the merging of two (spherical) units to form a larger structure, by the reason that bond breaking requires high energy. Later, the coalescence of fullerenes has been reported as an experimental fact and modeled in view of understanding non-obvious details. The observed diameter doubling of carbon nanotubes was interpreted as a lateral coalescence of such suitably aligned objects.

The first coalescence experiment was performed by laser desorption of a C_{60} film.¹³ In another experiment, C_{120}^+ appeared by collision between C_{60} and C_{60}^+ . Further studies found that the fusion barrier lies in the region between 60 and 80 eV and increases as the number of atoms participating to the collision increases.^{14,15}

It is quite difficult to assign structures to such coalesced fullerenes. Theoretical studies have proposed several classes, including peanut-shaped dimers or cylindrical tubulenes, the most studied dimer being C_{120} . Atomically precise routes for complete coalescence of fullerene cages have been presented.

A class of all sp^2 peanut-shaped structures can be constructed by connecting the caps $C_{60}(6(56)^3(665)^3(656)^3(*6)^3-A[12,0])$ and $C_{60}(6(56)^3(665)^3(656)^3(5*)^3-A[12,0])$, derived from C_{60} by deleting the three p and h edges, respectively, of a hexagonal polar ring (Figures 1-5a,b). The asterisk in the above symbols denotes the missing polygon(s).¹⁶

The free valences of the caps will be connected to another unit, avoiding the formation of four-membered rings. The three resulting peanut dimers are denoted by the complementary edges remaining in the cut polar ring (Figures 1-5c-1-5e).

The construction of our all sp^2 peanut-shaped dimers makes use of quite different caps: $C_{60}(56^5(56)^5(65)^5(1*)^5-Z[10,0])$ and $C_{60}(6(56)^3(665)^3(656)^3(*1)^6-Z[12,0])$ with "1" denoting the dangling bonds (Figures 1-6a,b). The short symbols are C_{60} -*pd*-cap and C_{60} -*hd*-cap, respectively. It is easily seen that the number of dangling bonds

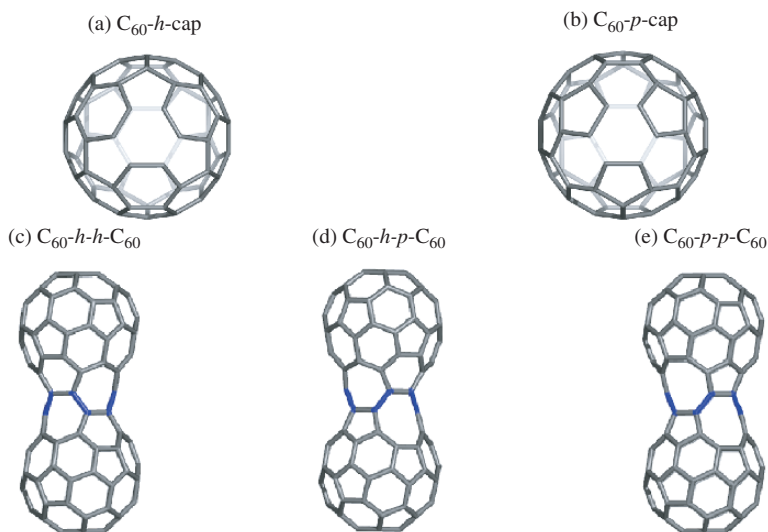


Figure 1-5. Caps derived from C_{60} and the all sp^2 corresponding peanut dimers. The junction between the two caps is of armchair A type.

equals the size of the polar ring, the mixing caps being thus prohibited. The isomers are named $C_{120}(56^5(56)^5(65)^57^57^5-Z[10,1])$ and $C_{120}(6(56)^3(665)^3(656)^3(67)^3(76)^3-Z[12,0])$, according to the tubulene nomenclature, proposed by us in ref.¹⁷. The proposed short symbols, specifying the junction covering, are C_{120-77} and C_{120-67} , respectively (Figures 1-6c,d).

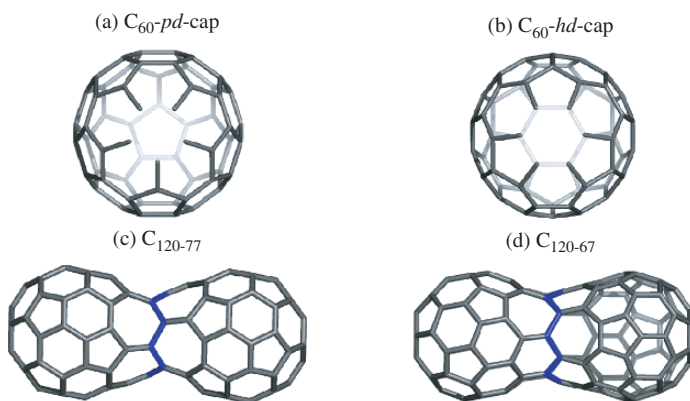


Figure 1-6. Caps resulted by elimination of all bonds in a pentagon or hexagon and the corresponding peanut dimers. The junction between the two caps is of zig-zag Z type.

Topological analysis suggests that the merging process of two fullerene molecules can be achieved by a sequence of Stone-Wales SW bond rotations. The first step in the coalescence is the formation of a $[2+2]$ (sp^3 -joined) cycloadduct. An intermediate step is the formation of all sp^2 C_{120-77} peanut structure, subsequent SW bond flipping, in a circumferential order, transforms the heptagon-pentagon junction into a hexagonal (6,3) covering (see below). In case when C_{60} coalesced from a different orientation, the process was believed to stop at a peanut shaped structure. In view of the negative curvature relief (in the junction zone) a complete restructuring of the end caps is required. In this way, abutting pentagons could occur, which considerably raises the energy barrier.¹⁸

Similar coalescence paths were recently proposed for several tubulenes having a pentagonal polar ring: (a) two nanotubes $A[10,n]$ capped by $C_{30}(5\ 6^5(5\ *)^5-A[10,0])$, with an energy barrier of 3.7eV; (b) two $A[20,n]$ nanotubes capped by $C_{90}(5\ 6^5\ 6^{10}\ 6^{15}(5\ *)^5-A[10,0])$, requiring 8eV; and (c) the fusion of C_{60} with the tubulene resulted as described at point (b).¹⁹

T-shaped junctions can result by cap-to-wall coalescence, involving SW flipping. Recently, a process of C_{60} penetration through the wall of a nanotube, to form a peapod, was described.²⁰

The SW edge rotation is known to have a high energy barrier; however, the overall process is exothermic. The reason is that the strain energy of a spherical cage (*i.e.*, fullerene) is much higher than that of a (capped) tube (*i.e.*, tubulene), thus the energy gain, associated with a reduced local curvature, provides the driving force of the coalescence, up to the cylindrical tubulene.

Using a graphical search program, a 23 SW steps topological pathway, from the hh $[2+2]$ cycloadduct to the C_{120} tubulene, was found. The same tubulene is obtained when the SW cascade process starts from the C_{120} - pp - t cycloadduct.²¹

It was believed that, the initial $[2+2]$ cycloaddition pays the most energy cost in the process of coalescence, probably being the rate-limiting step. For this first step, the proximity of two double bonds in each fullerene is necessary. At lower temperature, polygons rather than double bonds should preferentially face to each other, preventing the fusion. Only at high enough temperature, fullerene cages start to rotate, making effective the bond to bond addition. In bulk reaction, C_{60} molecules may undergo multiple coalescence reaction. It is possible that further SW transformation of one connection to interfere with another fusion process on the same fullerene cage, which would probably stop the fusion. Such reactions will be restrained in the case of one-dimensional space (*e.g.*, in nanopeapods, with the cages aligned in a chain), where polymerization is possible only on the opposite faces of a cage.²²

Note that the activation barrier of a Stone-Wales transformation is significantly lower in non-planar structures in comparison to the graphite, due to the pyramidalization of sp^2 atoms. However, the presence of hydrogen atoms stabilizes the transition state in the SW rotation, and reduces the energy barrier to 4.1 eV.²³

1.1.3. Coalescence in Peapods

The knowledge about the structural diversity of carbon allotropes has recently been enriched by the discovery of nanopeapods, a hybrid structure consisting of fullerene molecules encapsulated in single-walled nanotubes. The symbol for such structures is inspired from the endohedral metal doped fullerenes: for example $(C_{60})_n@SWNT$ is for the C_{60} nanopeapod.²⁴

Nanopeapods represent a promise for new applications. For example, a positively charged C_{60}^+ molecule inside a nanocapsule could serve as a *memory element*, in which the position of the ion encodes the information. An important aspect is that fullerene molecules can rotate freely in the space of the tube at room temperature, and this rotation will affect the peapod electronic properties significantly.²⁵

A nanopeapod can be considered as a nano-furnace in which the coalescence of fullerenes can be monitored (see below). Usually they are prepared in gas phase at 400°C or higher,²⁶ when C_{60} molecules sublime and enter the SWNTs from the open ends or sidewall defects. In liquid phase, the affinity of the solvent to the tube and fullerenes dictates the direction of the process.²⁷

By pulsed laser vaporization of graphite, in the presence of a metal catalyst, besides carbon nanotubes, also appear C_{60} molecules. Although C_{60} and other residues are separated from nanotubes, it was suggested that fullerene molecules might be encapsulated inside the nanotube. This was confirmed by high-resolution transmission electron microscopy HRTEM. It was observed that the fullerene molecules are arranged in a chain at a nearly uniform distance from each other. By exposure at an electron beam, fullerenes inside the nanotube coalesce into larger capsules, capped by C_{60} halves. The length of such capsules corresponds to three-four fullerene units, and the diameter is constrained by the outer nanotube dimensions.²⁸

After the insertion of fullerene molecules inside nanotubes in vapor phase, it is difficult to reverse the process by heat treatment. The fullerene array is stable up to 800°C and further heating induces coalescence, rather than un-doping. The coalescence process becomes more rapid as the temperature increases, and it completes around 1200°C. The diameter of the inner tube was found to be smaller by 0.71 nm than the outer nanotube. Thus, the growing of the inner tube is dependent on the size of the doping fullerene.²⁹

To elucidate intermediates in the transformation of nanopeapods to double-walled nanotubes DWNT (Figure 1-7), the heating was performed at low temperatures (800–900°C) and for a much longer time (200–300 hours). The growth of the inner tube was monitored by Raman study. After a short heating period the inner tube diameter corresponds to that of C_{60} . This is the result of the polymerization of adjacent C_{60} molecules. Further heating induces the increase of the inner tube diameter until the difference between the inner and outer tube fits the van der Waals distance.³⁰

In case of C_{60} , the polymerization takes place easily because the probability of having two fullerenes oriented in a preferential way is high, as expected by the

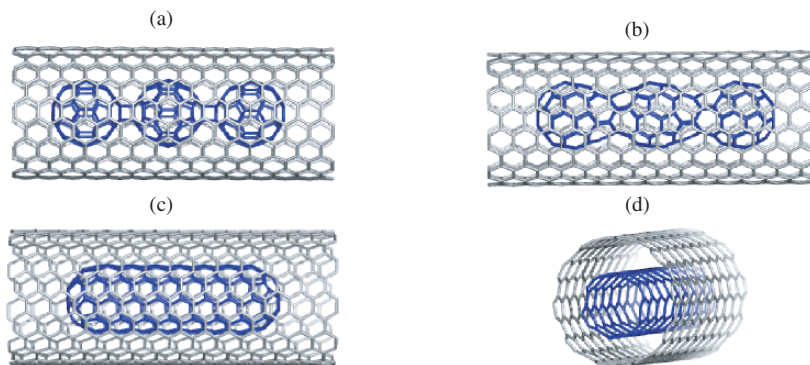


Figure 1-7. From the [2+2] cycloadduct of C_{60} (a), to peapods (b, c) and double walled nanotube DWNT (d).

free rotation of C_{60} . But when C_{70} was heated at 800°C polymerization proceeded very slowly, and most of the C_{70} molecules were found untransformed. This could be explained by that, the C_{70} molecules must arrange in a zigzag way as the polymerization to take place. Indeed, the Raman spectrum indicated a larger inner tube than in the case of C_{60} .

As above mentioned, the dimer of C_{60} can be considered as a subunit in further polymerization. Therefore, the dimer must have h bonds at the both tips, since it cannot rotate freely, anymore. If the resulted dimer has a C_{60} like cap, with a pentagon at the tip, no further polymerization is expected to occur. It was proposed that, instead of C_{120} , the primary unit be C_{114} , which has C_{60} -like caps but with hexagons at the tip. For this, at every merging step, six carbon atoms have to be released, eventually moved around the inner tube. It is expected that tube diameter transformation occurs by the expense of these migrating carbon atoms.

Besides the thermal annealing, fullerenes can easily coalesce by electron irradiation. Under such conditions, carbon atoms are displaced from the fullerene cage by knock-on effects. The formation of vacancies and dangling bonds increase considerably the energy of the system, but the formation of fully coalesced products up to double walled nanotube will finally stabilize the system. Theoretical studies have proposed that such inside tubes contain heptagons and octagons, acting as links between fullerene cages, like in peanut dimers. These internal corrugate carbon nanotubes resemble to the Haeckelite structure. The topology of junction depends of the initial orientation of the molecules.³¹

1.2. Results and Discussion

In the following, we present our own results, on nanostructure building and semiempirical and strain energy calculations, a comparison between the previously proposed structures for fullerene epoxy dimers and our epoxides built up on coalesced

fullerenes; novel dimeric structures possibly appearing in the coalescence of C_{60} molecules, and cages that could be formed by loss of carbon atoms from the starting molecules.

1.2.1. The sp^3 Adducts: C_{120} , $C_{120}O$ and $C_{120}O_2$

It was discussed above that functionalized dimeric derivatives are synthesized from a mixture of $C_{60}/C_{60}O_n$. In the following we propose a pathway, analogous to that for the coalescence of fullerenes, leading to epoxy tubulenes.

First we have modeled the C_{60} epoxides to find out which is the preferential position of the oxygen atoms. If we consider the C_{60} molecule as a Kekulé structure with alternating single and double bonds, the oxygen atom will bound to one of these double bonds (h bond). We found that the position of the oxygen atom does not influence very much the stability of the coalesced dimer (Table 1-1).

Among the C_{120} dimers presented in Figure 1-1 the most stable is the hh isomer. The energy of dimers increases with the number of p bonds involved in the cycloaddition. The data listed in Table 1-2 are comparable to those reported in literature.

The isomers of $C_{120}O$ (Figure 1-8) are constructed by analogy to the C_{120} dimers; actually, the four-membered ring is replaced by a furanoid bridge. The isomers are named similarly to C_{120} dimers.

Table 1-1. PM3 data for C_{60} and isomers of $C_{60}O_n$; $n = 1, 2$

Name	ν	Sym	HF/ ν (kcal/mol)	GAP (eV)
C_{60}	60	I_h	13.512	6.594
$C_{60}O-p$	61	C_s	12.857	6.412
$C_{60}O-h$	61	C_{2v}	12.964	6.446
$C_{60}O_2-5$	62	C_s	11.989	6.293
$C_{60}O_2-6-p$	62	C_s	12.757	6.388
$C_{60}O_2-6-h$	62	C_s	12.389	6.491

Table 1-2. PM3 data for the dimeric $C_{120} sp^3$ cycloadducts

Name	ν	Sym	HF/ ν (kcal/mol)	GAP (eV)
hh	120	C_{2v}	13.204	6.349
ph	120	C_s	13.373	5.854
$pp-c$	120	C_{2v}	13.544	5.749
$pp-t$	120	C_2	13.542	5.707

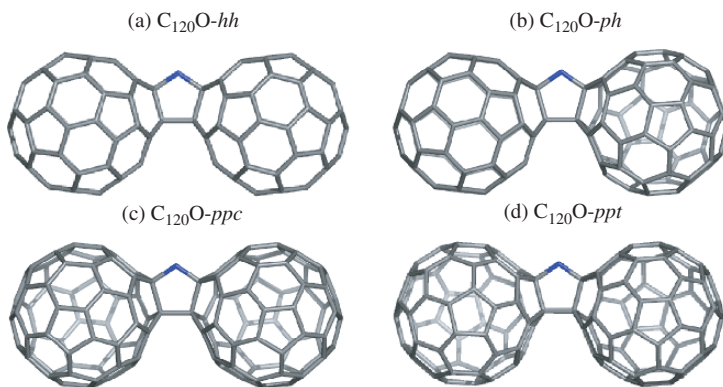
Figure 1-8. Structural isomers of $C_{120}O$.

Table 1-3 lists the results of semiempirical calculations performed on the four isomers in Figure 1-1. They are in agreement with the literature data, the most stable being the isomer $C_{120}O$ -*hh*, with C_{2v} symmetry. Note that their heat of formation increases as more *p* bonds are involved in the furanoid ring.

The construction of all possible dimers, containing two oxygen atoms, was done keeping in mind the following: there are four dimers of C_{120} , linked by a four-membered ring and the furanoid bridges are adjacent to this ring. If the two furanoid rings are on the same side of the four-membered ring, the isomer is denoted *cis*, while they are in the opposite sites, the structure is named *trans*. Thus, for each C_{120} dimer there are at least two possible structures of formula $C_{120}O_2$. In the case of *hp* and *ppc* dimmers, because there are different bond types on the two sides of the cyclobutane ring, one more dimer is possible. All together, ten structural isomers of $C_{120}O_2$ formula can be constructed (Figure 1-9). All carbon atoms involved in the junction are sp^3 hybridized.

Calculations, carried out on the ten isomers in Figure 1-9, are presented in Table 1-4. Once again, the heat of formation decreases with the number of *h* bonds involved in the furanoid bridges, the most stable being $C_{120}O_2$ -*hph/hph-c*. Again the dimer C_{120} -*hh* was the lowest energy isomer.

Table 1-3. PM3 data for the furanoid $C_{120}O$ sp^3 isomers

Name	ν	Sym	HF/ ν (kcal/mol)	GAP (eV)
$C_{120}O$ - <i>hh</i>	121	C_{2v}	12.793	6.356
$C_{120}O$ - <i>ph</i>	121	C_1	12.944	5.888
$C_{120}O$ - <i>ppc</i>	121	C_s	13.095	5.837
$C_{120}O$ - <i>ppt</i>	121	C_1	13.094	5.832

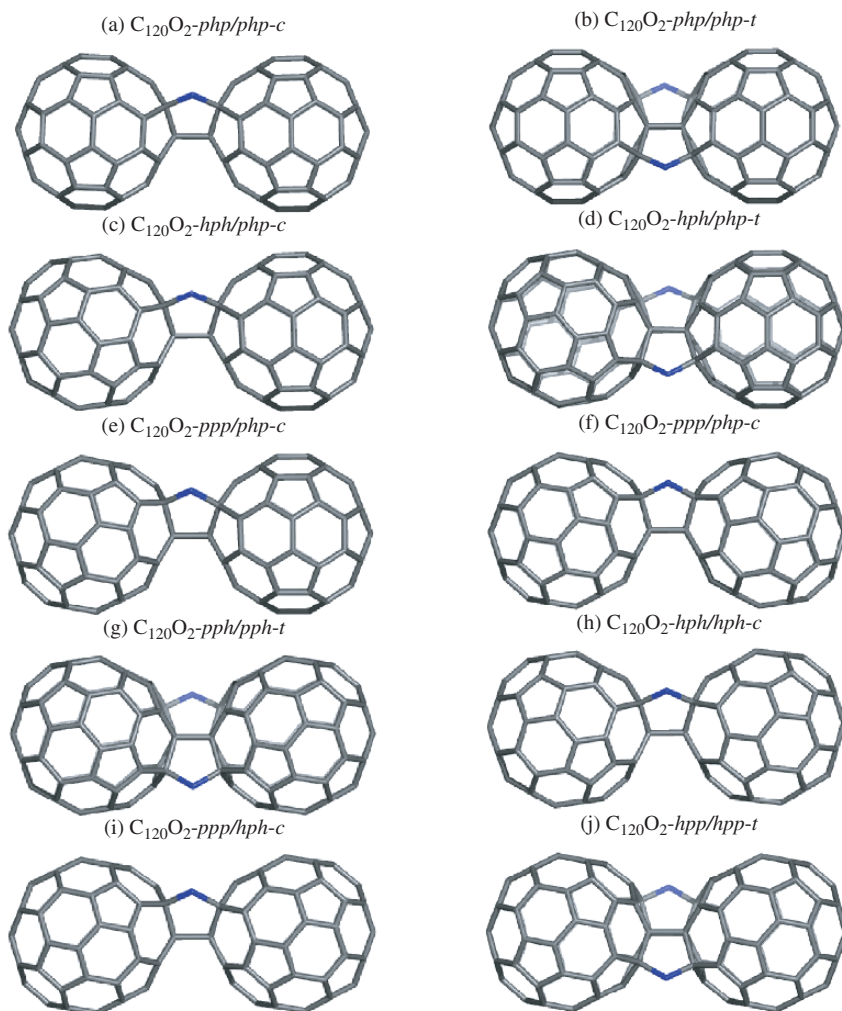


Figure 1-9. The ten possible sp^3 -joined isomers of $C_{120}O_2$ connected by a pair of furanoid bridging rings.

The initial cycloaddition between C_{60} and $C_{60}O_n$ molecules takes place in such a manner, the further transformation to a $C_{120}O$ tubulene could be possible (see below).

1.2.2. Coalescence by Stone-Wales Bond Flipping

Interconversion of fullerene isomers is possible by rotation of atom pairs in the molecules about their mutual bond centre. Such atomic rearrangement, called Stone-Wales (SW) or pyraclenic transformation,³² is suitable for describing the coalescence between fullerenes and/or nanotubes.

Table 1-4. PM3 data for $C_{120}O_2$ sp^3 isomers

Dimer	Isomer	ν	Sym	HF/ ν (kcal/mol)	GAP (eV)
<i>hh</i>	<i>php-php-c</i>	122	C_{2v}	12.257	6.414
	<i>php-php-t</i>	122	C_{2h}	13.168	2.680
<i>hp</i>	<i>hph-php-c</i>	122	C_S	12.184	6.437
	<i>hpp-php-t</i>	122	C_1	12.771	3.231
	<i>ppp-php-c</i>	122	C_S	12.604	5.689
<i>ppc</i>	<i>ppp-ppp-c</i>	122	C_{2v}	12.828	5.645
	<i>hph-hph-c</i>	122	C_{2v}	12.109	6.467
	<i>pph-pph-t</i>	122	C_S	12.433	5.878
<i>ppt</i>	<i>hph-ppp-c</i>	122	C_S	12.533	5.695
	<i>hpp-hpp-t</i>	122	C_I	12.486	5.866
	<i>cis-1 syn</i>	122	C_1	10.148	6.332
	<i>cis-1 anti</i>	122	C_1	10.170	6.318

The initial orientation of the two cages will affect the pathway of the coalescence. But, regardless of the starting cycloadduct, the very first steps are similar, leading to all sp^2 peanut-shaped dimers. Further, there are several ways for completing transformation up to the perfect tubulene (*i.e.*, tessellated by only hexagons and pentagons). The interconversion among various coalesced species is also possible. The energy diagram of the SW transformation of the four cycloadducts of C_{60} to the corresponding peanut dimers is presented in Figure 1-10. The lowest energy peanut dimer is C_{120-77} (Figure 1-6c). Geodesic projections of lattice transform of C_{60} upto its peanut dimer are given in Figure 1-11.

A series of C_{120} epoxy derivatives, which energy varied with the location of the oxygen atom, has been modeled.³³ The most stable isomers $C_{120}O$ and $C_{120}O_2$ are shown in Figure 1-12.

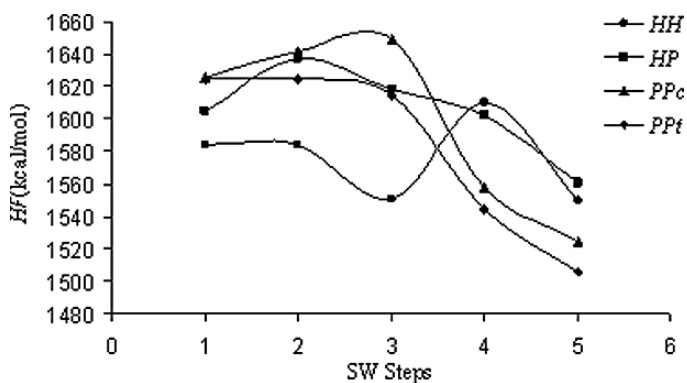


Figure 1-10. Energy diagram of the SW transformation from sp^3 cycloadducts to sp^2 peanuts, in case of C_{60} . HF/ ν .

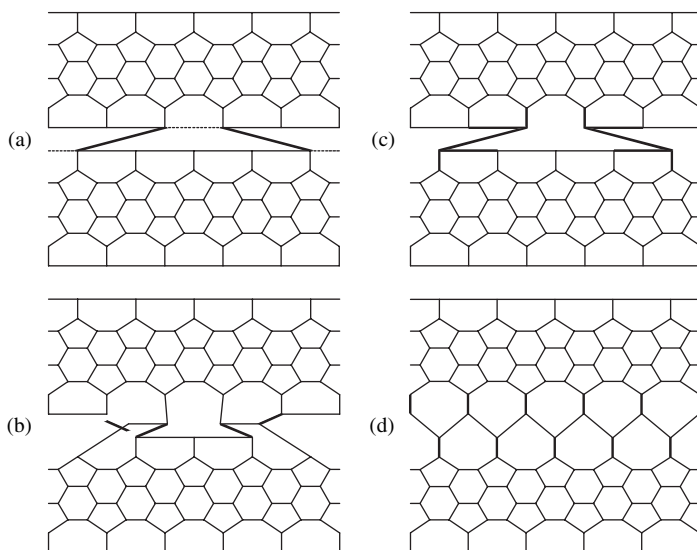


Figure 1-11. The complete lattice transformation, from [2+2] cycloadduct to peanut dimer, in case of C_{60} .



Figure 1-12. The most stable epoxy and di-epoxy dimeric tubulenes derived from C_{60} .

The energy difference between the C_{120} dimer and $C_{120}O_n$ epoxy derivatives is almost constant at every SW step, as shown in Figure 1-13.

A question arises about the proper route, if trimerization or oligomerization occurs. The transformation of a junction could terminate at a peanut shape, which results in an oligomer with multiple necks, or it could continue until a perfect tubule is formed. Figure 1-14 illustrates such possibilities in the coalescence of four C_{60} molecules.

Table 1-5 lists semiempirical data for both trimers and tetramers of C_{60} . It can be seen that, the heat of formation HF increases as the number of necks in oligomers increases. Thus, it seems that a new cycloaddition is favored only after the tubular shape was reached. The energy gain can be associated with the relief of strain originating in the negative curvature of the necks. However, in nanopeapods

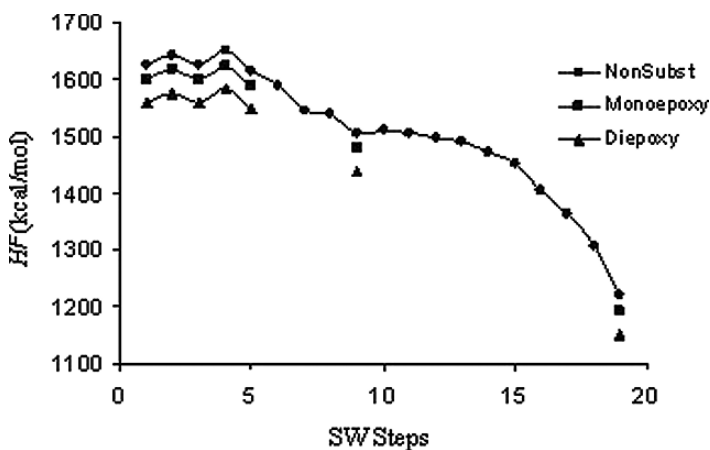


Figure 1-13. Comparative coalescence energy plot for C_{60} , $C_{60}O$, and $C_{60}O_2$ molecules.

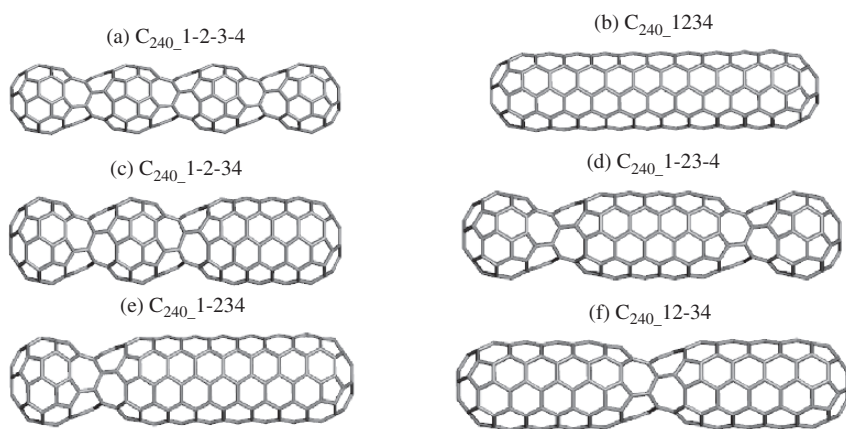


Figure 1-14. Multi-necked peanut and tubular tetramers of C_{60} .

annealed at moderate temperature, corrugated tubules could be seen by TEM.³¹ The strain relief is obtained at higher temperature, when DWNT is obtained.³⁰

The $C_{120}(56^5(56)^5-A[10,6])$ dimeric armchair tubulene is the ultimate dimeric structure, irrespective of the starting cycloadduct (Figure 1-15a).

In the study of SW transformation of peanut dimers we found pathways leading to armchair or zigzag tubulenes, having pentagons or hexagons as the polar ring. Such tubulenes have also been identified by molecular dynamics.³⁴

Figure 1-15 illustrates several C_{120} dimers (where the dimer is a tubulene). These dimers have a properly closed shell, associated with a perfect Clar PC structure (see

Table 1-5. PM3 data for all sp^2 C_{60} trimers and tetramers; the dashed line denotes a neck

Name	ν	Sym	HF/ ν (kcal/mol)	GAP (eV)
C_{180_1-2-3}	180	D_{5d}	12.224	5.917
C_{180_12-3}	180	C_5	10.602	4.830
C_{180_123}	180	D_{5d}	9.052	4.057
$C_{240_1-2-3-4}$	240	D_{5d}	12.062	5.819
C_{240_12-3-4}	240	C_5	10.846	4.831
C_{240_1-23-4}	240	D_{5d}	10.826	4.870
C_{240_123-4}	240	C_5	9.663	4.088
C_{240_12-34}	240	D_{5d}	9.630	4.791
C_{240_1234}	240	D_{5d}	8.500	3.697

Table 1-6. PM3 data, strain energy SE and spectral data for C_{120} cages in Figure 1-15

	ν	Sym	HF/ ν (kcal/mol)	Gap (eV)	SE/ ν (kcal/mol)	Spectral Data	
						$x_{\nu/2}$	$x_{\nu/2+1}$
(A)	120	D_{5d}	10.156	4.793	5.162	0.310	-0.061
(B)	120	D_{5h}	10.271	3.706	4.664	0.319	0.319
(C)	120	D_{5d}	10.175	5.789	4.903	0.521	-0.099
(D)	120	D_{6d}	9.8195	5.015	4.788	0.350	0.000
(E)	120	D_{6d}	9.9375	4.587	4.504	0.402	0.336
(F)	120	D_{3d}	10.295	4.419	4.928	0.271	0.137

below). Their HF is similar but there is a considerable difference in the HOMO-LUMO gap, the highest values corresponding to those structures which are PC. Tubulenes with hexagonal polar rings have a more relaxed surface, as it can be seen by the strain energy values. Data are summarized in Table 1-6.

Further transformation of $C_{120(56^5(56)^5-A[10,6])}$ is possible, leading to different tubulenes. Because of similar H_f , a mixture of the molecules shown in Figure 1-15 is expected. Figure 1-16 gives the energetic plot of some SW transformations, starting from $C_{120(56^5(56)^5-A[10,6])}$ and $C_{120(66^6(56)^6-A[12,4])}$.

1.2.3. Pathway to C_{114} Tubulene

It was mentioned above that, the primary coalescence products can further polymerize only if the formation of a new cycloadduct between two h bonds is possible. In this respect, it is required that dimeric structures have hexagons at both ends. The tubulene that preserves the position of pentagons as in C_{60} would be C_{114} , which corresponds to a polar face distance of ~ 1.3 nm, as measured by TEM in nanopeapods. The formation of such a unit involves the displacement of six carbon

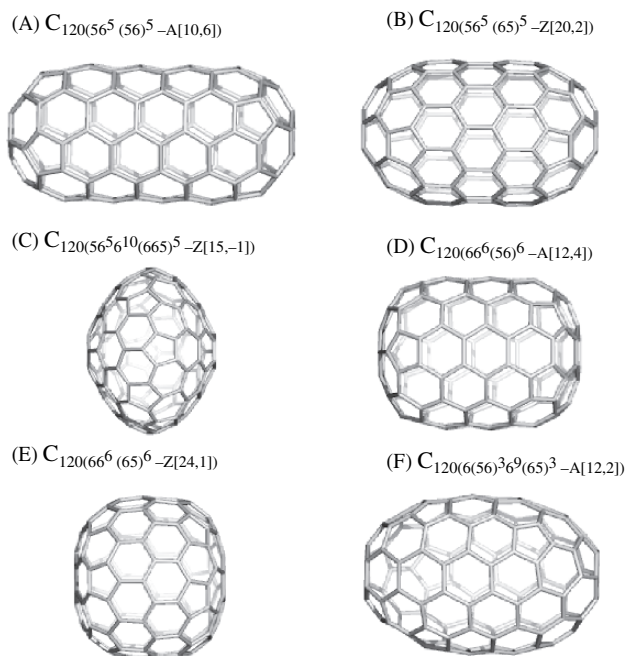


Figure 1-15. Dimeric cages possibly appearing in the coalescence of C_{60} .

atoms per junction. Here we propose a possible way to C_{114} which includes several SW steps (Figure 1-17).

Electron beam irradiation could result in defects of nano-lattice so that the coalescence is promoted (see the next section for merging nanotubes). By controlled irradiation, the displacement of three carbon atoms from a hexagonal face would

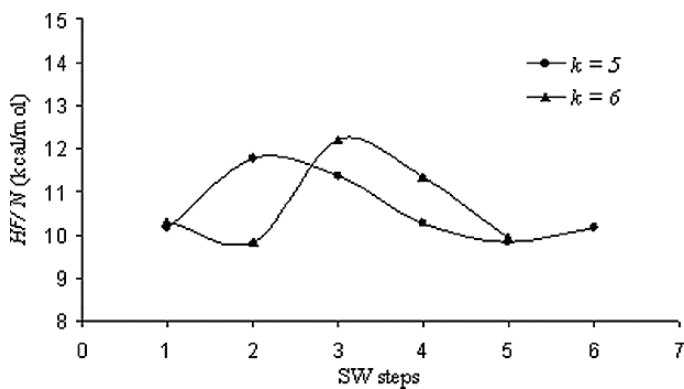
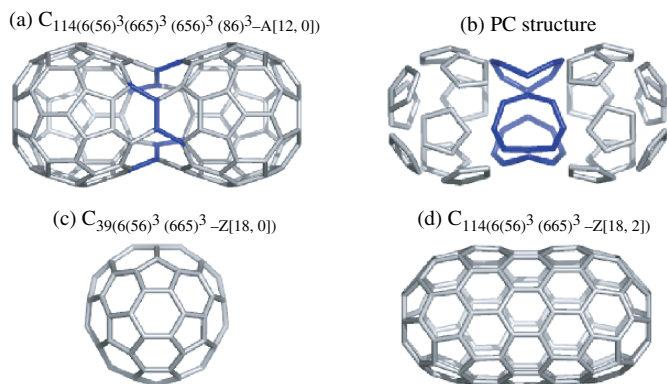


Figure 1-16. Energetic diagram of the SW interconversion of the objects in Figure 1-15.

Figure 1-17. Pathway to C_{114} cage.

be possible. The resulted units could increase their stability by dimerization (Figure 1-17a). This peanut-shaped intermediate is a PC (Figure 1-17b); it further isomerizes to C_{114} (Figure 1-17,c,d) by SW edge rotation.

In C_{114} peanut structure, there are three bonds in the equatorial/junction zone. The removal of these bonds (together with their end-atoms) would generate two caps $C_{54}(6(56)^3(665)^3(656)^3-Z[12,0])$, perfectly oriented to form a C_{108} peanut cage (a PC), with three hexagon-octagon pairs in the junction (Figure 1-18a). This could isomerize to a cage $C_{108}-(7)$ with a fully heptagonal covering in the equatorial zone (Figure 1-18b). Peanut structures observed in annealed or irradiated peapods show a length identical to that of $C_{108}-(7)$ cage. Figures 1-18c,d presents other two structures which could result from C_{114} by stepwise elimination of six atoms. The formation of C_{108} from C_{114} can be viewed as a retro-Endo-Korto reaction (see Chapter 6).

Table 1-7 lists the semiempirical data for the four objects in Figure 1-18, in comparison to C_{114} peanut (Figure 1-17a). It suggests that no major differences exist among these intermediates possibly appearing in the annealed/irradiated peapods of C_{60} .

Table 1-7. PM3 and strain energy for peanut structures in Figures 1-17 and 1-18

Name	v	Sym	HF/ v (kcal/mol)	GAP (eV)	SE/ v (kcal/mol)
C_{114} (peanut)	114	D_{3h}	12.7894	6.0814	6.711
C_{112}	112	C_{2v}	13.0186	5.3058	6.605
C_{110}	110	C_{2v}	13.2559	5.4234	6.476
$C_{108}-(68)$	108	D_{3h}	13.0038	5.2419	6.380
$C_{108}-(7)$	108	D_{3d}	12.9526	4.8702	6.491

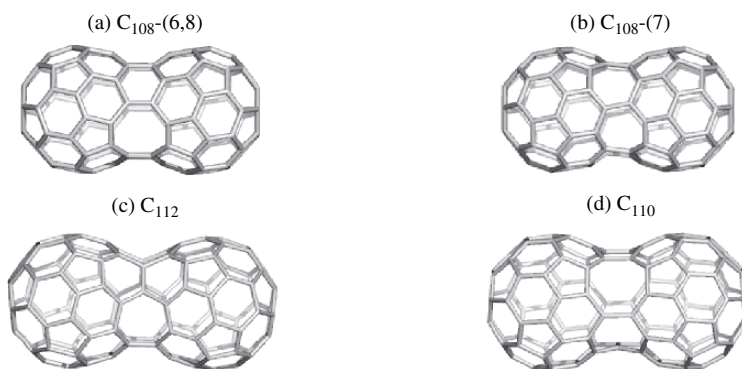


Figure 1-18. Structures resulted from C_{114} peanut cage.

1.3. Closed Nanotubes Viewed as Coalescence Products

A single-walled carbon nanotube (SWNT) consists of a piece of graphene sheet wrapped into a cylinder with a nanometer size diameter. The structure of SWNTs is represented by a chiral vector $C = na_1 + ma_2$, where a_1 and a_2 denote the primary lattice vectors of the graphene sheet. According to theoretical calculations under periodic boundary conditions, SWNTs become metallic or semiconducting, depending on their chirality (n, m) and the tube diameter. These assumptions apply to nanotubes long enough to neglect the effect of end caps.³⁵ Classification of SWNTs is facilitated by the observation that any infinite-length carbon tube is uniquely defined by a construction that involves rolling of a single graphite layer (a graphene sheet) in such a way that the end of the vector (conveniently represented by an $[n, m]$ pair of integer numbers) connecting two centers of hexagons is superimposed on its origin. SWNTs are chiral unless m equals either n or 0. In the former case, the armchair $[n, n]$ SWNTs consist of layers of hexagons with the long axis perpendicular to the tube axis, whereas in case of $[n, 0]$ zigzag SWNTs the axes are parallel (Figure 1-19).

However, the electronic structures of finite-length nanotubes capped with fullerene hemispheres should be different from those of infinite-length nanotubes. Such finite-length nanotubes with fullerene hemispheres have been observed inside a SWNT by heating “ C_{60} peapods”, in which the C_{60} molecules are incorporated.³⁶ Bando *et al.*³⁷ revealed using resonance Raman spectroscopy that the tubular structures generated in the C_{60} coalescence have a diameter of ~ 7 Å, which is identical to that of C_{60} . Therefore the fullerene caps should be significant for the C_{60} coalescence as initial stages of the formation of nanotubes inside a SWNT.³⁸

1.3.1. Finite-Length Carbon Nanotubes Related to C_{60}

C_{60} can be partitioned into one cyclic *cis*-polyene chain with 20 carbon atoms and two **corannulene**-like caps along a C_5 rotation axis, and it can also be viewed

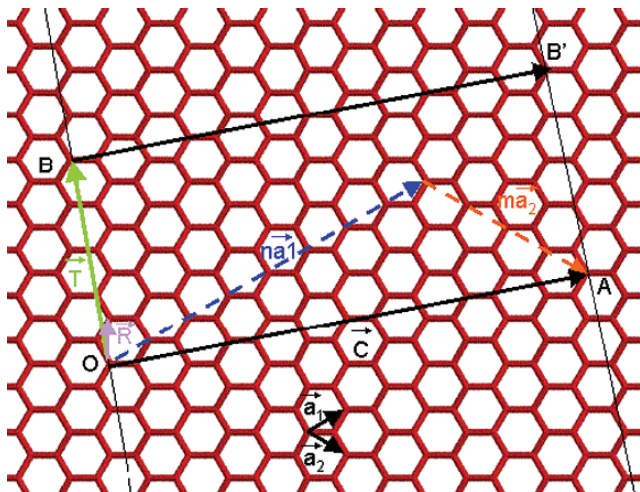


Figure 1-19. Wrapping a graphite sheet to an (n,m) -nanotube (8,4,4,-5).

as one cyclic *trans*-polyene chain with 18 carbon atoms and two **sumanene**-like caps along a C_3 rotation axis.³⁹ We therefore consider two possible finite-length nanotubes capped with fullerene hemispheres: the (5,5) armchair nanotubes with the C_5 rotation axis and the (9,0) zigzag nanotubes with the C_3 rotation axis, as shown at the left-hand side of Figure 1-20.

A general rule based on simple Hückel theory and symmetry considerations was described:⁴⁰ for every $v = 60 + 6k$, where k is either zero or an integer greater than one, there is at least one closed-shell cluster with 12 pentagonal and $v/2 - 10$ hexagonal faces. This is known as the leapfrog principle, named by the geometrical construction (*i.e.*, map operation – see Chapter 5) used to generate the closed-shell clusters.

There is a second potentially infinite family of clusters based on C_{70} , every member of which has a closed electronic shell topped by an empty, non-degenerate, non-bonding LUMO. Clusters in the new sequence have $70 + 30m$ or $84 + 36m$



Figure 1-20. From C_{60} fullerene, the two smallest IPR caps can be derived: corannulene- [5:6]₅ (left) and sumanene-[6:(5,6)₃]₃ cap (right).

atoms and, together with those in the leapfrog series, account for all the non-trivial closed shells so far catalogued for carbon cages.⁴⁰

These rules of thumb have been generalized by Diudea⁴¹ and they read as:

Leapfrog rule (for armchair cylinders). Fullerenes of k -fold cylindrical symmetry, of general formula $C_{12k(k-6)^k(5-6)^{k-2k-2n}}$ have a closed shell at each vertex number: $v = 12k + 2k \cdot 3m$; $m = 0, 1, 2, \dots$, ($k = 4$ to 7); the above considerations were made for $k = 5$.

Cylinder rule (for armchair cylinders). Fullerenes of k -fold cylindrical symmetry, of general formula $C_{12k(k-6)^k(5-6)^{k-2k-2n}}$ have a closed shell at each vertex number: $v = 12k + 2k(1 + 3m)$; $m = 0, 1, 2, \dots$, ($k = 4$ to 7). These cages have a (usually non-degenerate) non-bonding LUMO separated by a gap from the HOMO; $n_+ = 1 + n_-$. There are special cases, *e.g.*, the classical fullerene C_{84} which is the first term of series $k = 6$, has a triply degenerate LUMO, and the first term of series $k = 7$, C_{98} has a bonding LUMO and a non-bonding orbital NBO at $n_{v/2+3}$. Observe the difference between the two rules, which is only in the start structure: C_{60} for leapfrog and C_{70} for the cylinder rule.

Leapfrog rule (for zig-zag cylinders). Fullerenes of $k/2$ -fold cylindrical symmetry, of general formula $C_{13k(k-6)^{k/2}(6-5)^{k/2-2k-2n}}$ have a closed shell at each vertex number: $v = 13k + 3km$; $m = 0, 1, 2, \dots$, ($k = 4, 6, 8, \dots$); this rule can be viewed as a true “zig-zag” cylinder rule. The series $k = 6$ starts at C_{78} , a classical, isolated fullerene. The special cases are the first terms of $0(k \bmod 4)$, whose LUMO is a non-bonding orbital but their gap is non-zero. Note that structure C_{114} is the third term in the series $k = 6$. All the members of this series show PC structure by virtue of the leapfrog operation.

1.3.2. Simple Hückel Theory

Hückel theory⁴² is essentially a graph-theoretical model of some basic chemical concepts. In Hückel theory, the molecular-orbital energies are determined by diagonalising the vertex adjacency matrix of the graph associated to the carbon cage. (Two vertices are adjacent when they share an edge.) Positive eigenvalues correspond to bonding and negative to antibonding orbitals. The spectrum of a cage is given as non-increasing sequence of its eigenvalues: $x_1 \geq x_2 \geq \dots \geq x_v$. If the eigenvalues $x_{v/2}$ and $x_{v/2+1}$ are equal, then the configuration is **open-shell**. If, conversely, $x_{v/2} > x_{v/2+1}$, then three possibilities arise. If the $v \times v$ matrix has exactly $v/2$ positive eigenvalues, $x_{v/2} > 0$, $x_{v/2+1} \leq 0$, then the neutral carbon cage has a **properly closed-shell** configuration in which all $v/2$ bonding orbitals are doubly occupied. If $x_{v/2} > x_{v/2+1} > 0$, then the neutral carbon cage has a **pseudo-closed** shell in which all electrons are in doubly occupied orbitals but some bonding orbitals are left empty. The third possibility, $0 > x_{v/2} > x_{v/2+1}$, in which all electrons are also in doubly occupied orbitals but some are forced to be in non-bonding or antibonding orbitals, (not yet encountered in neutral fullerenes) is called **meta-closed**. A properly closed shell is no guarantee of maximal overall stability, as steric and electronic require-

ments generally pull in opposite directions, but there is considerable chemical interest in identifying the conditions under which closed shells occur.

1.3.3. Leapfrog Transformation and Leapfrog Structures

The leapfrog⁴³ construction is a geometrical-topological method of generating structures for large fullerenes from the smaller ones. A fullerene polyhedron with v vertices, 12 pentagonal and $(v/2-10)$ hexagonal faces, and $(3v/2)$ edges, is first capped on every face and then the dual is taken. The final polyhedron is also a fullerene but with $3v$ atoms. A leapfrog fullerene always has a closed π -electronic shell, irrespective of the electronic configuration of the starting fullerene. Since pentagon + hexagon polyhedra exist for all even values of $v \geq 20$ (except 22), at least one closed shell structure can be found for $v = 60 + 6k$ ($k \neq 1$). Truncated icosahedral C_{60} is the leapfrog of dodecahedral C_{20} and repetition of the process yields C_{180} , C_{540} , C_{1620} , *etc.*

The number of closed-shell leapfrog isomers of C_{3v} is equal to the total isomer count for C_v ; C_{60} , C_{72} and C_{78} have a single closed-shell isomer apiece, C_{84} has two leapfrog (and one cylindrical) closed shells while C_{90} has three.

The maximum number of benzenoid hexagons in a localized Kekulé structure of a fullerene with v atoms is $v/3$.

A Kekulé structure for a leapfrog fullerene can always be found that attains this maximum number of hexagons and, in addition, has no double bond inside a pentagon. More about leapfrog operation the reader can find in Chapter 5.

1.3.4. Construction and Classification of Nanotube Caps

Carbon caps resemble half-fullerenes.⁴⁴ They are composed of six pentagons and a number hexagons. The six pentagons are necessary by Euler's theorem of closed polyhedra to introduce the positive Gaussian curvature. There are three methods to represent carbon caps on a flat plane: flattening the cap onto a hexagonal lattice,⁴⁵ unwrapping a half tube with the cap attached to it,⁴⁶ and a network representation based on graph theory.⁴⁷ The flattening method, best highlights the pattern of six hexagons and its correlation to the nanotube chiral vector.

For caps obeying the isolated pentagon rule IPR, the number of caps is smaller for small diameters than for general caps. The (5,5) nanotube is the smallest diameter tube fitting an IPR cap; this cap is just "half a C_{60} fullerene". The other tubes with only one IPR cap are (9,0), (9,1), (8,2), and (6,5) with diameters $d = 6.8-7.5$ Å.

The (10,10) tube, in spite of its predominance in the crystalline ropes of nanotubes prepared by laser vaporization can be capped in C_5 fashion by a hemisphere of the icosahedral C_{240} fullerene, but it can also be capped 9297 other ways with isolated-pentagon patches.

For a given nanotube diameter there are fewer caps for armchair and zigzag tubes than for chiral tubes. This is due to the higher symmetry of achiral tubes,

which reduces the choice of caps. Although a given nanotube can have thousands of distinct caps, quite the opposite is true for the inverse problem. A given cap only fits onto one particular nanotube. The arrangement of pentagons in the cap defines the chirality of the fitted nanotube.

Figure 1-21 gives the mapping diagram used to generate armchair, zig-zag and chiral caps where a six-membered ring is the primary base ring.⁴⁸ The eventual end caps will contain six pentagons and a varying number of hexagons; this configuration will induce a cylindrical geometry during the growth of the tubular nanostructure. In order to obtain a base end cap for a zig-zag tube, the six pentagons must be sited at any of the blue locations. Likewise, an armchair end cap is produced when the five-membered rings are located at the red colored sites. Chiral tubes are created when the pentagons are placed in a combination of the red and blue locations, or when placed in a white location.

1.4. Armchair and Zig-Zag Closed Nanotubes

1.4.1. Construction of Nanotube Caps

The end caps with an armchair circumference have a five-fold or six-fold symmetry axis, which corresponds to the size of the polar ring (marked in dark blue- Figure 1-22). These caps result according to the scheme in Figure 1-21 by replacing the hexagons marked with a red color with pentagons. All structures have a PC network, the light blue bonds corresponds to localized double bonds, and thus the number of benzenoid rings is maximal. The first one is the smallest armchair IPR cap that fits to the (5,5) nanotube; actually it is half of the C_{60} fullerene.

End caps with a zig-zag circumference were constructed in a similar way, except the replacing hexagons by pentagons were now in the light blue domains (Figure 1-23). Since the attention was here focused on perfect Clar structures, only two caps (one with a pentagonal and the other with a hexagonal polar ring) were

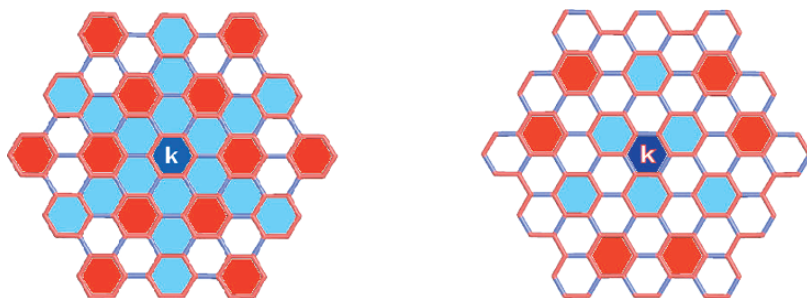


Figure 1-21. Placement of pentagons in different locations determines the chirality of the capped nanotube: in light blue locations will result in zig-zag, while in red locations will result in armchair nanotubes; any combination of red, blue or white will result in chiral tubes.

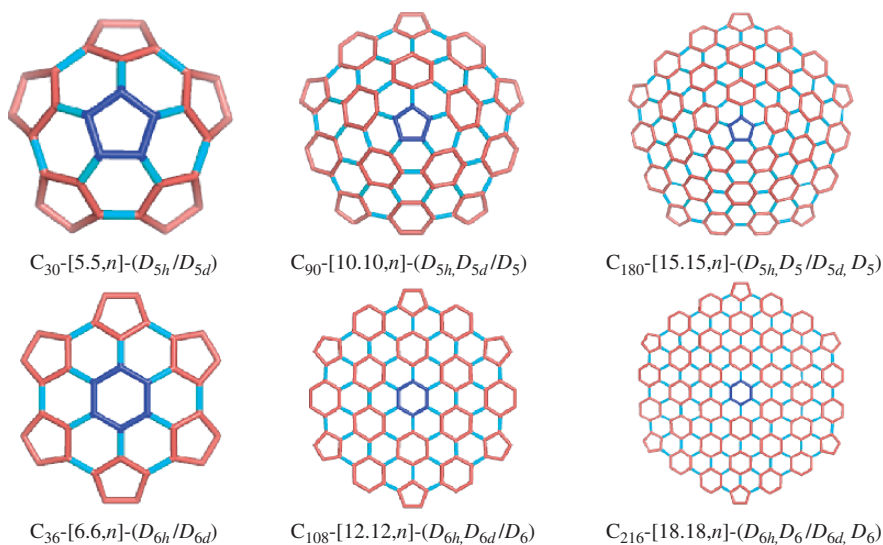


Figure 1-22. Nanotube caps with an armchair circumference with a pentagon/hexagon base ring; in the notation of caps the first point group counts for odd and the second one for even values of n .

used for construction of tubular fullerenes, with limited number of atoms. The first cap with a pentagon as polar ring results from the icosahedral C_{180} fullerene (*i.e.*, the leapfrog of C_{60}) by cutting off the equatorial zig-zag belt.

According to the second diagram in Figure 1-21, the construction of caps must start with an even-membered face. The arrangement of the pentagons reduces the symmetry, thus all structures have a $k/2$ symmetry axis. Only caps with a hexagonal polar ring (with a C_3 symmetry axis) were here constructed, three of them having an armchair edge while the last one a zig-zag edge. Note that, this last cap is C_{60} -derivable and matches to the (9,0) nanotube (Figure 1-24).

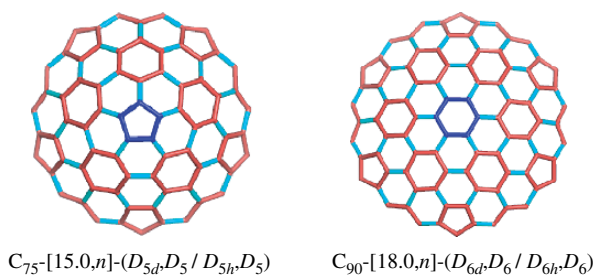


Figure 1-23. Nanotube caps with a zig-zag circumference, having a pentagon/hexagon polar ring.

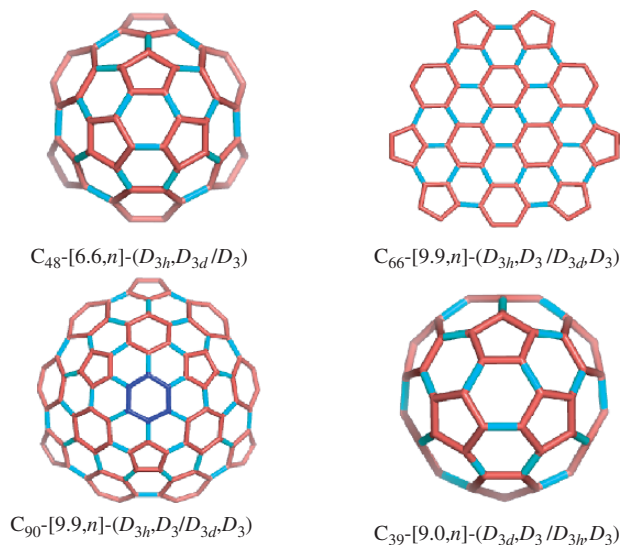


Figure 1-24. Nanotube caps constructed on the basis of the second diagram from figure 1-21.

1.4.2. Construction of Capped Armchair Nanotubes

The construction of tubular structures is achieved by connecting the two fullerenic hemispheres to an armchair nanotube with a length of n . The first structure in every series consists exactly of the two caps connected by a tube of length $n = 0$.

In the case of (5,5) nanotube, capped by $C_{30}\text{-}[5.5,n]$ (Figure 1-25), addition of n rows of atoms results in structures C_{60+10n} , of symmetry D_{5d} , for n -even, and D_{5h} , for n -odd. Whenever the tube length is $3n + 3$, $n = 0, 1, 2, \dots$, the whole structure has a PC network (assuming the caps used have a PC structure).

This periodicity by three can be seen within all capped armchair nanotube series and it is expected to be reflected in the energy calculations. In case of small diameter caps, there is only one possible fitted cap and their mutual position dictates the symmetry of the resulting cage.

Capping (10,10) nanotube with $C_{90}\text{-}[10.10,n]$ cap results in two series of objects, since at every n -value there are two possible positions to fit the second cap. The larger the tube diameter, the many ways in connection of the second cap. As in the previous case, whenever n is divisible by 3, the structure is PC, and this is true for the both series (see Figure 1-26, dark blue hexagons are the benzenoid faces in the tubular section).

At the beginning, four series of capped armchair nanotubes were modeled, since the caps have a similar way of construction, only the size of polar ring ($k = 5$ or 6) and the size of circumference is different. These caps matches to (5,5)/(6,6) and (10,10)/(12,12) nanotubes. The resulted tubular fullerenes have the highest possible symmetry: D_k , D_{kh} and D_{kd} . Construction of the other three armchair series, with

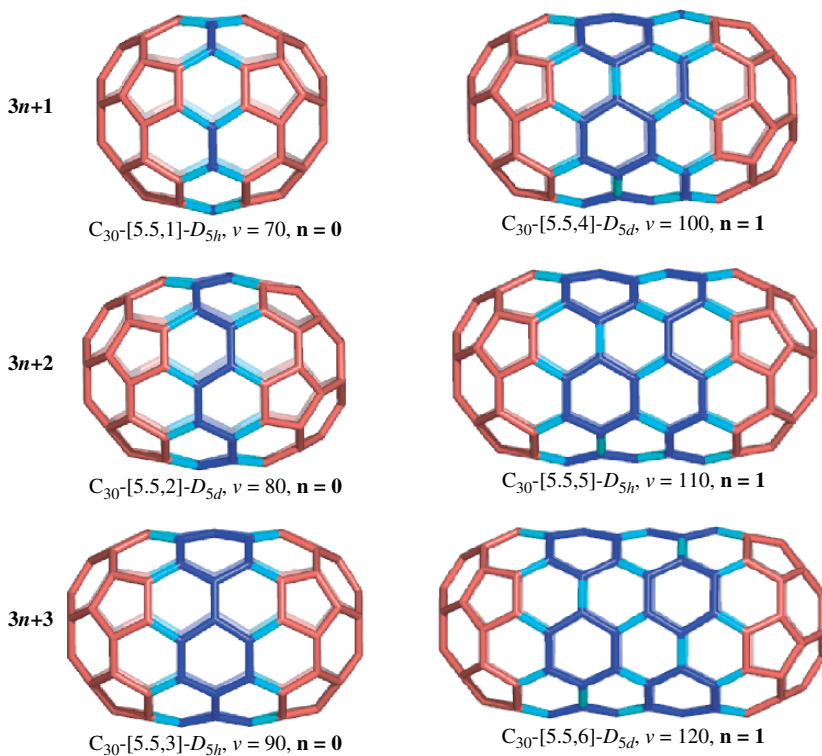


Figure 1-25. The structural periodicity in armchair tubulenes.

elements having $D_{k/2}$, $D_{k/2h}$ and $D_{k/2d}$ symmetry as well as the semiempirical data support the previously observed periodicity.

1.4.3. Construction of Capped Zig-Zag Nanotubes

The smallest diameter tube possibly capped by an IPR cap is the (9,0) zig-zag nanotube. Capping it with two C_{39} hemispheres produces two families of C_{78+18n} fullerenes. The members of the first family possess D_{3d} symmetry for even n and D_{3h} for odd n . The members of the second family are related to the D_{3d}/D_{3h} capped tubes by a $\pi/3$ rotation of one of the caps and possess D_3 symmetry for both even and odd n . The first two members of this series are two isomers of the IPR fullerene C_{78} .

To study the effect of increasing diameter, two similar zig-zag series were constructed: (15,0) and (18,0) tubes, closed by caps with a pentagon/hexagon as the polar ring (see Figure 1-27). In both cases it is possible to construct two families; in this case the symmetries are D_{kd}/D_{kh} and D_k respectively.

In case of zig-zag tubulenes, a PC structure appears at every n - value, which always belongs to the same family, the one with the higher symmetry.

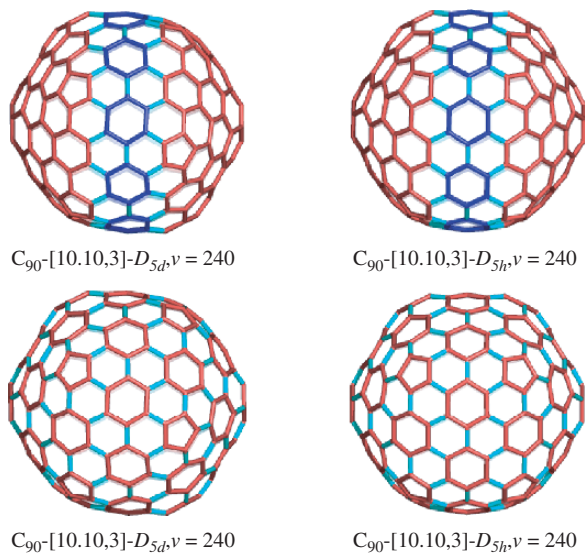


Figure 1-26. Two possible ways of connecting armchair caps with large diameter.

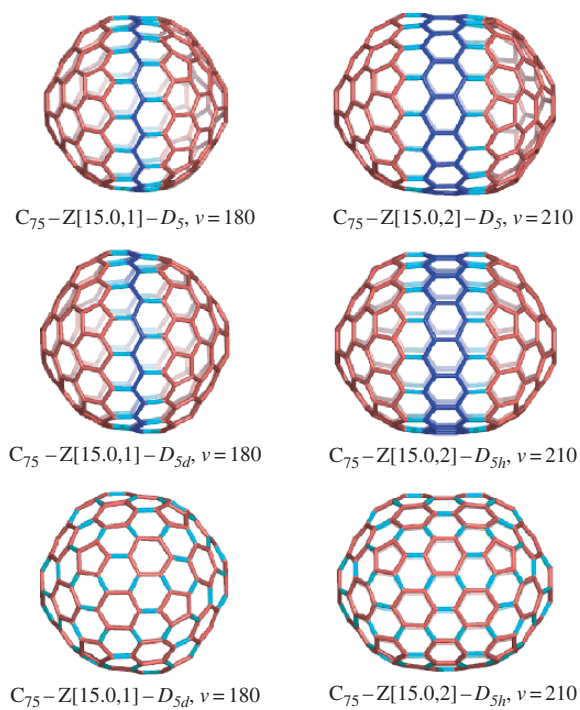


Figure 1-27. Leapfrog fullerenes result at every value of n when constructing zigzag tubulenes.

1.5. Energetics of Capped Nanotubes

1.5.1. Methods

The geometry optimization and single point computations (heat of formation, total energy, molecular orbital energy levels, *etc.*) were performed using the PM3 semi-empirical quantum-chemical method supplied by the HyperChem (Hypercube, Inc., version 7.52)⁴⁹ molecular modeling package. Several series of armchair and zigzag capped nanotubes were optimized to a gradient below 0.009 (kcal/ Å mol). Simple Hückel band gaps (supplied by TOPOCLUIJ package) and strain energy calculations (SE/ ν at the POAV1 level of theory,⁵⁰ supplied by JSCHEM package) were also performed and compared to semi-empirical results.

The construction of capped tube series followed three steps:

- modeling nanotube caps by the help of HyperChem software;
- generating matching nanotube coordinates by the JSCHEM package;⁵¹
- capping nanotubes at both ends, also done in HyperChem.

The lack of powerful PC limited the number of atoms for a structure, so the last element in a series has at most ~ 350 atoms.

For ray tracing of chemical images the powerful Pymol (DeLano Scientific, 2004, version 0.97)⁵² was used.

1.5.2. Stability of Capped Armchair Nanotubes

Strain is attributed to the deviation from planarity (in a graphite sheet all carbon atoms are in the same plane). Nanotubes result by rolling up a graphite sheet, and in this way strain is introduced. For closure 12 pentagons are necessarily introduced in the honeycomb network. This will increase more the energy than in the case of nanotubes, assigned to the decrease in bond angles from 120° in case of graphite, to 108° in case of pentagonal faces. In case of tubular fullerenes, the longer the tubular section, the much strain relief, resulting a more relaxed structure.

By synthesis, nanotubes are usually capped at both ends. Closure occurs to eliminate dangling bonds, which gets additional stability. However, this is the case of long enough nanotubes, so that the curvature induced by pentagons does not affect very much the overall energy. In this work the tubular segment of structures starts from zero, and ends at a very short length. It is thus expected that stability descriptors for a series of structures are not linear.

The heat of formation per atom HF/ ν is presented as a function of tube length n (Figure 1-28). The four series differ from each other by the polar ring size, and the tube diameter. It can be seen that the smallest diameter tube (5,5) has the highest energy values, since deviation from planarity increases with decreasing tube diameter. In all cases the energy decreases exponentially with the tube length, but some of the values clearly deviate from it. This becomes more clear in case of the

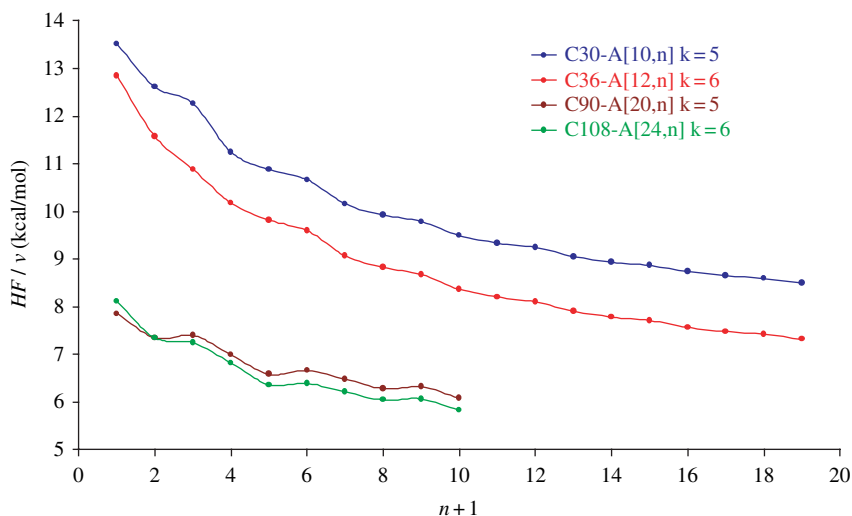


Figure 1-28. Variation of the heat of formation HF of the four armchair series.

(10,10) and (12,12) tube series, where every third value is higher than the previous one. The HOMO-LUMO gap alternation will be discussed below.

The strain energy data (Figure 1-29) show almost the same tendency, as for HF. It is expected that in long enough nanotubes, the strain energy SE and the heat of formation HF curves become almost linear. It can be observed that in the case of large diameter tubes, the value of the energy is higher than it would be expected.

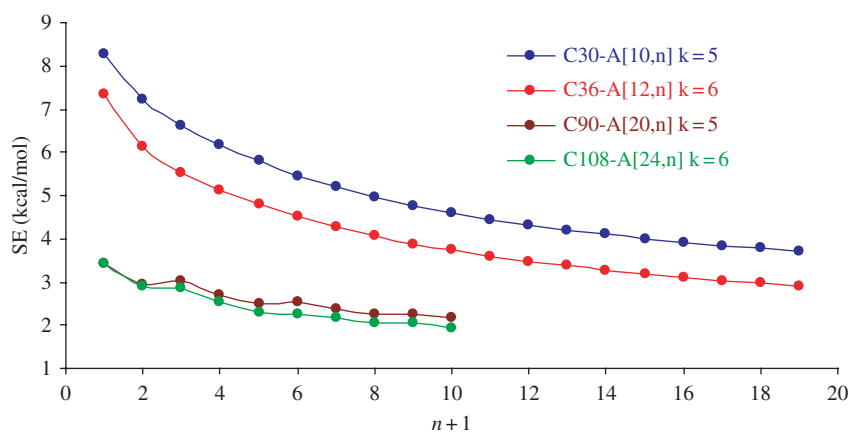


Figure 1-29. Strain energy SE data of the four armchair series.

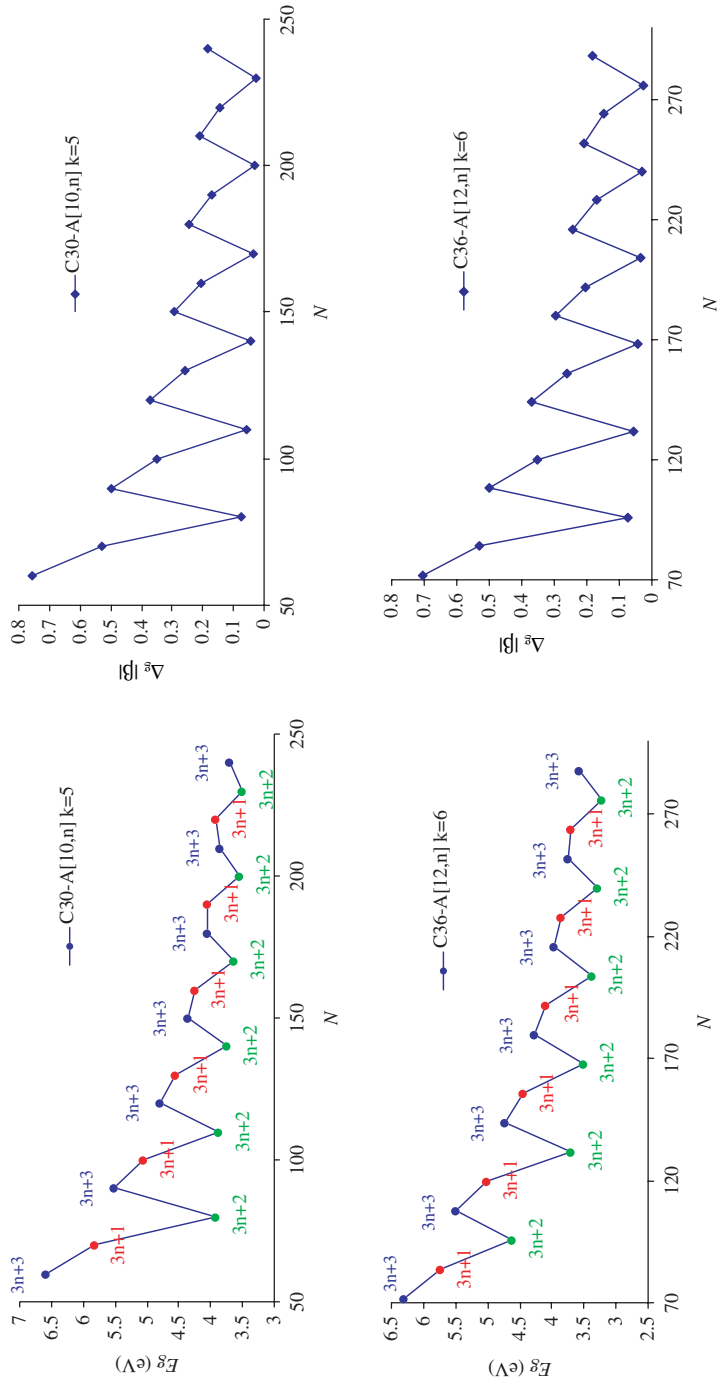


Figure 1-30. HOMO-LUMO gap variation in the armchair series, in both semiempirical (left) and simple Hückel calculation (right); it clearly reflects the periodicity of molecular structures.

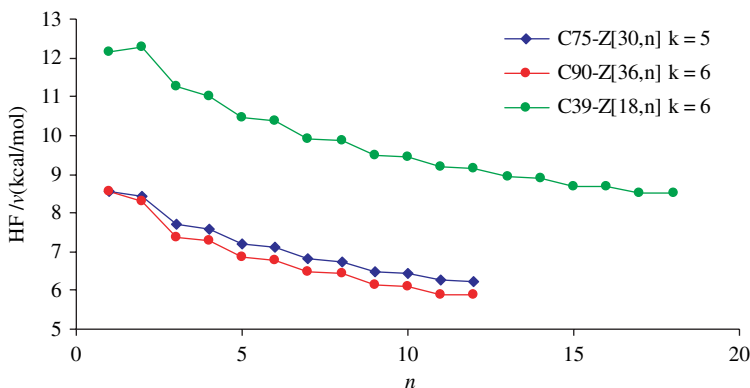


Figure 1-31. Heat of formation HF variation in zig-zag tubulene series; structures at $n/n+1$ have the same number of atoms.

The HOMO-LUMO gap values are presented for the first two series, both in semiempirical and simple Hückel calculations (Figure 1-30). The all members of both series have a PC structure, as they are leapfrog fullerenes and show the highest gap values and properly closed shells, in simple Hückel theory.

The next tubulenes of the series have $3n+1$ rows of atoms in the equatorial zone. They also show high enough gaps in PM3 calculation; in simple Hückel they have a closed shell but in an empty, non-degenerate, non-bonding LUMO orbital.

The sub-series of $3n+2$ rows of atoms show fullerenes of the lowest stability, as suggested by the smallest gap values, in semiempirical terms. In simple Hückel, they have an open shell configuration, with a very small gap. Clearly, these structures will show a HF different from expectations. At large diameters they also appear more strained than the other members of the series.

1.5.3. Stability of Capped Zig-Zag Nanotubes

Three series of structures have been constructed and all of them have two families. The members of these families have the same number of atoms thus being easily to compare. The first two series with C_5 and C_6 symmetry axis have different diameters, but they are constructed in a similar way. The increase in diameter contributes to the stability (Figure 1-31), as in the case of armchair tubes. Also, leapfrog fullerenes present a lower energy, thus being more stable.

The difference in the stability of leapfrog (marked in blue color) and its matching rotated structure (marked in red color, having D_k point group) is more obvious by comparing their HOMO-LUMO gap values (Figure 1-32).

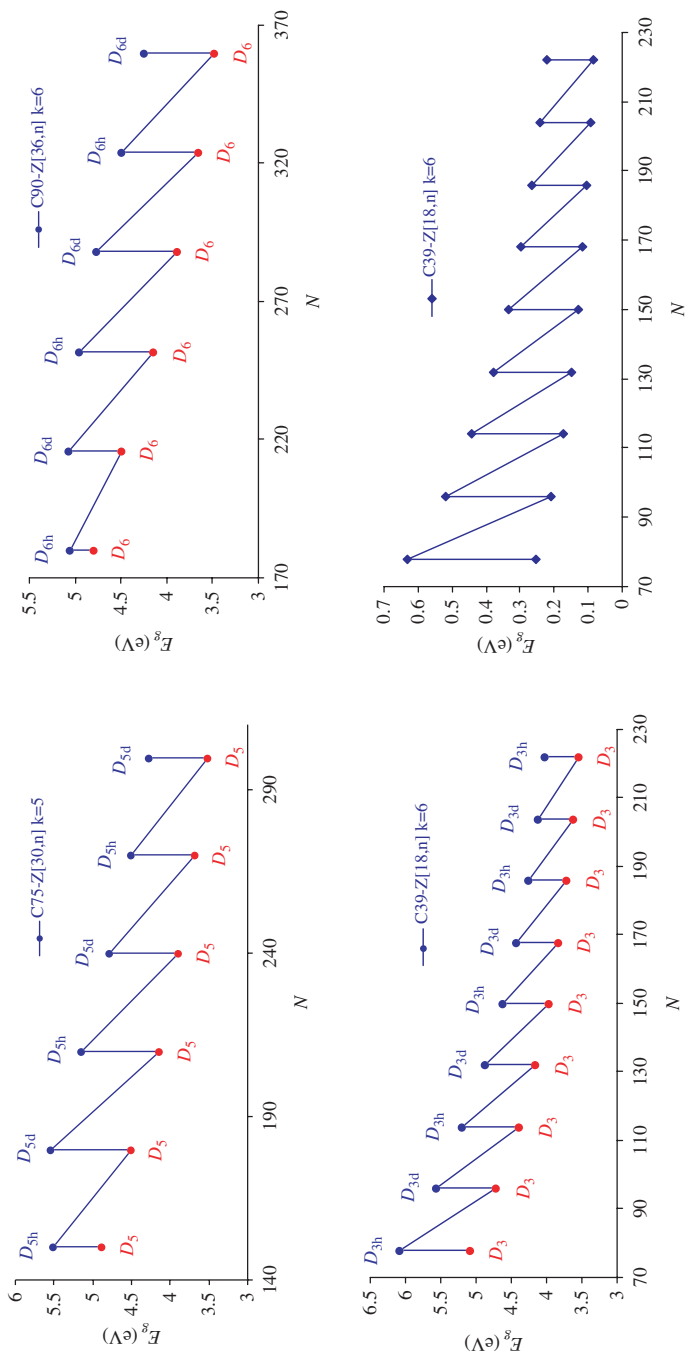


Figure 1-32. HOMO-LUMO gap variation in the zig-zag series, in both semiempirical (left) and simple Hückel calculation (right); the periodicity of molecular structures is well reflected.

Conclusions

The goal of this chapter was to prove the existence of a relationship between the structure of carbon tubulenes and their stability. In this respect, several series of armchair and zig-zag capped tubes were constructed and semiempirical, simple Hückel and strain energy calculations were performed in order to see how these descriptors (and lastly the stability) vary with the length of the tubular section.

Comparison of the results showed that leapfrog fullerenes are the most stable ones; this was confirmed in all the type of calculations made. Other structural parameters involved in the stability of fullerenes are the length and diameter of the tubular section. Stability of structures increases as the values of both these parameters increase.

Chiral structures were not modeled due to the large number of possible caps for a given tube. However, a similar behavior is expected.

Our results are in very good agreement with similar calculations in the literature.

References

1. M. Rao, P. Zhou, K.-A. Wang, G. T. Hager, J. M. Holden, Y. Wang, W.-T. Lee, X.-X. Bi, P. C. Eklund, D. S. Cornett, M. A. Duncan, I. J. Amster, *Science*, 1993, **259**, 955–957.
2. Y. Iwasa, T. Arima, R. M. Fleming, T. Siegrist, O. Zhou, R. C. Haddon, L. J. Rothberg, K. B. Lyons, H. L. Carter Jr., A. F. Hebard, R. Tycko, G. Dabbagh, J. J. Krajewski, G. A. Thomas, T. Yagi, *Science*, 1994, **264**, 1570–1572.
3. G.-W. Wang, K. Komatsu, Y. Murata, M. Shiro, *Nature*, 1997, **387**, 583–586.
4. S. Lebedkin, A. Gromov, S. Giesa, R. Gleiter, B. Renker, H. Rietschel, W. Krätschmer, *Chem. Phys. Lett.*, 1998, **285**, 210–215.
5. P. W. Fowler, D. Mitchell, R. Taylor, G. Seifert, *J. Chem. Soc., Perkin Trans.*, 1997, **2**, 1901–1905.
6. S. Lebedkin, S. Ballenweg, J. Gross, R. Taylor, W. Krätschmer, *Tetrahedron. Lett.*, 1995, **36**, 4971–4974.
7. Gromov, S. Lebedkin, S. Ballenweg, A. G. Avent, R. Taylor, W. Krätschmer, *Chem. Comm.*, 1997, 209–210.
8. Gromov, S. Lebedkin, W. E. Hull, W. Krätschmer, *J. Phys. Chem. A*, 1998, **102**, 4997–5005.
9. A. Hirsch, *Synthesis*, 1995, **139**, 895–913.
10. S. Giesa, J. H. Gross, W. E. Hull, S. Lebedkin, A. Gromov, R. Gleiter, W. Krätschmer, *Chem. Commun.*, 1999, 465–466.
11. S. W. McElvany, J. H. Callahan, M. M. Ross, L. D. Lamb, D. R. Huffman, *Science*, 1993, **260**, 1632–1634.
12. S. Lebedkin, H. Rietschel, G. B. Adams, J. B. Page, W. E. Hull, F. H. Hennrich, H.-J. Eislner, M. M. Kappes, W. Krätschmer, *J. Chem. Phys.*, 1999, **110**, 11768–11778.
13. Yeretzyan, K. Hansen, F. Diedrich, R. L. Whetten, *Nature*, 1992, **359**, 44–47.
14. E. E. B. Campbell, V. Schyja, R. Ehlich, I. V. Hertel, *Phys. Rev. Lett.*, 1993, **70**, 263–266.
15. F. Rohmund, A. V. Glotov, K. Hansen, E. E. B. Campbell, *J. Phys. B: At. Mol. Opt. Phys.*, 1996, **29**, 5143–5161.
16. L. Strout, R. L. Murry, C. Xu, W. C. Eckhoff, G. K. Odom, G. E. Scuseria, *Chem. Phys. Lett.*, 1993, **214**, 576–582.
17. M. V. Diudea, C. L. Nagy, I. Silaghi-Dumitrescu, A. Graovac, D. Janežić, D. Vikić-Topić, *J. Chem. Inf. Model*, 2005, **45**(2) 293–299.
18. Y. Zhao, B. I. Yakobson, R. E. Smalley, *Phys. Rev. Lett.*, 2002, **88**, 18, 185501(4).

19. Y. Zhao, R. E. Smalley, B. I. Yakobson, *Phys. Rev. B*, 2002, **66**, 195409(9).
20. Y. F. Zhao, Y. Lin, B. I. Yakobson, *Phys. Rev. B*, 2003, **68**, 233403(1)–(4).
21. H. Ueno, S. Osawa, E. Osawa, K. Takeuchi, *Fullerene Sci. Technol.*, 1998, **6**, 319–338.
22. S. Han, M. Yoon, S. Berber, N. Park, E. Osawa, J. Ihm, D. Tománek, *Phys. Rev. B*, 2004, **70**, 113402(1)–(4).
23. B. R. Eggen, M. I. Heggie, G. Jungnickel, C. D. Latham, R. Jones, P. R. Briddon, *Science*, 1996, **272**, 87–90.
24. J. Lu, S. Nagase, S. Zhang, L. Peng, *Phys. Rev. B*, 2003, **68**, 121402(1)–(4).
25. Y.-K. Kwon, D. Tománek, S. Iijima, *Phys. Rev. Lett.*, 1999, **82**, 1470–1473; J. Chen, J. Dong, *J. Phys. Condens. Matter*, 2004, **16**, 1401–1408.
26. M. Monthieux, *Carbon*, 2002, **40**, 1809–1823.
27. M. Yudasaka, K. Ajima, K. Suenaga, T. Ichihashi, A. Hashimoto, S. Iijima, *Chem. Phys. Lett.*, 2003, **380**, 42–46.
28. B. W. Smith, M. Monthieux, D. E. Luzzi, *Nature*, 1998, **396**, 323–324.
29. S. Bandow, M. Takizawa, K. Hirahara, M. Yudasaka, S. Iijima, *Chem. Phys. Lett.*, 2001, **337**, 48–54.
30. S. Bandow, T. Hiraoka, T. Yumura, K. Hirahara, S. Iijima, *Chem. Phys. Lett.*, 2004, **384**, 320–325.
31. Hernández, V. Meunier, B. W. Smith, R. Rurali, H. Terrones, M. Buongiorno Nardelli, M. Terrones, D. E. Luzzi, J.-C. Charlier, *Nano Lett.*, 2003, **3**, 1037–1042.
32. A. J. Stone, D. J. Wales, *Chem. Phys. Lett.*, 1986, **128**, 501–503.
33. M. V. Diudea, Cs. L. Nagy, O. Ursu, T. S. Balaban, *Fuller. Nanotub. Carbon Nanostruct.*, 2003, **11**, 245–255.
34. Y.-H. Kim, I.-H. Lee, K. J. Chang, S. Lee, *Phys. Rev. Lett.*, 2003, **90**, 065501–065504.
35. M. S. Dresselhaus, G. Dresselhaus, R. C. Eklund, *Science of fullerenes and carbon nanostructures*. Academic Press: New York, 1996.
36. B. W. Smith, M. Monthieux, D. E. Luzzi, *Nature*, 1998, **396**, 323–324.
37. (a) S. Bandow, M. Takizawa, K. Hirahara, M. Yudasaka, S. Iijima, *Chem. Phys. Lett.*, 2001, **337**, 48–54. (b) S. Bandow, T. Hiraoka, T. Yumura, K. Hirahara, S. Iijima, *Chem. Phys. Lett.*, 2004, **384**, 320–325.
38. T. Yumura, S. Bandow, K. Yoshizawa, S. Iijima, *J. Phys. Chem. B*, 2004, **108**(31), 11426–11434.
39. (a) T. Yumura, D. Nozaki, S. Bandow, K. Yoshizawa, S. Iijima, *J. Am. Chem. Soc.*, 2005, **127**(33), 11769–11776. (b) T. Yumura, S. Bandow, K. Yoshizawa, S. Iijima, *J. Phys. Chem. B*, 2004, **108**(31), 11426–11434.
40. P. W. Fowler, *J. Chem. Soc. Faraday Trans.*, 1990, **86**(12), 2073–2077.
41. M. V. Diudea, *Phys. Chem. Chem. Phys.*, 2004, **6**(2), 332–339.
42. P. W. Fowler, T. Pisanski, *J. Chem. Soc. Faraday. Trans.*, 1994, **90**(19), 2865–2871.
43. (a) P. W. Fowler, *J. Chem. Soc. Perkin Trans.*, 1992, **2**, 145. (b) P. W. Fowler, M. Fujita, M. Yoshida, *J. Chem. Soc., Faraday Trans.*, 1996, **92**(19), 3673–3675. (c) P. W. Fowler, J. I. Steer, *J. Chem. Soc., Chem. Commun.*, 1987, 1403.
44. S. Reich, L. Li, J. Robertson, *Phys. Rev. B*, 2005, **72**, 165423.
45. T. Y. Astakhova, G. A. Vinogradov, E. Osawa, *Fullerene Sci. Technol.*, 1999, **7**, 1999.
46. M. Fujita, R. Saito, G. Dresselhaus, M. S. Dresselhaus, *Phys. Rev. B*, 1992, **45**, 13834–13836.
47. G. Brinkmann, P. W. Fowler, D. E. Manolopoulos, A. H. R. Palser, *Chem. Phys. Lett.*, 1999, **315**, 335–347.
48. S. L. Lair, W. C. Herndon, L. E. Murr, S. A. Quinones, *Carbon*, 2006, **44**, 447–455.
49. HyperChem 7.52, Hypercube, Inc., <http://www.hyperchem.com>.
50. R. C. Haddon, *Ietrahedron*, 1988, **44**, 764.
51. JSCHEM software program, Cs. L. Nagy, M. V. Diudea, Babes-Bolyai University, Cluj.
52. PyMol 0.97, DeLano Scientific, <http://www.pymol.org>.

Chapter 2

Polyhex Tori

2.1. Introduction

Among the carbon allotropes, intensively studied in the last decade,^{1–5} the only orientable closed surface S entirely coverable by a benzenoid lattice is the torus. A polyhedral (combinatorial) torus obeys the Euler theorem⁶

$$v - e + f = \chi(S) \quad (2.1)$$

where $\chi(S)$ is the Euler characteristic: $\chi(S) = 2 - 2g$ (v , e , f , and g being respectively the number of vertices, edges, faces, and genus-unity, in case of the torus).

“Circle crops” structures were first observed by Liu *et al.*⁷ and then by other groups.^{8–10} Martel *et al.*¹⁰ argued that the observed rings were coils rather than perfect tori, but these structures have continued to attract a multitude of theoretical studies, dealing with construction, mathematical and physical properties of graphitic tori.^{11–19}

The *graphite zonefolding* procedure^{12, 17–19} is most often used to cover a torus by hexagons. The method defines an equivalent planar parallelogram on the graphite sheet and identifies a pair of opposite sides to form a tube. Finally the two ends of the tube are glued together in order to form a torus. The resulting polyhex torus is completely defined by four independent integer parameters,^{6–18, 20} reducible to three parameters.^{17–21}

A second procedure uses the so-called topological coordinates, extracted from the adjacency matrix eigenvectors.^{22–25}

2.2. Construction of Polyhex Tori from Square Tiled Tori

A third way to polyhex tori starts from the tetragonal (4,4) covering embedded in the torus, as (4,4)[c, n] objects.^{26,27} The embedding of the (4,4) net is made by circulating a c -fold cycle, circumscribed to the toroidal tube cross-section of radius r , around the large hollow of the torus, of radius $R > r$ (Figure 2-1). Its subsequent n images, equally spaced and joined with edges, point by point, form a polyhedral torus tiled by a tetragonal pattern. The position of each of the n images of the “circulant” around the central hollow is characterized by angle θ while angle φ locates the c points across the tube. In all, $c \times n$ points are generated. The parameters R and r are not directly involved in the topological characterization of the lattice.

The parameters are calculated by the following formulas:

$P(x, y, z) :$

$$x = \cos(\theta)(R + r \cos \varphi)$$

$$y = \sin(\theta)(R + r \cos \varphi)$$

$$z = r \sin \varphi$$

$$\theta_i = \frac{2\pi}{n} i \quad ; \quad i = 0, \dots, n-1$$

$$\varphi_j = \frac{2\pi}{c} j \quad ; \quad j = 0, \dots, c-1 \quad (2.2)$$

The squares are changed to hexagons (or other tiling patterns, suitable from chemical point of view) by appropriate edge-cutting^{27–32} (or by performing some map operations – see Chapter 5). To obtain the (6,3) lattice, each second edge is cut off.

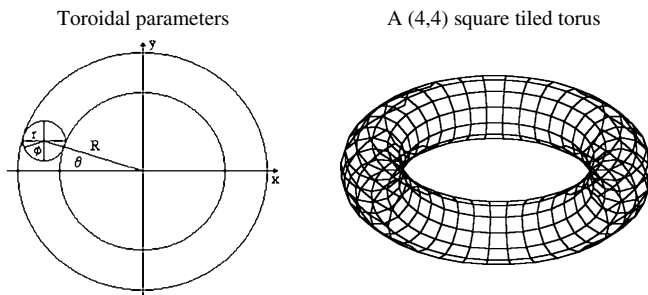


Figure 2-1. Embedding of the (4,4) net in the torus.

Two embedding isomers could result at each given $[c, n]$ pair, as the cut edges lie either horizontally or vertically (*i.e.*, perpendicularly and parallel to the Z axis of the torus). The two isomers are called H (or “zig-zag” Z) and V (or “armchair” A), respectively, according to the cut edge location (or to their tube cross-section shape). The name of such a torus is a string of characters including the tiling, type of embedding and tube dimensions $[c, n]$.

Note that each hexagon consumes exactly two squares in the (4,4) net. By construction, the number of hexagons in the (6,3)H/Z pattern is half the number of squares on dimension c of the (4,4) torus. The same is true for the (6,3)V/A, but on dimension n . Thus, $T(6,3)H[2c, n]$ has the same number of hexes as its embedding isomer $T(6,3)V[c, 2n]$. However, they represent topologically distinct objects (see below), and correspond to two different classes of aromatic chemical compounds: phenacenes and acenes, respectively.

After optimization, by a Molecular Mechanics procedure, the polyhex tori look like in Figure 2-2. The objects in these examples are non-chiral and their embedding shows $c < n$; hereafter, such an embedding is called a “normal” one.

The shape of polyhex tori tends to that of the ideal torus (*i.e.*, a circular tube cross-section) at a sufficiently large ratio n/c . Figure 2-3 gives some cross-sections on polyhex tori along with their geometric eccentricity (in %, taken as the ratio of the difference of the two diameters).

When $c > n$, the objects show a more elongated cross-section, as illustrated in Figure 2-4. Such elongated tori³³ have been inferred in multi walled nanotube growth.^{34,35}

Successive torus opening and tube closing, as in the sequence: $T(6,3)H[c, n]$; $TU(6,3)H[c, n]/TU(6,3)V[n, c]$; $T(6,3)V[n, c]$, leads to pair tori of different embedding but having the same topology.

Twisted, chiral, tori can be generated by the following two procedures: (1) twisting the horizontal layer connections (Figure 2-5a) and (2) twisting the vertical layer (offset) connections (Figure 2-5b).

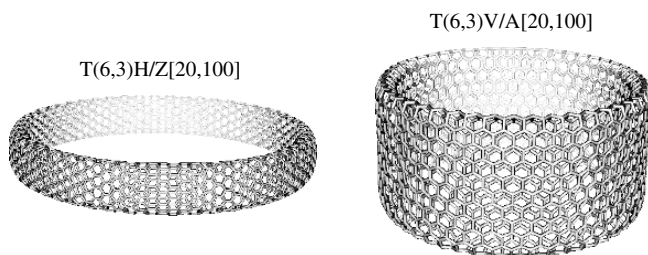


Figure 2-2. Optimized polyhex tori on 20×100 atoms, in the H/Z (zig-zag) and V/A (armchair) embedding, respectively.

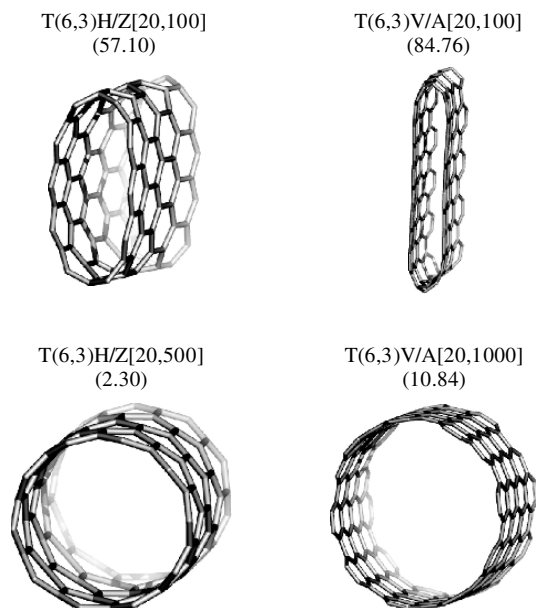


Figure 2-3. Cross-sections on polyhex tori and their geometric eccentricity (in%).

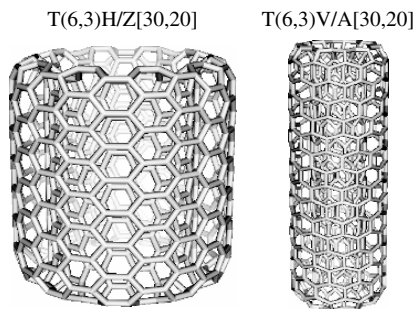


Figure 2-4. Elongated polyhex tori, in H/Z and V/A embedding, respectively.

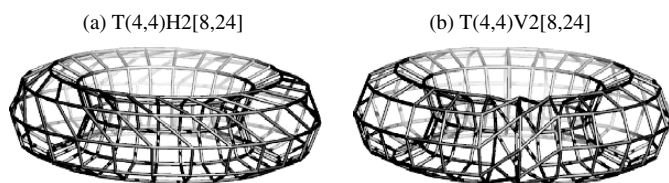


Figure 2-5. An H-twisted (a) and a V-twisted (offset – b) (4,4) net.

2.3. Topology of Polyhex Tori

Each of the above twistings superimpose on the two basic cuttings, thus resulting four classes of twisted tori: (i) H-twist, H-cut $\text{HHt}[c, n]$; (ii) H-twist, V-cut, $\text{HVT}[c, n]$; (iii) V-twist, H-cut, $\text{VHT}[c, n]$; and (iv) V-twist, V-cut, $\text{VVT}[c, n]$. The type of cutting will dictate the type of embedding and, ultimately, the shape of objects. Conversely, the type of twisting is involved in the π -electron structure of polyhex tori (see Section 2.5). Figure 2-6 illustrates some (non-optimized) twisted polyhex tori.

The twist number t is just the deviation (in number of hexagons) of the chiral (*i.e.*, rolling-up) vector to the zigzag line, in the graphite sheet representation.^{12,16–18,36} Accordingly, a toroidal object is drawn as an equivalent planar parallelogram, that needs the specification (in two integer parameter notation³⁶) of the two involved tubes (Figure 2-7). One tube is built on the rolling-up vector R , which in terms of the primitive lattice vectors of graphite is written as:

$$R = ka_1 + la_2 \quad (2.3)$$

The second tube is formally defined on the translating vector T :

$$T = pa_1 + qa_2 \quad (2.4)$$

Going from a torus, generated as above, to its composing vectors, the first tube can be identified by cutting the object across the tube while the second one results by cutting it around the large hollow. Anyway, a four integer parameter description (k, l, p, q) is obtained.

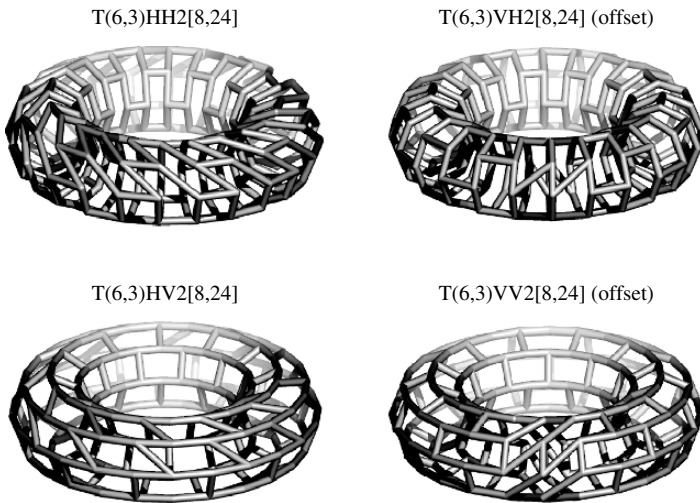


Figure 2-6. The four classes of twisted polyhex tori (non-optimized geometry).

The coordinates of THH4[14,6] torus depicted in Figure 2-7 are: $(5, -4, 3, 3)$. Note that this representation is not unique and is reducible to three parameter notation, theorized by Kirby *et al.*^{17,21}

In our procedure, H-twisting involves a chiral (HH or HV) R -based tube (winding around the tube) and a non-twisted T -based tube (winding around the torus-Table 2-1, entries 3 and 4). Conversely, in V-twisting, the R -based tube is non-chiral (H/Z or V/A) while the T -based tube is twisted (Table 2-1, entries 5 and 6). The resulting tori are all different, at least as 3D structures, because of distinct embedding. However, some of the embedding isomers could represent one and the same topological object, as will be seen in Section 2.6. The correspondence between the two notations: $TXt[c, n]$ and (k, l, p, q) is detailed in Table 2-1.

Encoding the type of tessellation can be done, for example, by the spiral code, which was first proposed for coding and constructing spherical fullerenes.^{37–39} We adapted the spiral code for tubular structures.³¹ In a periodic tubular net, the spiral code brings information on size and sequence of faces and embedding the actual object on the parent $(4,4)[c, n]$ lattice. The α -spiral code for the polyhex toroids is given in Table 2-2.

The number t inside the brackets equals the helicity⁴⁰ while the number out the brackets gives the steps of a helix. Note that the helicity could be less than t , if an integer number of steps appear.

A different topological description of polyhex tori is possible by means of the Omega polynomial (Chapter 4).

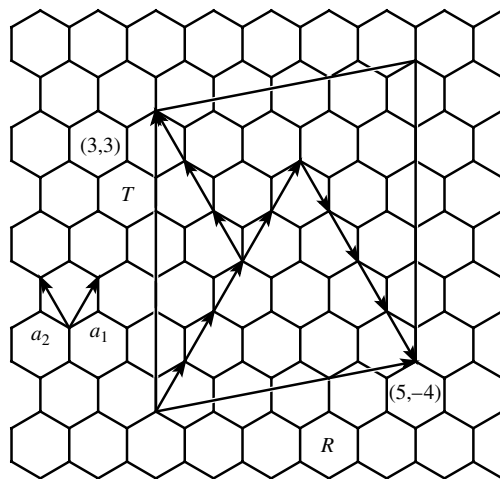


Figure 2-7. Representation of the torus THH4[14,6] by an equivalent parallelogram needs the specification of two tubes: one defined on the rolling-up vector R (with integer coordinates (k, l)) and the other on the translating vector T (given by the pair (p, q)). The four parameter specification of the depicted torus is $(5, -4, 3, 3)$.

Table 2-1. Correspondence between the $\text{TXt}[c, n]$ and (k, l, p, q) notations

	Torus $[c, n]$	Tube R	Tube T	Torus $(k, l, p, q)^*$	v
1	H	H/Z	V/A	$(c/2, -c/2, n/2, n/2)$	$2(kq - lp) = cn$
2	V	V/A	H/Z	$(c/2, c/2, n/2, -n/2)$	$2(lp - kq) = cn$
3	HH t	HH (tw)	V/A	$[(c-t)/2, -t, n/2, n/2]$	$2(2kq - lp) = cn$
4	HV t	HV (tw)	H/Z	$[(c+t)/2, (c-t)/2, n/2, -n/2]$	$2(lp - kq) = cn$
5	VH t (offset)	H/Z	HV (tw)	$[c/2, -c/2, (n+t)/2, (n-t)/2]$	$2(kq - lp) = cn$
6	VV t (offset)	V/A	HH (tw)	$[c/2, c/2, (n-t)/2, -t]$	$2(2lp - kq) = cn$

* First pair (k, l) denotes the rolling-up vector R while last pair (p, q) specifies the translating vector T . The representation $(m, -m) = (m, 0)$, is an H/Z-tube while (m, m) is a V/A-tube (see Figure 2-7).

Table 2-2. Ring spiral code of polyhex tori

	Series	Ring spiral code
1	H/Z $[c, n]$	$[6^{c/2}]^n$
2	HH $[c, n]$	$[(6^{c/2})^t]^{n/t}$
3	HV $[c, n]$	$[(6^c)^t]^{n/2t}$
4	VH $[c, n]$	$[(6^n)^t]^{c/2t}$
5	VV $[c, n]$	$[(6^{n/2})^t]^{c/t}$
6	V/A $[c, n]$	$[6^c]^{n/2}$

2.4. Strain Energy Calculation

Our TORUS 3.0 software package^{41,42} enables the generation of huge tori, up to 20,000 atoms, which could be optimized by a Molecular Mechanics procedure. As shown in Figure 2-3, the cross-section of a sufficiently large torus (*i.e.*, a large ratio h_n/h_c of the number of hexes on the two dimensions) tends to the circular shape. Our objects approach that shape at the ratios 50 and 25, in case of H/Z $[20, n]$ and V/A $[20, n]$ series, respectively.

In the POAV1 theory,^{43–45} the π -orbital axis vector makes equal angles $\theta_{\sigma\pi}$ to the three σ -bonds of the sp^2 carbon atom and the *pyramidalization* angle is obtained as:

$$\theta_p = \theta_{\sigma\pi} - 90^\circ \quad (2.5)$$

This angle is used for estimating the strain energy, induced by a pyramidalized carbon atom, by:

$$SE = 200 \cdot (\theta_p)^2 \quad (2.6)$$

with θ_p being measured in radians. The difference $120 - (1/3) \cdot \sum \theta_{ij}$ gives the deviation to the planarity. POAV analysis provides a reliable description of electronic structure of non-planar conjugated molecules.

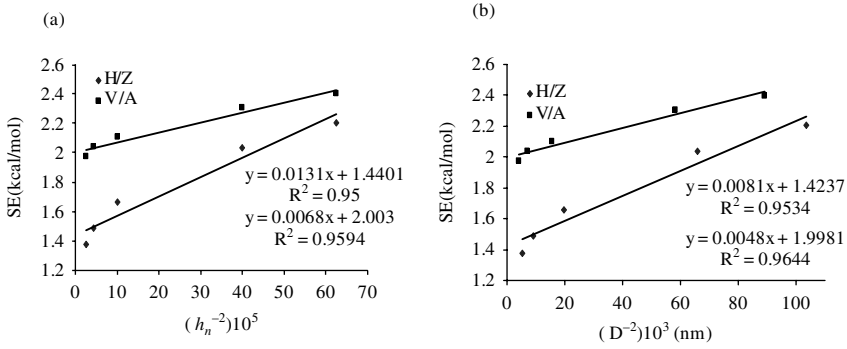


Figure 2-8. Strain energy per atom of thick tori, TH/Z[40, n], $n = 40, \dots, 500$ and TV/A[20, n], $n = 80, \dots, 1000$: (a) function of the number of hexes h_n on dimension n and (b) function of the large diameter, in nm, respectively.

In a first test, we varied the n -dimension and found a dependence of the strain energy by D^{-2} , with D being the large diameter of the torus. A similar result was reported by Han.⁴⁶ This is true in large tori built up on both thick ($h_c = 20$, Figure 2-8) and thin ($h_c = 10$, Figure 2-9) tubes. In both cases, the V/A tori were found more strained. Observe the proportionality between D and n .

In a second test, the n -dimension was kept constant (at $n = 100$) and the c -dimension was varied. The strain energy showed a dependency by h_c^{-2} in thin tori (the most strained subset) and by h_c^{-1} in thick tori of the H/Z series (Figure 2-10). The series V/A appeared split in two subseries, $0 \bmod(c,4)$ (having at apex a strain up to 11 times the average value) and $2 \bmod(c,4)$ (with up to 17 times the average strain at apex), respectively. Strain of the both series depends on h_c^{-1} (Figure 2-11). The two series are, however, not directly comparable.

Compare the strain energy per atom of tori with that of C_{60} (8.26 kcal/mol) and find the polyhex tori as more relaxed structures.

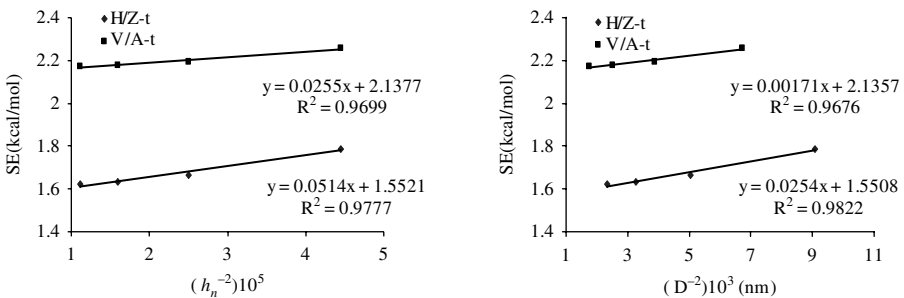


Figure 2-9. Strain energy per atom of thin tori, TH/Z[20, n], $n = 100, \dots, 300$ and TV/A[10, n], $n = 200, \dots, 600$: (a) function of the number of hexes h_n on dimension n and (b) function of the large diameter, in nm, respectively.

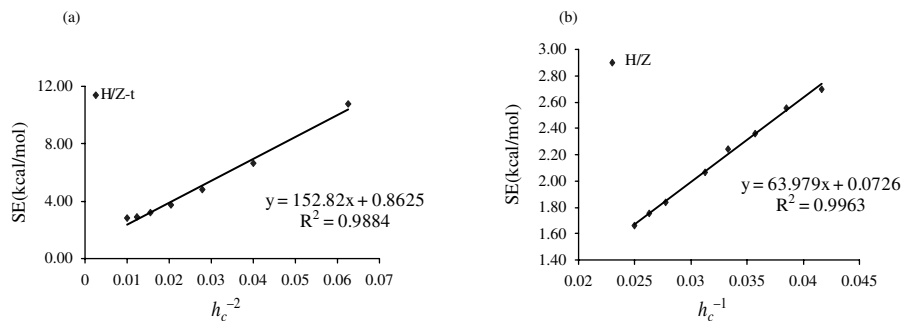


Figure 2-10. Strain energy per atom of: (a) thin tori, TH/Z[c,100], $h_n = 100$, $c = 8, \dots, 20$ and (b) thick tori TH/Z[c,100], $c = 24, \dots, 40$, function of the number of hexes h_c on dimension c .

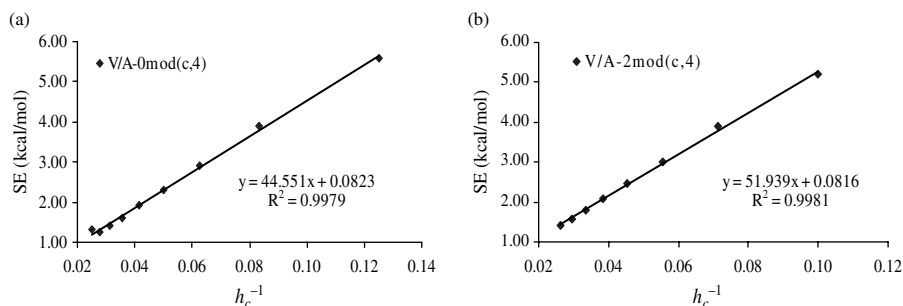


Figure 2-11. Strain energy per atom of tori TV/A[c,100], $h_n = 50$, $c = 8, \dots, 40$, series 0mod(c,4) (a) and 2mod(c,4) (b), function of the number of hexes h_c on dimension c .

2.5. π -Electronic Structure of Polyhex Tori

In the Spectral Theory, at the simple π -only Hückel⁴⁷ level of theory, the energy of the i^{th} molecular orbital $E_i = \alpha + x_i\beta$ is evaluated by calculating the solutions x_i of the characteristic polynomial $Ch(G)$ or the eigenvalues of the adjacency matrix associated to the molecular hydrogen depleted graph (see Chapter 4).

The π -electronic shells of neutral graphitic objects are classified,^{48,49} function of their eigenvalue spectra, as *closed*, when $x_{v/2} > 0 \geq x_{v/2+1}$ or *open*, when the HOMO and LUMO molecular orbitals are degenerate, $x_{v/2} = x_{v/2+1}$.

The *metallic* character involves the existence of a zero HOMO-LUMO gap (a particular case of the open shell) and the degeneracy of some non-bonding orbitals⁵⁰ (NBOs) favoring the spin multiplicity, cf. the Hund rule. In polyhex tori, the metallic behavior is ensured by *four* NBOs, also present in the graphite sheet. The gap (in β units) is taken as the absolute value of the difference $E_{\text{HOMO}} - E_{\text{LUMO}}$.

A perfect Clar structure^{51,52} PC (Figure 2-12a) is a vertex disjoint set of faces whose boundaries form a 2-factor. A k -factor is a regular k -valent spanning

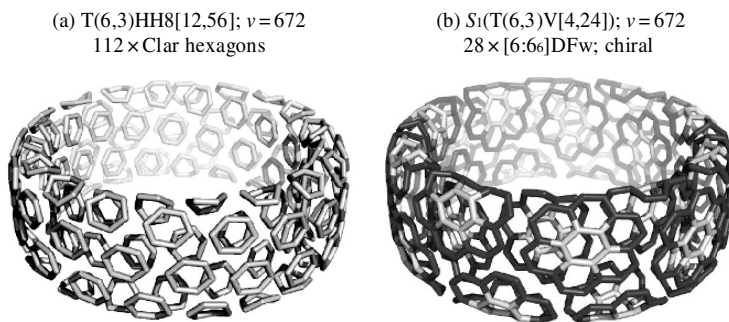


Figure 2-12. Perfect Clar and disjoint coronenic $[6:6_6]\text{DFw}$ structures of H/Z polyhex torus (2,8,12,-24).

subgraph. A PC includes each vertex of G once and only once. It is associated with a Fries structure,⁵³ which is a Kekulé structure drawn over the maximum possible number of benzenoid (alternating single-double edge) hexagonal faces. A Kekulé structure is a set of pairwise disjoint edges of G (covering all its vertices) that coincides with a perfect matching and a 1-factor in Graph Theory.⁵⁴ A trivalent polyhedral graph has a PC if and only if it has a Fries structure.⁵⁵ Such structures represent *total resonant sextet* TRS benzenoid molecules and is expected to be maximally stable, in the valence bond theory.^{55,56} There exist some coverings by large numbers of conjugated 10-circuits (*i.e.*, naphthalenoids and azulenoids), only slightly less favorable, in the valence-bond based conjugated-circuit theory.^{57,58}

By extension, a similar corannulenic system can be imagined. The operation sequence $Le\&Q$, or the generalized (2,2) operation,^{59–62} applied on trivalent maps, provides a Clar-like disjoint corannulenic DCor structure, *e.g.*, the coronenic flowers $[6:6_6]\text{DFw}$, with the associated Fries-like structure defined on all the vertices of graph, excepting the corannulenic core. Figure 2-12b presents the equivalent torus of $T(6,3)HH8[12,56]$, obtained by applying the S_1/Capra operation on $T(6,3)V[4,24]$, with the disjoint coronenic flowers in blue.

Table 2-3 gives the criteria for metallic shell in (6,3) tori of various types. These criteria superimpose over those for PC structure: divisibility by 6 of the net dimensions (see also^{50, 55, 56}). In the opposite, Clar fullerenes (available by Le operation)⁶² show closed-shell structure.^{50,55}

The last column in Table 2-3 gives criteria for the disjoint coronenic DCor structure. Any DCor is a PC but the reciprocal is not necessarily obeyed. Divisibility by twelve and four, of the net dimensions, give the new criterion.

At this stage, it is not clear if the supra organized corannulenic system would bring a supplementary stability in such possible molecules, in comparison to the total resonant benzenoid (Clar) structures. Out of the energetic aspects, it is possible that such molecules behave in the magnetic field similarly to planar corannulenes, for which evaluation of the ring currents was made by the CTOCD-DZ (continuous transformation of origin of current density – diamagnetic zero) method.^{63–67}

Table 2-3. Covering criteria for metallic M, perfect Clar PC and Disjoint Coronenic DCor structures in polyhex tori

	Torus	M & PC	DCor
	Non-Twisted		
1	H/Z[c,n]	0 mod (c,6)	0 mod (c,12); 0 mod (n,4)
2	V/A[c,n]	0 mod (n,6)	0 mod (c,4); 0 mod (n,12)
	H-Twisted		
3	HHt[c,n]	0 mod (c,6)	0 mod (c,12); 0 mod (n,4); 0 mod (t,4)
4	HVt[c,n]	0 mod (n,6) 0 mod(t,6)	0 mod (c,4); 0 mod (n,12) 0 mod (t,12)
	V-Twisted		
5	VHt[c,n]	0 mod (c,6) 0 mod (t,6)	0 mod (c,12); 0 mod (n,4); 0 mod (t,12)
6	VVt[c,n]	0 mod (n,6)	0 mod (c,4); 0 mod (n,12); 0 mod (t,4)

2.6. Identical Polyhex Toroidal Graphs

Toroidal objects generated by the TORUS software, even correctly named to reflect different embeddings, could represent one and the same graph.

Let consider normal tori (*i.e.*, those with $c < n$). Their net dimensions can be written as: $n = c + r$; $r = 0, 2, ..c - 2, c, ..$ and $t = 0, 2, .., c, ...$ Investigating the spectra of the characteristic polynomial of families of polyhex tori led to the following:

*Rules of Valencia*⁶⁸

- (i) The maximum value of t to provide distinct topological objects, in a family of H-twisted polyhex tori, equals $n/2$.
- (ii) The maximum value of t to provide distinct topological objects, in a family of V-twisted polyhex tori, equals $c/2$.

As, by construction of the H-twisted polyhex tori, the maximum possible t -value is $t_{\max} = c$, the immediate consequence of Rule (i) is that n must be *at least twice* higher than c for having *all distinct topological objects*. Higher values for n will only repeat the already generated structures so that the rule was formulated for the case: n higher than c *at most twice*. When $n/2 < c$, some duplicate objects appear, as indicated in Table 2-4.

In case of V-twisted polyhex tori, t does not depend of the ratio c/n ; since t can take values up to n (by construction), with periodicity at $k(c/2)$, $k = 1, 2, ..$, the Rule (ii) was formulated for $t = c$ at most. Details are given in Table 2-4.

In non-twisted tori, the HOMO-LUMO gap remains constant, at a given c -(in H/Z[c, n] series) and n -(in V/A[c, n]) values, respectively. The same is true for the twisted tori, according to the second capital letter in their name.

Note the identity of graphs $H[c, n] = V[n, c]$ but having different embedding. At $c = n$, $H[c, c] = V[c, c]$ and $HVt[c, c] = VHt[c, c]$.

Table 2-4. Identical graphs in families of twisted polyhex tori according to the Rules of Valencia

	Case	Characters
1	General	$n = c + r; \quad r = 0, (2, \dots, c-2), c, \dots; \quad t = 0, 2, \dots, c, \dots$
2	H-twist	$t = 0, 2, \dots, n/2$; distinct objects
2a	H-twist	$n = 2c \rightarrow t_{\max} = c$; all distinct objects
	Case: $r = c$	
2b	H-twist	$n = c \rightarrow V - \text{twist}$
	Case: $r = 0$	
2c	H-twist	$t = 0, 2, \dots, (r-2)$; distinct objects
	Case: $0 < r < c$	$t = r + 0, 2, 4, \dots, (c-r)/2 \equiv c-0, 2, 4, \dots, (c-r)/2$; distinct pairs
3	V-twist	$t = 0, 2, \dots, c/2$; distinct objects
3a	V-twist	$t = 0 + 0, 2, 4, \dots, c/2 \equiv c-0, 2, 4, \dots, c/2$; distinct pairs
	Any case: note	When $c/2$ or $n/2$ are odd, then $t_{\max} = t - 1$

2.7. Resonance Energy in Polyhex Tori

Resuming to the aromaticity of polyhex tori, recall that “resonance energy” RE is defined as the difference $E_{\pi} - E_{\pi, ref}$ between the total π -energy of a conjugated (aromatic) system and the energy of some reference structure. Several approaches have been developed so far.⁶⁹

A system having $RE > 0$ is classified as “aromatic”, that having $RE < 0$ as “antiaromatic” while that for which $RE \approx 0$ as “non-aromatic”.

There exists a theorem⁷⁰ enabling the calculation of resonance energy from the number of Kekulé structures K , by means of eigenvalues of the molecular graph:

$$K = \prod_{i=1}^{v/2} \lambda_i \quad (2.7)$$

$$RE = A \cdot \ln K \quad (2.8)$$

with A being 1.185 (eV). We used this approach to evaluate the aromaticity/stability of series of toroidal objects $TXt[c, n]$, the results being listed in Table 2-5.

The π -electronic shell of the toroids, in the above series, is either closed or metallic M . The value of RE per atom, averaged for the whole family of embedding isomers, is larger for those families entirely consisting of metallic (specified as: Metallic, Clar and Cor, in Table 2-5) objects than for those having mixes metallic& closed or only closed shell members. This result could support the expectation for a higher stability of metallic/aromatic polyhex tori (even the values of RE , at the Hückel level of theory, are supra-estimated, in comparison to those related in ref.⁶⁹). The values in Table 2-5 have been averaged only for the distinct graphs of the embedding isomers, according to Valencia’s rules (Section 2.6).

Table 2-5. Twisted Tori families, topology, π -electronic shell and resonance energy RE

	Torus	t	Shell and Covering	RE (eV)	Observation
T(6,3)Xt[12,56]; $v = 672$					
1	HH	0	Metallic; Clar; Cor	0.1911	H/Z; non-twisted
2		2	Metallic; Clar	0.1917	twisted
3		4	Metallic; Clar; Cor	0.1935	twisted
4		6	Metallic; Clar	0.1961	twisted
5		8	Metallic; Clar; Cor	0.1978	twisted
6		10	Metallic; Clar	0.1988	twisted
7		12	Metallic; Clar; Cor	0.1995	twisted
8				0.1955	average
9	HV		Closed	0.1912	average
10	VH		Metallic & Closed	0.1850	average
11	VV		Closed	0.1883	average
T(6,3)Xt[16,24]; $v = 384$					
	HH		Closed	0.19355	average
	HV		Metallic & Closed	0.19699	average
	VH		Closed	0.19362	average
	VV	0	Metallic; Clar; Cor	0.20480	V/A; non-twisted
		2	Metallic; Clar	0.20481	twisted
		4	Metallic; Clar; Cor	0.20482	twisted
		6	Metallic; Clar	0.20483	twisted
		8	Metallic; Clar; Cor	0.20484	twisted
		10	Metallic; Clar	0.20483	twisted
		12	Metallic; Clar; Cor	0.20482	twisted
		14	Metallic; Clar	0.20481	twisted
		16	Metallic; Clar; Cor	0.20480	V/A; non-twisted
				0.20482	average
T(6,3)Xt[12,18]; $v = 216$					
	HH		Metallic; Clar	0.21025	average
	HV		Metallic & Closed	0.19939	average
	VH		Metallic & Closed	0.19397	average
	VV		Metallic; Clar	0.21206	average

Conclusions

Construction of polyhex (6,3) tori starting from the square tiled (4,4) tori proved to be a robust and versatile procedure. The topology of polyhex tori can be described by the α -spiral code, adapted for tubular objects. Strain energy calculation, in terms of the POAV1 theory, revealed toroidal polyhex objects even more relaxed than the well-known C_{60} . The π -electronic structure was evaluated at the Hückel level of theory, criteria for the metallic character in (6,3) tori being given in terms of the $[c, n]$ net dimensions. These criteria superimpose over those of perfect Clar PC

and disjoint Corannulenic DCor structures, envisaging the metallic polyhex tori as total resonant benzenoid/corannulenoid molecules. Resonance energy calculations provided support for the aromaticity of the hypothetical metallic tori. The study of the graph spectra in families of embedding isomers, generated by the TORUS software, enabled the formulation of two simple rules for distinct isomers provided by the mentioned generator.

References

1. M. Endo, S. Iijima, M. S. Dresselhaus, *Carbon Nanotubes*, Pergamon, 1996.
2. P. W. Fowler, D. E. Manolopolous, *An atlas of fullerenes*, Clarendon Press, Oxford, 1995.
3. M. S. Dresselhaus, G. Dresselhaus, P. C. Eklund, *Science of fullerenes and carbon nanotubes*, Acad. Press, San Diego, 1996.
4. K. Tanaka, T. Yamabe, K. Fukui, *The science and technology of carbon nanotubes*, Elsevier, Amsterdam, 1999.
5. A. T. Balaban, (Ed.), *From Chemical Topology to Three – Dimensional Geometry*, Plenum Press, New York, 1997.
6. L. Euler, *Novi Comment. Acad. Sci. I. Petropolitanae*, 1758, **4**, 109–160.
7. J. Liu, H. Dai, J. H. Hafner, D. T. Colbert, R. E. Smalley, S. J. Tans, C. Dekker, *Nature*, 1997, **385**, 780–781.
8. M. Ahlskog, E. Seynaeve, R. J. M. Vullers, C. Van Haesendonck, A. Fonseca, K. Hernadi, J. B. Nagy, *Chem. Phys. Lett.*, 1999, **300**, 202–206.
9. R. Martel, H. R. Shea, Ph. Avouris, *Nature*, 1999, **398**, 299–299.
10. R. Martel, H. R. Shea, Ph. Avouris, *J. Phys. Chem. B*, 1999, **103**, 7551–7556.
11. D. Babić, D. J. Klein, T. G. Schmalz, *J. Mol. Graphics Model*, 2001, **19**, 222–231.
12. A. Ceulemans, L. F. Chibotaru, P. W. Fowler, *Phys. Rev. Lett.*, 1998, **80**, 1861–1864.
13. J. K. Johnson, B. N. Davidson, M. R. Pederson, J. Q. Broughton, *Phys. Rev., B*, 1994, **50**, 17575–17582.
14. V. Meunier, Ph. Lambin, A. A. Lucas, *Phys. Rev. B*, 1998, **57**, 14886–14890.
15. M. F. Lin, D. S. Chuu, *Phys. Rev. B*, 1998, **57**, 6731–6737.
16. E. C. Kirby, *Croat. Chem. Acta*, 1993, **66**, 13–26.
17. E. C. Kirby, R. B. Mallion, P. Pollak, *J. Chem. Soc. Faraday Trans.*, 1993, **89**, 1945–1953.
18. S. A. Bovin, L. F. Chibotaru, A. Ceulemans, *J. Molec. Catalys.*, 2001, **166**, 47–52.
19. D. Marušić, T. Pisanski, *Croat. Chem. Acta*, 2000, **73**, 969–981.
20. D. J. Klein, *J. Chem. Inf. Comput. Sci.*, 1994, **34**, 453–459.
21. E. C. Kirby, P. Pollak, *J. Chem. Inf. Comput. Sci.*, 1998, **38**, 66–70.
22. T. Pisanski, J. Shawe-Taylor, *J. Chem. Inf. Comput. Sci.*, 2000, **40**, 567–571.
23. A. Graovac, D. Plavšić, M. Kaufman, T. Pisanski, E. C. Kirby, *J. Chem. Phys.*, 2000, **113**, 1925–1931.
24. I. Laszlo, A. Rassat, P. W. Fowler, A. Graovac, *Chem. Phys. Lett.*, 2001, **342**, 369–374.
25. I. Laszlo, A. Rassat, *J. Chem. Inf. Comput. Sci.*, 2003, **43**, 519–524.
26. M. V. Diudea, A. Graovac, *MATCH, Commun. Math. Comput. Chem.*, 2001, **44**, 93–102.
27. M. V. Diudea, I. Silaghi-Dumitrescu, B. Parv, *MATCH, Commun. Math. Comput. Chem.*, 2001, **44**, 117–133.
28. M. V. Diudea, E. C. Kirby, *Fullerene Sci. Technol.*, 2001, **9**, 445–465.
29. M. V. Diudea, *Bull. Chem. Soc. Japan*, 2002, **75**, 487–492.
30. M. V. Diudea, *Fullerenes, Nanotubes, Carbon Nanostruct.*, 2002, **10**, 273–292.
31. M. V. Diudea, *Phys. Chem., Chem. Phys.*, 2002, **4**, 4740–4746.
32. M. V. Diudea, B. Parv, E. C. Kirby, *MATCH, Commun. Math. Comput. Chem.*, 2003, **47**, 53–70.
33. S. Itoh, S. Ihara, *Phys. Rev., B*, 1993, **48**, 8323–8328.

34. M. Endo, K. Takeuchi, K. Kobory, K. Takahashi, H. W. Kroto, A. Sarkar, in: M. Endo, S. Iijima, M. S. Dresselhaus, *Carbon Nanotubes*, Pergamon, 1996, pp. 1–9.
35. A. Sarkar, H. W. Kroto, M. Endo, in: M. Endo, S. Iijima, M. S. Dresselhaus, *Carbon Nanotubes*, Pergamon, 1996, pp. 105–109.
36. N. Hamada, S. Sawada, A. Oshiyama, *Phys. Rev. Lett.*, 1992, **68**, 1579.
37. D. E. Manolopoulos, J. C. May, S. E. Down, *Chem. Phys. Lett.*, 1991, **181**, 105–111.
38. G. Brinkmann, P. W. Fowler, *J. Chem. Inf. Comput. Sci.*, 1998, **38**, 463–468.
39. P. W. Fowler, T. Pisanski, A. Graovac, J. Žerovnik, *DIMACS Ser. Discrete Maths. Theor. Comput. Sci.*, 2000, **51**, 175–187.
40. D. J. Klein, W. A. Seitz, T. G. Schmalz, *J. Phys. Chem.*, 1993, **97**, 1231–1236.
41. M. V. Diudea, B. Parv, O. Ursu, TORUS 3.0, “Babes-Bolyai” University, 2003.
42. M. V. Diudea, in: M. V. Diudea, (Ed.), *Nanostructures-Novel Architecture*, NOVA, New York, 2005, 111–126.
43. R. C. Haddon, *J. Am. Chem. Soc.*, 1990, **112**, 3385–3389.
44. R. C. Haddon, S.-Y. Chow, *J. Am. Chem. Soc.*, 1998, **120**, 10494–10496.
45. R. C. Haddon, *J. Phys. Chem. A*, 2001, **105**, 4164–4165.
46. J. Han, *Chem. Phys. Lett.*, 1998, **282**, 187–191.
47. E. Hückel, *Z. Phys.*, 1931, **70**, 204–286.
48. P. W. Fowler, *J. Chem. Soc., Faraday Trans.*, 1997, **93**, 1–3.
49. P. W. Fowler, *J. Chem. Soc., Faraday Trans.*, 1990, **86**, 2073–2077.
50. M. Yoshida, M. Fujita, P. W. Fowler, E. C. Kirby, *J. Chem. Soc., Faraday Trans.*, 1997, **93**, 1037–1043.
51. E. Clar, *Polycyclic Hydrocarbons*, Acad. Press, London, 1964.
52. E. Clar, *The Aromatic Sextet*, Wiley, New York, 1972.
53. K. Fries, *J. Liebigs Ann. Chem.*, 1927, **454**, 121–324.
54. W.-Ch. Shiu, P. Ch. B. Lam, H. Zhang, *Theochem* 4, 2000, p. 0210.
55. P. W. Fowler, T. Pisanski, *J. Chem. Soc., Faraday Trans.*, 1994, **90**, 2865–2871.
56. J. R. Dias, *J. Chem. Inf. Comput. Sci.*, 1999, **39**, 144–150.
57. D. J. Klein, H. Y. Zhu, *From Chemical Topology – to Three Dimensional Geometry*, A. T. Balaban, (Ed.), Plenum Press, New York, 1997, pp. 297–341.
58. E. C. Kirby, *MATCH, Commun. Math. Comput. Chem.*, 1996, **33**, 147–156.
59. M. V. Diudea, P. E. John, A. Graovac, M. Primorac, T. Pisanski, *Croat. Chem. Acta*, 2003, **76**, 153–159.
60. M. Ștefu, M. V. Diudea, P. E. John, *Studia Univ. “Babes-Bolyai”*, 2005, **50**(2), 165–174.
61. M. V. Diudea, M. Ștefu, P. E. John, A. Graovac, *Croat. Chem. Acta*, 2006, **79**, 355–362.
62. P. W. Fowler, *Chem. Phys. Lett.*, 1986, **131**, 444–450.
63. T. A. Keith, R. F. W. Bader, *Chem. Phys. Lett.*, 1993, **210**, 223–231.
64. A. Acocella, R. W. A. Havenith, E. Steiner, P. W. Fowler, L. W. Jenneskens, *Chem. Phys. Lett.*, 2002, **363**, 64–72.
65. P. W. Fowler, E. Steiner, *Chem. Phys. Lett.*, 2002, **363**, 259–266.
66. P. Lazzaretti, in: J. W. Emsley, J. Feeney, L. H. Sutcliffe (Eds.) *Progress in Nuclear Magnetic Resonance Spectroscopy*, Elsevier, Amsterdam, 2000, **36**, 1–88.
67. M. Lillington, P. W. Fowler, M. V. Diudea, *Polish J. Chem.* 2007 (in press).
68. M. V. Diudea, *J. Math. Chem.* 2006 (submitted); These rules have been elaborates at the University of Valencia, 2006, when M. V. Diudea was visiting the Group of Molecular Connectivity, leaded by Prof. Jorge Galvez.
69. M. Randić, *Chem. Rev.*, 2003, **103**, 3449–3605.
70. N. Trinajstić, *Chemical Graph Theory*, CRC Press, Boca Raton, FL, 1992, pp. 125, 160, 161, 188.

Chapter 3

New Classes of Toroidal Structures

3.1. Distinct Walled Tori

3.1.1. DWNT as DWT Precursors

The final product in the thermal annealing of nanopeapods is a double-walled carbon nanotube DWNT. It was discussed above (Chapter 1) that coalescence can be induced by electron beam irradiation, when vacancies and dangling bonds appear in the carbon lattice and energy reduction is achieved by elimination of such defects. Field emission electron guns, already available, permit the controlled irradiation of a small region at the nanometer scale. The dangling bonds, generated by irradiation, could stabilize themselves by forming new bonds between the two interlaced tubular units. This would result in formation of an elongated torus, named hereafter “distinct-walled torus” DWT, to indicate different number of atoms on the inner and outer walls, respectively. Various types of DWTs, derived from armchair nanotubes, are further presented.

The inner tube is shown in Figure 3-1 as the top hexagons. Breaking of the boldface bonds results in two dangling bonds. To remake the valence of three, each dangling bond has to connect with two carbon atoms from the outer tube (see dotted bonds in Figure 3-1). That is why twice as much carbon atoms in a row in the outer tube are needed. Of course, the growth of the inner tube depends on the outer tube diameter.

The junction between the two tubes consists of alternating pentagon/octagon/pentagon *POP* triplets, which ensure the complementary curvature and stability of the structure. The elimination of octagons is possible by Stone-Wales rotation of the bonds connecting two vicinal pentagons. However, the pentagon-heptagon *PH* containing junction appears more strained, after optimization, as suggested by increased HF values (see below). The covering of both these junctions exhibits

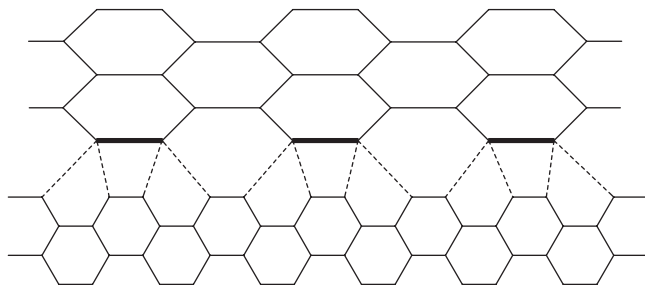


Figure 3-1. Joining scheme of the two distinct tubes in DWT formation.

a PC structure (see Figure 3-2 and below): $[n]$ radialenic substructures appear for $n = \text{odd}$ and the odd-membered rings consist of only single bonds, while the double bonds lie in the even-membered faces.

Considering armchair nanotubes with even or odd number of atom rows, the combination of different nanotubes leads to four distinct classes of DWTs, which resembles in their point group symmetry. The torus will have a horizontal plane of symmetry only in case when both tubes have an even number of rows. Figure 3-3 presents the repeat units of these tori. By copying the lines in boldface for $l_e/l_i \doteq 0, 1, 2 \dots$ the tube length increases. In case $l_e/l_i = 0$, the smallest possible torus, having abutting pentagons (*i.e.*, pentalenes), is obtained.

The torus width w can be increased by adding more repeat units (in brackets). Although it is possible to construct a torus from one unit, the strain at the apex is appreciably reduced at values $w \geq 4$. The name of these DWTs includes the type of tubes and their dimensions, in Diudea's nomenclature (see Chapter 2), the first being the outer tube and the last the inner tube: $V/A[2c, 2n+1]$ corresponds to a "V"-outer tube of $2c$ atoms in a row and odd number of rows ($2n+1$) in length, while the inner tube $V/A[c, 2m+1]$ has half as many atoms in a row and again an odd number of rows ($2m+1$) in length. The length of two tubes can

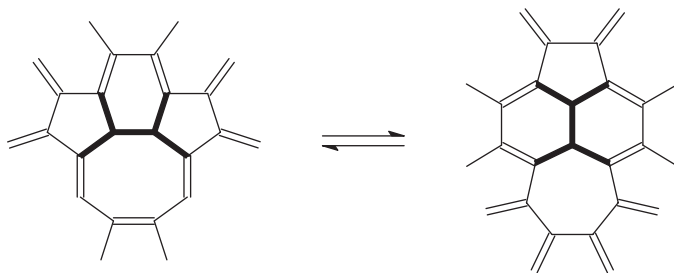


Figure 3-2. Stone-Wales isomerization of the junction between the inner and outer tube of a DWT; the edges involved are boldface.

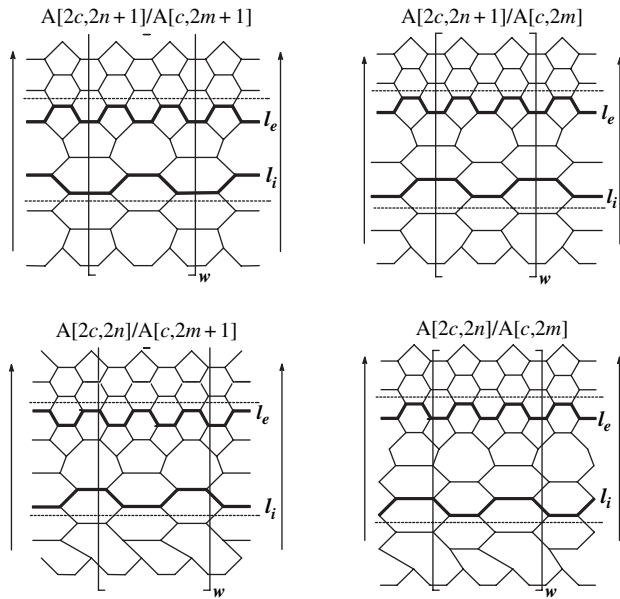


Figure 3-3. Units of the four types of POP-DWT, in geodesic projection.

be either equal, when $n = m$, or different (Figure 3-3). Note the symbols V or A and H or Z are equivalent.

For every class of POP-DWTs an example is presented in Figures 3-4 and 3-5 both as top and side view; the non-hexagonal faces are shown in dark color. In all these examples, the inner tube is the armchair A[10, n], which is the tube that can

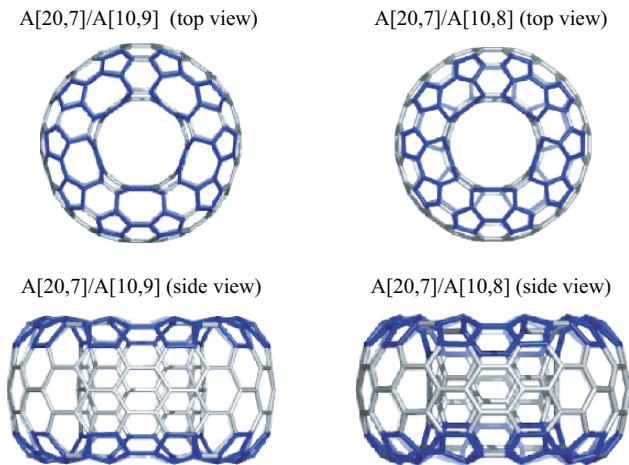


Figure 3-4. POP-DWTs with an odd number of rows in the outer tube.

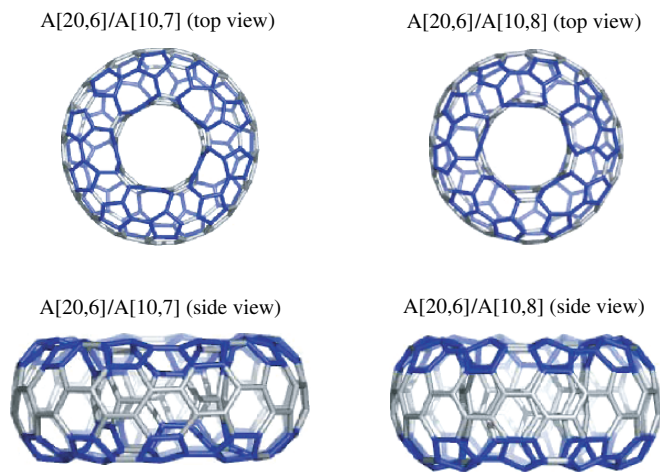


Figure 3-5. POP-DWTs with an even number of rows in the outer tube.

result in the coalescence of two C_{60} molecules. Figure 3-4 presents POP-DWTs with odd number of rows in the external tube. The structures in the left column have the highest point group symmetry, D_{5h} .

Figure 3-5 presents tori with even number of rows in the outer tube.

It is well known that, in case of polyhex tori, the minimal energy is reached only at a perfect circular tube section. This happens at very large central hollow of the torus.¹

With DWTs the situation is different. If the length of both tubes is small enough, the cross section of the torus wall is near circular. As the tube length increases, the cross section becomes an elongated, elliptic-shaped one. The heat of formation decreases as the tube length increases, in all the four classes of DWTs (Table 3-1).

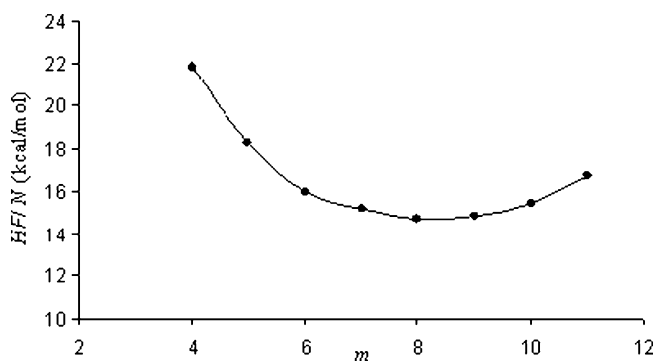
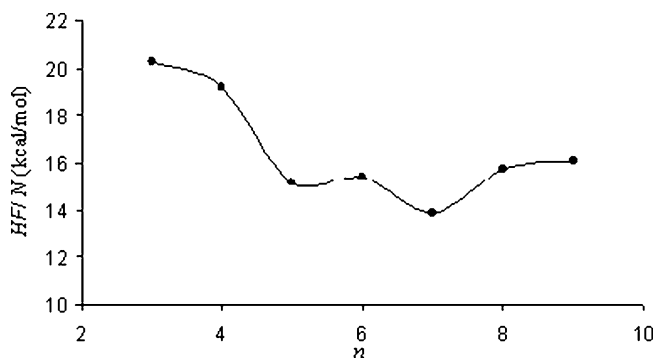
Note that similar tori have been previously proposed by several authors,^{2,3,4,5} but no relation with peapods, coalescence and DWNT was suggested. Also note that hemitori, resembling with our DWTs, have been observed by TEM^{6,7} and inferred in multi walled nanotube growth.

The topology of the junction zone of a DWT influences both the strain and heat of formation. Keeping constant one tube and varying the length of the other enabled construction of a series of tori. Semiempirical calculations are presented in Table 3-1 and Figures 3-6–3-7. The minimal energy corresponds to the most relaxed structure. When there is a notable difference between the tubes length, the energy increases due to hexagons forced to lie at the apex. At extreme low/high values of m , the structure could not be optimized anymore. Figure 3-6 shows the energy curve for a series of POP-DWTs, where the inner tube length varied in the range $m = 4, 5 \dots$. The structure with lowest energy was found A[20,5]/A[10,8].

The plot in Figure 3-7 shows a series of POP-DWTs with the inner tube length maintained constant.

Table 3-1. PM3 data for three classes of POP-DWTs

Name	ν	Sym	HF/ ν (kcal/mol)	Gap (eV)
A[20,5]/A[10,7]	170	D_{5h}	15.159	5.031
A[20,7]/A[10,9]	230	D_{5h}	12.122	5.685
A[20,9]/A[10,11]	290	D_{5h}	10.827	4.218
A[20,11]/A[10,13]	350	D_{5h}	9.890	3.767
A[20,3]/A[10,4]	100	D_{5d}	32.213	6.274
A[20,5]/A[10,6]	160	D_{5d}	15.978	5.134
A[20,7]/A[10,8]	220	D_{5d}	12.678	5.589
A[20,9]/A[10,10]	280	D_{5d}	11.376	4.092
A[20,4]/A[10,6]	140	D_5	20.306	5.967
A[20,6]/A[10,8]	200	D_5	14.408	4.988
A[20,8]/A[10,10]	260	D_5	12.319	4.051
A[20,10]/A[10,12]	320	D_5	10.756	4.760

Figure 3-6. Heat of formation values for the series A[20, 5]/A[10, m] $m = 4, 5 \dots 11$. of POP-DWTs.Figure 3-7. Heat of formation values for the series A[20, n]/A[10, 7] $n = 3, 5 \dots 9$ of POP-DWTs.

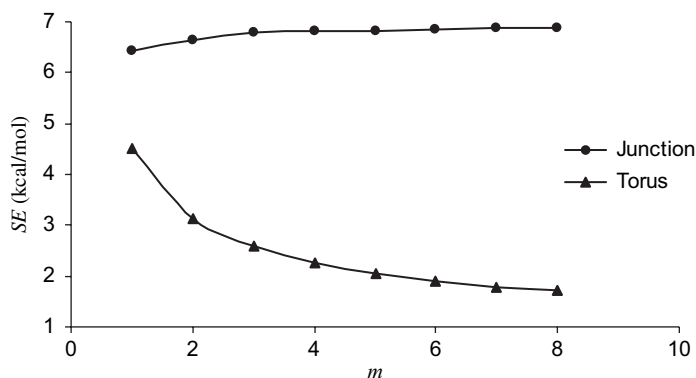


Figure 3-8. Strain energy for the series $A[20, n]/A[10, m]$, $n = 7, 13, \dots, 49$; $m = 11, 17, \dots, 53$ of POP-DWTs.

If the length of both tubes was increased by the same number of rows, the junction zone showed an almost constant strain. The global strain energy decreases as the tube length increases (Figure 3-8).

We limited here to only $A[20, n]/A[10, m]$ tori, because these DWTs could result in the coalescence of fullerene molecules. DWTs with larger central hollow have also been modeled, in studying the influence of the primary tube diameter on the structure stability. In this respect, a series of tori was constructed: the length was kept unchanged but the number of repeat units was varied. The tori consisting of one to three repeat units were very strained, they could not be optimized. Figure 3-9 presents tori with four and six repeat units, respectively.

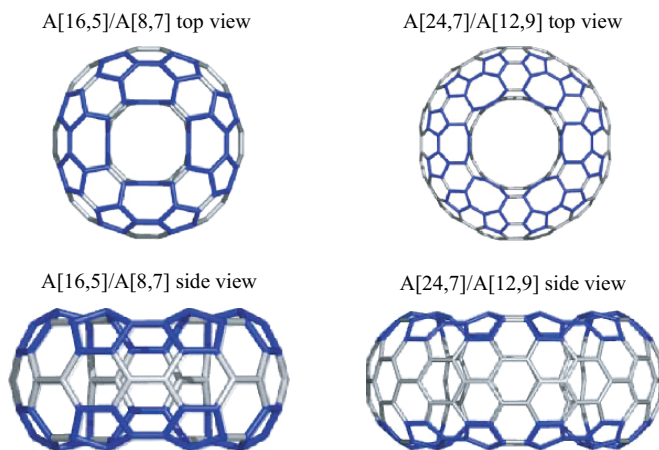


Figure 3-9. POP-DWTs with four/six repeat units.

Table 3-2. PM3 data for a series of POP-DWTs having different number of repeat units

Name	ν	Sym	HF/ ν (kcal/mol)	Gap (eV)
[12,5]/[6,7]	102	D_{3h}	28.146	4.059
[16,5]/[8,7]	136	D_{4h}	18.542	4.687
[20,5]/[10,7]	170	D_{5h}	15.159	5.031
[24,5]/[12,7]	204	D_{6h}	14.635	5.053
[28,5]/[14,7]	238	D_{7h}	15.647	5.278

The data in Table 3-2 show that both thermodynamic and kinetic stability increases as the tube diameter increases. The strain of these structures decreases as the primary tube width increases.

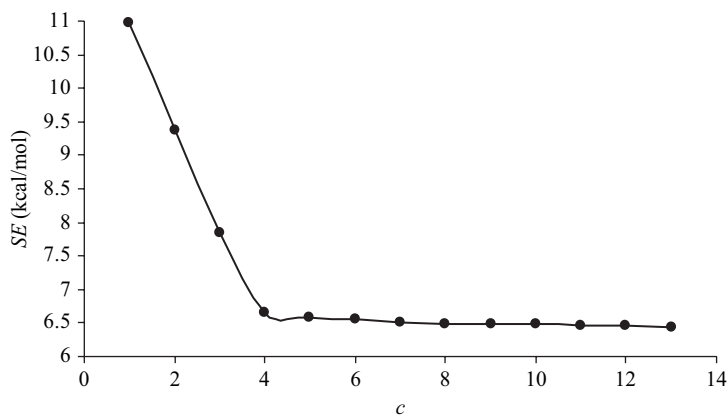
Since semiempirical calculations are size limited, we performed only strain energy calculations (Figure 3-10).

The Stone-Wales rotation can change the triple *POP* to the *PH* pair, in the junction zones (Figure 3-11).

Table 3-3 lists data for sets of *PH*-DWT, SW-related to tori in Table 3-1. The conclusion is that *PH*-junctions rise the strain of the tori, as shown by HF-values.

3.1.2. Perfect Clar DWTs

A molecule is more aromatic (eventually more stable) if it has a perfect Clar PC structure^{8,9} (see also Chapter 6). It is a disjoint set of faces, built up on all vertices in molecule, whose boundaries form a 2-factor (*i.e.*, a set of disjoint cycles). A PC structure is associated with a Fries structure, which is a Kekulé valence structure having the maximum possible number of benzenoid faces. A Kekulé

Figure 3-10. Strain energy SE for the series $A[2c, 7]/A[c, 5]$, $c = 4, 6, \dots, 30$ of POP-DWTs.

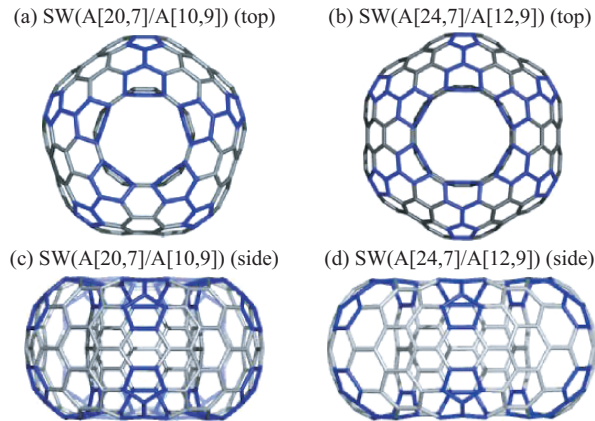


Figure 3-11. PH-DWTs resulted by the SW rotation of bonds joining two pentagons.

structure is a set of pairwise disjoint edges/bonds of the molecule (over all its atoms). Molecules having PC/Fries structures represent *totally resonant sextet* TRS benzenoid molecules and it is expected to be extremely stable, in the valence bond theory.¹⁰ Leapfrog *Le* (see Chapter 5) is the only operation on maps that provides PC transforms. s In DWT, the apex junction of the two tubes looks as shown in Figure 3-2 (with no double bonds in the odd-membered rings) and is suitable for a PC structure. The criterion for PC realization (given below) refers only to the polyhex tubular zone; for armchair A[*c*,*n*] nanotubes, it reads:

POP-DWTs: A[2*c*,3(*n*+1)+1]/A[*c*,3(*m*+1) –1]

PH-DWTs: A[2*c*, 3(*n* + 2)]/A[*c*, 3(*m* + 2)]

Recall the *Leapfrog Le* operation on maps: $Le(M) = Du(P_3(M))$. Keeping in mind that dual of dual returns the original map, the *Retro-Leapfrog RLe*, leading to the parent torus. can be written as: $RLe(M) = RP_3(Du(Le(M)))$, with RP3 being the *retro*-operation of stellation P_3 .

Table 3-3. PM3 data for three series of PH-DWTs

Name	ν	Sym	HF/ ν (kcal/mol)	Gap (eV)
SW(A[20,5]/A[10,7])	170	D_{5h}	18.202	4.815
SW(A[20,7]/A[10,9])	230	D_{5h}	14.311	4.547
SW(A[20,9]/A[10,11])	290	D_{5h}	12.249	5.078
SW(A[20,5]/A[10,6])	160	D_{5d}	17.032	4.719
SW(A[20,7]/A[10,8])	220	D_{5d}	13.731	4.584
SW(A[20,9]/A[10,10])	280	D_{5d}	11.870	4.825
SW(A[20,4]/A[10,6])	140	D_5	20.306	5.967
SW(A[20,6]/A[10,8])	200	D_5	14.408	4.988
SW(A[20,8]/A[10,10])	260	D_5	12.319	4.051

Figure 3-12a presents retro-leapfrog parent of a *POP*-DWT, which has the corresponding vertices of valence four (in dark). It is known that a bounding polygon, of size $2d_0$, is formed around each original vertex (Chapter 5); it is now obvious that the octagonal face in *POP*-DWT came out by the leapfrog operation and the object in Figure 3-12a exhibits a PC covering.

The SW-pair *PH*-DWT has an all trivalent, parent map (Figure 3-12b). Noticeably, the SW operation preserves the PC character of the original map. The corresponding junction zones are detailed in Figure 3-12c,d and the PC structure of $A[20,7]/A[10,8]$ and $SW(A[20,9]/A[10,9])$ tori are given in Figure 3-12e,f.

As above mentioned, DWTs with a *PH* junction are less stable than their corresponding *POP* SW-pair. It is generally true, excepting the case of PC *PH*-DWT; both the kinetic and thermodynamic stability of such tori is higher than its pair PC *POP*-DWT. Table 3-4 presents semiempirical data performed on PC DWTs.

It was found that DWTs become more relaxed by increasing the tube length. A supplementary stability is brought by the PC covering. We limited here to the armchair achiral nanotubes, but it is also possible to construct tori by chiral nanotubes.

By extension, a perfect corannulenic *PCor* structure was proposed by Diudea¹¹ (Figure 3-13). It is a *disjoint set* of (supra) faces covering all vertices in the molecular graph (see Chapter 6). A molecule has a PCor if and only if it has a PC but the reciprocal is not always true. The supra-organized corannulenic units are expected

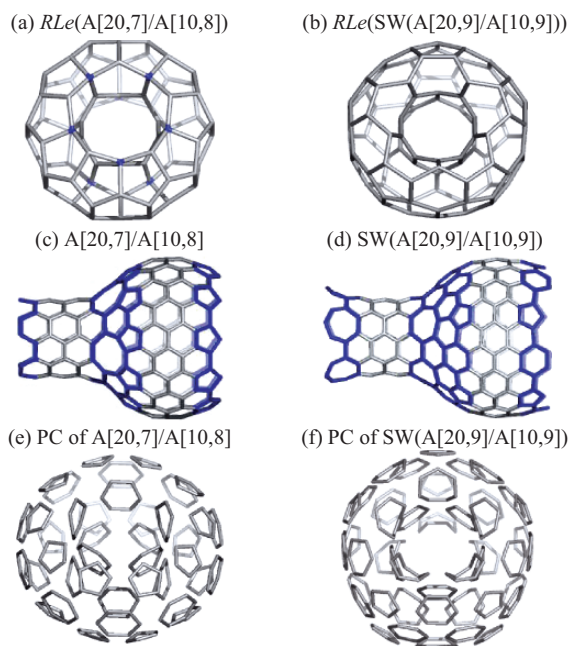


Figure 3-12. Retro-Leapfrog (a, b); PC junctions (c, d) and PC DWTs (e, f).

Table 3-4. PM3 data for PC DWTs

Name	ν	Sym	HF/ ν (kcal/mol)	GAP (eV)	Junction type
A[20,4]/A[10,5]	130	D_5	23.830	5.635	POP
A[20,4]/A[10,8]	160	D_5	18.603	5.624	POP
A[20,4]/A[10,11]	190	D_5	20.994	6.190	POP
A[20,7]/A[10,5]	190	D_{5h}	17.926	5.409	POP
A[20,7]/A[10,8]	220	D_{5d}	12.678	5.589	POP
A[20,7]/A[10,11]	250	D_{5h}	12.274	4.518	POP
A[20,7]/A[10,14]	280	D_{5d}	14.917	5.181	POP
A[20,10]/A[10,8]	280	D_5	15.652	3.875	POP
SW(A[20,6]/A[10,6])	180	D_5	16.855	5.033	PH
A[20,9]/A[10,9]	270	D_{5h}	12.441	3.725	POP
SW(A[20,9]/A[10,9])	270	D_{5h}	12.051	4.266	PH

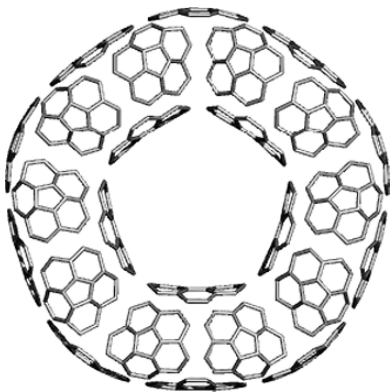


Figure 3-13. The PCor of A[20,7]/A[10,5] POP-DWT.

to contribute to the stability of the whole molecule and to a particular behavior in the magnetic field.

Note that any DWT can be covered with a PCor structure by using generalized map operations.

3.2. Conetori

If a graphene sheet is divided into six sectors, each with an angle of 60° (Figure 3-14), and if m of these sectors (with m varying from 1 to 5) are selected sequentially with the dangling bonds being fused together, a series of five single-walled nanocones is obtained, with a linear angle α at the cone apex equal to 112.9°, 83.6°, 60.0°, 38.9°, and 19.2°. These values correspond to the formula:¹² $\alpha = 2 \arcsin(m/6)$.

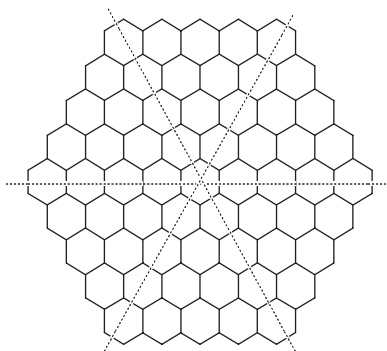


Figure 3-14. The six sectors on a honeycomb lattice.

One can add two extreme cases: (i) the graphene sheet, with all $m = 6$ sectors being involved, corresponding to a “cone” with an angle of 180° ; and (ii) when $m = 6$, one obtains a “cone angle” equal to zero, corresponding to a nanotube capped at one end with any combination of hexagons and six pentagons, *e.g.*, a “half-buckminsterfullerene”. Thus a nanotube capped at one end can be considered as a case of nanocones, as Ebbesen has observed by transmission electron microscopy.^{13,14}

In the hereafter text, only cones ending in polygons of $s = 3$ to 5 , with no other polygonal defect of the graphite sheet, will be considered. The name of such objects includes: {[tip polygon] CN_length of the cone body} (in number of hexagon rows – Figure 3-15).

Conical zones may be involved in the construction of the DWT, suggested¹⁵ to result by sealing, with an electron beam, a double-walled carbon nanotube DWNT in two distinct positions. Proposals of toroidal structures bearing polygonal defects are known since the pioneering times of nanoscience.^{16,17,18} Such structures, of genus 1, including conical zones and called hereafter conetori, are built up by joining the cones with two tubes, one internal and the other external, of distinct diameters. Their name includes: {[apex:length]CT(junction, internal tube type, length), (junction, external tube type, length)}, the length being given in number of hexagon rows. The tube is either a H/Z (zig-zag) or V/A (armchair) one.¹⁹

The idea of possible synthesis of this kind of tori originates in the experimental evidence of nanopeapods, a hybrid structure consisting of (coalesced) fullerene molecules encapsulated in single-walled nanotubes.^{20,21,22}

Two conical units could be connected to form a fullerene, an hourglass (Figure 3-16), or a torus.

3.2.1. Conetori with: Internal H/Z-Tube, External V/A-Tube

In the case of conetori, the junction between the external and internal tubes is: pentagon/ heptagon/pentagon: (5,7,5). Figure 3-17 presents a conetorus of such junction, in the optimized form. The PM3 data are given in the top of figure.

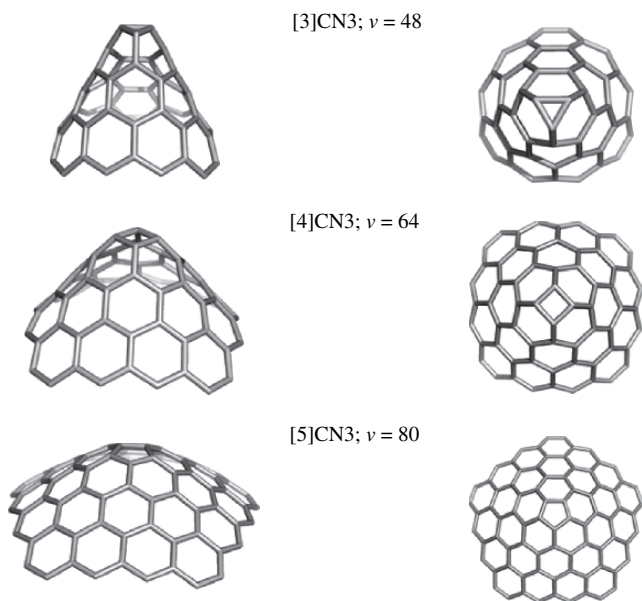


Figure 3-15. Nanocones ending in a trigonal, tertagonal or pentagonal apex.

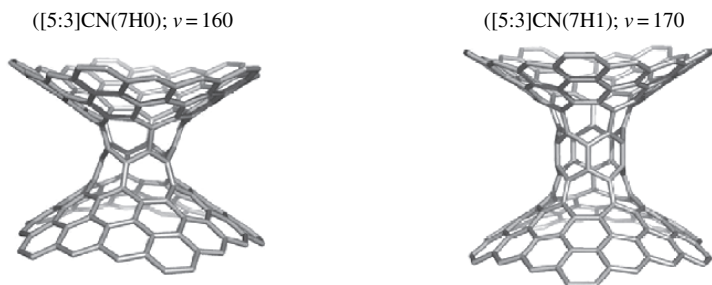


Figure 3-16. Conical units joined to form hourglasses.

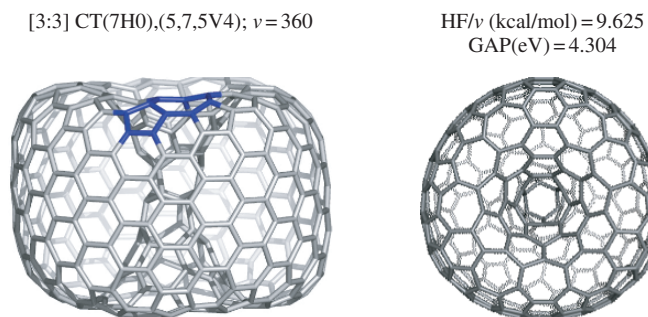


Figure 3-17. A conetorus with internal H/Z-tube, external V/A-tube.

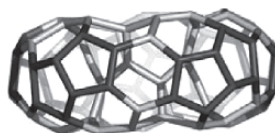
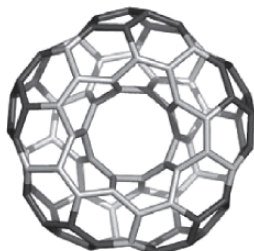
Within a series of increasing size, the clear trend exists: the larger object the higher molecular stability, mainly achieved by strain relief.

3.2.2. Conetori with: Internal H/Z-Tube, External Cone (Without Tube)

A series of conetori with no external tube is presented in Figure 3-18. The two conical shirts fit in a single joining zone: $((5, 6_k, 5); k = 0, 1, \dots)$. Their general name is: $[n : k + 1]\text{CT}(7\text{H}0), (5, 6_k, 5) k = 0, 1, \dots$. Note that, these tori have no internal tube (see "0" in their name, above) but the junction of the two conical zones is made as in the H-tubes. The positive curvature is induced by the presence of pentagons. The PM3 data for these tori are given in Table 3-5. Again, the stability of molecules increases with the size.

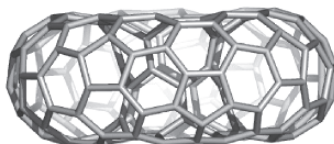
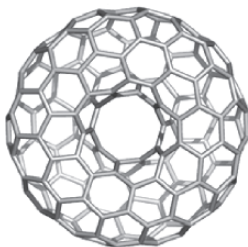
[5:1]CT(7H0),(5,6_k,5,6); $\nu = 90$; (top)

(side)



[5:2]CT(7H0),(5,6_k,5); $\nu = 160$; (top)

(side)



[5:3]CT(7H0),(5,6_k,5); $\nu = 360$; (top)

(side)

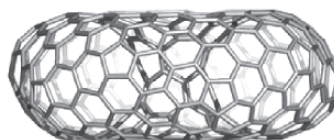
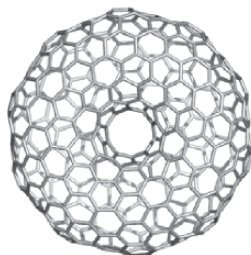


Figure 3-18. Conetori $[5:k + 1]\text{CT}(7\text{H}0), (5, 6_k, 5); k = 0, 1, \dots$ with internal H/Z-tube, external cone.

Table 3-5. PM3 data for tori $[5:k+1]\text{CT}(7\text{H}0),(5,6_k,5)$ $k = 0, 1, \dots$ having internal H/Z- tube and “external” cone

Name	ν	Sym.	HF/ ν (kcal/mol)	Gap (eV)	SE/ ν (kcal/mol)
$[5:1]\text{CT}(7\text{H}0),(5,6_k,5,6)$	90	D_5	21.987	5.569	9.458
$[5:2]\text{CT}(7\text{H}0),(5,6_k,5)$	160	D_{5d}	12.723	5.210	4.994
$[5:3]\text{CT}(7\text{H}0),(5,6_k,5)$	360	C_1	7.640	4.773	2.315

Table 3-6. PM3 data for conetori with internal V/A-tube and external cone

Name	ν	Sym.	HF/ ν (kcal/mol)	Gap (eV)	SE/ ν (kcal/mol)
$[5:2]\text{CT}(7,6,7\text{V}3),(5,6,5)$	220	CI	19.580	4.259	4.475
$[5:3]\text{CT}(7,6,7\text{V}3),(5,6,6,5)$	310	CI	14.071	3.731	3.875
$[5:4]\text{CT}(7,6,7\text{V}4),(5,6,6,5)$	420	CI	9.570	4.633	2.934

Table 3-6. gives the PM3 data for these tori, which indicate moderate stability, which increases with the size.

3.2.3. Conetori with: Internal V/A-Tube, External Cone (Without Tube)

In full analogy to the objects presented in Section 3.2.2., tori with internal V-tube and “external” cone can be built up. Figure 3-19 presents previous steps in construction of such tori. The subscript RO indicates the SW rotation used to change the junction zone. Their general name is: $[n : k + 1]\text{CT}(5,8,5\text{V}m),(5,6_k,5)$; $k = 0, 1, \dots$

Even the small conetori of this type are strained structures (see above), it could be imagined that, by increasing the number of atoms, they become more relaxed molecules, as suggested in Figure 3-20. This huge object can be covered by disjoint coronenes (by using the generalized map operation (2,2) – see Chapter 5); it offers the opportunity to address the question of aromaticity of such totally resonant molecular systems and consequently the possible increase of molecular stability.

$[5:2]\text{CT}(5,8,5\text{V}2),(5,6,5)$; $\nu = 220$ $[5:2]\text{CT}(7,6,7_{\text{RO}}\text{V}3),(5,6,5)$; $\nu = 220$

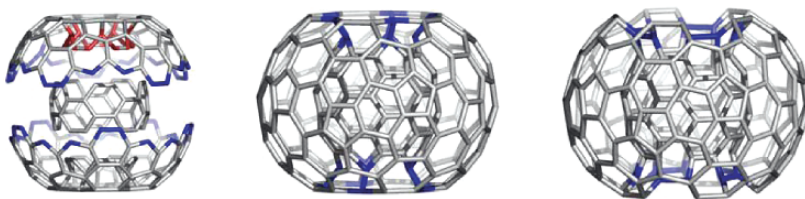


Figure 3-19. Steps in construction of tori with internal V-tube, external cone.

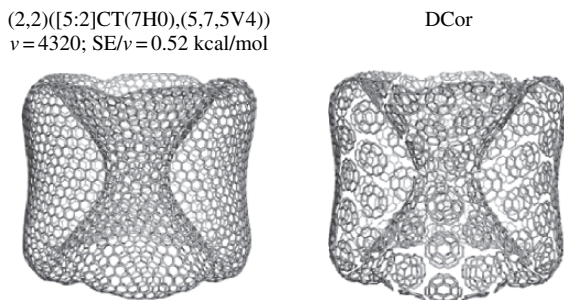


Figure 3-20. A conetorus with disjoint coronenic units. The strain energy SE/v is calculated in terms of POAVI theory.

3.3. Diameter Doubling of SWNT

Diameter doubling of single-walled carbon nanotubes has been observed experimentally. Armchair tubes were annealed at 1400 or 1500°C under vacuum, flowing argon, flowing hydrogen atmosphere, *etc.* As many as 60% of the nanotubes so treated coalesced with their neighbors, the proportion depending on the atmosphere. The coalesced nanotubes show twice (and occasionally three times) the diameter of the initial tubes. Only nanotubes with identical chirality are believed to undergo coalescence.^{24,25}

Studies by high-resolution transmission electron microscopy HRTEM, allowed access to a variety of structural changes in carbon systems. Electron irradiation removes carbon atoms from their lattice sites, by knock-on displacements. The atoms can either be ejected from the tube, or migrate as interstitials along the inner or outer surface. The high temperature ensures a high mobility of interstitials and hence a rapid annealing of defects. Because of the vacancies, the system becomes energetically unstable. When tubes are assembled in bundles, the irradiated tubes will establish links in order to satisfy most of the dangling bonds. The fusion is driven by the minimization of strain energy so that tubes with larger diameter are created.²⁶

Generation of interstitials at a graphite-diamond interface can lead to the transformation of graphite to diamond.²⁷ This phenomenon has also been studied by electron microscopy.

A zipper mechanism was proposed for armchair nanotube coalescence. The initial steps are similar to the formation of the local bridge between spherical fullerenes, followed by a sequence of SW transformations. The resulted Y-junction consists of an octagon and four heptagons, and it propagates axially, similar to a zipper. The transformation cycle requires nine SW steps, the process being exothermic. This transformation was evidenced experimentally by HRTEM. Nanotubes, lying close and parallel to each other, at 800°C start to merge fast after the initial connection. The main advantage of this mechanism is that such systems are vacancy free.²⁸

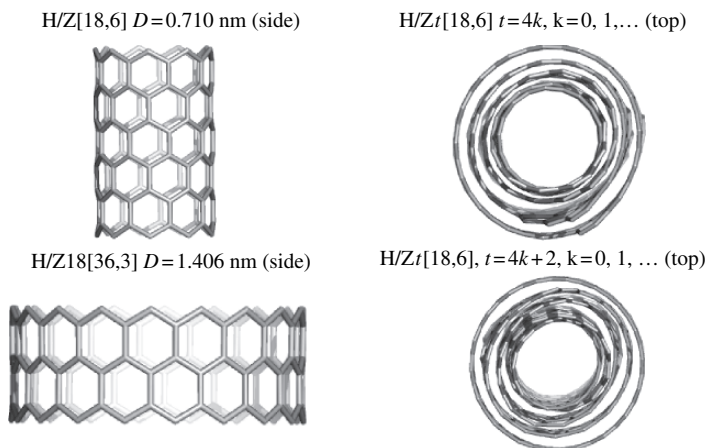


Figure 3-21. Zig-zag H/Z nanotubes before and after twisting.

In experiments with nanopeapods, the inner tube diameter growth, up to 0.71 nm distance from the host nanotube wall, was observed. The authors proposed a model based on formation of achiral zig-zag nanotubes at the beginning of fullerene coalescence. In the light of our previous results,²⁹ we propose the formation of chiral/twisted zigzag tubes, a process often appearing in the synthesis of nanotubes, which stepwise enlarges the diameter, up to the doubling one. Note that the final tube is again achiral (and zigzag as well), and its length is half of the initial tube. Figure 3-21 illustrates the diameter doubling by twisting (right hand column, top view) of a zigzag polyhex nanotube.

The twisting leads to more relaxed molecules, by decreasing the strain of their surface, as shown in Figure 3-22.

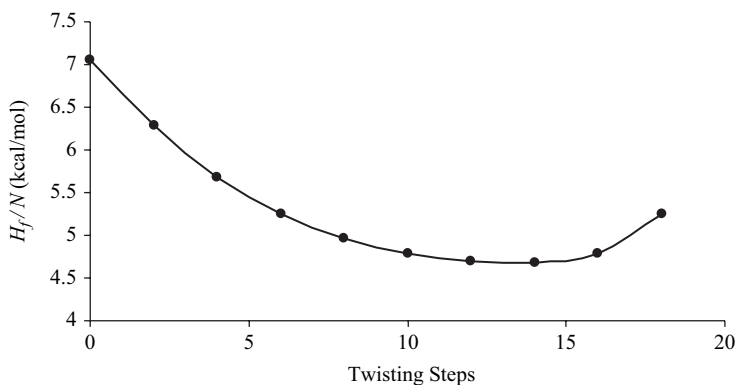


Figure 3-22. Energy curve of the twisting process of H/Z[18,6].

The armchair tubes change to zigzag ones at the complete twisting ($t = c$), but without diameter doubling. Such tubes can enlarge the diameter, either by the zipper mechanism, or by previous transformation in zig-zag tubes, again by SW isomerization (see Chapter 5).

Joining single-walled carbon nanotubes to form X, Y and T molecular junctions are experimentally achieved by electron beam irradiation of crossed tubes. The ultrasonic dispersion of SWNTs in solution leads to a random crisscrossing distribution. These arrangements were monitored under TEM, and the crossing points were irradiated for a short time. The two tubes merged together resulting an X shaped junction. By further careful irradiation it was possible to remove the arms of the junction in order to create a Y or T junction.³⁰

The reason why the merging process takes place is the formation of dangling bonds, under electron beam. It is noticeable that, in the absence of irradiation, the process does not occur. The energy of the system is lowered by connecting the dangling bonds in both tubes, which results in the junction. In the new surface, heptagons and octagons appear to introduce a smooth negative curvature (see Chapter 7).

Conclusions

The coalescence of fullerene molecules, experimentally observed by TEM in annealed/irradiated peapods, can be described by a sequence of Stone-Wales SW bond rotations. Tubulenes can further be transformed, by SW, in other tubular forms. The finally resulted double-walled nanotubes DWNTs could be precursors of distinct-walled tori DWTs, with the apex zones decorated by non-hexagonal faces. Semiempirical calculations proved that such tori are far more stable than the classical polyhex ones, at least at small and moderate size.

References

1. J. Han, *Chem. Phys. Lett.*, 1998, **282**, 187–191.
2. S. Itoh, S. Ihara, J.-I. Kitakami, *Phys. Rev. B*, 1993, **47**, 1703–1704.
3. S. Ihara, S. Itoh, J. Kitakami, *Phys. Rev. B*, 1993, **47**, 12908–12911.
4. S. Itoh, S. Ihara, *Phys. Rev. B*, 1994, **49**, 13970–13974.
5. S. Itoh, S. Ihara, *Phys. Rev. B*, 1993, **48**, 8323–8328.
6. M. Endo, K. Takeuchi, K. Kobory, K. Takahashi, H. W. Kroto, A. Sarkar, in: M. Endo, S. Iijima, M. S. Dresselhaus, *Carbon Nanotubes*, Pergamon, 1996, pp. 1–9.
7. A. Sarkar, H. W. Kroto, M. Endo, in: M. Endo, S. Iijima, M. S. Dresselhaus, *Carbon Nanotubes*, Pergamon, 1996, pp. 105–109.
8. Clar, *The Aromatic Sextet*, Wiley, New York, 1972.
9. Clar, *Polycyclic Hydrocarbons*, Acad. Press, London, 1964.
10. J. R. Dias, *J. Chem. Inf. Comput. Sci.*, 1999, **39**, 144–150.
11. M. V. Diudea, Covering forms in nanostructures, *Forma* (Tokyo), 2004, **19**, 131–163.
12. A. T. Balaban, in: M. V. Diudea (Ed.), *Nanostructures-Novel Architecture*, Nova, New York, 2005, 113–142.
13. A. Krishnan, E. Dujardin, M. M. J. Treacy, J. Higdahl, S. Lynum, T. W. Ebbesen, *Nature*, 1997, **388**, 451–454.

14. T. W. Ebbesen, *Acc. Chem. Res.*, 1998, **31**, 558–566.
15. Csaba L. Nagy, Mircea V. Diudea, Teodor S. Balaban, in: M. V. Diudea (Ed.), *Nanostructures-Novel Architecture*, Nova, New York, 2005, 35–81.
16. S. Itoh, S. Ihara, J.-i. Kitakami, *Phys. Rev., B*, 1993, **47**, 1703–1704.
17. S. Ihara, S. Itoh, J.-i. Kitakami, *Phys. Rev., B*, 1993, **47**, 12908–12911.
18. D. Babić, D. J. Klein, T. G. Schmalz, *J. Mol. Graphics Modell*, 2001, **19**, 222–231.
19. M. V. Diudea, T. S. Balaban, E. C. Kirby, A. Graovac, *Phys. Chem., Chem. Phys.*, 2003, **5**, 4210–4214.
20. J. Lu, S. Nagase, S. Zhang, L. Peng, *Phys. Rev. B*, 2003, **68**, 121402(1)–(4).
21. M. Monthieux, *Carbon*, 2002, **40**, 1809–1823.
22. M. Yudasaka, K. Ajima, K. Suenaga, T. Ichihashi, A. Hashimoto, S. Iijima, *Chem. Phys. Lett.*, 2003, **380**, 42–46.
23. R. C. Haddon, *J. Am. Chem. Soc.*, 1987, **109**, 1676–1685.
24. P. Nikolaev, A. Thess, A. G. Rinzier, D. T. Colbert, R. E. Smalley, *Chem. Phys. Lett.*, 1997, **266**, 422–426.
25. S. L. Fang, A. M. Rao, P. C. Eklund, P. Nikolaev, A. G. Rinzier, R. E. Smalley, *J. Mater. Res.*, 1998, **13**, 2405–2411.
26. M. Terrones, H. Terrones, F. Banhart, J.-C. Charlier, P. M. Ajayan, *Science*, 2000, **288**, 1226–1229.
27. F. Banhart, *J. of Electron. Microsc.*, 2002, **27**, 189–194.
28. M. Yoon, S. Han, G. Kim, S. B. Lee, S. Berber, E. Osawa, J. Ihm, M. Terrones, F. Banhart, J.-C. Charlier, N. Grobert, H. Terrones, P. M. Ajayan, D. Tománek, *Phys. Rev. Lett.*, 2004, **92**, 075504-(1)–(4).
29. M. V. Diudea, T. S. Balaban, E. C. Kirby, A. Graovac, *Phys. Chem. Chem. Phys.*, 2003, **5**, 4210–4214.
30. M. Terrones, F. Banhart, N. Grobert, J.-C. Charlier, H. Terrones, P. M. Ajayan, *Phys. Rev. Lett.*, 2002, **89**, 075505(1)–(4).

Chapter 4

Counting Polynomials of Nanostructures

4.1. Graph Theory Background

Graph theory applied in the study of molecular structures is an interdisciplinary science, called chemical graph theory or molecular topology.¹ A *graph*, $G = G(V, E)$ is a pair of two sets: $V = V(G)$ is a finite, nonempty set of points (*i.e.*, vertices) and $E = E(G)$, the set of unordered pairs of distinct points of V . In a graph, $v = |V(G)|$ and $e = |E(G)|$ are the cardinalities of the sets V and E , respectively. Each pair of points (v_i, v_j) (or simply (i, j)) is a line (*i.e.*, edge), $e_{i,j}$, of G if and only if $(i, j) \in E(G)$. Two vertices are *adjacent* if they are joined by an edge. If two distinct edges are incident with a common vertex, they are *adjacent edges*. The angle between edges as well as the edge length is disregarded. The term *graph* was introduced by Sylvester.² A *complete graph*, K_v , is the graph with any two vertices adjacent. The number of edges in a complete graph is $v(v-1)/2$. A *bipartite graph* is a graph whose vertex set V can be partitioned into two disjoint subsets: $V_1 \cup V_2 = V$; $V_1 \cap V_2 = \emptyset$ such that any edge $(i, j) \in E(G)$ joins V_1 with V_2 . A graph is bipartite if and only if all its cycles are even.^{3,4}

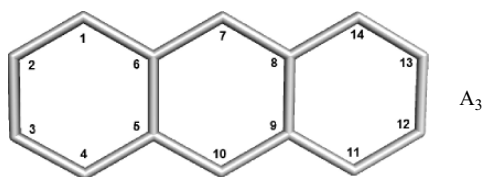
A *walk* w is an alternating string of vertices and edges, $w(1, n) = (v_1, e_1, v_2, e_2, \dots, v_{n-1}, e_m, v_n)$, $v_i \in V(G)$, $e_i \in E(G)$, $m \geq n-1$, such that any subsequent pair of vertices $(v_{i-1}, v_i) \in E(G)$. Revisiting of vertices and edges is allowed. Then $V(w(1, n)) = \{v_1, v_2, \dots, v_{n-1}, v_n\}$ is the set of vertices of $w(1, n)$. Similarly, $E(w(1, n)) = \{e_1, e_2, \dots, e_{m-1}, e_m\}$ is the set of edges of $w(1, n)$. The *length* of a walk, $l(w(1, n)) = |E(w_{1,n})| \geq |V(w_{1,n})| - 1$, equals to the number of its traversed edges. The walk is *closed* if $v_1 = v_n$ (*i.e.*, its *endpoints* coincide) and is *open* otherwise.

A *path* p is a walk having all its vertices and edges distinct: $v_i \neq v_j$, $(v_{i-1}, v_i) \neq (v_{j-1}, v_j)$ for any $1 \leq i < j \leq n$. As a consequence, revisiting of vertices and edges, as

well as branching, is prohibited. The *length* of a path is $l(p(1, n)) = |E(p(1, n))| = |V(p(1, n))| - 1$. A closed path is a *cycle* (i.e., *circuit*). A graph is *connected* if every pair of vertices is joined by a path. A path is *Hamiltonian* if it visits once all the vertices of G . If such a path is a closed one, then it is a *Hamiltonian circuit*.^{1,3,4}

To any organic molecule, an *adjacency matrix*, $\mathbf{A}(G)$, can be associated.^{1,4} This is a square table, of dimensions $v \times v$, whose entries are defined as:

$$[\mathbf{A}(G)]_{ij} = \begin{cases} 1 & \text{if } i \neq j \text{ and } (i, j) \in E(G) \\ 0 & \text{if } i \neq j \text{ or } (i, j) \notin E(G) \end{cases} \quad (4.1)$$



$\mathbf{A}(A_3)$

	1	2	3	4	5	6	7	8	9	10	11	12	13	14	RS
1	0	1	0	0	0	1	0	0	0	0	0	0	0	0	2
2	1	0	1	0	0	0	0	0	0	0	0	0	0	0	2
3	0	1	0	1	0	0	0	0	0	0	0	0	0	0	2
4	0	0	1	0	1	0	0	0	0	0	0	0	0	0	2
5	0	0	0	1	0	1	0	0	0	1	0	0	0	0	3
6	1	0	0	0	1	0	1	0	0	0	0	0	0	0	3
7	0	0	0	0	0	1	0	1	0	0	0	0	0	0	2
8	0	0	0	0	0	0	1	0	1	0	0	0	0	1	3
9	0	0	0	0	0	0	0	1	0	1	1	0	0	0	3
10	0	0	0	0	1	0	0	0	1	0	0	0	0	0	2
11	0	0	0	0	0	0	0	0	1	0	0	1	0	0	2
12	0	0	0	0	0	0	0	0	0	0	1	0	1	0	2
13	0	0	0	0	0	0	0	0	0	0	0	1	0	1	2
14	0	0	0	0	0	0	0	1	0	0	0	0	1	0	2
CS	2	2	2	2	3	3	2	3	3	2	2	2	2	2	32

$\mathbf{A}(G)$ characterizes a graph up to isomorphism. It is symmetric vs. its main diagonal and allows the reconstruction of the graph. The sum of entries in the i^{th} row/column equals the degree of i^{th} vertex, which is a graph invariant. All the following examples are given for the graph A_3 associated to the anthracene.

The *distance matrix*, $\mathbf{DI}(G)$, introduced in 1969 by Harary,³ is a square symmetric table, of dimensions $v \times v$, whose entries count the number of edges along the shortest path $p(i, j)$ joining vertices i and j :

$$[\mathbf{DI}(G)]_{ij} = \begin{cases} l(p(i, j)) = \min, & \text{if } i \neq j \\ 0 & \text{if } i = j \end{cases} \quad (4.2)$$

The entries in $\mathbf{DI}(G)$ represent just the topological distances in G . The matrix \mathbf{DI} of the graph A_3 is presented below. The half sum of all the entries in the distance matrix is the well-known Wiener W topological index:⁵

$$W = \sum_{i < j} [\mathbf{DI}(G)]_{ij} \quad (4.3)$$

$\mathbf{DI}(A_3)$															
	1	2	3	4	5	6	7	8	9	10	11	12	13	14	RS
1	0	1	2	3	2	1	2	3	4	3	5	6	5	4	41
2	1	0	1	2	3	2	3	4	5	4	6	7	6	5	49
3	2	1	0	1	2	3	4	5	4	3	5	6	7	6	49
4	3	2	1	0	1	2	3	4	3	2	4	5	6	5	41
5	2	3	2	1	0	1	2	3	2	1	3	4	5	4	33
6	1	2	3	2	1	0	1	2	3	2	4	5	4	3	33
7	2	3	4	3	2	1	0	1	2	3	3	4	3	2	33
8	3	4	5	4	3	2	1	0	1	2	2	3	2	1	33
9	4	5	4	3	2	3	2	1	0	1	1	2	3	2	33
10	3	4	3	2	1	2	3	2	1	0	2	3	4	3	33
11	5	6	5	4	3	4	3	2	1	2	0	1	2	3	41
12	6	7	6	5	4	5	4	3	2	3	1	0	1	2	49
13	5	6	7	6	5	4	3	2	3	4	2	1	0	1	49
14	4	5	6	5	4	3	2	1	2	3	3	2	1	0	41
CS	41	49	49	41	33	33	33	33	33	33	41	49	49	41	558

Randić has proposed a *hyper-Wiener* index,⁶ which is calculable as the half sum of entries in the *distance-combinatorial* matrix $\mathbf{DI}_p(G)$:¹

$$WW = \sum_{i < j} [\mathbf{DI}_p(G)]_{ij} \quad (4.4)$$

The entries of the $\mathbf{DI}_p(G)$ matrix count all the paths $n_{p \subset p(i, j)}$ included in the shortest path $p(i, j)$, as defined below:^{1,7}

$$[\mathbf{DI}_p(G)]_{ij} = \begin{cases} n_{p \subset p(i, j)}; l(p(i, j)) = \min, & \text{if } i \neq j \\ 0 & \text{if } i = j \end{cases} \quad (4.5)$$

$$n_{p \in p(i,j)} = \binom{[\mathbf{DI}]_{ij} + 1}{2} = \{([\mathbf{DI}]_{ij})^2 + [\mathbf{DI}]_{ij}\}/2 \quad (4.6)$$

The matrix \mathbf{DI}_p of the graph A_3 is presented in the following.

$\mathbf{DI}_p(A_3)$															
	1	2	3	4	5	6	7	8	9	10	11	12	13	14	RS
1	0	1	3	6	3	1	3	6	10	6	15	21	15	10	100
2	1	0	1	3	6	3	6	10	15	10	21	28	21	15	140
3	3	1	0	1	3	6	10	15	10	6	15	21	28	21	140
4	6	3	1	0	1	3	6	10	6	3	10	15	21	15	100
5	3	6	3	1	0	1	3	6	3	1	6	10	15	10	68
6	1	3	6	3	1	0	1	3	6	3	10	15	10	6	68
7	3	6	10	6	3	1	0	1	3	6	6	10	6	3	64
8	6	10	15	10	6	3	1	0	1	3	3	6	3	1	68
9	10	15	10	6	3	6	3	1	0	1	1	3	6	3	68
10	6	10	6	3	1	3	6	3	1	0	3	6	10	6	64
11	15	21	15	10	6	10	6	3	1	3	0	1	3	6	100
12	21	28	21	15	10	15	10	6	3	6	1	0	1	3	140
13	15	21	28	21	15	10	6	3	6	10	3	1	0	1	140
14	10	15	21	15	10	6	3	1	3	6	6	3	1	0	100
CS	100	140	140	100	68	68	64	68	68	64	100	140	140	100	1360

A matrix counting the edges on the longest path between vertices i and j , is called the *detour matrix*, $\mathbf{DE}(G)$ ^{8,9}

$$[\mathbf{DE}(G)]_{ij} = \begin{cases} l(p_{(i,j)}) = \max, & \text{if } i \neq j \\ 0 & \text{if } i = j \end{cases} \quad (4.7)$$

The matrix \mathbf{DE} of the graph A_3 is presented in the following.

The half sum of all the entries in the detour matrix is the *detour w index*:^{10,11}

$$w = \sum_{i < j} [\mathbf{DE}(G)]_{ij} \quad (4.8)$$

In full analogy to the hyper-Wiener index, a *hyper-detour index*^{10,11} is defined:

$$ww = \sum_{i < j} [\mathbf{DE}_p(G)]_{ij} \quad (4.9)$$

$\mathbf{DE}(A_3)$															
	1	2	3	4	5	6	7	8	9	10	11	12	13	14	RS
1	0	13	12	11	10	13	12	11	12	13	11	10	11	12	151
2	13	0	13	12	11	12	11	10	11	12	10	9	10	11	145
3	12	13	0	13	12	11	12	11	10	11	11	10	9	10	145
4	11	12	13	0	13	10	13	12	11	12	12	11	10	11	151
5	10	11	12	13	0	9	8	7	12	13	11	10	11	12	139
6	13	12	11	10	9	0	13	12	7	8	12	11	10	11	139
7	12	11	12	13	8	13	0	13	8	7	13	12	11	12	145
8	11	10	11	12	7	12	13	0	9	8	10	11	12	13	139
9	12	11	10	11	12	7	8	9	0	13	13	12	11	10	139
10	13	12	11	12	13	8	7	8	13	0	12	11	12	13	145
11	11	10	11	12	11	12	13	10	13	12	0	13	12	11	151
12	10	9	10	11	10	11	12	11	12	11	13	0	13	12	145
13	11	10	9	10	11	10	11	12	11	12	12	13	0	13	145
14	12	11	10	11	12	11	12	13	10	13	11	12	13	0	151
CS	151	145	145	151	139	139	145	139	139	145	151	145	145	151	2030

The *detour-combinatorial* matrix \mathbf{DE}_p is defined as:^{1,10}

$$[\mathbf{DE}_p(G)]_{ij} = \begin{cases} n_{p \subset p(i,j)}; l(p(i,j)) = \max, & \text{if } i \neq j \\ 0 & \text{if } i = j \end{cases} \quad (4.10)$$

Number of paths $n_{p \subset p(i,j)}$ included in the longest path joining i and j is calculated by:

$$n_{p \in p(i,j)} = \binom{[\mathbf{DE}]_{ij} + 1}{2} = \{([\mathbf{DE}]_{ij})^2 + [\mathbf{DE}]_{ij}\} / 2 \quad (4.11)$$

The matrix \mathbf{DE}_p of the graph A_3 is presented in the following.

According to the *principle of unsymmetric characterization of a path*, Diudea proposed^{1,12} the *unsymmetric Szeged matrices*, \mathbf{USZ} , on the basis of Gutman's counting of non-equidistant vertices with respect to the endpoints of any edge/path (i, j) in G , giving the well-known Szeged SZ index:¹³

$$[\mathbf{USZX}(G)]_{ij} = \begin{cases} n_{i,(i,j)} & \text{if } i \neq j \\ 0 & \text{if } i = j \end{cases} \quad (4.12)$$

$\mathbf{DE}_p(\mathbf{A}_3)$															
	1	2	3	4	5	6	7	8	9	10	11	12	13	14	RS
1	0	91	78	66	55	91	78	66	78	91	66	55	66	78	959
2	91	0	91	78	66	78	66	55	66	78	55	45	55	66	890
3	78	91	0	91	78	66	78	66	55	66	66	55	45	55	890
4	66	78	91	0	91	55	91	78	66	78	78	66	55	66	959
5	55	66	78	91	0	45	36	28	78	91	66	55	66	78	833
6	91	78	66	55	45	0	91	78	28	36	78	66	55	66	833
7	78	66	78	91	36	91	0	91	36	28	91	78	66	78	908
8	66	55	66	78	28	78	91	0	45	36	55	66	78	91	833
9	78	66	55	66	78	28	36	45	0	91	91	78	66	55	833
10	91	78	66	78	91	36	28	36	91	0	78	66	78	91	908
11	66	55	66	78	66	78	91	55	91	78	0	91	78	66	959
12	55	45	55	66	55	66	78	66	78	66	91	0	91	78	890
13	66	55	45	55	66	55	66	78	66	78	78	91	0	91	890
14	78	66	55	66	78	66	78	91	55	91	66	78	91	0	959
CS	959	890	890	959	833	833	908	833	833	908	959	890	890	959	12544

$$n_{i,p(i,j)} = |\{v \mid v \in V(G); x_{iv} < x_{jv}\}| \quad (4.13)$$

In the above, $\mathbf{X} = \mathbf{DI}$; \mathbf{DE} and x denotes the metric of the elements of these matrices. They can be symmetrized by the Hadamard multiplication with their transposes \mathbf{T} :

$$\mathbf{SM}_p = \mathbf{UM} \bullet (\mathbf{UM})^T \quad (4.14)$$

$$\mathbf{SM}_e = \mathbf{SM}_p \bullet \mathbf{A} \quad (4.15)$$

where \mathbf{A} is the adjacency matrix. The symbol \bullet indicates the Hadamard (pairwise) matrix product¹⁴ (*i.e.*, $[\mathbf{M}_a \bullet \mathbf{M}_b]_{ij} = [\mathbf{M}_a]_{ij} [\mathbf{M}_b]_{ij}$). For the symmetric matrices, the letter \mathbf{S} is usually missing. The subscript e / p denotes the calculation “on edge” ((i, j) is an edge) or “on path” ((i, j) is a path).

The Szeged matrix (defined on distances) of the graph \mathbf{A}_3 is presented in the following. The elements of the corresponding “ e ”-calculated matrix are given in bold-red.

USZDI(A_3)

	1	2	3	4	5	6	7	8	9	10	11	12	13	14	RS
1	0	11	6	7	2	3	3	6	4	5	7	7	8	6	75
2	3	0	7	2	3	2	4	4	5	3	5	7	6	6	57
3	2	7	0	3	2	3	3	5	4	4	6	6	7	5	57
4	7	6	11	0	3	2	5	4	6	3	6	8	7	7	75
5	6	11	10	11	0	7	4	7	6	7	8	8	9	7	101
6	11	10	11	6	7	0	7	6	7	4	7	9	8	8	101
7	7	10	8	9	4	7	0	7	4	7	9	8	10	7	97
8	8	8	9	7	7	6	7	0	7	4	6	11	10	11	101
9	7	9	8	8	6	7	4	7	0	7	11	10	11	6	101
10	9	8	10	7	7	4	7	4	7	0	7	10	8	9	97
11	7	7	8	6	6	4	5	2	3	3	0	11	6	7	75
12	5	7	6	6	4	5	3	3	2	4	3	0	7	2	57
13	6	6	7	5	5	4	4	2	3	3	2	7	0	3	57
14	6	8	7	7	4	6	3	3	2	5	7	6	11	0	75
CS	84	108	108	84	60	60	59	60	60	59	84	108	108	84	1126

A Cluj fragment,^{1,15,16,17,18} symbolized $CJ_{i,j,p}$, collects vertices v lying closer to i than to j , the endpoints of a path $p(i, j)$. In other words, such a fragment collects the vertex proximity of i against any vertex j , joined by the path p , with the distances measured in the subgraph $G-p$, as shown in the following equation:

$$CJ_{i,j,p} = \{v \mid v \in V(G); D_{(G-p)}(i, v) < D_{(G-p)}(j, v)\} \quad (4.16)$$

In cycle-containing graphs, more than one path could join the pair (i, j) , thus resulting more than one fragment related to i (with respect to j and a given path p). By definition, the entries in the Cluj matrix are taken as the maximum cardinality among all such fragments:

$$[UCJX(G)]_{i,j} = \max_p |CJ_{i,j,p}| \quad (4.17)$$

When the path p belongs to the set of distances $DI(G)$, the suffix DI is added to the name of matrix: $X = DI$. When path p belongs to the set of detours $DE(G)$, the suffix is DE. The Cluj matrices are defined in any graph and are, in general, unsymmetric, excepting some symmetric graphs. They can be symmetrized by the Hadamard multiplication with their transposes, as shown above for the Szeged matrices.

In trees, due to the unicity of paths joining any two vertices, $CJDI = CJDE$ and $CJ_{i,j,p}$ counts the paths going to j through i . Also, $CJDI_e = SZDI_e$ in any graph (compare the red-marched entries in SZDI and CJDI of A_3) but the p -counted matrices are different $CJDI_p \neq SZDI_p$.

Basic properties of the Cluj matrices and applications of single number derived descriptors have been presented elsewhere.^{15,16,17,18} The Cluj matrices of the graph

A_3 are presented in the following. The elements of the corresponding “ e ”-calculated matrix are given in bold-red.

UCJDI(A_3)															
	1	2	3	4	5	6	7	8	9	10	11	12	13	14	RS
1	0	11	6	6	2	3	4	4	4	4	6	6	5	5	66
2	3	0	7	2	2	2	4	3	3	3	5	5	4	5	48
3	2	7	0	3	2	2	3	3	3	4	5	4	5	5	48
4	6	6	11	0	3	2	4	4	4	4	5	5	6	6	66
5	10	10	10	11	0	7	6	6	6	7	8	7	7	7	102
6	11	10	10	10	7	0	7	6	6	6	7	7	7	8	102
7	8	8	8	8	4	7	0	7	4	4	8	8	8	8	90
8	8	7	7	7	6	6	7	0	7	6	10	10	10	11	102
9	7	7	7	8	6	6	6	7	0	7	11	10	10	10	102
10	8	8	8	8	7	4	4	4	7	0	8	8	8	8	90
11	6	6	5	5	4	4	4	2	3	4	0	11	6	6	66
12	5	5	4	5	3	3	3	2	2	4	3	0	7	2	48
13	5	4	5	5	3	3	4	2	2	3	2	7	0	3	48
14	5	5	6	6	4	4	4	3	2	4	6	6	11	0	66
CS	84	94	94	84	53	53	60	53	53	60	84	94	94	84	1044

UCJDE(A_3)															
	1	2	3	4	5	6	7	8	9	10	11	12	13	14	RS
1	0	1	1	2	2	1	1	2	1	1	3	3	1	1	20
2	1	0	1	1	2	1	3	3	2	2	4	4	2	2	28
3	1	1	0	1	1	2	2	2	3	3	2	2	4	4	28
4	2	1	1	0	1	2	1	1	2	1	1	1	3	3	20
5	2	2	1	1	0	3	3	6	1	1	2	2	2	2	28
6	1	1	2	2	3	0	1	1	6	3	2	2	2	2	28
7	1	2	1	1	1	1	0	1	1	4	1	1	2	1	18
8	2	2	2	2	6	1	1	0	3	3	2	2	1	1	28
9	2	2	2	2	1	6	3	3	0	1	1	1	2	2	28
10	1	1	2	1	1	1	4	1	1	0	1	2	1	1	18
11	3	3	1	1	2	1	1	2	1	1	0	1	1	2	20
12	4	4	2	2	3	2	2	2	1	3	1	0	1	1	28
13	2	2	4	4	2	3	3	1	2	2	1	1	0	1	28
14	1	1	3	3	1	2	1	1	2	1	2	1	1	0	20
CS	23	23	23	23	26	26	26	26	26	26	23	23	23	23	340

4.2. Counting Polynomials

It is well-known that a graph can be described by: a connection table, a sequence of numbers, a matrix, a polynomial or a derived number (called a topological index). In Quantum Chemistry, the early Hückel theory calculated the levels of π -electron energy of the molecular orbitals, in conjugated hydrocarbons, as roots of the *characteristic polynomial*:^{19,20,21}

$$P(G, x) = \det[x\mathbf{I} - \mathbf{A}(G)] \quad (4.18)$$

In the above, \mathbf{I} is the unit matrix of a pertinent order and \mathbf{A} the adjacency matrix of the graph G . The characteristic polynomial is involved in the evaluation of topological resonance energy TRE, the topological effect on molecular orbitals TEMO, the aromatic sextet theory, the Kekulé structure count, etc.^{19,20,21,22,23,24,25}

The coefficients $m(G, k)$ in the polynomial expression:

$$P(G, x) = \sum_k m(G, k) \cdot x^k \quad (4.19)$$

are calculable from the graph G by a method making use of the *Sachs graphs*, which are subgraphs of G . Relation (2) was found independently by Sachs, Harary, Mili, Spialter, Hosoya, *etc.*¹ The above method is useful in small graphs but, in larger ones, the numeric methods of linear algebra, such as the recursive algorithms of Le Verrier, Frame, or Fadeev, are more efficient.^{26,27}

An extension of relation (4.18) was made by Hosoya²⁸ and others^{29,30,31,32} by changing the adjacency matrix with the distance matrix and next by any square topological matrix.

Relation (4.19) is a general expression of a counting polynomial, written as a sequence of numbers, with the exponents showing the extent of partitions $p(G)$, $\cup p(G) = P(G)$ of a graph property $P(G)$ while the coefficients $m(G, k)$ are related to the occurrence of partitions of extent k .

Counting polynomials have been introduced, in the Mathematical Chemistry literature, by Hosoya,^{33,34} with his Z-counting (independent edge sets) $Z(G, x)$ and the distance degree (initially called Wiener and later Hosoya)^{35,36} $H(G, x)$ polynomials. Their roots and coefficients are used for the characterization of topological nature of hydrocarbons.

Hosoya also proposed the sextet polynomial^{37,38,39,40} for counting the resonant rings in a benzenoid molecule. The sextet polynomial is important in connection with the Clar aromatic sextets,^{41,42} expected to stabilize the aromatic molecules.

The independence polynomial^{43,44,45} counts selections of k -independent vertices of G . Other related graph polynomials are the *king*, *color*, *star* or *clique polynomials*.^{46,47,48,49,50} More about polynomials the reader can find in ref 1.

Some distance-related properties can be expressed in the polynomial form, with coefficients calculable from the layer and shell matrices.^{51,52,53,54,55} These matrices are built up according to the vertex distance partitions of a graph, as provided by the TOPOCLUJ software package.⁵⁶

4.3. Layer/Shell Matrices and Polynomial Coefficients

Let us define the k^{th} layer/shell of vertices v with respect to the vertex i as:⁵⁴

$$G(i)_k = \{ v \mid v \in V(G); \quad d_{iv} = k \} \quad (4.20)$$

The collection of all its layers defines the partition of G with respect to i :

$$G(i) = \{ G(i)_k ; k \in [0, 1, \dots, ecc_i] \} \quad (4.21)$$

with ecc_i being the *eccentricity* of i (i.e., the largest distance from i to the other vertices in G). The entries in the layer matrix (of *vertex property*) **LM** are defined as:

$$[\mathbf{LM}]_{i,k} = \sum_{v \mid d_{i,v}=k} p_v \quad (4.22)$$

The zero column is just the column of vertex property $[\mathbf{LM}]_{i,0} = p_i$. Any atomic/vertex property can be considered as p_i . More over, any square matrix **M** can be taken as *info matrix*, i.e., the matrix supplying local/vertex properties as *row sum RS*, *column sum CS* or *diagonal entries* given by the *Walk matrix*,¹ as implemented in the TOPOCLUJ software.⁵⁶

The *layer matrix* is a collection of the above defined entries:

$$\mathbf{LM} = \{ [\mathbf{LM}]_{i,k}; i \in V(G); k \in [0, 1, \dots, d(G)] \} \quad (4.23)$$

with $d(G)$ being the *diameter* (i.e., the largest distance) of G .

The entries in the *shell matrix* **SM** (of *vertex pair property*) are defined as:⁵⁴

$$[\mathbf{SM}]_{i,k} = \sum_{v \mid d_{i,v}=k} [\mathbf{M}]_{i,v} \quad (4.24)$$

where **M** is any square topological matrix. Any other operation over the square matrix entries $[\mathbf{M}]_{i,v}$ can be used. The shell matrix is a collection of the above defined entries:

$$\mathbf{SM} = \{ [\mathbf{SM}]_{i,k}; i \in V(G); k \in [0, 1, \dots, d(G)] \} \quad (4.25)$$

The zero column $[\mathbf{SM}]_{i,0}$ could collect the diagonal entries in the parent (weighted) square matrix. In the case that they are zero, by definition, $[\mathbf{SM}]_{i,0} = 1$. However, we prefer to leave out the zero column, without losing the generality. This is because the distance-related properties are better counted for $k \geq 1$.

Vertex contributions to a polynomial $P(G, x)$, based on distance counting, can be written as:

$$P(i, x) = (1/2) \sum_k p(i, k) \cdot x^k \quad (4.26)$$

where $p(i, k)$ is the contribution of vertex i to the partition $p(G, k)$ of the global molecular property $P = P(G)$. Note that $p(i, k)$'s are just the entries in \mathbf{LM} or \mathbf{SM} (more exactly $1/2$ the value because the contribution of each vertex is counted twice).

Usually, the vertex/atom contributions to the molecular property vary, so that the polynomial for the whole molecule is obtained by summing all atomic contributions:

$$P(G, x) = \sum_i P(i, x) \quad (4.27)$$

In a vertex transitive graph, the vertex contribution is simply multiplied by N :

$$P(G, x) = N \cdot P(i, x) \quad (4.28)$$

Thus, the coefficients $p(G, k)$ are obtained as the column (half) sums of the entries in \mathbf{LM} or \mathbf{SM} . Hence, $P(G)$ is easily obtained as the polynomial value in $x=1$:

$$P(G) = P(G, x)|_{x=1} \quad (4.29)$$

A distance-extended/weighted property $D_P(G)$ can be calculated by the first derivative of the polynomial, in $x = 1$:

$$D_P(G) = P'(G, x) = \sum_k k \cdot p(G, k) \cdot x^{k-1}|_{x=1} \quad (4.30)$$

Any square matrix can be used as an info matrix for the layer/shell matrices, thus resulting an unlimited number of (distance-based) counting polynomials. The property P can be taken either as a crude property (*i.e.*, column zero in \mathbf{LM}) or within some weighting scheme (*i.e.*, transformed by the sequence: \mathbf{W} -operator $\mathbf{W}(\mathbf{M}_1, \mathbf{M}_2, \mathbf{M}_3)$, $\mathbf{W}(\mathbf{M})$ matrix, \mathbf{LM}/\mathbf{SM}) as implemented in TOPOCLUJ.^{1,45,56}

Some examples (calculated on the anthracene ($G = A_3$) molecule) are given in the following:

Layer Matrices. Case: $p_i = 1$; the layer matrix of counting \mathbf{LC} , and the counting polynomial $P(\mathbf{LC}, G, x)$, written in the second bottom row of the table, is just the Hosoya polynomial $H(G, x)$, with the meaning of a *distance degree sequence*.¹ The distance-extended property is the well-known Wiener index⁵ W .

LC(A ₃)										
	<i>k</i>	1	2	3	4	5	6	7	v	Meaning
	1	2	3	3	2	2	1	0	14	
	2	2	2	2	2	2	2	1	14	
	3	2	2	2	2	2	2	1	14	
	4	2	3	3	2	2	1	0	14	
	5	3	4	3	2	1	0	0	14	
	6	3	4	3	2	1	0	0	14	
	7	2	4	5	2	0	0	0	14	
	8	3	4	3	2	1	0	0	14	
	9	3	4	3	2	1	0	0	14	
	10	2	4	5	2	0	0	0	14	
	11	2	3	3	2	2	1	0	14	
	12	2	2	2	2	2	2	1	14	
	13	2	2	2	2	2	2	1	14	
	14	2	3	3	2	2	1	0	14	
									196	
<i>m</i> (LC, A ₃ , <i>k</i>)*		16	22	21	14	10	6	2	98	paths
<i>D_P</i>		16	44	63	56	50	36	14	279	<i>W</i>

**P*(LC,*G*, *x*)=*H*(*G*, *x*)

Shell Matrices. The info matrix is the detour matrix **DE**:

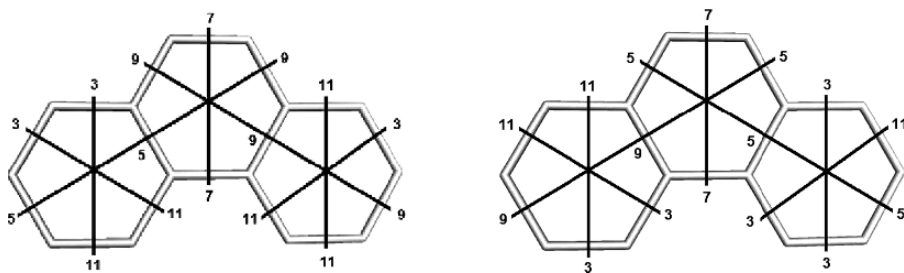
SM (DE(A ₃))										
	<i>k</i>	1	2	3	4	5	6	7	CS(DE)	Meaning
<i>m</i> (SDE, A ₃ , <i>k</i>)	1	26	34	35	24	22	10	0	151	
	2	26	24	22	22	22	20	9	145	
	3	26	24	22	22	22	20	9	145	
	4	26	34	35	24	22	10	0	151	
	5	35	42	29	22	11	0	0	139	
	6	35	42	29	22	11	0	0	139	
	7	26	40	55	24	0	0	0	145	
	8	35	42	29	22	11	0	0	139	
	9	35	42	29	22	11	0	0	139	
	10	26	40	55	24	0	0	0	145	
	11	26	34	35	24	22	10	0	151	
	12	26	24	22	22	22	20	9	145	
	13	26	24	22	22	22	20	9	145	
	14	26	34	35	24	22	10	0	151	
										2030
	200	240	227	160	110	60	18	1015		<i>w</i>
<i>D_P</i>	200	480	681	640	550	360	126	3037		DE_H_DI

Info matrix is the (unsymmetric) Cluj Distance matrix **UCJDI**:

SM(UCJDI(A ₃))										
	<i>k</i>	1	2	3	4	5	6	7	CS(CJDI)	Meaning
<i>m</i> (UCJDI,A ₃ , <i>k</i>)	1	14	12	14	9	11	6	0	66	
	2	10	4	6	6	8	9	5	48	
	3	10	4	6	6	8	9	5	48	
	4	14	12	14	9	11	6	0	66	
	5	25	32	24	14	7	0	0	102	
	6	25	32	24	14	7	0	0	102	
	7	14	24	36	16	0	0	0	90	
	8	25	32	24	14	7	0	0	102	
	9	25	32	24	14	7	0	0	102	
	10	14	24	36	16	0	0	0	90	
	11	14	12	14	9	11	6	0	66	
	12	10	4	6	6	8	9	5	48	
	13	10	4	6	6	8	9	5	48	
	14	14	12	14	9	11	6	0	66	
										1044
		112	120	124	74	52	30	10	522	
	<i>D_P</i>	112	240	372	296	260	180	70	1530	CJDI_H_DI

Info matrix is the (unsymmetric) Cluj Detour **UCJDE**:

SM(UCJDE(A ₃))										
	k	1	2	3	4	5	6	7	CS(UCJDE)	Meaning
	1	2	4	5	2	4	3	0	20	
	2	2	2	5	5	4	6	4	28	
	3	2	2	5	5	4	6	4	28	
	4	2	4	5	2	4	3	0	20	
	5	5	7	10	4	2	0	0	28	
	6	5	7	10	4	2	0	0	28	
	7	2	4	10	2	0	0	0	18	
	8	5	7	10	4	2	0	0	28	
	9	5	7	10	4	2	0	0	28	
	10	2	4	10	2	0	0	0	18	
	11	2	4	5	2	4	3	0	20	

Table 4-2. Edge cut procedure for calculating Cluj polynomial in phenanthrene Ph_3 

$$\begin{aligned}
 CJD I_{e-i}(Ph_3, x) &= 3x^3 + 2x^5 + 2x^7 + 4x^9 + 5x^{11} & CJD I_{e-j}(Ph_3, x) &= 5x^3 + 4x^5 + 2x^7 + 2x^9 + 3x^{11} \\
 D1|_{x=1} &= 124 & D1|_{x=1} &= 100 \\
 CJD I_e(Ph_3, x) &= 8x^3 + 6x^5 + 4x^7 + 6x^9 + 8x^{11}; & P1|_{x=1} &= 32 = 2e; & D1|_{x=1} &= 224 \\
 CJD I_p(Ph_3, x) &= 18x^2 + 20x^3 + 36x^4 + 20x^5 + 14x^6 + 20x^7 + 28x^8 + 6x^9 + 12x^{10} + 8x^{11}; & D1|_{x=1} &= 1050 \\
 CJDE_e(Ph_3, x) &= 28x + 4x^3; & P1|_{x=1} &= 32 = 2e; & D1|_{x=1} &= 40 \\
 CJDE_p(Ph_3, x) &= 84x + 64x^2 + 30x^3 + 2x^4 + 2x^6; & D1|_{x=1} &= 322
 \end{aligned}$$

to the endpoint j of the edge $e(i, j)$ (and to the second triangle of the mentioned matrix) can be written. However, they depend on the numbering and only their sum polynomial is invariant (see Tables 4-1 and 4-2). This last polynomial will only be taken into consideration in the following discussion.

4.5. Properties of the Cluj Polynomials

Among the properties of counting polynomials, the value in $x = 1$ and the first derivative in $x = 1$ are the most important. In the case of $CJD I_e$ polynomial, the value in $x = 1$, $P1|_{x=1} = 2e$. It is evident, since every edge is visited twice.

The first derivative, in $x = 1$, gives the meaning of the topological property collected by a matrix/polynomial. In this case, the following theorem holds:⁵⁷

Theorem 4.1. *In a bipartite graph, the sum of all edge-counted vertex proximities equals the product $v \times e$ of the number of vertices and edges in G .*

Demonstration. In a bipartite, planar graph, permitting orthogonal edge-cuts, for every edge $e(i, j) \in E(G)$ there is a clear separation of proximities $\{p_{e,i}\}$ and $\{p_{e,j}\}$ of its endpoints. Let's denote by $p_{e,i}$ and $p_{e,j}$ the cardinalities of the above sets. In a bipartite graph, we always can write

$$p_{e,i} + p_{e,j} = v \quad (4.32)$$

It follows that, for all edges, $e \in E(G)$, the total of edge-counted vertex proximities p_e equals the product $v \times e$, thus demonstrating the theorem.

Recall that an orthogonal (or an elementary) edge-cut of a (polycyclic) bipartite planar graph G , is a straight line segment, passing through the centers of some edges of the graph, being orthogonal to these edges, and intersecting the perimeter of G exactly two times, so that at least one polygon lies between these two intersection points.^{1,58,59} Note that trees also allow elementary edge-cuts.

In the orthogonal edge-cut procedure for calculating the $CJDI_e$ index, (i.e., the sum of all entries in the matrix \mathbf{UCJDI}_e), the total of edge-counted vertex proximities $p_e = CJDI_e(G, x); D1|_{x=1}$ is calculated as:

$$p_e = \sum_c m(G, c) \cdot c \cdot (p_{e,i} + p_{e,j}) = v \cdot \sum_c m(G, c) \cdot c = v \times e \quad (4.33)$$

where the coefficients $m(G, c)$ are related to the occurrence of co-distant edge-cuts (see below) of extent c and $\sum_c m(G, c) \cdot c = e(G)$. The above theorem can be extended to 3D bipartite molecular structures, although the separation of the proximities is not so evident. In toroidal polyhexes, $CJDI_e(G, x) = 3cn \cdot x^{cn/2}$ and $CJDI_e(G, x); D1|_{x=1} = (3/2)(cn)^2 = v \times e$ irrespective of embedding and twisting.

Corollary to theorem 4.1. *In bipartite graphs there are no equidistant vertices with respect to the two endpoints of any edge.*

The Cluj matrix counts the vertices lying closer to each of the endpoints of any edge and leaves the equidistant vertices uncounted. Because of relation (4.32), it follows that, in bipartite graphs, all vertices are counted and *no equidistant vertices* exist. Next, for all of the edges in G , one obtains the total of vertex proximities, p_e , equal to $v \times e$. This is the main result provided by the Cluj matrix/polynomial. The vertex proximity calculation could be of interest in calculating the *bond polarity* and molecular dipole moments. In this respect, weighted molecular graphs must be used.

Recall that, in calculating the Szeged index^{13,60,61,62,63,64,65} (a topological index related to the Wiener index,⁵ which counts all the shortest distances in a graph), equidistant vertices are also not counted.

Another basic property is expressed by the following:⁵⁷

Theorem 4.2. *In a tree graph, the sum of all path-counted vertex proximities is twice the sum of all distances in G or twice the Wiener index W : $p_p = CJDI_p(G, x); D1|_{x=1} = 2W$.*

Demonstration. The column sums in the \mathbf{UCJDI}_p matrix equals the column sums in the matrix of distances while the row sums in \mathbf{UCJDI}_p matrix are identical to those in the Wiener matrix.^{1,59} It is well-known that the half sum of entries in these matrices counts all the distances in a tree graph, or the Wiener index. Since the first derivative of the $CJDI_p$ polynomial is the sum of all entries in \mathbf{UCJDI}_p , it follows that $p_p = CJDI_p(G, x); D1|_{x=1} = 2W$, thus demonstrating the theorem.

In cycle-containing graphs, the Cluj index $CJDI_p$ is different from both the Wiener and Szeged indices.^{1,59}

Table 4-3. Formulas for Cluj-edge polynomials in acenes A_h ; h = no. of hexagons in molecule

$CJDI_e(A_{h-even}, x) = 8 \cdot \sum_{k=1}^{h/2} x^{(4k-1)} + 2(h+1) \cdot x^{(2h+1)} + 8 \cdot \sum_{k=(h+2)/2}^h x^{(4k-1)}; D1 _{x=1} = 2(2h+1)(5h+1)$ $= v \cdot e$
$CJDI_e(A_{h-odd}, x) = 8 \cdot \sum_{k=1}^{(h-1)/2} x^{(4k-1)} + (2(h-3)+16) \cdot x^{(2h+1)} + 8 \cdot \sum_{k=(h+3)/2}^h x^{(4k-1)}; D1 _{x=1} = v \cdot e$
$CJDE_e(A_{h-even}, x) = (8h+4) \cdot x + 4 \cdot \sum_{k=2}^{h/2} x^{(2k-1)} + 2 \cdot x^{(h+1)}; D1 _{x=1} = h^2 + 10h + 2$
$CJDE_e(A_{h-odd}, x) = (8h+4) \cdot x + 4 \cdot \sum_{k=2}^{(h+1)/2} x^{(2k-1)}; D1 _{x=1} = h^2 + 10h + 1$

Table 4-4. Formulas for Cluj-edge polynomials in phenacenes Ph_h ; h = no. of hexagons in molecule

$CJDI_e(Ph_{h-even/odd}, x) = 8 \cdot x^3 + 4 \cdot \sum_{k=2}^{h-1} x^{(4k-1)} + 6 \cdot \sum_{k=1}^{h-1} x^{(4k+1)} + 8 \cdot x^{4h-1}; D1 _{x=1} = v \cdot e$
$CJDI_e(A_h/Ph_h) = D1 _{x=1} = v \cdot e = 2(2h+1) \cdot (5h+1) = 2(10h^2 + 7h + 1)$
$CJDE_e(Ph_{h-even}, x) = (8h+4) \cdot x + h \cdot x^3 + 2 \cdot \sum_{k=2}^{h/2} x^{(4k-1)}; D1 _{x=1} = h^2 + 12h - 2$
$CJDE_e(Ph_{h-odd}, x) = (8h+4) \cdot x + (h+1) \cdot x^3 + 2 \cdot \sum_{k=2}^{(h-1)/2} x^{(4k-1)}; D1 _{x=1} = h^2 + 10h + 1$

Formulas for calculating the Cluj polynomial $CJDI_e$ in acenes A_h and phenacenes Ph_h , function of the number of their hexagons h , are given in Tables 4-3 and 4-4, respectively.

Theorem 4.3. A full Hamiltonian graph FH shows the minimal exponent value, 1, and the minimal value of the first derivatives of Cluj-detour polynomials: $CJDE_p; D1|_{x=1} = v(v-1)$ and $CJDE_e; D1|_{x=1} = 2e$.

Demonstration. A full Hamiltonian FH graph¹⁷ (Figure 4-1) has any pair of its vertices joined by a Hamiltonian path (*i.e.*, a path visiting all the vertices of G). Considering that the Cluj fragments/proximities are counted by deleting the path $p(i, j)$ excepting its endpoints, the proximity of i is always 1, vs any other vertex j in G . Thus, the exponent takes the minimal (unity) value. The coefficient of this unique term of $CJDE_p$ polynomial is $v(v-1)$, as counted from the \mathbf{CJDE}_p matrix (which shows all its non-diagonal entries equal to unity) by deleting the zeroes of the diagonal. For $CJDE_e$, the demonstration is immediate. Any FH graph shows all the non-diagonal entries in \mathbf{CJDE}_p matrix equal to unity but the reciprocal is not always true.

Corollary to theorem 4.2. If the FH graph is a complete graph, then: $CJDE_p; D1|_{x=1} = CJDE_e; D1|_{x=1} = 2e$.

In complete graphs, all the vertices are adjacent. Thus, the two polynomials, defined on edges and paths, respectively, coincide, thus $v(v-1) = 2e$.

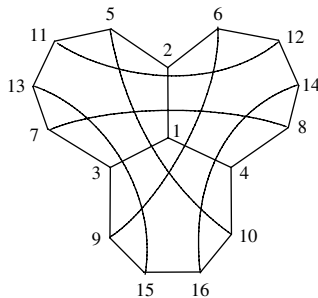


Figure 4-1. A full Hamiltonian FH graph.

4.6. Omega-type Polynomials

Two polynomials related to the Cluj polynomial are introduced in the following. One is the Omega polynomial,⁶⁶ $\Omega(G, x)$, which counts orthogonal edge-cuts and the second one is the “non-Omega” $N\Omega(G, x)$, which is, in some extent, complementary to the Omega polynomial.

Let $G(V, E)$ be a connected bipartite graph. Two edges $e = (1, 2)$ and $e' = (1', 2')$ of G are called *codistant* (briefly: $ecoe'$) if for $k = 0, 1, 2, \dots$ there exist the relations: $d(1, 1') = d(2, 2') = k$ and $d(1, 2') = d(2, 1') = k + 1$ or vice versa. For some edges of a connected graph G there are the following relations satisfied:^{67,68}

$$ecoe \quad (4.34)$$

$$ecoe' \Leftrightarrow e'coe \quad (4.35)$$

$$ecoe' \& e'coe'' \Rightarrow ecoe'' \quad (4.36)$$

though the relation (4.36) is not always valid. A simple counterexample is given in Figure 4-2. By performing the medial Me operation on maps^{69,70,71,72,73,74} edges become vertices, in the transform (Figure 4-2, b), and “*codistant*” (edges) could be changed by “*opposite*” (vertices), as proposed by John *et al.*⁶⁷ The algorithm on medial works on trivalent maps but complications appear in higher-valent vertex maps, where virtual faces (corresponding to multivalent vertices) appear.

Let $C(e) := \{e' \in E(G); e'coe\}$ denote the set of all edges of G which are codistant to the edge e . If all the elements of $C(e)$ satisfy the relations (4.34–4.36) then $C(e)$ is called an *orthogonal cut* “*oc*” of the graph G . The graph G is called *co-graph* if and only if the edge set $E(G)$ is the union of disjoint orthogonal cuts: $C_1 \cup C_2 \cup \dots \cup C_k$ and $C_i \cap C_j = \emptyset$ for $i \neq j$, $i, j = 1, 2, \dots, k$. If any two edges of an edge-cut sequence are codistant (obeying the relations (4.34) and (4.35)) and belong to one and the same face of the covering, such a sequence is called a *quasi-orthogonal cut* “*qoc*” strip. This means that the transitivity relation (4.36) is not necessarily obeyed. Any *oc* strip is a *qoc* strip but the reverse is not always

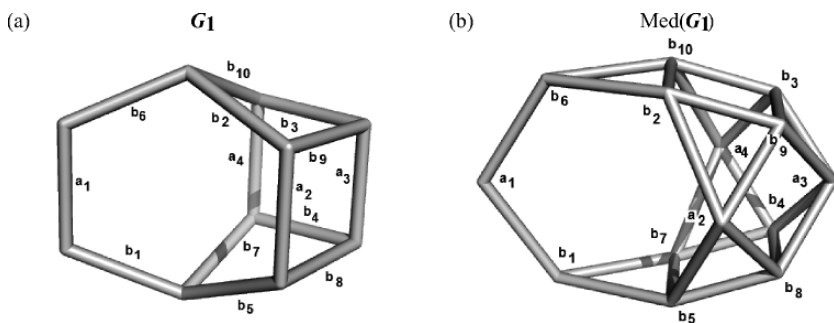


Figure 4-2. Codistant edges, *cf* relations (4.34-4.36): {a} is an *oc* strip; {b} does not have all elements codistant to each other (e.g., b_1 & b_5 ; b_7 & b_{10}), so that {b} is a *qoc* strip (see text). $\Omega(G_1, x) = x^4 + x^{10}$; $CI = 80$; $I_\Omega = 5.672086$; $N\Omega(G_1, x) = 4x^9 + 8x^{10} + 2x^{11}$; $PI = 138$.

true.^{75,76} The term “co-distant” is synonym (in some extent) with “equidistant” or “topologically parallel”.

Let $m(G, c)$ denote the multiplicity of the edge-cut of length c (i.e., the number of edges cut-off). In a bipartite planar graph the two polynomials are defined as:

$$\Omega(G, x) = \sum_c m(G, c) \cdot x^c \quad (4.37)$$

$$N\Omega(G, x) = \sum_c m(G, c) \cdot c \cdot x^{(e-c)} \quad (4.38)$$

Their $D1|_{x=1}$ give the total number of equidistant and non-equidistant edges vs each edge in G .

$$\Omega(G, x) D1|_{x=1} = e = |E(G)| \quad (4.39)$$

$$N\Omega(G, x) D1|_{x=1} = PI(G) \quad (4.40)$$

where $PI(G)$ is the Khadikar's topological index.⁷⁷ Note that Ashrafi *et al.*⁷⁸ have proposed for $N\Omega(G, x)$ the name $PI(G, x)$, because its first derivative gives the Khadikar's PI topological index, eq (4.40).

Two indices have been defined on the Omega polynomial. The first one, CI , is derived from the first and second derivatives, in $x = 1$, as:

$$CI(G) = (\Omega(G, x) D1)^2 - (\Omega(G, x) D1 + \Omega(G, x) D2)|_{x=1} \quad (4.41)$$

The second descriptor is calculable from all possible derivatives Dn , in $x = 1$, and normalized to the first one (which equals the number of edges in G)

$$I_\Omega(G) = (1/\Omega(G, x) D1) \cdot \sum_n (\Omega(G, x) Dn)^{1/n}|_{x=1} \quad (4.42)$$

Analytical formulas for calculating the two polynomials and derived descriptors in acenes and phenacenes are listed in Tables 4-5 and 4-6.

Table 4-5. Formulas for Omega-type polynomials in acenes A_h ; h = no. of hexagons in molecule

$$\begin{aligned} \Omega(A_h, x) &= 2h \cdot x^2 + x^{(h+1)}; |D1|_{x=1} = e = 5h + 1; D2|_{x=1} = h(h+5) \\ CI(A_h) &= (\Omega'(A_h))^2 - (\Omega'(A_h) + \Omega''(A_h)) = (5h+1)^2 - (5h+1 + h(h+5)) = 24h^2 \\ \Omega(A_h, x)|_{x=1} &= v/2 = 2h + 1 \\ N\Omega(A_h, x) &= 4h \cdot x^{(5h-1)} + (h+1) \cdot x^{4h}; D1|_{x=1} = 24h^2 \end{aligned}$$

Table 4-6. Formulas for Omega-type polynomials in phenacenes Ph_h ; h = no. of hexagons in molecule

$$\begin{aligned} \Omega(Ph_h, x) &= (h+2) \cdot x^2 + (h-1) \cdot x^3; D1|_{x=1} = e = 5h + 1; D2|_{x=1} = 8h - 2 \\ CI(Ph_h) &= (5h+1)^2 - (5h+1 + 8h-2) = 25h^2 - 3h + 2 \\ \Omega(Ph_h, x)|_{x=1} &= v/2 = 2h + 1 \\ N\Omega(Ph_h, x) &= 2(h+2) \cdot x^{(5h-1)} + 3(h-1) \cdot x^{(5h-2)}; D1|_{x=1} = 25h^2 - 3h + 2 \end{aligned}$$

Theorem 4.3. *In a bipartite planar graph, CI and PI indices are identical.*

Demonstration. From (4.41) and writing $m(G, c)$ as simply m , CI is calculable as:

$$\begin{aligned} CI(G) &= \sum_c \{(m \cdot c)^2 - [m \cdot c + m \cdot c(c-1)]\} = \sum_c [(m \cdot c)^2 - m \cdot c^2] \\ &= e^2 - \sum_c m \cdot c^2 \end{aligned} \quad (4.43)$$

On the other hand, from (4.38) and (4.40), PI is calculated as:

$$PI(G) = \sum_c m \cdot c \cdot (e - c) = e \sum_c m \cdot c - \sum_c m \cdot c^2 = e^2 - \sum_c m \cdot c^2 \quad (4.44)$$

Clearly, the two indices are identical, because they transform into one and the same ultimate expression, also proposed by John *et al.*⁶⁷ for calculating PI in benzenoid hydrocarbon graphs. In the above, the following relation holds:

$$e(G) = \sum_c m \cdot c = \Omega(G, x)D1|_{x=1} = N\Omega(G, x)|_{x=1} \quad (4.45)$$

However, relation (4.38) is not always valid, so that CI is, in general, different from PI , excepting the case of bipartite planar graphs.

In bipartite graphs embeddable in surfaces of $g > 0$, *e.g.*, in toroidal polyhexes, relation (4.38) is still more hidden, despite $CI = PI$. In case of the torus $T(6,3)H[8,12]: \Omega(G, x) = 12x^4 + 4x^{24}$; $e = 144$; $CI = 18240$; $N\Omega(G, x) = 96x^{122} + 48x^{136}$; $PI = 18240$. According to (4.38) the polynomial would be: $N\Omega(G, x) = 96x^{120} + 48x^{140}$ that gives the same PI index value. At this moment no generalization of this case was found.

We stress here that polynomials $CJDI(G, x)$ and $N\Omega(G, x)$ describe, in a same manner, collections of non-equidistant subgraphs (vertices and edges, respectively), with addition being the most simple and natural operation.

4.7. Hosoya Polynomial in Toroidal Nanostructures

4.7.1. Polyhex (6,3) Covering

The general form of the (vertex) Hosoya polynomials, in vertex transitive graphs such as tori $T(6,3)H[c, n]$ and $T(6,3)V[c, n]$, (regular graphs, having $v = c \times n$ - Figure 4-3), in going from normal $T(6,3)H$ to normal $T(6,3)V$ tori, are:^{79,80}

Case: $T(6,3)H[c, n], n > c$.

$$H(i, x) = 1 + 3kx^k,_{k=1,2,\dots,(c/2-1)} + (3c/2 - 1)x^{c/2} + (3c/2 - k)x^{(c/2+k)},_{k=1,2,\dots,(c/2-1)} + cx^k,_{k=c,c+1,\dots,(n-1)} + (c/2)x^n \quad (4.46)$$

Case: $T(6,3)H[c, n] = (6,3)V[c, n], n = c$:

$$H(i, x) = 1 + 3kx^k,_{k=1,2,\dots,(c/2-1)} + (3c/2 - 1)x^{c/2} + (3c/2 - k)x^{(c/2+k)},_{k=1,2,\dots,(\frac{c}{2}-1)} + (c/2)x^n \quad (4.47)$$

Case: $T(6,3)V[c, n], c + 2 \leq n \leq 2(c - 1)$:

$$H(i, x) = 1 + 3kx^k,_{k=1,2,\dots,(n/2-1)} + (3n/2 - 1)x^{n/2} + (3n/2 - k)x^{(n/2+k)},_{k=1,2,\dots,(c-1-n/2)} + (2n - 3c/2 - 1)x^c + [2(n - c) - 4k]x^{(c+k)},_{k=1,2,\dots,((n-c)/2-1)} + x^{(c+n)/2} \quad (4.48)$$

Case: $T(6,3)A[c, n], n = 2c$:

$$H(i, x) = 1 + 3kx^k,_{k=1,2,\dots,(c-1)} + (5c/2 - 2)x^c + (2c - 4k)x^{(c+k)},_{k=1,2,\dots,(c/2-1)} + x^{(c+n)/2} \quad (4.49)$$

(a) $T(6,3)H[12,50]; v = 600$



(b) $T(6,3)V[20,100]; v = 2000$

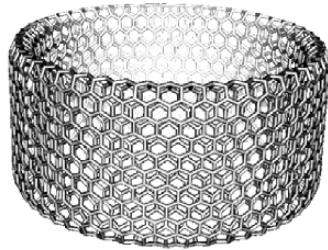


Figure 4-3. The (6,3) covering embedded in the torus.

Case: $T(6,3)A[c, n], n \geq 2(c+1)$.

$$H(i, x) = 1 + 3kx^k,_{k=1,2,\dots,(c-1)} + (5c/2 - 1)x^c + 2cx^k,_{k=c+1,c+2,\dots,(n/2-1)} + \\ + (2c-1)x^{n/2} + (2c-4k)x^{(n/2+k)},_{k=1,2,\dots,(c/2-1)} + x^{(c+n)/2} \quad (4.50)$$

A “normal” torus, in the above relations, means a toroidal net having the number of hexes across the tube smaller than around the torus. The “normal” status is already reached at $n > c$, in $(6,3)H$ tori, while $n \geq 2(c+1)$ is needed in case of $(6,3)V$ tori.

As mentioned in Section 4.3, the coefficients of the vertex Hosoya polynomial are just the entries in the LC matrix^{1,51} or the (vertex) Distance Degree Sequence $DDS(i)$ (*i.e.*, the number of vertices lying at distance k from the vertex i).

The polynomial coefficients can be viewed as a “distance degree” spectrum, useful in topological characterization of graphenes. In case of the (normal) $T(6,3)[20, n]$ series, the spectra (per vertex $d(i, k)$ values) are shown in Figures 4-4 and 4-5.

The repeat terms: $cx^k,_{k=c,c+1,\dots,n-1}$ and $2cx^k,_{k=c+1,c+2,\dots,n/2-1}$, respectively, are the only changes, as n increases, in the spectrum of a given series (*i.e.*, a series of fixed c). By changing the series, the spectrum will change drastically, according to the general formulas (4.46 to 4.50).

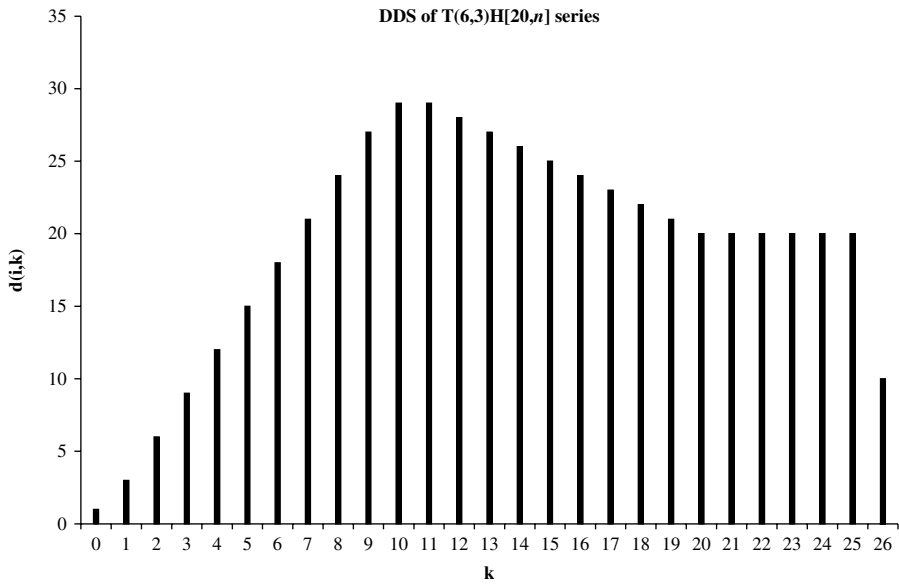


Figure 4-4. The distance degree spectrum of the tori $T(6,3)H[20, n]$.

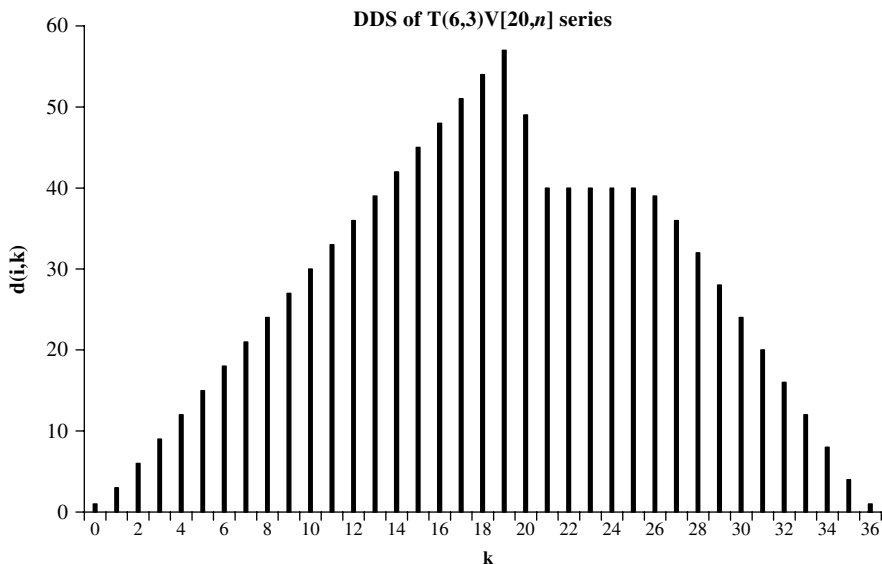


Figure 4-5. The distance degree spectrum of the tori $T(6,3)V[20,n]$.

The first derivative³⁵ of the Hosoya polynomial (in $x = 1$) enables the calculation of the well-known Wiener⁵ number W .

In case of the normal series of tori, the first derivative of the Hosoya polynomial gives the following formulas.^{79,80}

Case: $T(6,3)H[c,n]$

$$W = \frac{nc}{2} \left[\sum_{k=1}^{c/2-1} 3k^2 + (3c/2 - 1)c/2 + \sum_{k=1}^{c/2-1} (3c/2 - k)(c/2 + k) + \sum_{k=c}^{n-1} ck + nc/2 \right] \quad (4.51)$$

Case: $T(6,3)A[c,n]$

$$W = \frac{nc}{2} \left[\sum_{k=1}^{c-1} 3k^2 + (5c/2 - 1)c + \sum_{k=c+1}^{n/2-1} 2ck + (2c - 1)n/2 + \sum_{k=1}^{c/2-1} (2c - 4k)(n/2 + k) + (n/2 + c/2) \right] \quad (4.52)$$

By expanding the sums one obtains:

$$T(6,3)H[c,n]: \quad W = \frac{1}{24}nc^2(6n^2 + c^2 - 4) \quad (4.53)$$

$$T(6,3)V[c,n]: \quad W = \frac{1}{24}nc^2(3n^2 + c^2 + 3nc - 4) \quad (4.54)$$

Expansion of (4.48) (case $T(6,3)V[c,n]$; $c+2 \leq n \leq 2(c-1)$) also leads to (4.54). Moreover, the formulas for the other two cases:

$$n = c : \quad W = \frac{c^3}{24}(7c^2 - 4) \quad (4.55)$$

$$n = 2c : \quad W = \frac{c^3}{12}(19c^2 - 4) \quad (4.56)$$

can be deduced from the first derivative of the corresponding polynomials (eqs. 4.47 and 4.49, respectively), as well as from eq. 4.54. Relation (4.55) is also a particular case of eq (4.53), proving the self-consistency of the formulas (4.53) and (4.54) for calculating the Wiener index in polyhex tori.

As examples, the (vertex) Hosoya polynomials and Wiener numbers for the pair of isomers $(T(6,3)H[24,72]; T(6,3)V[24,72])$ are given below.

$T(6,3)H[24,72]$ (12×72 hexes)

$$\begin{aligned} H(i, x) = & 1 + 3x + 6x^2 + 9x^3 + 12x^4 + 15x^5 + 18x^6 + 21x^7 + 24x^8 + \\ & 27x^9 + 30x^{10} + 33x^{11} + 35x^{12} + 35x^{13} + 34x^{14} + 33x^{15} + 32x^{16} + 31x^{17} + \\ & 30x^{18} + 29x^{19} + 28x^{20} + 27x^{21} + 26x^{22} + 25x^{23} + 24x^{24-71} + 12x^{72} \end{aligned}$$

$$W(T(6,3)H[24,72]) = 5.4736128 \times 10^7$$

$T(6,3)V[24,72]$ (24×36 hexes)

$$\begin{aligned} H(i, x) = & 1 + 3x + 6x^2 + 9x^3 + 12x^4 + 15x^5 + 18x^6 + 21x^7 + 24x^8 + \\ & 27x^9 + 30x^{10} + 33x^{11} + 36x^{12} + 39x^{13} + 42x^{14} + 45x^{15} + 48x^{16} + 51x^{17} + \\ & 54x^{18} + 57x^{19} + 60x^{20} + 63x^{21} + 66x^{22} + 69x^{23} + 59x^{24} + 48x^{25-35} \\ & + 47x^{36} + 44x^{37} + 40x^{38} + 36x^{39} + 32x^{40} + 28x^{41} + 24x^{42} + 20x^{43} \\ & + 16x^{44} + 12x^{45} + 8x^{46} + 4x^{47} + x^{48} \end{aligned}$$

$$W(T(6,3)V[24,72]) = 3.6820224 \times 10^7$$

4.7.2. Twisted $T(6,3)HV_t[c, n]$ Tori

By twisting some rows of squares in the (4,4) net, the polyhex (6,3) net, resulted by a cutting procedure,^{81,82} will appear as twisted and the object is chiral (Figure 4-6 – see also Chapter 2). In the name of twisted tori, t indicates the number of twisted rows (in the range 0, 2, ..., c).

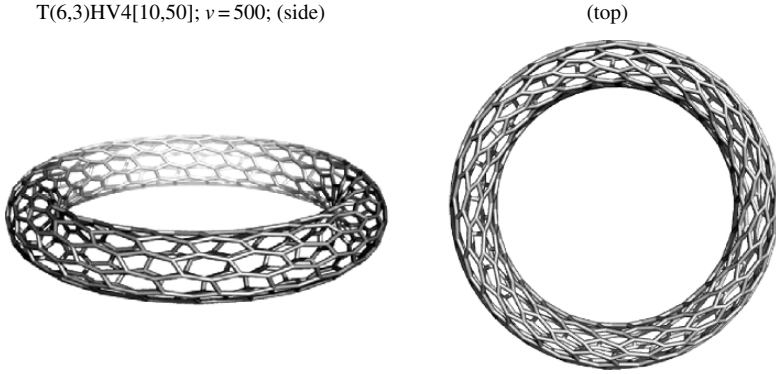


Figure 4-6. An H-twisted, V-cut polyhex torus (non-optimized geometry).

General formulas for the Hosoya polynomial and the Wiener index in tori of T(6,3)HVt[c, n] series are:⁸⁰

Case: $(n/2) > 2(c+1)$; $t < c$:

$$\begin{aligned}
 H(i, x) = & 1 + 3kx^k,_{k=1,2,\dots,(c-1)} + [3c-1-(c-t)/2]x^c + \\
 & + (2c+t-k+1)x^{(c+k-1)},_{k=2,3,\dots,t} + 2cx^k,_{k=c+t,c+t+1,\dots,(n/2-1)} + \\
 & + (2c-1)x^{n/2} + (2c-4k)x^{(n/2+k)},_{k=1,2,\dots,[(c-t)/2-1]} + (t+1)x^{[n/2+(c-t)/2]}
 \end{aligned} \tag{4.57}$$

$$\begin{aligned}
 W = \frac{cn}{2} \left[\sum_{k=1}^{c-1} 3k^2 + [3c-1-(c-t)/2]c + \sum_{k=2}^t (2c+t-k+1)(c+k-1) + \right. \\
 \left. + \sum_{k=c+t}^{n/2-1} 2ck + (2c-1)n/2 + \sum_{k=1}^{(c-t)/2-1} (2c-4k)(n/2+k) \right]
 \end{aligned} \tag{4.58}$$

$$W = \frac{cn}{24} [c^3 + 3c^2n + 3cn^2 + 3ct^2 + 4t^3 - 3nt^2 - 4c - 4t] \tag{4.59}$$

Case: $(n/2) > 2(c+1)$; $t = c$.

$$\begin{aligned}
 H(i, x) = & 1 + 3kx^k,_{k=1,2,\dots,(c-1)} + (3c-1)x^c + (3c-k)x^{(c+k)},_{k=1,2,\dots,(c-1)} \\
 & + 2cx^k,_{k=2c,2c+1,\dots,(n/2-1)} + cx^{n/2}
 \end{aligned} \tag{4.60}$$

$$W = \frac{cn}{2} \left[\sum_{k=1}^{c-1} 3k^2 + (3c-1)c + \sum_{k=1}^{c-1} (3c-k)(c+k) + \sum_{k=2c}^{n/2-1} 2ck + cn/2 \right] \quad (4.61)$$

$$W = \frac{c^2n}{24} (8c^2 + 3n^2 - 8) \quad (4.62)$$

4.7.3. Covering ((4,8)3)S

The ((4,8)3) covering is a trivalent decoration consisting of alternating squares and octagons. Such a net can be derived, from the (4,4) net, either by a cutting procedure⁸³ or by the leapfrog map operation,⁸¹ or also by the Stone-Wales⁸⁴ edge rotation in a polyhex (6,3) net.^{71,85} Optimized ((4,8)3) nanotori are illustrated in Figure 4-7.

The isomer $T((4,8)3)HS[c,n]$ contains, on dimension “ c ”, half of the number of (4,8) pairs in $T((4,8)3)VS[c,n]$. Conversely, the number of (4,8) pairs in $T((4,8)3)VS[c,n]$, on dimension “ n ”, is half of that in $T((4,8)3)HS[c,n]$. The leapfrog operation provides the the “ RLe ” embedding.

General formulas for the Hosoya polynomial and Wiener index in tori $T((4,8)3)S[c,n]$ of both H- and V-series are given in the following.⁸³ Several cases can be delimited:

4.7.3.1. Tori $T((4,8)3)HS[c,n]$; $0 \bmod(c,4)$

Case: $c < n$; normal $T((4,8)3)HS[c,n]$ torus; $c = 4p$; $n = 2r$

$$\begin{aligned} H(i, x) = & 1 + m_k x^k,_{k=1, \dots, (2p-1)} + (m_{2p} - 1) x^{2p} + (m_{(2p+k)} - 4k) x^{(2p+k)},_{k=1, \dots, (p-1)} \\ & + 4p x^k,_{k=3p, \dots, (2r-1)} + (4p - 1) x^{2r} + (4p - 4k) x^{(2r+k)},_{k=1, \dots, (p-1)} + \\ & + x^{(2r+p)} \end{aligned} \quad (4.63)$$

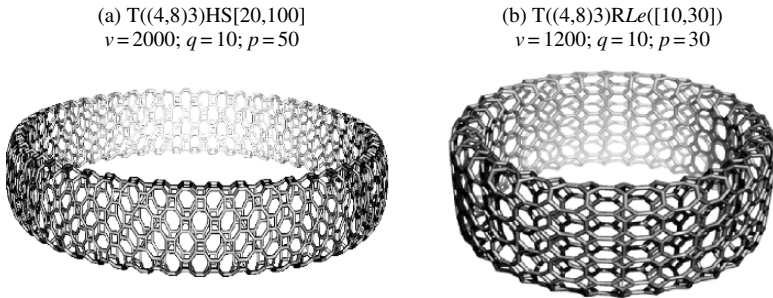


Figure 4-7. The ((4,8)3) covering, in S and R embedding, respectively.

$$\begin{aligned}
 W = 4pr \left[\sum_{k=1}^{2p-1} m_k k + (m_{2p} - 1)2p + \sum_{k=1}^{p-1} (m_{(2p+k)} - 4k)(2p+k) + \right. \\
 \left. + \sum_{k=3p}^{2r-1} 4pk + (4p-1)2r + \sum_{k=1}^{p-1} (4p-4k)(2r+k) + (p+2r) \right]
 \end{aligned}
 \tag{4.64}$$

where m_k is defined by the following recursion:

$$\begin{aligned}
 m_0 = 0; \quad m_1 = 3; \quad m_2 = 5, \quad \text{and} \\
 m_k = m\left(\frac{k - \text{mod}(k, 2)}{2} + 1\right) + m\left(\frac{k + \text{mod}(k, 2)}{2} - 1\right) = m\left[\frac{k+2}{2}\right] + m\left[\frac{k-1}{2}\right]
 \end{aligned}
 \tag{4.65}$$

with $\lfloor x \rfloor$ being the greatest integer part of a real number x .

Alternatively, for $k = 3s + t$, and $t = 0, 1, 2$:

$$m_k = \frac{2 \cdot 3^{1/2} \sin\left(2k \frac{\pi}{3}\right)}{9} + 8k/3 = 8s + \begin{cases} 0, & \text{if } t = 0 \\ 3, & \text{if } t = 1 \\ 5, & \text{if } t = 2 \end{cases}
 \tag{4.66}$$

With (4.66), recursion (4.65) becomes:

$$\begin{aligned}
 m_k = 8 \left[(k - \text{mod}(k, 3))/3 \right] + 3 \text{mod}(k, 3)(2 - \text{mod}(k, 3)) - \\
 - [(1 - \text{mod}(k, 3))(5 \text{mod}(k, 3)/2)]
 \end{aligned}
 \tag{4.67}$$

Expansion of relation (4.64) leads to the formula:

$$W = \frac{16}{3} p^2 r (p^2 + 6r^2 + 3pr - 1)
 \tag{4.68}$$

which can be translated to $[c, n]$ dimensions as:

$$W = c^2 n (c^2 + 24n^2 + 6cn - 16) / 96
 \tag{4.68'}$$

Case: $c = n$;

$$\begin{aligned}
 T((4,8)3)HS[c,c] = T((4,8)3)VS[c,c], \text{ or } T((4,8)3)HS[4p,4p] = T((4,8)3) \\
 VS[4p,4p]
 \end{aligned}$$

$$\begin{aligned}
 H(i, x) = 1 + m_k x^k,_{k=1, \dots, (2p-1)} + (m_{2p} - 1)x^{2p} + (m_{(2p+k)} - 4k)x^{(2p+k)},_{k=1, \dots, (p-1)} \\
 + 4px^k,_{k=3p, \dots, (4p-1)} + (4p-1)x^{4p} + (4p-4k)x^{(4p+k)},_{k=1, \dots, (p-1)} + x^{5p}
 \end{aligned}
 \tag{4.69}$$

The summation of the corresponding terms, after appropriate handling, leads to the following simple relation for the Wiener index:

$$W(p) = \frac{32}{3} p^3 (31p^2 - 1) \quad (4.70)$$

$$W(c) = c^3 (31c^2 - 16) / 96 \quad (4.70')$$

Case: $c > n$; $T((4,8)3)HS[c,n]$; this case turns to $T((4,8)3)VS[n,c]$.

4.7.3.2. *Tori* $T((4,8)3)VS[c,n]$; $0 \bmod(n,4)$; $c = 2p$; $n = 4r$.

Case: $2p < 4r < 4p$. Two additional parameters are needed:

$$d = 3r - 2p \quad (4.71)$$

$$s = |2p - 2r| \quad (4.72)$$

Case: $d < 0$

$$\begin{aligned} H(i, x) = & 1 + m_k x^k,_{k=1, \dots, (2r-1)} + (m_{2r} - 1) x^{2r} + (m_{(2r+k)} - 4k) x^{(2r+k)},_{k=1, \dots, (r-1)} \\ & + n \cdot x^k,_{k=3r, \dots, (2p-1)} + (4r - 1) x^{2p} + (4r - 4k) x^{(2p+k)},_{k=1, \dots, (r-1)} + \\ & + x^{(2p+r)} \end{aligned} \quad (4.73)$$

Case: $d > 0$

$$\begin{aligned} H(i, x) = & 1 + m_k \cdot x^k,_{k=1, \dots, (2r-1)} + (m_{2r} - 1) \cdot x^{2r} \\ & + (m_{(2r+k)} - 4k) \cdot x^{(2r+k)},_{k=1, \dots, (2p-2r-1)} \\ & + (m_{2p} - (4s + 1)) \cdot x^{2p} + (m_{(2p+k)} - 4(s + 2k)) \cdot x^{(2p+k)},_{k=1, \dots, d} \\ & + (4r - 4k) \cdot x^{(2p+k)},_{k=(d+1), \dots, (r-1)} + x^{(2p+r)} \end{aligned} \quad (4.74)$$

Case: $n = 2c$

$$\begin{aligned} H(i, x) = & 1 + m_k x^k,_{k=1, \dots, (2p-1)} + (m_{2p} - 2) x^{2p} + \\ & + (m_{(2p+k)} - 8k) x^{(2p+k)},_{k=1, \dots, (p-1)} + x^{3p} \end{aligned} \quad (4.75)$$

The Wiener index corresponding to relation (4.75) is:

$$W(p) = \frac{p^3}{6} (436p^2 - 19) \quad (4.76)$$

or

$$W(c) = 2c^3(109c^2 - 16)/96 \quad (4.76')$$

Case: $4p < 4r < 6p$. The additional d parameter is of the form:

$$d = 3p - 2r \quad (4.77)$$

while s is the same as in (4.72).

$$\begin{aligned} H(i, x) = & 1 + m_k \cdot x^k,_{k=1, \dots, (2p-1)} + (m_{2p} - 1) \cdot x^{2p} + \\ & + (m_{(2p+k)} - 4k) \cdot x^{(2p+k)},_{k=1, \dots, (2r-2p-1)} \\ & + (m_{2r} - (4s + 1)) \cdot x^{2r} + (m_{(2r+k)} - 4(s + 2k)) \cdot x^{(2r+k)},_{k=1, \dots, d} \\ & + (4r - 4k) \cdot x^{(3p+k)},_{k=1, \dots, (r-1)} + x^{(p+2r)} \end{aligned} \quad (4.78)$$

Case: $6p \leq 4r$; normal torus $T((4,8)3)VS[2p,4r]$.

$$\begin{aligned} H(i, x) = & 1 + m_k x^k,_{k=1, \dots, (2p-1)} + (m_{2p} - 1)x^{2p} + (m_{(2p+k)} - 4k)x^{(2p+k)},_{k=1, \dots, (p-1)} \\ & + 4x^k,_{k=3p, \dots, (2r-1)} + (4p - 1)x^{2r} + (4p - 4k)x^{(2r+k)},_{k=1, \dots, (p-1)} + x^{(p+2r)} \end{aligned} \quad (4.79)$$

$$\begin{aligned} W = & 4pr \left[\sum_{k=1}^{2p-1} m_k k + (m_{2p} - 1)2p + \sum_{k=1}^{p-1} (m_{(2p+k)} - 4k)(2p + k) + \right. \\ & \left. + \sum_{k=3p}^{2r-1} 4pk + (4p - 1)2r + \sum_{k=1}^{p-1} (4p - 4k)(2r + k) + (p + 2r) \right] \end{aligned} \quad (4.80)$$

By developing (4.80) results in the formulas:

$$W = \frac{16}{3} p^2 r (p^2 + 6r^2 + 3pr - 1) \quad (4.81)$$

$$W = c^2 n (2c^2 + 3n^2 + 3cn - 8)/24 \quad (4.81')$$

Observe that relations [(4.64), (4.80)] and [(4.68), (4.81)] are identical. This is a consequence of the isotropy of the $((4,6)3)S$ net. In the above, "normal" torus means the torus having the number of $(4,8)$ pairs around the tube smaller than

Table 4-7. Wiener Index in Tori $T((4,8)3)S$.

Torus $T((4,8)3)S$	W	$[p,r]$	Equivalent torus
H[12,12]	80,064	[3,6]	V[12,12]* V[6,24]
H[12,14]	122,640	[3,7]	V[6,28]
H[12,16]	178,176	[3,8]	V[6,32]
H[12,24]	564,480	[3,12]	V[6,48]
H[24,6]*	80,064	[3,6]	V[6,24]
H[24,8]*	155,136	[4,6]	V[8,24]
H[24,10]*	264,000	[5,6]	V[10,24]
H[24,12]*	413,568	[6,6]	V[12,24]
V[12,12]*	80,064	[3,6]	V[6,24]
V[12,20]	264,000	[6,5]	V[10,24]
V[16,20]*	563,200	[5,8]	V[10,32]
V[16,24]*	864,768	[6,8]	V[12,32]
V[16,28]	1,254,400	[7,8]	V[14,32]
V[16,32]	1,744,896	[8,8]	V[16,32]
V[8,20]	96,000	[4,5]	V[10,16]
V[8,24]	155,136	[4,6]	V[12,16]*
V[8,28]	234,752	[4,7]	V[14,16]*
V[12,36]	1,180,224	[6,9]	V[18,24]*
V[12,40]	1,564,800	[6,10]	V[20,24]*

* values non-calculable by eqs (4.68), (4.81), (4.68'), and (4.81')

around the large hollow of the torus. Formulas (4.68), (4.81), (4.68'), and (4.81') are applicable particularly in normal tori. On domains where no close formula is given, the following relations (accounting for the involved embedding isomers) are useful:⁸³

$$W_{T((4,8)3)HS[c,n]} = W_{T((4,8)3)VS[c/2,2n]} \quad (4.82)$$

$$W_{T((4,8)3)VS[c,n]} = W_{T((4,8)3)HS[2c,n/2]} = W_{T((4,8)3)VS[n/2,2c]} \quad (4.83)$$

Always an equivalent torus will be found, to verify the true result. Table 4-7 gives examples of Wiener index calculation, along with some of the equivalent tori.

4.8. Omega Polynomial in Tubular Nanostructures

4.8.1. Polyhex (6,3) Covering

In the Schlegel-like representation⁸⁶ of a nanotube (Figure 4-8), the points lying on the central circle have to be identified to those on the external circle to give the corresponding torus.

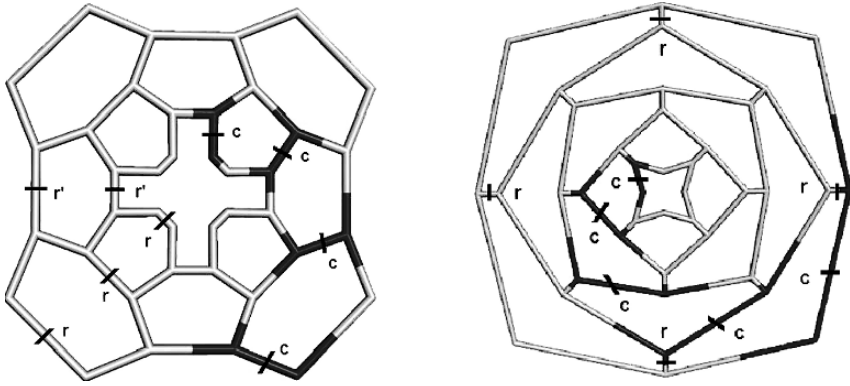


Figure 4-8. (a) Armchair tube TUV[8,5]; $p = 4$; $q = 5$; TH[4,8] (b) zig-zag tube TUH[8,5]; $p = 4$; $q = 5$; TV[4,8]; for the corresponding tori $q = 4$.

Two types of cuts appear in such polyhex, untwisted structures: one radial (denoted R) and another circular (denoted C), as shown in the corresponding polynomial:

$$\Omega(G, x) = R(G, x) + C(G, x) \quad (4.84)$$

4.8.1.1. Armchair Tubes $TU(6,3)V[2p,q]$ and Tori $T(6,3)H[q,2p]$

Case of “armchair” tubes, TUV[2p,q], or TUV[c,n] in general, in Diudea’s nomenclature,^{87,88} with $p = c/2$ and $q = n$, as given in Figure 4-8a. For all polyhex armchair tubes the circular term C is the same:⁷⁵

$$C(G, x) = 2p \cdot x^{q-1} \quad (4.85)$$

The radial term R varies function of the tube structure:

$q = \text{even}$:

$$R(G, x) = 2p \cdot x^{q/2} \quad (4.86)$$

$q = \text{odd}$:

$$R(G, x) = p \cdot x^{(q+1)/2} + p \cdot x^{(q-1)/2} \quad (4.87)$$

The corresponding CI indices are:

$$CI(TUV[2p, q_e]) = p^2(3q-2)^2 - 2p(q-1)^2 - pq^2/2 \quad (4.88)$$

$$CI(TUV[2p, q_o]) = p^2(3q-2)^2 - 2p(q-1)^2 - (p/2)(q^2 + 1) \quad (4.89)$$

For the example in Figure 4-8a: $\Omega(\text{TUV}[8, 5], x) = 4 \cdot x^2 + 4 \cdot x^3 + 8 \cdot x^4$; $CI = 2524$; $I_\Omega = 1.404541$

Case of tori, $\text{TH}[q, 2p]$. An “armchair” nanotube $\text{TUV}[2p, q+1]$ (Figure 4-8a, $p = 4$; $q = 4$), is transformed in a torus $\text{H}[q, 2p]$ as above mentioned, with q ($q = \text{even}$, always by this construction) winding around the tube while p around the central hollow of the torus.

The radial term in such tori is the same for all the cases:⁷⁵

$$R(G, x) = 2p \cdot x^{q/2} \quad (4.90)$$

and the circular term C vary as:

$$C(G, x) = k \cdot x^{2pq/k} \quad (4.91)$$

with k being the greatest common divisor of q and $2p$.

In $[c, n]$ terms, the Omega polynomial is:

$$\Omega(\text{TH}[c, n], x) = n \cdot x^{c/2} + k \cdot x^{cn/k} \quad (4.92)$$

The index is calculated as:

$$CI(\text{TH}[q, 2p]) = 9p^2q^2 - k(2pq/k)^2 - 2p(q/2)^2 \quad (4.93)$$

For the example in Figure 4-8a: $\Omega(\text{H}[4, 8], x) = 8 \cdot x^2 + 4 \cdot x^8$; $CI = 2016$; $I_\Omega = 2.247207$.

4.8.1.2. Zig-zag Tubes $\text{TU}(6, 3)\text{H}[2p, q]$ and Tori $\text{T}(6, 3)\text{V}[q, 2p]$

Case of zig-zag tubes $\text{TUH}[2p, q]$ (Figure 4-8b, $p = 4$; $q = 5$).

The circular and radial terms are as follows:⁷⁵

$$C(G, x) = (q - 1) \cdot x^p \quad (4.94)$$

$$R(G, x) = 2p \cdot x^q \quad (4.95)$$

and the corresponding index:

$$CI(\text{TUH}[2p, q]) = p^2(3q - 1)^2 - (q - 1)p^2 - 2pq^2 \quad (4.96)$$

For the example in Figure 4-8b: $\Omega(\text{TUH}[8, 5], x) = 4 \cdot x^4 + 8 \cdot x^5$; $CI = 2872$; $I_\Omega = 1.578425$

Case of tori, $\text{TV}[q, 2p]$.

These tori correspond to “zig-zag” tubes, in a Schlegel-like projection (Figure 4-8b, $p = 4$; $q = 4$). The circular term C is the same for all the cases:⁷⁵

$$C(G, x) = q \cdot x^p \quad (4.97)$$

and the radial term R varies as follows:

$$R(G, x) = k \cdot x^{2pq/k} \quad (4.98)$$

with k being as above.

In $[c, n]$ terms, the Omega polynomial is:

$$\Omega(\text{TV}[c, n], x) = c \cdot x^{n/2} + k \cdot x^{cn/k} \quad (4.99)$$

The index is calculable as:

$$CI(\text{TV}[q, 2p]) = 9p^2q^2 - k(2pq/k)^2 - p^2q \quad (4.100)$$

For the example in Figure 4-8b: $\Omega(\text{TV}[4, 8], x) = 4 \cdot x^4 + 4 \cdot x^8$; $CI = 1984$;
 $I_\Omega = 2.274070$.

4.8.1.3. Twisted/Chiral Tori $T(6,3)\text{VVt}[c,n]$

The interest was oriented to the chiral/twisted $T(6,3)\text{VVt}[c,n]$ objects, because they offer cases of single term Omega polynomials, with direct interpretation of their spirality. We present here a *factorization* procedure enabling the derivation of formulas for a whole class of chiral polyhex toroids.

Within the present *factorization* procedure,^{89,90} the Omega polynomial of a torus T is written (cf. (4.101)) as the product:

$$\Omega(T, x) = f_{k/k_i} \cdot \Omega(T_i, x) = \sum_{c_i} f_{k/k_i} \cdot m(T_i, c_i) \cdot x^{f_{k/k_i} \cdot c_i} \quad (4.101)$$

In the above relation, k is the *size* factor multiplying the net ratio $r = c/n$ to give the actual size s : $s = r \cdot k$. Next, k_i refers to the divisors of k and, correspondingly, T_i and c_i refer to the object showing the k_i size factor. Finally, f_{k/k_i} is the factor to be used in the actual procedure.

Case: $T(6,3)\text{VVt}[c,n]$. The chosen class shows a net ratio $(c/n) = (4/6)$ and the size factor is: $k = c/4 = n/6$. Next, $c = kc_1$; $n = kn_1$, with $c_1 = 4$ and $n_1 = 6$ being the net dimensions of the first (smallest) family of objects in this class. A family of twisted tori includes all the objects having the same $[c,n]$ -dimensions (implying the same k) and $0 \leq t \leq c$, in Diudea's system.⁸⁷ In the case of $T(6,3)\text{VVt}[c,n]$, the maximum twisting is taken $t = c/2$, to ensure all the objects are distinct (see Section 2.6). Figure 4-9 illustrates a torus of this class, which shows a single term Omega polynomial.

The procedure to derive formulas for a whole family of chiral polyhex toroids is as follows.⁹⁰

1. If k is *odd*, ($k = 1, 3, \dots$) and *prime* number, formulas for two sub-series of tori can be written: (a) objects having the twisting $t = 4s + 2$ and (b) objects with

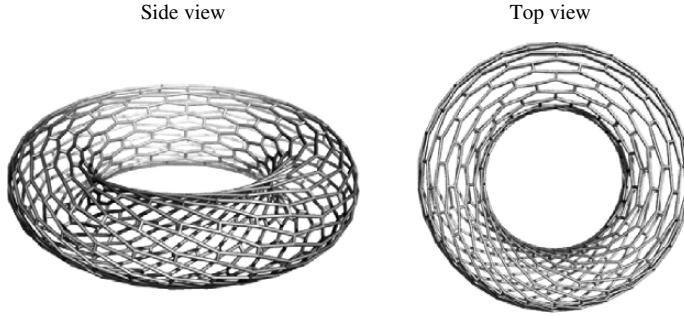


Figure 4-9. Torus T(6,3)VV10[20,30], with the twisted region in the front (non-optimized).

$t = 4s$, the limits for s being given in Table 4-8. The objects of series (a) show a single term in the Omega polynomial while those in the series (b) show a double term polynomial. Formulas for the non-twisted objects are also included. All the formulas in Table 4-8 are given in three forms: (i) general, non-factorized; (ii) factorized vs. $k_1 = 1$ and (iii) factorized vs. any divisor of k , $k_i = i$.

2. Take a *non-prime* k -value and find its divisors. Factorize first the t -parameter of the divisors and next write the corresponding (distinct) polynomial formulas (by using the factors f_{k/k_i} - see Tables 4-8 and 4-9) for all the possible divisors. Complete the actual t -parameter up to $t = c/2$ and use the corresponding formulas

Table 4-8. Formulas for the Omega polynomial of T(6,3)VVt[c,n] polyhex tori; $(c/n) = (4/6) \cdot k$

k	t -mode	s	Omega polynomial
odd	0	-	(a) $c \cdot x^{n/2} + (c/2) \cdot x^{2n}$; non-twisted; non-chiral
			(b) $kc_1 \cdot x^{kn_1/2} + k(c_1/2) \cdot x^{2kn_1}$
			(c) $f_{k/k_i}(c_i) \cdot x^{f_{k/k_i}(n_i/2)} + f_{k/k_i}(c_i/2) \cdot x^{f_{k/k_i}(2n_i)}$
	4s+2	0, 1, 2, ..., $(c-12/8)$	(a) $n/k \cdot x^{kn}$
			(b) $n_1 \cdot x^{k^2 n_1}$
			(c) $f_{k/k_i}(n_i/k_i) \cdot x^{f_{k/k_i}(k_i n_i)}$
	4s	1, 2, ..., $(c-4)/8$	(a) $c/k \cdot x^{kn/2} + c/2k \cdot x^{2kn}$
			(b) $c_1 \cdot x^{k^2 n_1/2} + c_1/2 \cdot x^{2k^2 n_1}$
			(c) $f_{k/k_i}(c_i/k_i) \cdot x^{f_{k/k_i}(k_i n_i/2)} + f_{k/k_i}(c_i/2k_i) \cdot x^{f_{k/k_i}(2k_i n_i)}$
	4s+2	$(c-4)/8$; $t = c/2$	(a) $3t \cdot x^{cn/2t} = n \cdot x^n$
			(b) $kn_1 \cdot x^{kn_1}$
			(c) $f_{k/k_i}(n_i) \cdot x^{f_{k/k_i}(n_i)}$
even	0	-	as for $k = \text{odd}$
	4s+2	0, 1, 2, ..., $(c-8/8)$	(a) $c/2k \cdot x^{kn} + c/2k \cdot x^{2kn}$
			(b) $c_1/2 \cdot x^{k^2 n_1} + c_1/2 \cdot x^{2k^2 n_1}$
			(c) $f_{k/k_i}(c_i/2k_i) \cdot x^{f_{k/k_i}(k_i n_i)} + f_{k/k_i}(c_i/2k_i) \cdot x^{f_{k/k_i}(2k_i n_i)}$
	4s	$c/8$; $t = c/2$	as for $k = \text{odd}$

Table 4-9. Examples of Omega Polynomial and CI Index in Polyhex Tori of T(6,3)VVi[c,n] Series

$k; [c,n]$	t –mode & f_{k/k_i}	s	t	Omega polynomial	CI
k =odd					
1; [4,6]	0		0	$4x^3+2x^{12}$	972
	<u>4s+2</u>	<u>0</u>	<u>2; c/2</u>	<u>6x⁶</u>	<u>1080</u>
3; [12,18]	0		0	$12x^9+6x^{36}$	96228
	4s+2	0	2	$6x^{54}$	87480
	4s	1	4	$4x^{27}+2x^{108}$	78732
	4s+2	1	6; c/2	$18x^{18}$	99144
5; [20,30]	0		0	$20x^{15}+10x^{60}$	769500
	4s+2	0	2	$6x^{150}$	675000
	4s	1	4	$4x^{75}+2x^{300}$	607500
	4s+2	1	6	$6x^{150}$	675000
	4s	2	8	$4x^{75}+2x^{300}$	607500
	4s+2	2	10; c/2	$30x^{30}$	783000
9; [36,54]	0		0	$36x^{27}+18x^{108}$	8266860
	4s+2	0	2	$6x^{486}$	7085880
	4n	1	4	$4x^{243}+2x^{972}$	6377292
	$f_{9/3}$	-	6	$18x^{162}$	8030664
	4s	2	8	$4x^{243}+2x^{972}$	6377292
	4s+2	2	10	$6x^{486}$	7085880
	$f_{9/3}$	-	12	$12x^{81}+6x^{324}$	7794468
	4s+2	3	14	$6x^{486}$	7085880
	4s	4	16	$4x^{243}+2x^{972}$	6377292
	4s+2; $f_{9/3}$	4	18; c/2	$54x^{54}$	8345592
k =even					
2; [8,12]	0		0	$8x^6+4x^{24}$	18144
	4s+2	0	2	$2x^{24}+2x^{48}$	14976
	4s	1	4; c/2	$12x^{12}$	19008
4; [16,24]	0		0	$16x^{12}+8x^{48}$	311040
	4s+2	0	2	$2x^{96}+2x^{192}$	239616
	$f_{4/2}$	-	4	$4x^{48}+4x^{96}$	285696
	4s+2	1	6	$2x^{96}+2x^{192}$	239616
	4s; $f_{4/2}$	2	8; c/2	$24x^{24}$	317952
6; [24,36]			0	$24x^{18}+12x^{72}$	1609632
	4s+2	0	2	$2x^{216}+2x^{432}$	1213056
	$f_{6/3}$	-	4	$12x^{108}$	1539648
	$f_{6/2}$	-	6	$6x^{72}+6x^{144}$	1524096
	$f_{6/3}$	-	8	$8x^{54}+4x^{216}$	1469664
	4s+2	2	10	$2x^{216}+2x^{432}$	1213056
	4s; $f_{6/2}$; $f_{6/3}$		12; c/2	$36x^{36}$	1632960

- for (prime number) odd k objects given in Table 4-8. Note that the factorizing mode is dominant with respect to the actual twisting t -mode.
3. Write formulas for the *even* series ($k = 2, 4, \dots$) analogously; remark the only new formula is for $t = 4s + 2$.
 4. Calculate the actual Omega polynomial and the corresponding CI index.

The actual procedure starts with $k = 1$ and, recursively, provides formulas for families of $k > 1$. Examples are given in Table 4-9. Note that, at various t -values within the same t -mode (either $4s+2$ or $4s$), degenerate polynomial and CI values appear.

The remark on spirality refers to the formula $3t \cdot x^{cn/2t} = n \cdot x^n$ for the single term Omega polynomial of the maximum twisted objects of this class. As a hexagon is the start of three edge-cut strips, $t = n/3$ is just the number of spirals of this object. For the other objects, t is more hidden, because of the degeneracy of edge-cut modes (Table 4-9).

4.8.2. Covering ((4,8)3)

In the Schlegel representation⁸⁶ of a ((4,8)3) nanotube (Figure 4-10), the points (of degree 2) lying on the central circle have to be pairwise joined to those on the external circle to give the corresponding torus.⁷⁶

4.8.2.1. Tori $T((4,8)3)S$

A torus $T((4,8)3)S[c,n]$, in Diudea's notation,^{1,55,87} is now written as $T((4,8)3)SH[2q,2p]$ and $T((4,8)3)SV[2p,2q]$, to specify the H/V embedding and

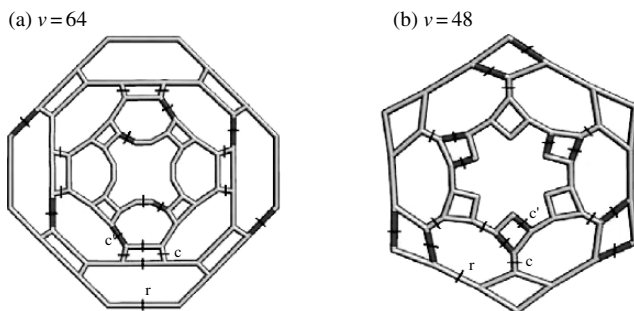


Figure 4-10. (a) Tube $TU((4,8)3)S[8,8]$; ($p=4; q=4$); $\Omega(G, x) = 4px^q + (q-1)x^{2p} = 16x^4 + 3x^8$ Torus $T((4,8)3)SH[8,8]$; ($p=4; q=4$); $\Omega(G, x) = 2px^q + 2qx^{2p} = 8x^4 + 8x^8$ (b) Tube $TU((4,8)3)RLe([6,2])$; $p=6; q=2$; $\Omega(G, x) = (q-1)x^p + px^q + 2px^{2q} = 6x^2 + 12x^4 + x^6$ Torus $T((4,8)3)RLe[2,6]$; $q=2$; $p=6$; $\Omega(G, x) = qx^p + px^q + 2mdx^{2pq/md} = 6x^2 + 2x^6 + 4x^{12}$ The points of degree 2 lying on the central circle of a tube have to be pairwise joined to the opposite ones on the external circle to give the corresponding torus.

Table 4-10. Tori $T((4,8)3)S[c,n]$

H-embedding: $[c,n] = [2q,2p]$; (q,p)		
1 Case: $p = kq$; $k = \text{even}$ $R(G, x) = p \cdot x^{2q}$	$C(G, x) = 4q \cdot x^p$	$H[16,96]; (8,48): 48X^{16}+32X^{48}$
2 Case: $p = kq$; $k = \text{odd}$; $p = (k/2)q$ $R(G, x) = 2p \cdot x^q$	$C(G, x) = 2q \cdot x^{2p}$	$H[12,12]; (6,6): 12X^6+12X^{12}$ $H[16,24]; (8,12): 24X^8+16X^{24}$ $H[16,48]; (8,24): 48X^8+16X^{48}$ $H[12,18]; (6,9): 18X^6+12X^{18}$
3 Case: $md > 1$; $(p = (k/3)q ; k = \text{even})$; $md = \text{maximum common divisor}$ $R(G, x) = 2p \cdot x^q$	$C(G, x) = q \cdot x^{2p}$ $C'(G, x) = md \cdot x^{2pq/md}$	$H[12,16]; (6,8): md = 2:$ $16X^6+6X^{16}+2X^{48}$ $H[24,32]; (12,16): md = 4:$ $2X^{12}+12X^{32}+4X^{96}$ $H[36,48]; (18,24): md = 6:$ $48X^{18}+18X^{48}+6X^{144}$
4 Case: $md = 1$ $R(G, x) = 2p \cdot x^q$	$C(G, x) = q \cdot x^{2p}$ $C'(G, x) = 2 \cdot x^{pq}$	$H[20,22]; (10,11): md = 1:$ $22X^{10}+10X^{22}+2X^{110}$
V-embedding: $[c,n] = [2p,2q]$; (p, q)		
1 Case: $q = 2p$ $C(G, x) = 3q \cdot x^q$	none	$V[8,16]; (4,8): 24X^8$
2 Case: $q = kp$; $k = \text{even}$ $R(G, x) = q \cdot x^{2p}$	$C(G, x) = 4p \cdot x^q$	$V[20,80]; (10,40): 40X^{20}+40X^{40}$
3 Case: $md > 1$; $(q = kp; q = (k/2)p; k = \text{odd})$ $R(G, x) = q \cdot x^{2p}$	$C(G, x) = 2p \cdot x^q$ $C'(G, x) = md \cdot x^{2pq/md}$	$V[16,48]; (8,24): md = 8:$ $24X^{16}+16X^{24}+8X^{48}$ $V[16,24]; (8,12): md=4:$ $16X^{12}+12X^{16}+4X^{48}$ $V[20,28]; (10,14): md = 2:$ $20X^{14}+14X^{20}+2X^{140}$
4 Case: $md > 1$; $(q = (k/3)p; k = \text{even})$ $R(G, x) = q \cdot x^{2p}$	$C(G, x) = 2p \cdot x^q$ $C'(G, x) = 2md \cdot x^{pq/md}$	$V[24,32]; (12,16): md = 4:$ $24X^{16}+16X^{24}+8X^{48}$
5 Case: $md = 1$ $R(G, x) = q \cdot x^{2p}$	$C(G, x) = 2p \cdot x^q$ $C'(G, x) = 2 \cdot x^{pq}$	$V[22,24]; (11,12): md = 1:$ $22X^{12}+12X^{22}+2X^{132}$

square/octagon units. In these tori, q (divisible by 4) is winding around the tube while p around the central hollow of the torus. The parameters of (4.102) are given in Table 4-10.

The contributions to the global polynomial can be expressed, as in the case of polyhex tori (Section 4.8.1):

$$\Omega(G, x) = R(G, x) + C(G, x) + C'(G, x) \quad (4.102)$$

The last C' term may fuse with C to give a unique “circular” contribution.⁷⁶

Domains eventually not covered by the formulas in Table 4-10 can be solved by using the following formulas which show the equivalence of the symbols (generated by the Torus software⁹¹), associated with identical graphs:

$$T((4, 8)3)SH[c, n] = T((4, 8)3)SV[n, c]$$

$$T((4, 8)3)SH[c, n] = T((4, 8)3)SH[2n, c/2]$$

$$T((4, 8)3)SV[c, n] = T((4, 8)3)SV[n/2, 2c]$$

4.8.2.2. Tori $T((4,8)3)R$

A torus $T((4,8)3)RLe((4,4)[q,p])$ is obtained by leapfrogging the torus $T(4,4)[c,n]$, so that the correspondence $c = q$ and $n = p$ is straightforward.⁷⁶ For such tori, the parameters of (4.102) are given in Table 4-11.

4.8.2.3. Tubes $TU((4,8)3)$

Tubes are generated from tori either by tube cross-cutting or by around hollow-cutting. In the case of tubes, the radial/circular specification from tori is however improper, so that we limit to give the terms of the sum simply as A, B, C terms:⁷⁶

$$\Omega(G, x) = A(G, x) + B(G, x) + C(G, x) \quad (4.103)$$

The parameters of (4.103) are given in Table 4-12.

All the Omega polynomial descriptors herein presented have been calculated by the Omega Counter software.⁹²

Table 4-11. Tori $T((4,8)3)RLe((4,4)[q,p])$ (unique embedding)

Case: $p = q$

$R(G, x) = 2p \cdot x^q$	$C(G, x) = 2q \cdot x^{2p}$	$Le [10,10]: 20X^{10}+20X^{20}$
--------------------------	-----------------------------	---------------------------------

Case: otherwise; md = maximum common divisor

$R(G, x) = p \cdot x^q$	$C(G, x) = q \cdot x^p$ $C'(G, x) = 2md \cdot x^{2pq/md}$	$Le[5,15]; md = 5:$ $15X^5+5X^{15}+10X^{30}$ $Le[5,12]; md=1:$ $12X^5+5X^{12}+2X^{120}$
-------------------------	--	--

Table 4-12. Tubes $TU((4,8)3)S[c,n]$ and $TU((4,8)3)RLe((4,4)[q,p])$

TU ((4,8)3)S[c, n]; tubes are obtained by cutting the tori as:

- (a) Cut torus $H[c,n]$: across-tube; (TUS(p,q)); $c = 4p$; $n = q$; around-hollow (TUG(p,q)); $c = 2q$; $n = 2p$
 (b) Cut torus $V[c,n]$: across-tube; (TUS(p,q)); $c = 2p$; $n = 2q$; around-hollow (TUG(p,q)); $c = q$; $n = 4p$

$A(G, x) = 4p \cdot x^q$	TUG($H[16,24]$); (12,8): $48X^8 + 7X^{24}$
$B(G, x) = (q-1) \cdot x^{2p}$	TUG($V[16,24]$); (6,16): $15X^{12} + 24X^{16}$
	TUS($H[16,24]$); (4,24): $23X^8 + 16X^{24}$
	TUS($V[16,24]$); (8,12): $32X^{12} + 11X^{16}$

TU ((4,8)3)R[c, n]; tubes are obtained by cutting the tori either across-tube or around-hollow

$A(G, x) = (p-1) \cdot x^q$	TUSR($Le[7,8]$); (7,8): $7X^7 + 7X^8 + 14X^{16}$
$B(G, x) = q \cdot x^p$	TUGR($Le[7,8]$); (8,7): $8X^7 + 6X^8 + 16X^{14}$
$C(G, x) = 2q \cdot x^{2p}$	

4.9. QSPR Studies by Omega-derived Descriptors

Among the single number descriptors provided by the Omega polynomial, one is of particular importance: n_p , the number of *pentagon fusions*, appearing as the *coefficient of the first power term*, which accounts for more than 90% of the variance in heat of formation HF of small fullerenes, *e.g.*, C_{40} and C_{50} .

Pentagon fusion is a major destabilizing factor in the classical fullerenes. To account for this, Albertazzi *et al.*⁹³ have proposed the number n_p , of pentagon-adjacency: $n_p \leq 30$ for any fullerene and varies from 20 to 10 within the C_{40} set. The maximum value occurs for the hemidodecahedral capped isomer 40:1, and the minimum for the two isomers 40: 38 and 40: 39.

Resuming to the n_p descriptor, it can be derived from the relations:

$$n_p = 180 - pv \quad (4.104)$$

$$pv_k = (1/2) \sum_{pi} [LV(Du(M))]_{i,k} \quad (4.105)$$

with summation running over all entries, in the layer matrix of valences LV, corresponding to pentavalent vertices in the *dual* of molecular graph. The pv_k parameter⁹⁴ is the sum of faces size at the k^{th} shell around each pentagon, in the original graph. In case $k = 1$, (the subscript k omitted), it varies between 150 (in C_{20}) and 180 (in IPR fullerenes), and from 160 to 170 within the set of C_{40} isomers (see below). In IPR fullerenes, $n_p = 0$, as expected. The number 180 is calculated as: $(12 \times 5 \times 6)/2$ and represents the maximum value of pv .

The other two indices CI and I_Ω , derived from the Omega polynomial, contribute rather poor to the global correlation.

Even better is correlated the strain energy SE, calculated according to POAV1 procedure.^{95,96,97} The less strained isomer is 38- D_2 .

The set of C_{40} fullerene graphs, are presented in Table 4-13, in an ordering given by their spiral codes.⁹⁸ The plots of the correlating study are given in Figures 4-11

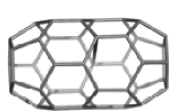
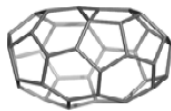
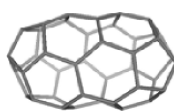
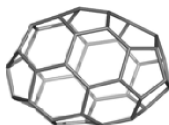
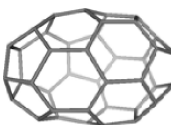
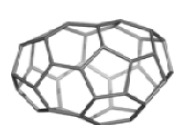
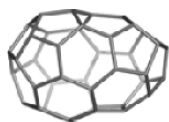
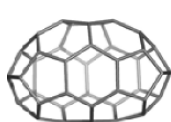
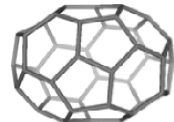
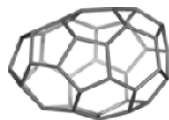
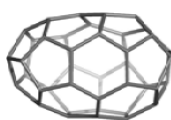
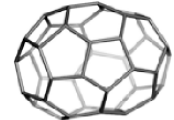
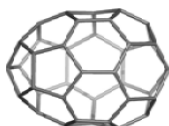
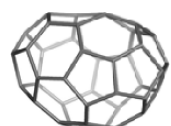
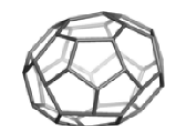
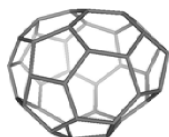
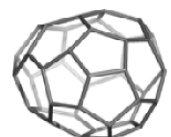
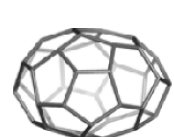
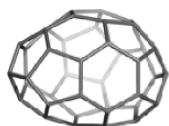
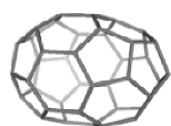
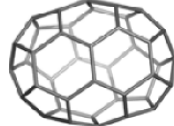
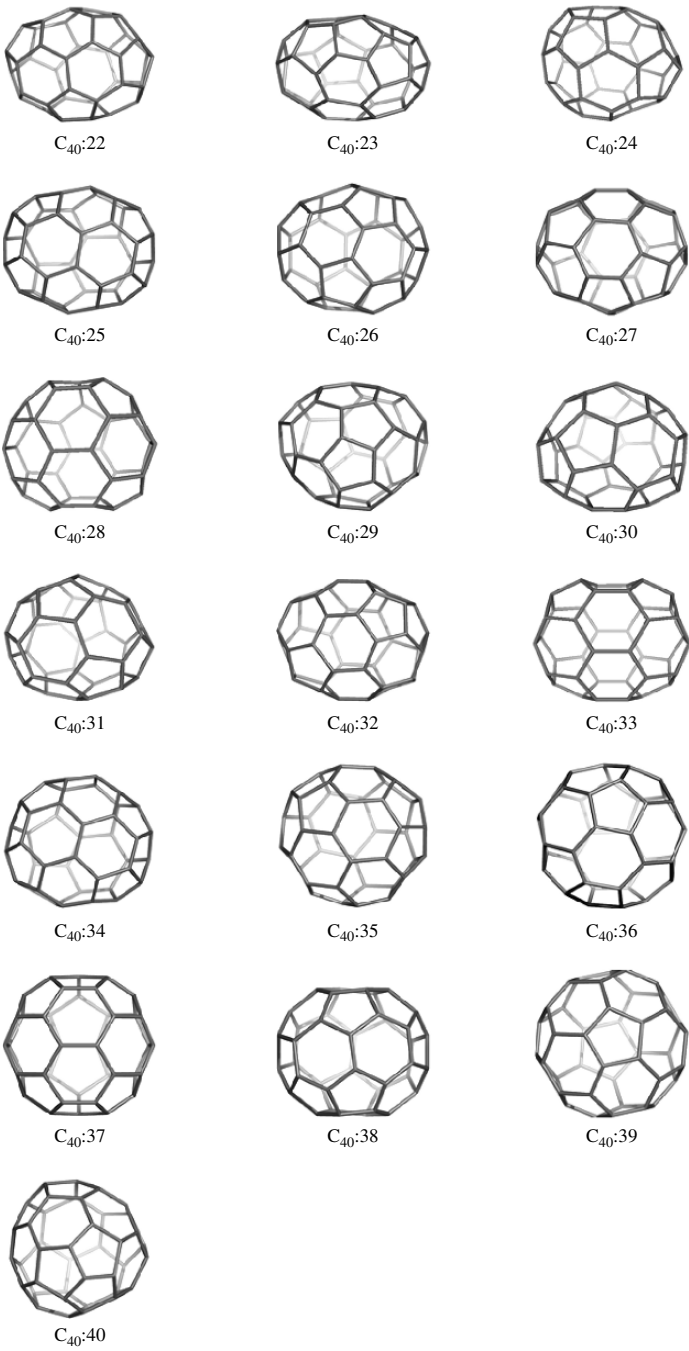
Table 4-13. Structure of the C_{40} isomers $C_{40}:1$  $C_{40}:2$  $C_{40}:3$  $C_{40}:4$  $C_{40}:5$  $C_{40}:6$  $C_{40}:7$  $C_{40}:8$  $C_{40}:9$  $C_{40}:10$  $C_{40}:11$  $C_{40}:12$  $C_{40}:13$  $C_{40}:14$  $C_{40}:15$  $C_{40}:16$  $C_{40}:17$  $C_{40}:18$  $C_{40}:19$  $C_{40}:20$  $C_{40}:21$

Table 4-13. (Continued)



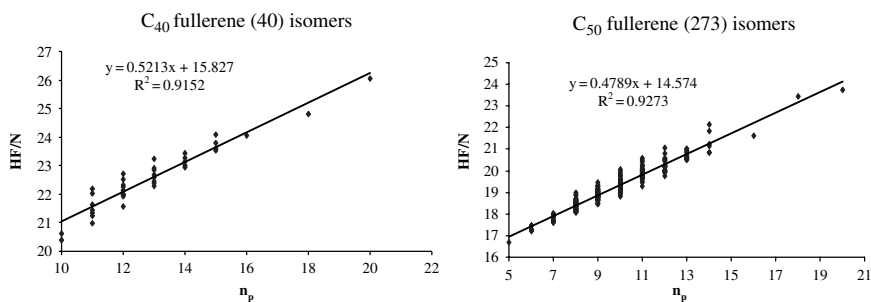


Figure 4-11. The plot heat of formation HF (kcal/mol) vs n_p in C₄₀ and C₅₀ fullerene isomers.

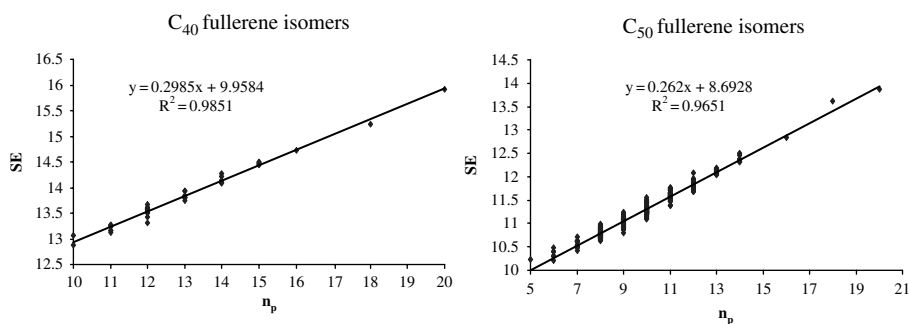


Figure 4-12. The plot POAV1 strain energy SE (kcal/mol) vs n_p in C₄₀ and C₅₀ fullerene isomers.

and 4-12 while the corresponding topological and energetic parameters are listed in Table 4-14.

Semiempirical calculations have been performed by using the PM3 Hamiltonian, in standard parametrization supplied by HyperChem software (optimization by

Table 4-14. Topological and Energetical Parameters of C₄₀ Isomers.

C _{40<i>i</i>}	n_p	pv	PM3 HF/atom (kcal/mol)	SE/atom (kcal/mol)
1- <i>D</i> _{5d}	20	160	26.053	15.908
2- <i>C</i> ₂	16	164	24.057	14.724
3- <i>D</i> ₂	18	162	24.809	15.243
4- <i>C</i> ₁	15	165	23.542	14.474
5- <i>C</i> _s	14	166	23.008	14.264
6- <i>C</i> ₁	14	166	22.960	14.111
7- <i>C</i> _s	15	165	23.811	14.443
8- <i>C</i> _{2v}	15	165	23.589	14.492
9- <i>C</i> ₂	13	167	22.847	13.838
10- <i>C</i> ₁	13	167	22.588	13.810

Table 4-14. (Continued)

$C_{40;i}$	n_p	pv	PM3 HF/atom (kcal/mol)	SE/atom (kcal/mol)
11- C_2	15	165	24.081	14.464
12- C_1	13	167	22.304	13.794
13- C_s	13	167	22.692	13.809
14- C_s	12	168	21.982	13.577
15- C_2	12	168	22.520	13.677
16- C_2	13	167	22.469	13.839
17- C_1	13	167	22.395	13.742
18- C_2	14	166	23.151	14.143
19- C_2	13	167	22.903	13.934
20- C_{3v}	12	168	22.721	13.552
21- C_2	12	168	22.325	13.603
22- C_1	12	168	21.991	13.527
23- C_2	13	167	23.235	13.935
24- C_s	11	169	21.638	13.281
25- C_2	12	168	22.134	13.578
26- C_1	11	169	21.444	13.249
27- C_2	12	168	21.967	13.431
28- C_s	12	168	21.927	13.597
29- C_2	11	169	21.328	13.227
30- C_3	12	168	22.272	13.610
31- C_s	11	169	20.972	13.166
32- D_2	14	166	23.425	14.082
33- D_{2h}	14	166	24.922	14.212
34- C_1	12	168	22.113	13.494
35- C_2	11	169	22.192	13.262
36- C_2	11	169	22.042	13.166
37- C_{2v}	11	169	21.231	13.123
38-D_2	10	170	20.408	12.887
39- D_{5d}	10	170	20.629	13.066
40- T_d	12	168	21.569	13.312

Polak-Ribiere conjugate-gradient method, at RMS gradient <0.01 kcal/(Å·mol)). Strain energies were supplied by our JSCHEM software program.⁹⁹

Conclusions

Counting polynomials represent a diverse class of polynomials, based or not on various topological matrices. The coefficients of some of the polynomials discussed in this chapter were calculated either from matrices or by means of orthogonal edge-cuts. Basic definitions and properties of the Hosoya, Cluj and Omega polynomials were given. Analytical formulas for calculating these polynomials in tubular nanostructures were presented. Utility of descriptors derived from the counting polynomials to predict some physico-chemical properties of fullerenes was exemplified.

References

1. M. V. Diudea, I. Gutman, and L. Jäntschi, *Molecular Topology*, NOVA, New York, 2002.
2. J. J. Sylvester, *Am. J. Math.* 1874, **1**, 64–90.
3. F. Harary, *Graph Theory*, Addison Wesley, Reading, M.A., 1969.
4. N. Trinajstić, *Chemical Graph Theory*, CRC Press, Inc., Boca Raton, Florida, 1983.
5. H. Wiener, *J. Amer. Chem. Soc.*, 1947, **69**, 17–20.
6. M. Randić, *Chem. Phys. Lett.*, 1993, **211**, 478–483.
7. M. V. Diudea, *J. Chem. Inf. Comput. Sci.*, 1996, **36**, 535–540.
8. D. Amić and N. Trinajstić, *Croat. Chem. Acta*, 1995, **68**, 53–62.
9. O. Ivanciuc and A. T. Balaban, *MATCH, Commun. Math. Comput. Chem.*, 1994, **30**, 141–152.
10. M. V. Diudea, G. Katona, I. Lukovits, and N. Trinajstić, *Croat. Chem. Acta*, 1998, **71**, 459–471.
11. I. Lukovits and M. Razinger, *J. Chem. Inf. Comput. Sci.*, 1997, **37**, 283–286.
12. M. V. Diudea, O. Minailiuc, G. Katona, and I. Gutman, I., *MATCH, Commun. Math. Comput. Chem.*, 1997, **35**, 129–143.
13. I. Gutman, *Graph Theory Notes New York*, 1994, **27**, 9–15.
14. R. A. Horn and C. R. Johnson, *Matrix Analysis*; Cambridge Univ. Press, Cambridge, 1985.
15. M. V. Diudea, *J. Chem. Inf. Comput. Sci.*, 1997, **37**, 300–305.
16. M. V. Diudea, *MATCH, Commun. Math. Comput. Chem.*, 1997, **35**, 169–183.
17. M. V. Diudea, B. Parv, and I. Gutman, *J. Chem. Inf. Comput. Sci.*, 1997, **37**, 1101–1108.
18. M. V. Diudea and G. Katona, in: *Advances in Dendritic Macromolecules*, Ed. G.A. Newkome, JAI Press Inc., Stamford, Con. 1999, vol.4, pp. 135–201.
19. M. V. Diudea and O. Ivanciuc, *Molecular Topology*, Complex, Cluj, 1995 (in Romanian).
20. M.V. Diudea, I. Gutman and L. Jäntschi, *Molecular Topology*. Nova Science, Huntington, New York, 2001.
21. N. Trinajstić, *Chemical Graph Theory*, IInd Ed. CRC Press, 1992.
22. I. Gutman, M. Milun, and N. Trinajstić, *MATCH, Commun. Math. Comput. Chem.*, 1975, **1**, 171–175.
23. J. Aihara, *J. Am. Chem. Soc.*, 1976, **98**, 2750–2758.
24. I. Gutman, M. Milun, and N. Trinajstić, *J. Am. Chem. Soc.*, 1977, **99**, 1692–1704.
25. A. Tang, Y. Kiang, G. Yan, and S. Tai, *Graph Theoretical Molecular Orbitals*; Science Press: Beijing, 1986.
26. P. S. Dwyer, *Linear Computations*, Wiley, N. Y. 1951.
27. D. K. Faddeev and I. S. Sominskii, *Problems in Higher Algebra*, Freeman, San Francisco, 1965.
28. H. Hosoya, M. Murakami and M. Gotoh, *Natl. Sci. Rept. Ochanomizu Univ.*, 1973, **24**, 27–34.
29. R. L. Graham and L. Lovasz, *Adv. Math.* 1978, **29**, 60–88.
30. M. V. Diudea, O. Ivanciuc, S. Nikolić, and N. Trinajstić, *MATCH, Commun. Math. Comput. Chem.*, 1997, **35**, 41–64.
31. O. Ivanciuc, M. V. Diudea, and P. V. Khadikar, *Indian J. Chem.*, 1998, **37A**, 574–585.
32. O. Ivanciuc, T. Ivanciuc, and M. V. Diudea, *Roum. Chem. Quart. Rev.* 1999, **7**, 41–67.
33. H. Hosoya, *Bull. Chem. Soc. Japan*, 1971, **44**, 2332–2339.
34. H. Hosoya, *Discrete Appl. Math.*, 1988, **19**, 239–257.
35. E. V. Konstantinova and M. V. Diudea, *Croat. Chem. Acta*, 2000, **73**, 383–403.
36. I. Gutman, S. Klavžar, M. Petkovšek, and P. Žigert, *MATCH, Commun. Math. Chem.*, 2001, **43**, 49–66.
37. H. Hosoya and T. Yamaguchi, *Tetrahedron Lett.*, 1975, 4659–4662.
38. N. Ohkami and H. Hosoya, *Theoret. Chim. Acta*, 1983, **64**, 153–170.
39. N. Ohkami, A. Motoyama, T. Yamaguchi, and H. Hosoya, *Tetrahedron*, 1981, **37**, 1113–1122.
40. H. Hosoya, *Topics Curr. Chem.*, 1990, **153**, 255–272.
41. E. Clar, *Polycyclic Hydrocarbons*, Acad. Press, London, 1964.
42. E. Clar, *The Aromatic Sextet*, Wiley, New York, 1972.
43. I. Gutman and H. Hosoya, *Z. Naturforsch.*, 1990, **45a**, 645–648.
44. I. Gutman, *MATCH, Commun. Math. Chem.*, 1992, **28**, 139–150.

45. D. Stevanović, *Graph Theory Notes New York*, 1998, **34**, 31–36.
46. A. Motoyama and H. Hosoya, *J. Math. Phys.*, 1977, **18**, 1485–1490.
47. K. Balasubramanian and R. Ramaraj, *J. Comput. Chem.*, 1985, **6**, 447–454.
48. E. J. Farrell, *Canad. Math. Bull.*, 1978, **2**, 35–46.
49. E. J. Farrell and C. De Matas, *Ark. Math.*, 1988, **26**, 185–190.
50. E. J. Farrell and C. De Matas, *Util. Math.*, 1988, **33**, 33–45.
51. M. V. Diudea, *J. Chem. Inf. Comput. Sci.*, 1994, **34**, 1064–1071.
52. M. V. Diudea, *Studia Univ. “Babes-Bolyai”*, 2002, **47**, 131–139.
53. M. V. Diudea, *MATCH, Commun. Math. Comput. Chem.*, 2002, **45**, 109–122.
54. M. V. Diudea and O. Ursu, *Indian J. Chem.*, 2003, **42A**, 1283–1294.
55. M. Ștefu and M. V. Diudea, in: M. V. Diudea, (Ed.), *Nanostructures – Novel Architecture*, Nova, New York, 2005, 127–165.
56. O. Ursu and M. V. Diudea, TOPOCLUJ software program, Babes-Bolyai University, Cluj, 2005; available at <http://chem.ubbcluj/~diudea>.
57. M. V. Diudea, *J. Math. Chem.*, 2007 (in press).
58. I. Gutman and S. Klavžar, *J. Chem. Inf. Comput. Sci.*, 1995, **35**, 1011–1014.
59. M. V. Diudea, M. S. Florescu and P. V. Khadikar, *Molecular topology and it's applications*, EfiCon Press, 2006, Bucharest, Romania.
60. A. A. Dobrynin and I. Gutman, *Graph Theory Notes of New York*, 1995, **28**, 21–23.
61. A. A. Dobrynin, I. Gutman, and G. Domotor, *Appl. Math. Lett.*, 1995, **8**, 57–62.
62. P. V. Khadikar, N. V. Deshpande, P. P. Kale, A. Dobrynin, I. Gutman, and G. Domotor, *J. Chem. Inf. Comput. Sci.*, 1995, **35**, 547–550.
63. S. Klavžar, A. Rajapakse, and I. Gutman, *Appl. Math. Lett.*, 1996, **9**, 45–49.
64. J. Žerovnik, *Croat. Chem. Acta*, 1996, **69**, 837–843.
65. A. A. Dobrynin and I. Gutman, *Croat. Chem. Acta*, 1996, **69**, 845–856.
66. M. V. Diudea, *Carp. J. Math.*, 2006, **22**, 43–47.
67. P. E. John, P. V. Khadikar, J. Singh, *J. Math. Chem.*, 2006, DOI:10.1007/s10910-006-9100-2.
68. John, P. E.; Vizitiu, A. E.; Cigher, S.; Diudea, M. V., *MATCH, Commun. Math. Comput. Chem.*, 2007, **57**, 479–484.
69. M. V. Diudea, P. E. John, A. Graovac, M. Primorac, and T. Pisanski, *Croat. Chem. Acta*, 2003, **76**, 153–159.
70. M. Ștefu, D. Butyka, M. V. Diudea, L. Jantschi, and B. Parv, in: M. V. Diudea, Ed., *Nanostructures–Novel Architecture*, NOVA, New York, 2005, 243–267.
71. M. V. Diudea, *Forma* (Tokyo), 2004, **19**(3), 131–163.
72. M. V. Diudea, *J. Chem. Inf. Model.*, 2005, **45**, 1002–1009.
73. M. Ștefu, M. V. Diudea and P. E. John, *Studia Univ. “Babes-Bolyai”*, 2005, **50**(2), 165–174.
74. M. V. Diudea, M. Ștefu, P. E. John, and A. Graovac, *Croat. Chem. Acta*, 2006, **79**, 355–362.
75. M. V. Diudea, S. Cigher, A. E. Vizitiu, O. Ursu and P. E. John, *Croat. Chem. Acta*, 2006, **79**, 445–448.
76. Vizitiu, A. E.; Cigher, S.; Diudea, M. V., Florescu, M. S. *MATCH, Commun. Math. Comput. Chem.*, 2007, **57**, 457–462.
77. P. V. Khadikar, *Nat. Acad. Sci. Lett.*, 2000, **23**, 113–118.
78. A. R. Ashrafi, M. Manoochehrian and H. Yousefi Azari, *Util. Math.*, 2007 (in press).
79. M. V. Diudea, *Bull. Chem. Soc. Japan*, 2002, **75**, 487–492.
80. M. V. Diudea, *MATCH, Commun. Math. Comput. Chem.*, 2002, **45**, 109–122.
81. M. V. Diudea and P. E. John, *MATCH, Commun. Math. Comput. Chem.*, 2001, **44**, 103–116.
82. M. V. Diudea, O. Ursu, and B. Parv, *Studia Univ. “Babes-Bolyai”*, 2003, **48**, 11–20.
83. M. V. Diudea, B. Parv, P. E. John, O. Ursu, and A. Graovac, *MATCH, Commun. Math. Comput. Chem.*, 2003, **49**, 23–36.
84. A. J. Stone and D. J. Wales, *Chem. Phys. Lett.*, 1986, **128**, 501–506.
85. M. V. Diudea, *Studia Univ. “Babes-Bolyai”*, 2003, **48**(2), 17–26.
86. V. Schlegel, *Verhandlungen der Kaiserlichen Leopoldinisch-Carolinischen Deutschen Akademie der Naturforscher*, 1893, **44**, 337–459.

87. Diudea, M. V., in: Diudea, M. V., Ed., *Nanostructures-Novel Architecture*, NOVA, N. Y., 2005, pp. 111–126.
88. Stefu, M.; Diudea, M. V., *MATCH Commun. Math. Comput. Chem.*, 2004, **50**, 133–144.
89. H. Hosoya, *J. Math. Chem.*, 1991, **7**, 289–305.
90. M. V. Diudea, *J. Math. Chem.*, 2007 (in press).
91. M. V. Diudea, B. Parv and O. Ursu, TORUS Software Program, Babes-Bolyai University, 2001; available at <http://chem.ubbcluj/~diudea>.
92. S. Cigher and M. V. Diudea, OMEGA COUNTER Software Program, Babes-Bolyai University, 2006; available at <http://chem.ubbcluj/~diudea>.
93. Albertazzi, E., Domene, C., Fowler, P. W., Heine, T., Seifert, G., Van Alsenoy, C. and Zerbetto, F., *Phys. Chem. Chem. Phys.*, 1999, **1**, 2913–2918.
94. M. Dinca, S. Ciger, M. Stefu, F. Gherman, K. Miklos, Cs. L. Nagy, O. Ursu and M. V. Diudea, *Carpath. J. Math.*, 2004, **20**(2), 211–221.
95. R.C. Haddon. *J. Am. Chem. Soc.*, 1987, **109**, 1676–1685.
96. R.C. Haddon. *J. Am. Chem. Soc.*, 1990, **112**, 3385–3389.
97. R.C. Haddon. *J. Am. Chem. Soc.*, 1997, **119**, 1797–1798.
98. P. W. Fowler, D. E. Manolopoulos. *An atlas of fullerenes*, Oxford Univ. Press, Oxford, 1995.
99. Cs. L. Nagy and M. V. Diudea, JSCHM Software Program, Babes-Bolyai University, 2005; available at <http://chem.ubbcluj/~diudea>.

Chapter 5

Operations on Maps

5.1. Introduction

Covering a local planar surface by various polygonal or curved regions is an ancient human activity, nowadays mathematically founded.^{1,2}

Three regular tessellations: (4,4), (6,3) and (3,6), called Platonic, are known back from the Greek and Roman mosaics and fascinated the viewers at all the times.

Lattice transformation is one of the ways in understanding the stability and chemical reactions occurring in nanostructures.³⁻⁵

A map M is a combinatorial representation of a (closed) surface.^{6,7} Several transformations (*i.e.*, operations) on maps are known and used for various purposes.

Let us denote in a map: v – the number of vertices, e – the number of edges, f – the number of faces and d – the vertex degree. A subscript “0” will mark the corresponding parameters in the parent map.

Recall some basic relations in a map:

$$\sum d v_d = 2e \quad (5.1)$$

$$\sum s f_s = 2e \quad (5.2)$$

where v_d and f_s are the number of vertices of degree d and number of s -gonal faces, respectively. The two relations are joined in the famous EULER (1758) formula:⁸

$$v - e + f = \chi(M) = 2(1 - g) \quad (5.3)$$

with χ being the Euler *characteristic* and g the genus⁹ of a graph (*i.e.*, the number of handles attached to the sphere to make it homeomorphic to the surface on which the given graph is embedded; $g = 0$ for a planar graph and 1 for a toroidal graph). Positive/negative χ values indicate positive/negative curvature of a lattice. This formula is useful for checking the consistency of an assumed structure.

5.2. Simple Operations on Maps

5.2.1. Dualization Du

Dualization of a map starts by locating a point in the center of each face. Next, two such points are joined if their corresponding faces share a common edge. It is the (Poincaré) *dual* $Du(M)$. The vertices of $Du(M)$ represent the faces of M and *vice-versa*.⁷ In the transformed map, the following relations exist:

$$Du(M) : \quad v = f_0; \quad e = e_0; \quad f = v_0 \tag{5.4}$$

Dual of the dual returns the original map: $Du(Du(M)) = M$. Tetrahedron is self dual while the other Platonic polyhedra form pairs: $Du(\text{Cube}) = \text{Octahedron}$; $Du(\text{Dodecahedron}) = \text{Icosahedron}$ (see Figure 5-1 for symbols hereafter used). It is also known the Petrie dual.

5.2.2. Medial Me

Medial is achieved by putting new vertices in the middle of the original edges.⁷ Join two vertices if the edges span an angle (and are consecutive within a rotation path around their common vertex in M). Medial is a 4-valent graph and $Me(M) = Me(Du(M))$, as illustrated in Figure 5-2a. The transformed map parameters are:

$$Me(M) : \quad v = e_0; \quad e = 2e_0; \quad f = f_0 + v_0 \tag{5.5}$$

The medial operation rotates parent s -gonal faces by π/s . Points in the medial represent original edges, thus this property can be used for topological analysis of



Figure 5-1. The five Platonic polyhedra.

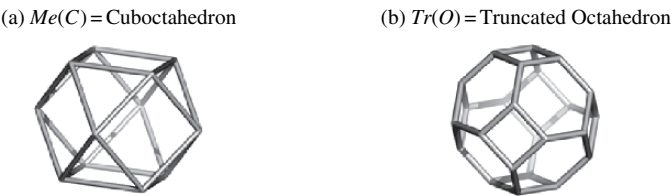


Figure 5-2. Medial and Truncation.

edges in the parent polyhedron. Similarly, the points in dual give information on the topology of parent faces.

5.2.3. Truncation Tr

Truncation is achieved by cutting off the neighborhood of each vertex by a plane close to the vertex, such that it intersects each edge incident to the vertex.⁷ Truncation is similar to the medial, the transformed map parameters being:

$$Tr(M) : \quad v = 2e_0 = d_0v_0; \quad e = 3e_0; \quad f = f_0 + v_0 \quad (5.6)$$

This was the main operation used by Archimedes in building its well-known 13 solids.⁵ Figure 5-2b illustrates a transform by this operation.

5.2.4. Polygonal P_n Capping

Polygonal capping ($n = 3, 4, 5$) of a map is achieved as follows: add a new vertex in the center of each face. Put $n-3$ points on the boundary edges. Connect the central point with one vertex on each edge (the end points included). Thus, the parent face is covered by triangles ($n = 3$), quadrilaterals ($n = 4$) and pentagons ($n = 5$). The P_3 operation is also called *stellation* or *triangulation*. When all the faces of a map are thus operated, it is referred to as an omnicapping P_n operation. The transformed map parameters are:

$$P_n(M) : \quad v = v_0 + (n-3)e_0 + f_0; \quad e = ne_0; \quad f = s_0f_0 \quad (5.7)$$

so that the Euler's relation holds.

Maps transformed by the above operations form dual pairs:

$$Du(P_3(M)) = Le(M) \quad (5.8)$$

$$Du(P_4(M)) = Me(Me(M)) \quad (5.9)$$

$$Du(P_5(M)) = Sn(M) \quad (5.10)$$

Vertex multiplication ratio by this dualization is always:

$$v(Du)/v_0 = d_0 \quad (5.11)$$

Relations (5.8) – (5.10) enable the construction of Archimedean objects, when applied on the Platonic solids.^{5,7} Their duals are known as the objects of Catalan. Relations (5.8) and (5.10) will be detailed below. Eq. 5.11 comes out from: $v(Du) = f(P_n(M)) = s_0f_0 = d_0v_0$ (eqs 5.4 and 5.7). Note that all the operation parameters herein presented refer to regular maps (*i.e.*, having all vertices and faces of the same valence/size). Figure 5-3 gives examples of the P_n operations realization.

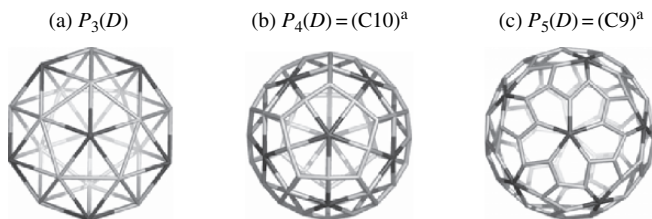


Figure 5-3. Polygonal P_n operations on the Dodecahedron D ; (a) Symbols in the brackets are identical to those used in ref.5 for Catalan objects (*i.e.*, duals of the Archimedean solids); (for other operation names see ref. 11).

5.2.5. Snub Sn

Snub is a composite operation¹⁰ that can be written as:

$$Sn(M) = Dg(Me(Me(M))) = Du(P_5(M)) \quad (5.12)$$

where Dg means the inscribing diagonals in the quadrilaterals resulting⁷ by $Me(Me(M))$. The true dual of the snub is the $P_5(M)$ transform: $Du(Sn(M)) = P_5(M)$. Similar to the medial operation, $Sn(M) = Sn(Du(M))$. In case of $M = T$, the snub $Sn(M) = I$.

Of chemical interest is the easy transformation of the snub (*i.e.*, regular pentavalent graph) into the leapfrog transform (*i.e.*, regular trivalent graph – see below), by deleting the edges of the triangle joining any three parent faces (Figure 5-4, in black). This is particularly true in the snub of trivalent parent maps.

The transformed parameters are derivable from eqs. 5.4, 5.7 and 5.10 (with $n = 5$):

$$Sn(M) : \quad v = s_0 f_0 = d_0 v_0; \quad e = 5e_0; \quad f = v_0 + 2e_0 + f_0 \quad (5.13)$$

The multiplication ratio is $v/v_0 = d_0$, the same as for $Le(M)$, both of them involving the dualization.

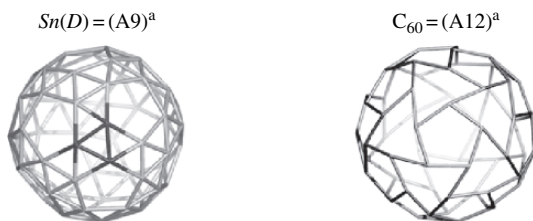


Figure 5-4. Snub of Dodecahedron; ^a Symbols in the brackets are identical to those used in ref.5 for the Archimedean solids. Note the insulated pentagons in C_{60} .

5.3. Composite Operations

5.3.1. Leapfrog Le

Leapfrog (*tripling*) is a composite operation^{12–19} that can be written as:

$$Le(M) = Du(P_3(M)) = Tr(Du(M)) \quad (5.14)$$

A sequence of stellation-dualization rotates the parent s -gonal faces by π/s . Leapfrog operation is illustrated, on a pentagonal face, in Figure 5-5.

A bounding polygon, of size $2d_0$, is formed around each original vertex. In the most frequent cases of 4- and 3-valent maps, the bounding polygon is an octagon and a hexagon, respectively.

If the map is a d_0 regular graph, the following theorem holds:^{17,18}

Theorem 5.1. *The number of vertices in $Le(M)$ is d_0 times larger than in the original map M , irrespective of the tessellation type.*

The demonstration follows from the observation that, for each vertex of M , d_0 new vertices result in $Le(M) : v/v_0 = d_0 v_0/v_0 = d_0$. The same result can be derived from eqs. 5.4, 5.7 and 5.8 (with $n = 3$) or directly from eqs. 5.8 and 5.11. The complete transformed parameters are:

$$Le(M) : \quad v = s_0 f_0 = d_0 v_0; \quad e = 3e_0; \quad f = v_0 + f_0 \quad (5.15)$$

being the same as for $Tr(M)$, eq. 5.6.

Note that in $Le(M)$ the vertex degree is *always* 3, as a consequence of the involved triangulation P_3 . In other words, the dual of a triangulation is a *cubic net*.⁷ It is also true that truncation always provides a trivalent lattice.

A nice example of using Le operation is: $Le(\text{Dodecahedron}) = \text{Fullerene } C_{60}$. The leapfrog operation can be used to insulate the parent faces by surrounding bounding polygons.

A retro-leapfrog¹⁹ RLe operation can be imagined:

$$RLe(M) = RP_3(Du(Le(M))) \quad (5.16)$$

It is performed by cutting all vertices in the dual (of leapfrogged map) with degree lower than the maximal one (Figure 5-6). Hereafter, the letter “ R ” in the front of a map operation name will denote the corresponding retro-operation. As a 3D realization, RLe is illustrated in Figure 5-7.

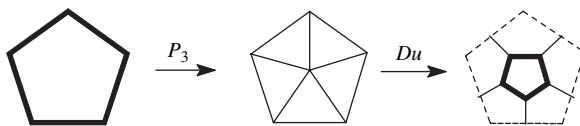


Figure 5-5. The Leapfrog Le operation on a pentagonal face.

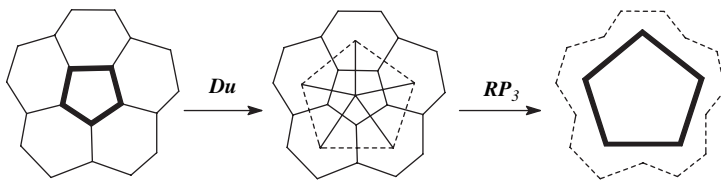


Figure 5-6. The Retro-Leapfrog RLe operation on a pentagonal face.

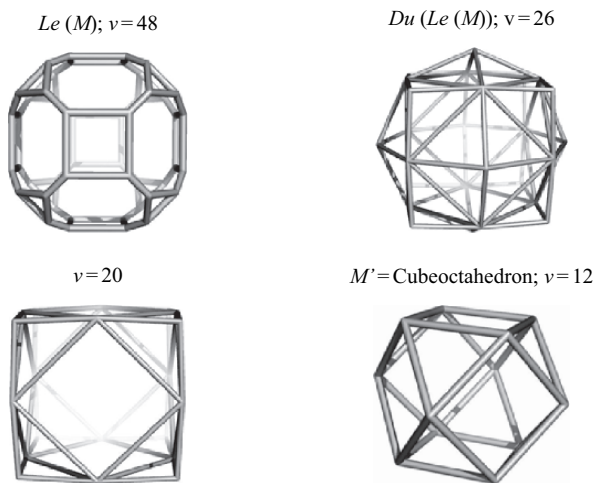


Figure 5-7. The Retro-Leapfrog RLe operation.

5.3.2. Quadrupling Q

Quadrupling (*chamfering*)^{17–20} is another composite operation, achieved by the sequence:

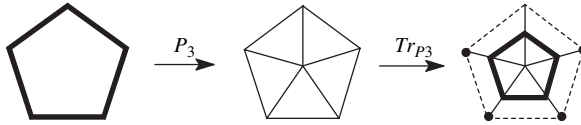
$$Q(M) = RE(Tr_{P_3}(P_3(M))) \quad (5.17)$$

where RE denotes the (old) edge deletion (dashed lines, in Figure 5-8) in the truncation Tr_{P_3} of each central vertex of the P_3 capping. The complete transformed parameters are:

$$Q(M) : \quad v' = (d+1)v; \quad e' = 4e; \quad f' = f + e \quad (5.18)$$

The Q operation leaves unchanged the initial orientation of the polygonal faces.

Theorem 5.2. *The vertex multiplication ratio in a Q transformation is $d_0 + 1$ irrespective of the original map tessellation.*


 Figure 5-8. The Quadrupling Q operation on a pentagonal face.

With the observation that, for each vertex of M , d_0 new vertices appear in $Q(M)$ and the old vertex is preserved, the demonstration is immediate:^{17,18} $v = d_0 v_0 + v_0$; $v/v_0 = d_0 + 1$. The complete transformed parameters are:

$$Q(M) : \quad v = (d_0 + 1)v_0; \quad e = 4e_0; \quad f = f_0 + e_0 \quad (5.19)$$

Q operation involves two π/s rotations, so that the initial orientation of the polygonal faces is preserved. Note that, the quadrupling transform of a 4-valent map is not a regular graph anymore (because of mixing the new trivalent vertices with the parent 4-valent ones). Only $Q(M)$ of a 3-valent map is a 3-regular graph.

Q insulates the parent faces always by hexagons. An example of this operation is: Q (Dodecahedron) = Fullerene C_{80} . It is also called “chamfering” (edge chamfering being equivalent to vertex truncation²⁰).

The retro-quadrupling¹⁹ RQ operation is based on the sequence:

$$RQ(M) = E(RTr_{P_3}(P_3(M))) \quad (5.20)$$

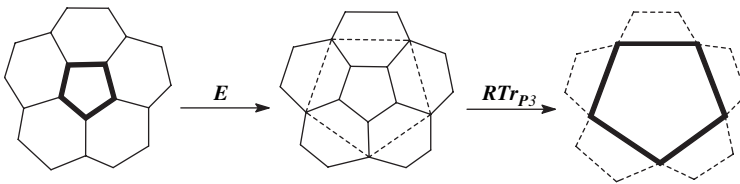
and it is performed by adding new edges parallel to the boundary edges of the parent faces (Figure 5-9) and deletion of these faces. As a 3D realization, RQ is illustrated in Figure 5-10.

5.3.3. Septupling Operations

Two main operations on maps, leading to Platonic tessellations in open lattices, are known: the septupling S_1 and S_2 operations.^{10,19,21,22–25}

The S_1 operation was also called²¹ Capra Ca – the goat, by the Romanian name of the English *leapfrog* children game. It is a composite operation that can be written as a sequence of simple operations:

$$S_1(M) = Tr_{P_5}(P_5(M)) \quad (5.21)$$


 Figure 5-9. The Retro-Quadrupling RQ operation on a pentagonal face.

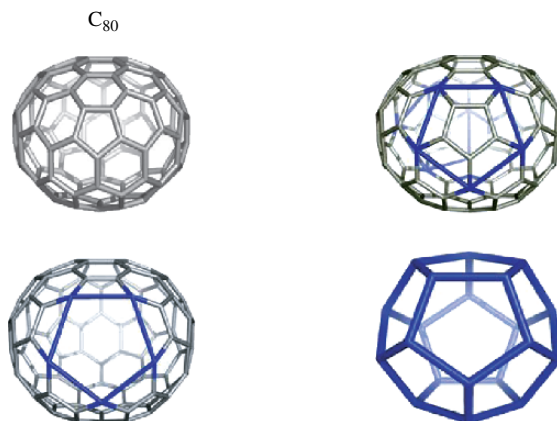


Figure 5-10. The Retro-Quadrupling RQ operation.

with Tr_{P_5} meaning the truncation of new, face centered, vertices introduced by P_5 pentagonal capping, which involves an E_2 (i.e., two new points put on each edge) operation.

The nuclearity of the GOLDBERG (1937) polyhedra²⁰ (related to the fullerenes) is obtained by using the parameter:

$$m = (a^2 + ab + b^2); \quad a \geq b; \quad a + b > 0 \quad (5.22)$$

which is the multiplication factor $m = v/v_0$: in a 3-valent map, $Le((1,1); m = 3; Q((2,0); m = 4$ and $S((2,1); m = 7$. The m factor was used since the ancient Egypt for calculating the volume of truncated pyramid, of height h : $V = mh/3$.

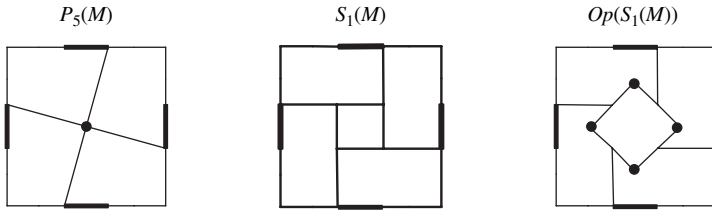
S_1 insulates any face of M by its own hexagons, which are not shared with any old face. It is an intrinsic chiral operation²⁴ (it rotates the parent edges by $\pi/(3/2)s$ and was extensively illustrated in ref. 25. Since pentangulation of a face can be done either clockwise or counter-clockwise, it results in an enantiomeric pair of objects: $S_{1S}(M)$ and $S_{1R}(M)$, with the subscript S and R given in terms of the *sinister/rectus* stereochemical isomery.

S_1 can continue with the *open* operation:

$$Op_k(S_i(M)) \quad (5.23)$$

where k represents the number of points added on the boundary of the parent faces, that become the *open* faces. The resulting open objects have all the polygons of the same $(6+k)$ size. The above operation sequence enables the construction of negatively curved networks. Figure 5-11 gives the steps of S_1 realization on a square face in a trivalent lattice, up to the open structure.

Theorem 5.3. *The vertex multiplication ratio in an S transformation is $2d_0 + 1$ irrespective of the original map tiling.*


 Figure 5-11. Septupling S_1 operation on a square face, up to the open structure.

For demonstration, observe that, for each old vertex, $2d_0$ new vertices (Figure 5-8) appear and the old vertex is preserved in the transformed map. Thus, $v = 2d_0v_0 + v_0$ and $v/v_0 = 2d_0 + 1$.

The S_2 operation^{10,22} is a simpler one (Figure 5-12); it can be achieved by putting four vertices on each edge of the parent map M (E_4 operation) and next join these new vertices in order $(-1, +3)$:

$$S_2 = J_{(-1,+3)}(E_4(M)) \quad (5.24)$$

It insulates the double sized parent faces by pentagons and parent vertices by pentagon d_0 -multiples; the transformed objects are non-chiral ones.

Chirality in S_2 is brought by the Op operation Op_{2a} , achieved by putting two points on alternative edges of the double sized parent face boundary (Figure 5-12).

In case of a closed product, the transformed lattice parameters are identical to those of S_1 (eq. 5.25); differences appear in case of open objects (eqs. 5.26 and 5.27). Note that both the septupling operations keep the parent vertices (see the vertex counting formulas – eq. 5.25).

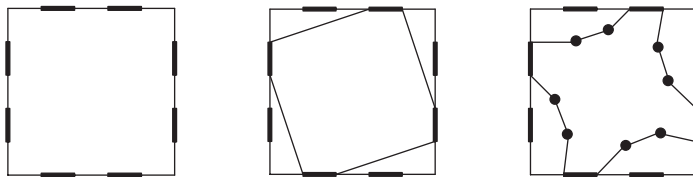
The transformed lattice parameters are shown in the following relations:

$$S_1(M) \& S_2(M) : \quad v = v_0(2d_0 + 1); \quad e = 7e_0; \quad f = f_0(s_0 + 1) \quad (5.25)$$

$$Op(S_1(M)) : \quad v_{Op} = v_0(3d_0 + 1); \quad e_{Op} = 9e_0; \quad f_{Op} = f_0s_0 \quad (5.26)$$

$$Op_{2a}(S_2(M)) : \quad v_{Op} = v_0(4d_0 + 1); \quad e_{Op} = 11e_0; \quad f_{Op} = f_0s_0 \quad (5.27)$$

where d and s are the vertex degree and face size, respectively; the subscript zero refers to the original map M .


 Figure 5-12. Septupling S_2 operation on a square face, up to the open structure.

The iterative n -time operating (on maps with any vertex degree, $d_0 \geq 3$) leads to the following lattice parameters, transformed by both S_1 and S_2 :

$$v_n = v_0 q_n \quad (5.28)$$

$$e_n = e_0 m^n$$

$$f_n = f_0(s_0 p_n + 1)$$

where:

$$q_n = 2d_0 p_n + 1; \quad n \geq 2 \quad (5.29)$$

$$p_n = \sum_{i=0}^{n-1} m^i = (m^n - 1)/(m - 1) = m(m \dots (m + 1) \dots + 1)_{n-2} + 1 \quad (5.30)$$

The parameter m is that defined in relation (5.22). From (5.29), it is obvious that:

$$p_n = (q_n - 1)/2d_0 \quad (5.31)$$

For trivalent maps (*i.e.*, those with $d_0 = 3$), the above parameters become:

$$q_n = m^n \quad (5.32)$$

$$p_n = (m^n - 1)/6 \quad (5.33)$$

$$v_n = v_0 m^n \quad (5.34)$$

$$e_n = e_0 m^n$$

$$f_n = f_0(s_0(m^n - 1)/6 + 1)$$

For S_1 and S_2 the transformed lattice parameters will be:

$$v_n = 7^n v_0; \quad e_n = 7^n e_0; \quad f_n = f_0(s_0(7^n - 1)/6 + 1) \quad (5.35)$$

In case of a cage opening after the n^{th} iteration, the lattice parameters are as follows:

$$v_{n,Op}(S_1) = v_0 q_n + f_0 s_0 = v_0(d_0 + q_n) \quad (5.36)$$

$$e_{n,Op}(S_1) = e_0 m^n + f_0 s_0 = e_0(m^n + 2)$$

$$f_{n,Op}(S_1) = f_0(s_0 p_n + 1) - f_0 = f_0 s_0 p_n$$

$$v_{n,Op_{2a}}(S_2) = v_0 q_n + 2f_0 s_0 = v_0(2d_0 + q_n) \quad (5.37)$$

$$e_{n,Op_{2a}}(S_2) = e_0 m^n + 2f_0 s_0 = e_0(m^n + 4)$$

$$f_{n,Op_{2a}}(S_2) = f_0(s_0 p_n + 1) - f_0 = f_0 s_0 p_n$$

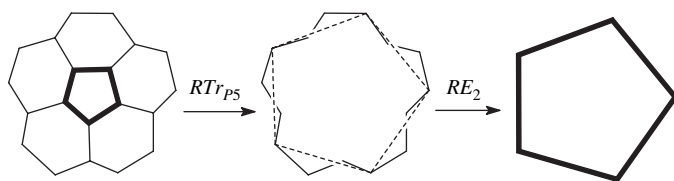


Figure 5-13. The Retro-Capra RCa operation on a pentagonal face.

The two septupling operations represent twin operations in that, the transformed objects, representing repeat units in D-, FRD- and P-type negatively curved surfaces, belong to the complementary labyrinths (see Chapter 7).

Retro-capra RCa operation is achieved by the sequence:

$$RCa(M) = RE_2(RTr_{P_5}(M)) \quad (5.38)$$

In words, delete the smallest faces of the actual map and continue with RE_2 (Figure 5-13).

As a 3D realization, RCa is illustrated in Figure 5-14.

Denote by F a fullerene and its retro operation by $R\Omega(F) = F'$. The question is: exists such an F' cage? The answer is no, in case the retro-operation will produce an irregular graph, eventually having dangling bonds. Some other information, like those comprised in eqs. (5.15), (5.19) and (5.25) will be helpful in getting the answer to the above question.

In case of a negative answer, no specific properties, derived from the above operations (see the next section), could be assigned to F . Let consider, for example, the fullerenes C_{80} : 80:1, D_{5d} and 80:6, D_{5h} in the Atlas of Fullerenes.²⁶ The first one is the quadrupling of C_{20} while the other is not. The molecule with the symmetry D_{5d} will preserve the character of the orbitals in C_{20} (the degeneracy of the orbitals HOMO, LUMO, LUMO+1, LUMO+2) which is not the case of that with the symmetry D_{5h} . The three discussed operations preserve, at least in part, the

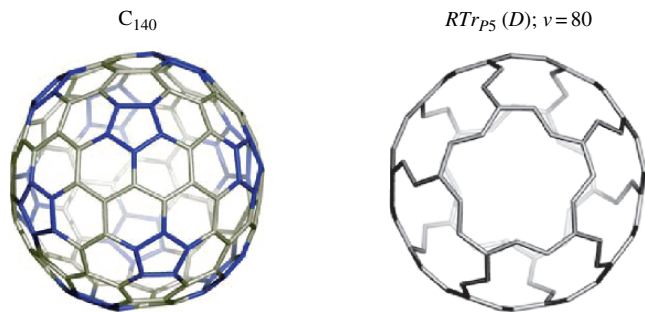


Figure 5-14. The Retro-Capra RCa operation.

symmetry of the parent structures, so that the knowledge on the operations involved in construction of a fullerene is useful in structure elucidation studies.²⁴

5.3.4. Molecular Realization of Septupling Operations

Examples for the molecular realization of septupling operations are given here only for closed objects. Involvement of these operations in building infinite lattices of negative curvature will be presented in Chapter 7.

As above mentioned, S_1 rotates the parent bonds, so that it provides chiral transforms. The iterative application of S_1 may lead to either chiral/twisted or non-chiral/non-twisted transforms: for example, the sequence $S_{1S}(S_{1S}(M))$ results in a twisted structure while $S_{1R}(S_{1S}(M))$ provides a non-twisted object (Figure 5-15).

When applied on fullerenes, S_1 leads to chiral structures. In this respect, C_{140} is the only fullerene with a Platonic covering (a single size of equivalent faces) of the form: $(([5]\text{Cor})_3)$, where $[5]\text{Cor}$ is the $[5]\text{corannulenic}$ supra-face²² (Figure 5-14). In other fullerenes, S_1 provides Archimedean coverings $(([5]\text{Cor}, [6]\text{Cor})_3)$.

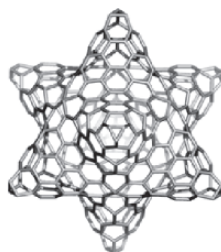
Applied on polyhex toroidal objects, S_1 provides the Platonic $(([6]\text{Cor})_3)$ covering (Figure 5-16).

In the opposite, S_2 applied to closed cages, leads to *non-twisted* objects. Its iterative application reveals the fractal fashion of the covering (Figure 5-17). The

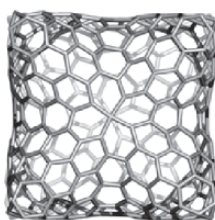
$S_{1S}(S_{1S}(O)); v=390$ (side)



$S_{1R}(S_{1S}(O)); v=390$ (side)



$S_{1S}(S_{1S}(O))$ (top)



$S_{1R}(S_{1S}(O))$ (top)

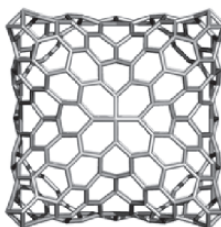


Figure 5-15. Sequence of S_1 pro-chiral operations on Octahedron: S_{1S}, S_{1S} transform is still twisted while S_{1R}, S_{1S} one is no more chiral.

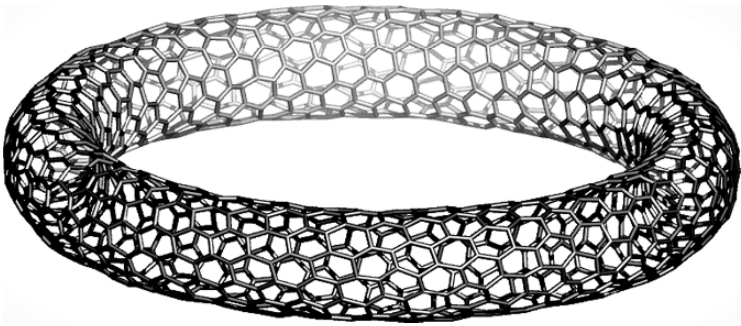
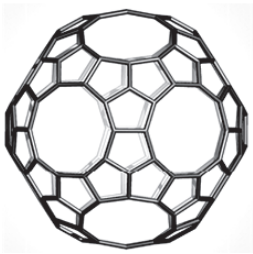


Figure 5-16. A chiral toroidal structure with the Platonic covering $(([6]\text{Cor})3)$.

(a) $S_2(D)$; I ; $v = 140$ (two-fold axis)



(b) $(S_2)^3(D)$; I ; $v = 6860$ (five-fold axis)

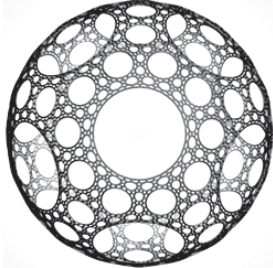


Figure 5-17. Iterative S_2 operation on Dodecahedron: observe the fractal covering in case of 3-time repetition (b).

$S_2(H[8,24]); v = 1344$

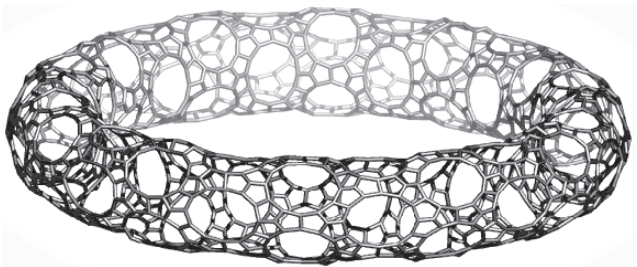


Figure 5-18. A toroidal lattice having Archimedean covering $((5,12)3) = S_2(6,3)$, with local signature $(3,0)$.

fractal characteristic^{22,27,28} can be seen even in the algebraic form of p_n parameter (eq. 5.30).

The only fullerene constructible by S_2 is C_{28} , when applied on the Tetrahedron. Applied on toroidal objects, S_2 leads to an Archimedean covering (Figure 5-18).

All the above closed objects show a positive curvature (*i.e.*, they have $\chi \geq 0$ – see eq. 5.3).

5.4. Generalized Operations

Recently, Peter E. John^{29,30} has proposed a generalization of operations on maps, inspired from the work of Goldberg,²⁰ and its representation of polyhedra in the (a, b) “inclined coordinates” (60° between axes). The multiplicity factor m for trivalent maps is given by eq. (5.22).

Figures 5-19 and 5-20 illustrate the method on the hexagonal face. The points of the “master” hexagon must lie either in the center of a lattice hexagon or on a

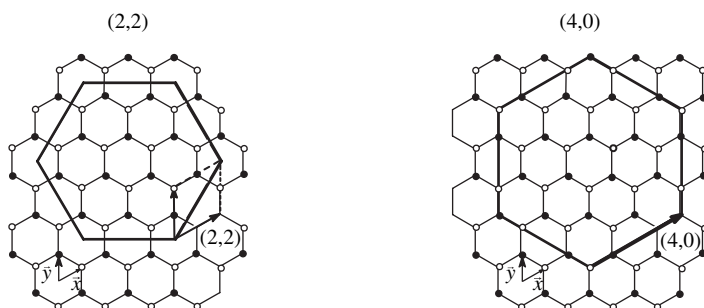


Figure 5-19. Generalized (a, a) and $(a, 0)$ operations.

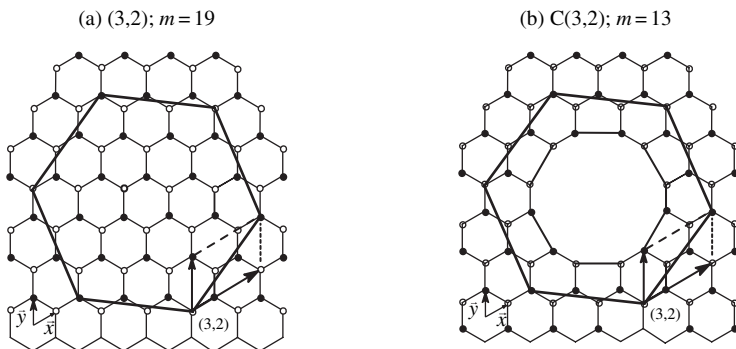


Figure 5-20. Generalized (a, b) operation: $a = b + 1$ (5a) and (central face and first connected atoms) “cut” $C(a, b)$ (5b), the last one corresponding to $m(3,1)=13$ factor.

Table 5-1. Inclined coordinates (a, b) , multiplication factor $m = (a^2 + ab + b^2)$, number of atoms v and operation symbols (running on Dodecahedron, C_{20})

	(a, b)	m	v	Operation	Obs.
1	(1, 0)	1	20	I	Identity
2	(1, 1)	3	60	$Le_{1,1}$	Rotated by π/s ; achiral
3	(2, 0)	4	80	$Q_{2,0}$	Non-rotated; achiral
4	(2, 1)	7	140	$Ca_{2,1}$	Rotated by $\pi/(3/2)s$; chiral
5	(2, 2)	12	240	$Le_{1,1}, Q_{2,0}$	Rotated by π/s ; achiral
6	(3, 0)	9	180	$Le_{1,1}, Le_{1,1}$	Non-rotated; achiral
7	(3, 1)	13	260	–	Rotated; chiral
8	(3, 2)	19	380	–	Rotated; chiral
8*	(3, 2) _c *	13	260	–	Rotated; chiral
9	(3, 3)	27	540	$Le_{1,1}, Le_{1,1}, Le_{1,1}$	Rotated by π/s ; achiral
10	(4, 0)	16	320	$Q_{2,0}, Q_{2,0}$	Non-rotated; achiral
11	(4, 1)	21	420	$Le_{1,1}, Ca_{2,1}$	Rotated; chiral**
12	(4, 2)	28	560	$Q_{2,0}, Ca_{2,1}$	Rotated by $\pi/2s$; chiral
13	(4, 3)	37	740	–	Rotated; chiral
14	(4, 4)	48	960	$Le_{1,1}, Q_{2,0}, Q_{2,0}$	Rotated by π/s ; achiral
15	(5, 0)	25	500	–	Non-rotated; achiral
16	(5, 1)	31	620	–	Rotated; chiral
17	(5, 2)	39	780	–	Rotated; chiral
18	(5, 3)	49	980	$Ca_{2,1}, Ca_{2,1}$	Chiral/achiral**
19	(5, 4)	61	1220	–	Rotated; chiral
20	(5, 5)	75	1500	–	Rotated; achiral

* c = cut; ** achiral, when the sequence $CaR(CaS(M))$ is used.

lattice vertex, so that in the center of the parent hexagon must be a new hexagon. The edge length of the parent hexagon is counted by the primitive lattice vectors (x, y) .

A similar procedure was used by Coxeter,³¹ who built up icosahedral polyhedra/fullerenes as dual master triangular patches, represented by pairs of integers.

For the (3,2) Cut operation – Figure 5-20b, the central face and first connected atoms were cut off.

Some of the generalized composite operations, corresponding to non-prime m , can be expressed as sequences of operations, as shown in Table 5-1. It is obvious that (a, a) also noted $Le_{a,a}$ and $(a,0)$ or $Q_{a,0}$ operations provide achiral transforms (e.g., fullerenes of the full I_h point group symmetry) while (a, b) , $a \neq b$, (also noted Ca_{ab}) result in chiral transformed maps (e.g., fullerenes of the rotational I point group symmetry).²⁴ The $(a,0)$ operations produce non-rotated maps. The above generalized operations, as implemented in the software package CageVersatile,³² work on any face and any vertex-degree maps.

In case of a trivalent regular map, relations (5.1) and (5.2) can be rewritten as:

$$3 \cdot v_0 = 2 \cdot e_0 = s_0 \cdot f_0$$

(5.39)

Keeping in mind the multiplication factor m (see (5.22)), the number of vertices in the transformed map is:

$$v = m \cdot v_0 \quad (5.40)$$

Eq. 5.39 leads to:

$$3 \cdot v = 3 \cdot m \cdot v_0 = 2 \cdot e \quad (5.41)$$

$$e = \frac{3}{2} \cdot m \cdot v_0 = \frac{3}{2} \cdot m \cdot \frac{2}{3} e_0 = m \cdot e_0 \quad (5.42)$$

The above operations introduce new hexagons, keeping the original faces. Thus, the number of faces of any size s in M is:

$$f_s = f_6 + f_0 \quad (5.43)$$

Relation (5.39) becomes:

$$2 \cdot e = \sum s \cdot f_s = 6 \cdot f_6 + s_0 \cdot f_0 \quad (5.44)$$

Substitution of e from (5.42-13) in (5.44-15) leads to:

$$f_6 = \frac{m-1}{6} \cdot s_0 \cdot f_0 \quad (5.45)$$

$$f_s = \frac{m-1}{6} \cdot s_0 \cdot f_0 + f_0 \quad (5.46)$$

In the case of n -iterative operations, eqs. 5.34 hold for all the presented operations running on a trivalent regular M_0 . The above relations are particularly true for the 3-valent Platonic solids: tetrahedron T , cube C and dodecahedron D .

For maps of different degree, some relations were above presented (in the case of Le , Q and Ca).

Figure 5-21 gives an example of molecular realization of a chiral generalized operation.

Sequences of operations or special single generalized operations, leading to corazulenic supra-coverings, have been created at the TOPO group Cluj (see Chapter 6.2).

5.5. Isomerization Routes on Tubular Nanostructures

A particular case of map operations, allowing only changes of connectivity, is the popular edge flipping, patterned by Stone and Wales.³³ Rotating a selected edge enlarges the size/folding of joint polygonal faces concomitant with reduction in size

of the previously shared faces (Figure 5-22). A corresponding transformation was found to occur in real fullerene molecules (a rearrangement reaction) and further gained a Quantum Chemical support.^{34,35} Routes of isomerization, by Stone-Wales SW operation, of the polyhex nanotubes have been proposed^{10,25,36} and will be presented in the following.

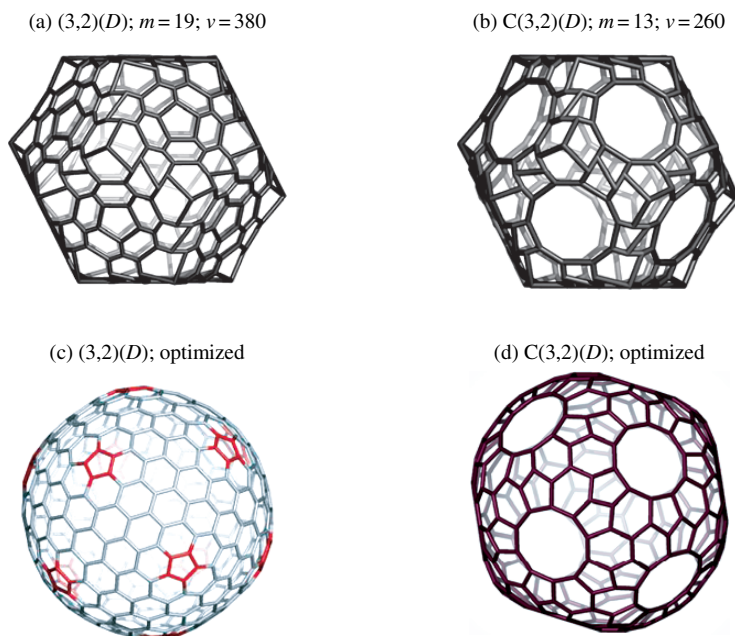


Figure 5-21. The generalized $(3,2)$ and $C(3,2)$ operations performed on the Dodecahedron.

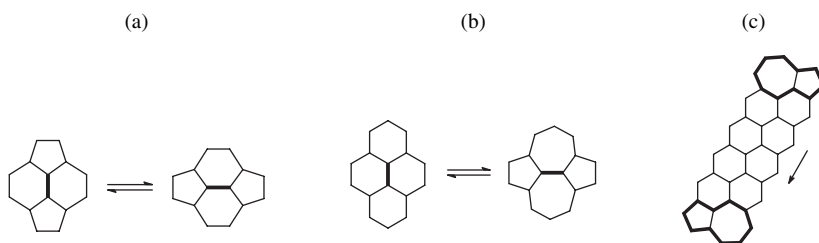


Figure 5-22. The Stone-Wales SW rearrangement, as local (a and b) or long-range transformation (c – the glide direction indicated by the arrow).

5.5.1. Isomerizations on (6,3) Net

Let the (6,3) net be embedded in the cylinder, as (6,3)H/Z or (6,3)V/A (Figure 5-23 a,b) and let denote by $H_{(i,j),(p,r)}$ the edges lying horizontal (*i.e.*, parallel to the horizontally oriented tube generator) in a schematic lattice representation. The first subscript bracket encodes the relative location of the start-point of rotating edges along the tube while the second one the location of edges around the tube. Mark $V_{(i,j),(p,r)}$ the edges lying vertical (*i.e.*, perpendicular to the tube generator). The marked edges will be rotated by the SW isomerization and the above symbols play the role of a true *rotational operator*.

The hexagonal (6,3) covering is transformed into the “rhomboidal-bathroom-floor” tiling³⁷ R((4, 8)3) (Figure 5-23c) by operations:

$$H_{(1,3),(1,3)}((6,3)H) = ((4,8)3)R = V_{(1,3),(1,3)}((6,3)V) \quad (5.47)$$

When edge rotation follows a spiral path, like that illustrated in Figure 5-24, the covering is, after optimization by an MM procedure, a “square-bathroom-floor” ((4,8)3)S lattice.³⁶

The operation can be written as:

$$V_{(1,5),(1,5)}((6,3)H) = ((4,8)3)S \quad (5.48)$$

Similarly, the operation:

$$V_{(1,5),(1,5),1a}((6,3)H) = ((5,7)3)SP \quad (5.49)$$

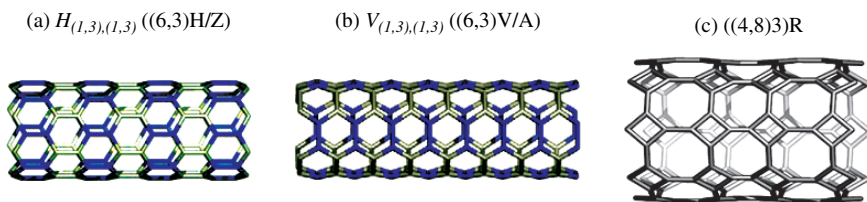


Figure 5-23. Zig-zag (6,3)H/Z and armchair (6,3)V/A nanotubes and the SW lattice resulted by rotating the marked bonds.

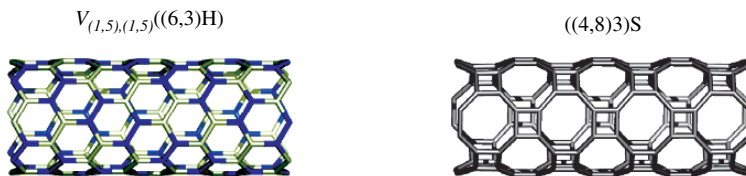


Figure 5-24. A spiral path of SW edge rotation and its transform.

provides a spiral $((5,7)3)$ SP net,³⁸ Figure 5-25. Note the combination V & H , for describing a spiral path and the subscript $1a$ for a “leave one row/column out” way in getting an “alternating” spiral net.

The same operation can be done on the $(6,3)V$ net, thus resulting the pair embedding isomers.

Different pentaheptite $((5,7)3)$ lattices⁴ can be obtained by the following operations:

$$H_{(1,5),(1,5)}((6,3)H) = ((5,7)3)V \quad (5.50)$$

$$V_{(1,5),(1,5)}((6,3)V) = ((5,7)3)H \quad (5.51)$$

These coverings will be illustrated in the next section.

5.5.2. Isomerizations on $((4,8)3)$ Net

The $((4,8)3)$ covering, particularly $((4,8)3)R$, transforms to either $(6,3)V$ or $(6,3)H$ net by operations:

$$H_{(1,4),(1,4)}(((4,8)3)R) = (6,3)V \quad (5.52)$$

$$V_{(1,4),(1,4)}(((4,8)3)R) = (6,3)H \quad (5.53)$$

as a unique intermediate in the isomerization of the $(6,3)$ net. Other isomerizations of this covering are rationalized by eqs. (5.54 and 5.55) and illustrated in Figures 5-26 and 5-27.

$$H_{(1,7),(1,7)}(((4,8)3)R) = ((5,7)3)H \quad (5.54)$$

$$V_{(1,7),(1,7)}(((4,8)3)R) = ((5,7)3)V \quad (5.55)$$

The pentaheptite $H/V((5,7)3)$ lattice is encountered³⁹ in the chemical net of ThMoB_4 . It is a *2-isohedral* tiling² (*i.e.*, it has only two face orbits), with the local signature $(t_5, t_7) = (1, 3)$. Crespi *et al.*⁴⁰ (1996) stated that such nanotubes would show metallic behavior. This statement appears quite strange, since these

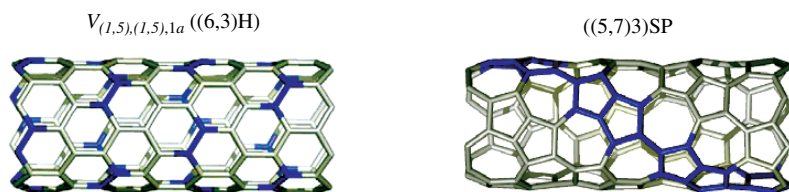


Figure 5-25. A spiral path of SW edge rotation and its spiral net product.

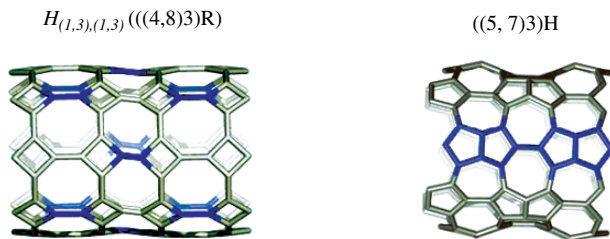


Figure 5-26. SW isomerization of $((4,8)3)R$ to $((5,7)3)H$ lattice.

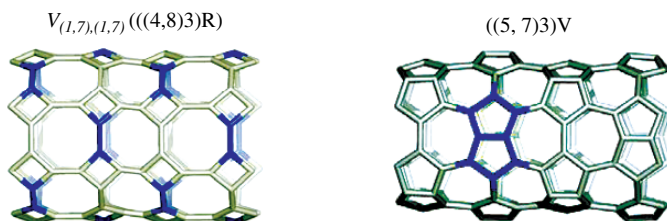


Figure 5-27. SW isomerization of $((4,8)3)R$ to $((5,7)3)V$ lattice.

pentaheptite nets can be termed *fully-pentalenoid* (well-known as an anti-aromatic unit) rather than fully-azulenoid, according to Kirby.⁴¹

Other combinations of SW rotation, on $((4,8)3)R$, are as follows:

$$V_{(1,3),(1,6)}(H_{(1,4),(1,7)}(((4,8)3)R) = ((5,7)3)HA \quad (5.56)$$

$$H_{(1,6),(1,3)}(V_{(1,7),(1,4)}(((4,8)3)R) = ((5,7)3)VA \quad (5.57)$$

The resulting net is a *2-isohedral* tiling with a $(2,4)$ signature. It is a periodic (*i.e.*, face-regular) covering, described as a capped tubulene.⁴² An example is given in Figure 5-28.

Other isomerizations are derivable from the two above ones:

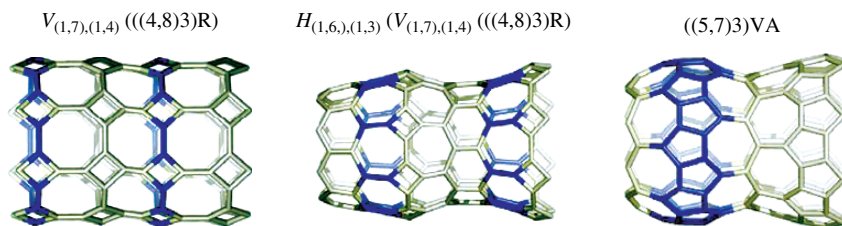
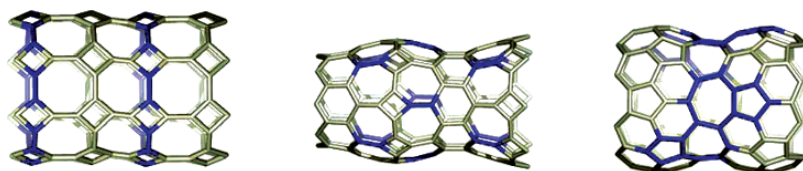
$$H_{(1,6),(1,5)}(V_{(1,7),(1,4)}(((4,8)3)R) = ((5,6,7)3)HA \quad (5.58)$$

$$V_{(1,5),(1,6)}(H_{(1,4),(1,7)}(((4,8)3)R) = ((5,6,7)3)VA \quad (5.59)$$

and the operation is illustrated in Figure 5-29. This novel lattice has the local signature: $t_{5j}(0, 4, 1)$; $t_{6j}(2, 2, 2)$; and $t_{7j}(1, 4, 2)$, $j = 5, 6, 7$.

In the VA embedding, $((5,6,7)3)$ covering is deducible from C_{60} by cutting off two hexagonal parallel rings. It was also described as a capped tubulene.⁴²

Note that the $((4,8)3)$ lattices are deducible from the square $(4,4)$ covering, by some basic operations on maps. The above SW edge rotations have been performed by the CageVersatile 1.1 original program.³²

Figure 5-28. The pathway to $((5,7)3)VA$ latticeFigure 5-29. The pathway to $((5,6,7)3)VA$ lattice.

Conclusions

Various covering lattices, encountered in spherical and tubular nanostructures, can be achieved, mainly by operations on maps, by cutting procedures or by Stone-Wales SW edge rotations. The most versatile and deeply involved in the electronic structure of nano-molecules are the geometrical-topological operations on maps.

In addition to the classical simple operations, like dualization and truncation, the first three operations in the list of Goldberg, leapfrog/tripling, chamfering/quadrupling and capra/septupling, play a central role in modelling nanostructures. The other operations, called here generalized operations, can be considered (at least those of non-prime multiplication factor) combinations of the three above operations. Some sequences of operations provide corazulenic supra-coverings.

Cutting procedures have been developed with the aim of generating large sized tubular and toroidal objects, associated to nanostructures. Stone-Wales edge rotations enable covering changes in both spherical and tubular objects. Several new coverings and routes of possible isomerization reactions have been presented.

References

1. B. Grünbaum, G. C. Shephard, *Tilings and Patterns*, Freeman, New York, 1985.
2. B. Grünbaum, H. D. Löckenhoff, G. C. Shephard, A. Temesvari, *Geom. Dedicata*, 1985, **19**, 109–174.
3. D. J. Klein, H. Zhu, in: *From Chemical Topology to Three – Dimensional Geometry*, A. T. Balaban (Ed.), Plenum Press, New York, 1997, pp. 297–341.
4. M. Deza, P. W. Fowler, M. Shtorgin, K. Vietze, *J. Chem. Inf. Comput. Sci.*, 2000, **40**, 1325–1332.

5. B. de La Vaissière, P. W. Fowler, M. Deza, *J. Chem. Inf. Comput. Sci.*, 2001, **41**, 376–86.
6. P. W. Fowler, T. Pisanski, *J. Chem. Soc. Faraday Trans.*, 1994, **90**, 2865–2871.
7. T. Pisanski, M. Randić, in: *Geometry at Work*, C. A. Gorini (Ed.) M. A. A. Notes, 2000, **53**, 174–194.
8. L. Euler, *Novi Comment. Acad. Sci.I. Petropolitanae*, 1758, **4**, 109–160.
9. F. Harary, *Graph Theory*, Addison-Wesley, Reading, MA, 1969.
10. M. V. Diudea, *Forma* (Tokyo), 2004, **19**(3), 131–163.
11. G. W. Hart, 2004, www.georgehart.com.
12. V. Eberhard, *Zur Morphologie der Polyeder*, Leipzig, Teubner, 1891.
13. P. W. Fowler, *Chem. Phys. Lett.*, 1986, **131**, 444–450.
14. P. W. Fowler and J. I. Steer, *J. Chem. Soc., Chem. Commun.*, 1987, 1403–1405.
15. P. W. Fowler, K. M. Rogers, *J. Chem. Soc., Faraday Trans.*, 1998, **94**, 1019–1027.
16. P. W. Fowler, P. W., K. M. Rogers, *J. Chem. Soc., Faraday Trans.*, 1998, **94**, 2509–2514.
17. M. V. Diudea, P. E. John, *MATCH, Commun. Math. Comput. Chem.*, 2001, **44**, 103–116.
18. M. V. Diudea, P. E. John, A. Graovac, M. Primorac, T. Pisanski, *Croat. Chem. Acta*, 2003, **76**, 153–159.
19. A. E. Vizitiu, M. V. Diudea, S. Nikolić, D. Janežič, *J. Chem. Inf. Model*, 2006, **46**, 2574–2578.
20. M. Goldberg, *Tôhoku Math. J.*, 1937, **43**, 104–108.
21. M. V. Diudea, *Studia Univ. “Babes-Bolyai”*, 2003, **48**(2), 3–16.
22. M. V. Diudea, *J. Chem. Inf. Model*, 2005, **45**, 1002–1009.
23. R. B. King, M. V. Diudea, *J. Math. Chem.*, 2005, **38**(4), 425–435.
24. R. B. King, M. V. Diudea, *J. Math. Chem.*, 2006, **39**, 597–604.
25. M. V. Diudea, in: M. V. Diudea, (Ed.), *Nanostructures-Novel Architecture*, NOVA, New York, 2005, 203–242.
26. P. W. Fowler, D. E. Manolopolous, *An atlas of fullerenes*, Oxford University Press, London, 1994, pp. 254, 255.
27. S. El-Basil, *Croat. Chem. Acta*, 1996, **69**, 1117–1148.
28. D. J. Klein, T. P. Živković, A. T. P. Balaban, *MATCH, Commun. Math. Comput. Chem.*, 1993, **29**, 107–130.
29. M. Stefu, M. V. Diudea, P. E. John, *Studia Univ. “Babes-Bolyai”*, 2005, **50**(2), 165–174.
30. M. V. Diudea, M. Stefu, P. E. John, A. Graovac, *Croat. Chem. Acta*, 2006, **79**, 355–362.
31. H. S. M. Coxeter, *Regular polytopes*, 3rd edn., Dover Pubs, Dover, 1973.
32. M. Stefu, M. V. Diudea, CageVersatile “Babes-Bolyai” University, Cluj, Romania, 2005.
33. A. J. Stone, D. J. Wales, *Chem. Phys. Lett.*, 1986, **128**, 501–503.
34. H. F. Bettinger, B. I. Yakobson, G. E. Scuseria, *J. Amer. Chem. Soc.*, 2003, **125**, 5572–5580.
35. Ge. G. Samsonidze, G. G. Samsonidze, B. I. Yakobson, *Comput. Mater. Sci.*, 2002, **23**, 67–72.
36. M. V. Diudea, *Studia Univ. “Babes-Bolyai”*, 2003, **48**(2), 17–26.
37. M. Stefu, M. V. Diudea, *MATCH, Commun. Math. Comput. Chem.*, 2004, **50**, 133–144.
38. M. V. Diudea, B. Parv, E. C. Kirby, *MATCH, Commun. Math. Comput. Chem.*, 2003, **47**, 53–70.
39. M. O’Keeffe, B. G. Hyde, *Crystal Structures*, Mineralogical Society of America, Washington DC, 1996.
40. V. H. Crespi, L. X. Benedict, M. L. Cohen, S. G. Louie, *Phys. Rev. B*, 1996, **53**, R13303–R13305.
41. E. C. Kirby, in: *Nanostructures-Novel Architecture*, M. V. Diudea, (Ed.), NOVA, New York, 2005, 175–191.
42. M. V. Diudea, Cs. L. Nagy, I. Silaghi-Dumitrescu, A. Graovac, D. Janežič, D. Vikić-Topić, *J. Chem. Inf. Model.*, 2005, **45**, 293–299.

Chapter 6

Aromaticity of Nanostructures

6.1. Introduction

Modeling nanostructures, scientist often used the embedding of a polygonal lattice in a given 3D surface S . Such a “combinatorial” surface is called¹ a map M . Analytical formulas, for generating a smooth surface, can be found in Mathematical recipes, available on internet. The coordinates of the lattice points are obtained by partitioning S , either by dedicated algorithms or by simply drawing vertices and edges on display, with the aid of some builders to switch from 2D to 3D. Another way uses templates, or unit blocks with a prescribed spatial arrangement. This last technique is also used (or naturally happens) in self assembling reactions, in experiments (or occurring *in vivo*).

The covering of a map can be transformed by several geometrical-topological operations, like the popular Stone-Wales edge flipping² or the operations on maps, detailed in Chapter 5. These operations have been proposed for rationalizing^{3,4} the transformations observed in nanostructures, in relation structure-stability^{5,6} or even in their growth mechanisms.^{7–10}

Recall that an *embedding* is the representation of a graph on a surface such that no crossing lines appear;^{11,12} the *genus* is the number of handles attached to the (or holes performed in a) sphere to make it homeomorphic to S .

A polyhedral cage obeys the Euler theorem:¹³

$$v - e + f = \chi(S) = 2(1 - g) \quad (6.1)$$

where $\chi(S)$ is the Euler characteristic, v , e , f , and g being the number of vertices, edges, faces, and genus, respectively.

The composite operations and some generalized map operations¹⁴ obey the truncated pyramid volume formula in calculating the nuclearity, in a 3-valent transformed map:

$$m = (a^2 + ab + b^2); a \geq b; a + b > 0 \quad (6.2)$$

with m being the multiplication factor ($m = v/v_0$) by a given operation. Thus, Le is: (1,1); $m = 3$; Q is: (2,0); $m = 4$ and Ca/S_1 corresponds to (2,1); $m = 7$.

Sequences of map operations are usually commutative, e.g., $Le(Q(M)) = Q(Le(M))$, irrespective of the vertex degree of M or its subsequent regular/irregular character. Some others are non-commutative, as will be shown below. All the operations on maps were performed by the CageVersatile¹⁵ software package, which works on any face, any vertex-degree maps and any type of surface.

6.2. Aromaticity of Nanostructures

The aromatic character is a multi-conditional molecular property, including energetics, electronic structure, magnetic response, geometric characteristics or chemical behaviour.^{16–18} Consequently, various orderings are expected in sets of molecules with respect to different aromaticity criteria.

An *energetic criterion* of aromaticity would say: more aromatic character, more stable structures.^{17,18} Despite the resonance energy^{19–21} play an important role in the stability of (at least) planar polyhex structures, the strain appearing in fullerenes, nanotubes, etc., will decide the overall stability (and reactivity) of such molecules. Data on the molecules discussed within this chapter are given immediately after their structure is presented. Tables include values of the heat of formation HF and HOMO-LUMO Gap (PM3 data) along with the strain energy, in terms of POAV1 theory.^{22–25} The π -energy per electron of these cages (in β units, in the simple Hückel approximation) is also included in the following tables. It parallels TRE²⁰ and appears to be larger for corannulenic closed-shell²⁶ cages than for corazulenic ones (see below).

An *electronic criterion* requires π -electron delocalization¹⁸ (and bond length equalization). However, aromaticity is a local property, in the sense that small benzenic or naphthalenic units, rather than larger circuits, firmly manifest in chemical reactions. The π -electron distribution is presented in terms of the *numerical Kekulé valence structure* representation:^{27–34} each double bond in a geometrical Kekulé structure gets the number 2 for the two π -electrons of the double bond; if the double bond is shared by two rings it gets only the number 1. Thus, the local flower covering can be described by the π -electron content. In contrast to the *geometrical* Kekulé structures, the numerical Kekulé structures enable construction of a single numerical structure to account for the superposition of the geometrical Kekulé structures as in the Clar representation^{35,36} (see below).

With regard to stability, a higher Kekulé structure count K is associated with a higher stability.^{18,37} There are, however, 20 C_{60} isomers with $K > 12,500$ (the K -value of Buckminsterfullerene C_{60}) although they are less stable (non-spherical, non-IPR, strained isomers).^{38–40} As above mentioned, strain in the σ -frame is an important energetic factor, particularly in non-planar molecules, where it may revert the expected ordering. Thus, in toroidal polyhexes, the thin-tubed tori, with the highest strain, have the largest K value.⁴¹ It appears that that K alone is not a reliable guess of energetically favorable structure. The conjugated circuits count has been proved to be more reliable.^{18–44}

A *magnetic criterion* would infer π -electron delocalization, with direct consequences on the magnetic properties, as reflected in the diamagnetic susceptibility and NMR chemical shifts. These effects can be rationalized in terms of ring currents induced by the external field. Ring-current effects have long been recognized as important indicators for aromaticity.¹⁸ Depending on the number of π -electrons, diatropic or paratropic ring currents may occur.

In fullerenes, enhanced aromaticity, as assessed by the magnetic criterion, does not necessarily imply additional stabilization. The considerable strain of the σ -frame can dominate the stability and reactivity.¹⁷

A *structural/geometric criterion* of aromaticity would predict for C_{60} a pronounced bond-length alternation between [6,6]- and [5,6]-bonds.^{17,18} Experimental data have also shown that, in neutral fullerenes, the bonds shared by two hexagons (*i.e.*, [6,6]-bonds) are shorter than the pentagon-hexagon bonds (*i.e.*, [5,6]-bonds).^{45,46} The bond-length alternation implies cyclohexatriene and $[n]$ radialene substructures, which is strongly supported by the regio-selectivity of addition reactions.¹⁷

Based to the geometric criterion, an index of aromaticity, called HOMA (harmonic oscillator model of aromaticity)^{47–51} was derived on the difference between the actual CC and the CC equalized bond lengths. The data in the following tables are calculated⁵² cf. ref.⁵¹. Within a single polycyclic conjugated structure, different rings normally show different local aromaticity,⁵³ which can be accounted for by the HOMA values (ranging from 1 for benzene to about zero for non-aromatic and negative values for anti-aromatic molecules).

Clearly, the aromaticity is a multi-dimensional phenomenon.^{54,55} Even so, the structural features of molecules have to prevail, in the aromaticity assessment, over the observable properties, as Kekulé himself has stressed in the early days of this theory.¹⁸

Also clear is that fullerenes are far from the “super-aromatic” dream of researchers, they approaching rather a “super-alkenic” character,³⁸ with the additions the most favored reactions. The electron deficiency of these molecules arises from the presence of 12 pentagons, instead of hexagons, in the sheet of graphite, needed to close a cage. Nanotubes are even less reactive, due to the low pyramidalization of the sp^2 carbon atoms. Attempts to predict the aromaticity of nanotubes of nanotori have been done^{56–58} (see also Chapter 2).

6.3. Corannulenic Cages

A Clar structure^{35,36} is a valence structure having the maximal number of disjoint aromatic π -sextets. It can be drawn by superposing all the Kekulé structures with the highest degree of freedom.¹⁸ Aromatic π -sextets are defined as six π -electrons localized to a single benzene ring separated from adjacent rings by formal CC single bonds. The Clar theory has attracted attention of many theorists.^{17,18 59–64}

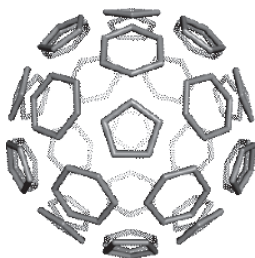
A polyhedral map may have a perfect Clar PC structure, which is a set of disjoint faces (built up on all vertices in M) whose boundaries form a 2-factor. Recall that a k -factor is a regular k -valent spanning subgraph. A PC structure is associated with a Fries structure,⁶⁵ which is a Kekulé structure having the maximum possible ($v/3$) number of benzenoid (alternating single-double edge) faces. A Kekulé structure is a set of pairwise disjoint edges/bonds of the molecule (defined over all its atoms) that coincides with a perfect matching and a 1-factor in Graph Theory.⁶⁶ A trivalent polyhedral graph, like that of fullerenes, has a PC structure if and only if it has a Fries structure.²⁶

Note that, only in polyhex structures (e.g., polyhex tori, where the assignment empty/full can be interchanged between two adjacent hexagons), the PC structure consists of $v/3$ disjoint hexagons (i.e., a 2-factor), as previously Clar suggested. In fullerenes, the PC structure must include all the odd faces (e.g., pentagons), usually assigned as empty π -electron faces. However, the associate Fries structure ensures the total resonance (i.e., conjugation, double-simple bond alternation).²⁶

Such structures represent *totally resonant sextet* TRS benzenoid molecules which it is expected to be extremely stable, according to the VB theory.^{26,67,68} Fully benzenoid hydrocarbons are $6n$ π -electron systems, whose Clar structures have only disjoint benzene rings, mutually connected by CC single bonds.¹⁸ The concept of *totally/fully-resonant* coverings (mainly benzenoids) has been discussed by several authors.^{68–77}

Leapfrog^{78,79} $Le_{(1,1)}$, or simply Le , is the only operation providing PC transforms, which can be embedded in surfaces of any genera (e.g., $g = 0; 2$, Figure 6-1).

(a) $Le(Le(D)) = C_{180}$; $v = 180$; $g = 0$
A2-factor [5,6]; PC



(b) $(2,2)(Op(S_1(T)))$; $v = 264$; $g = 2$
A2-factor [6,7]; PC



Figure 6-1. Perfect Clar PC structure embedded in the sphere ($g = 0$) and (open) tetrahedron ($g = 2$).

Patterns larger than benzene, *e.g.*, naphthalene or azulene (*i.e.*, a pair of pentagonal-heptagonal carbon rings) have been considered with respect to the Clar theory.^{35,36} By extension,^{80–83} corannulenic supra-faces (eventually called *flowers*) may be of interest.

A coronene-like flower is symbolized as $[n:x,y]\text{Fw}$, with n , x , y being the folding of the core and its surrounding polygonal faces, respectively. Such flowers could appear either as intersect, joint or disjoint units.

A tiling is called Platonic if it consists of a single type of faces (similar to the Platonic solids). Archimedean is that tiling consisting of more than one (usually two) type(s) of faces. Platonic and Archimedean will refer here to only supra-face tessellation. Our CageVersatile program¹⁵ enables the flower embedding in surfaces of any genera and lattices of any vertex degree.

A *joint corannulenic* JFw pattern can appear either as a Platonic (*e.g.*, $([5:6_5]\text{Fw},3)$, $([6:6_6]\text{Fw},3)$ or $([7:6_7]\text{Fw},3)$ in case of open structures) or an Archimedean (*e.g.*, $(([5:6_5]\text{Fw},[6:6_6]\text{Fw}),3)$ supra-covering. The degree of the net is, in the most cases, 3 so that it will be omitted in the hereafter Schäfli notations, excepting the cases of different degree.

The case $[5:6_5]\text{Fw}$ is unique ($S_1(D) = C_{140}$ (Figure 6-2). This is achieved by the sequence ($Le\&Ca/S_1$) or by the pro-chiral (4,1)-generalized operation.

The case $[6:6_6]\text{Fw}$ is encountered in polyhex tori tessellated by the ($Le\&S_1$) sequence (Figure 6-3a).

A *disjoint corannulenic* DFw structure is a disjoint set of flowers, covering all the vertices in the molecular graph. Some sequences of operations (*e.g.*, $Le\&Q$; $Q_{(4,0)c}\&Tr_s$) or the generalized $Le_{(2,2)}$ operation provide a DFw covering. Such a transform is necessarily associated with a PC structure, but the reciprocal is not always true. The cage C_{240} , in Figure 6-4a, is illustrated as a DFw Platonic covering. In the top of figures, the π -electron population of a covering is often given (Figure 6-4b).

By virtue of the involved $Le_{(1,1)}$, polyhex tori transformed by $Le_{(2,2)}$ are metallic (and eventually chiral). The torus in Figure 6-3 shows both JFw and DFw coronenic

$$S_1(D) = C_{140}; [5:6_5]\text{JFw}$$

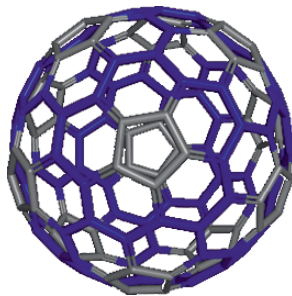


Figure 6-2. Platonic $[5:6_5]\text{JFw}$ tessellation; contour of flowers in dark/blue.

(a) $S_1(T(6,3)V[4,24])$; $v=672$; $g=1$
 Platonic $48 \times [6:6]$ JFw; chiral
 Clar hexagons: $7 \times 48/3 = 112$

(b) $S_1(T(6,3)V[4,24]) = (2,8,12,-24)$; $v=672$; $g=1$
 Platonic $28 \times [6:6]$ DFw; chiral
 Clar hexagons: $4 \times 28 = 112$

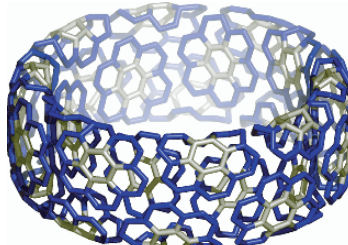
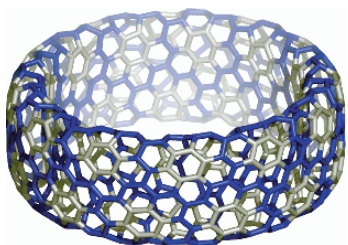


Figure 6-3. Coronenic patterns: joint JFw (a) and disjoint DFw (b – the torus is also given in four integer notation). Both JFw and DFw are associated to PC-Fries structures; flowers in dark/blue contour.

covering and also metallic character.⁸³ Criteria for metallic and coronenic DFw in polyhex tori are given in Chapter 2.

Figure 6-5 accounts for $[5:6_5]$ Fw corannulenic flowers by means of their complementary (connected) substructures.

Figure 6-6 illustrates the corannulenic flowers $[5:6_5]$ & $[6:6_6]$ JFw on C_{420} forming an Archimedean supra-covering.

The supra-organized corannulenic units are expected to contribute to the stability of the whole molecule.^{80,84,85} Semiempirical calculations (with the PM3 Hamiltonian) proved in part this expectation.⁸²

Data listed in Table 6-1 show IPR fullerenes, out of the destabilizing effect of abutting pentagons;^{77,86–90} they are also totally resonant structures and obey the Clar's $6n$ rule. It is reasonable to consider a molecule as more stable as its HF (a measure of thermodynamic stability) is lower and HOMO-LUMO gap (a measure of kinetic stability) is larger. Thus, the lower the ratio HF/Gap, the stable is a molecule.

The HF values, listed in column 3, decrease as the cage size increases and the same trend is valid for the Gap (column 4). The above trend is still preserved in case of

(a) $Le_{(2,2)}(D)$; $v=240$; Platonic $12 \times [5:6_5]$ DFw

(b) Coronene π -electron population: $(0(3^6))$

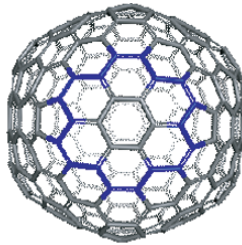
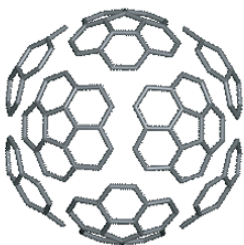
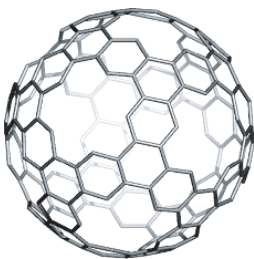


Figure 6-4. C_{240} ; Disjoint DFw structure (a); a coronene supra-face with a $[6]$ radialene substructure (b).

$$Q(Le(D)) = C_{240}; [5:6_5]DFw$$



$$Ca(Le(D)) = C_{420}; [5:6_5] \& [6:6_6]JFw$$

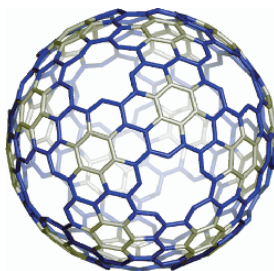
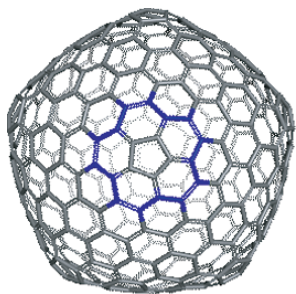


Figure 6-5. Corannulenic covering on Dodecahedron obtained by: *Le* (tripling), *Q* (quadrupling) and *Ca* (septupling, S_1); the flowers' contour is evident in the complementary (connected) substructures.

HF/Gap ratio (column 5) and this is also true for the strain energy SE, calculated in terms of POAV1 theory^{22–25} (column 6). For the total π -energy E_π , evaluated in terms of the simple Hückel theory (column 7) the trend is reversed. These data clearly indicate the effect of size on the stabilization of these molecules. Even C_{60} shows the highest SE value, its exceptional stability is due, in others, by the equal strain distribution over all equivalent atoms.

Table 6-2 lists the main topological and geometrical data for the corannulenic cages discussed here. The classes of equivalence of the three map parameters: vertices, edges and faces, have been obtained by investigating the graphs G (for vertices) and their medials $Me(G)$ (for edges) and duals $Du(G)$ (for faces). The actual bond lengths classes (column 7) confirmed those obtained by investigating the medials. The column 8 in Table 6-2 gives formulas for the π -electron content, referring to the original Platonic objects, transformed by appropriate map operations. The counting starts with the corannulenic core as the first number in the brackets while the second one refers

$$(a) Ca((Le(C_{20})) = C_{420}$$



$$(b) C_{420}; JFws$$

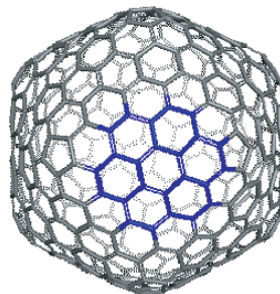


Figure 6-6. Archimedean $[5:6_5] \& [6:6_6]JFw$ tessellation, with radialenic $(0(3^5)) [5:6_5]$ (a) and alternating $(3(0,3)^3) [6:6_6]$ (b) supra-faces, in dark/blue contour.

Table 6-1. Data for corannulenic cages: heat of formation per atom, HF (kcal/mol); HOMO-LUMO GAP (eV); HF/GAP ($\times 100$; eV; PM3); strain energy per atom SE (kcal/mol; POAV1); total π -electron energy E_π (β -units; simple Hückel) and HOMA index of aromaticity

	Cage $6n$	Sym.	HF	Gap	HF/Gap	SE	E_π	HOMA	HOMA [5:6 ₅]Fw	HOMA [6:6 ₆]Fw
	1	2	3	4	5	6	7	8	9	10
1	C ₆₀	I_h	13.512	6.593	8.890	8.257	1.553	0.169	0.251	–
2	C ₁₈₀	I_h	7.594	5.542	5.946	3.154	1.567	0.478	0.502	0.529
3	C ₂₄₀	I_h	6.584	5.113	5.587	2.506	1.569	0.524	0.504 ^(a)	0.510 ^(b)
										0.582 ^(c)
4	C ₄₂₀	I	5.362	4.507	5.162	1.672	1.572	0.606	0.613 ^(a)	0.595 ^(b)
										0.642 ^(c)

(a) [5]radialenic: (0,3⁵); (b) alternating: (3(0,3)³); (c) [6]radialenic: (0,3⁶).

Table 6-2. Topological and geometrical data, tiling type and π -electron content of some leapfrog fullerenes

v	G	f	$Du(G)$	e	$Me(G)$	Bond length	π -Electron content* / $6n$ rule	Operation/ Tiling type	
1	2	3	4	5	6	7	8	9	
1	60	(60)	32	(12) (20)	90	(30) (60)	(30: 1.3990) (60: 1.4013)	$(03^s)^{f/3}$ / $n = 10$	$Le(M)$ PC
2	180	$3 \times (60)$	92	(12) (20) (60)	270	(30) $2 \times (60)$ (120)	(60: 1.3857) (60: 1.3875) (120: 1.4053) (30: 1.4257)	$(0\ 3^s)^f (0^s)^{f/3}$ / $n = 30$	$Le(Le(M))$ PC [5]Radialene
3	240	$2 \times (60)$ (120)	122	(12) (20) (30) (60)	360	$4 \times (60)$ (120)	(60: 1.3805) (60: 1.4134) (60: 1.4264) (60: 1.4384) (120: 1.4445)	$(0\ 3^s)^f (0\ d)^{sf/d}$ / $n = 40$	$Le(Q(M))$ DFw
4	420	$7 \times (60)$	212	(12) (20) $3 \times (60)$	630	(30) $10 \times (60)$	(60: 1.3821) (60: 1.4051) (30: 1.4066) (60: 1.4115) (60: 1.4251) (60: 1.4285) (60: 1.4358) (60: 1.4360) (60: 1.4364) (60: 1.4378) (60: 1.4387)	$(03^s)^f$ $(d\ (0\ 3)^d)^{sf/d}$ / $n = 70$	$Le(Ca(M))$ JFw

* Formulas refer to the original Platonic solids, transformed by map operations (see text).

to its surrounding hexagons. The superscripts d , s and f represent the vertex degree and size (*i.e.*, folding) and number of faces in the original map, respectively. All the cages obey the $6n$ rule of Clar.^{35,36} The column 9 indicates the map operation by which the cage is obtained from the dodecahedron and the tiling type as well. Note that PC and corannulenic DFW and JFW coverings account for the maximum possible ($v/3$) number of benzenoid faces, being an important structural feature defining the aromatic character.

Resuming to Table 6-1, the HOMA values for the whole molecules show again an increase of aromaticity, paralleling the E_{π} -values. The HOMA is useful to compare the aromaticity of some substructures, eventually to confirm an increased aromaticity for those supra-faces more populated with π -electrons. Coronene units $[6:6_6]\text{Fw}$ show a higher aromaticity for the Kekulé structures of radialenic type (with electron distribution: $(0,3^6)$ – Table 6-1, column 10) than for those of alternating type (with electron distribution: $(3(0,3)^3)$).

The corannulenic $[n:6_n]\text{Fws}$ show increasing aromaticity (Table 6-1, columns 9 and 10) as the number of atoms increases (the topological resonance energy TRE – an aromatic stabilization energy – was found higher in larger fullerenes¹⁸).

Note that coronene itself $[6:6_6]\text{Fw}$ is not a totally resonant hydrocarbon,¹⁸ because any one Kekulé structure leaves some carbon atoms outside sextet rings. However, Clar proposed⁹¹ that if the three sextets of coronene can migrate into the neighboring rings, an extra ring current will be formed. Thus, the sextet migration current is an argument in favor of the coronene enhanced aromaticity (compared to some other polycyclic hydrocarbons, *e.g.*, naphthalene and anthracene).⁹²

Counter circulation of “rim and hub” currents is a characteristic of the corannulenes $[n]\text{Fw}$, as shown by the ipsocentric⁹³ CTOCD (continuous transformation of origin of current density) calculations.^{94,95} This is one reason for the need of a disjoint DFW structure.

6.4. Corazulenic Cages

Corazulenic flowers,⁸⁰ analogue to the corannulenic $[n:6_n]\text{Fws}$, can be achieved *via* several map operation sequences. Any sequence of operations can be applied to any cage but we look here for minimal size cages, eventually of interest for chemists. The best results are obtained for triangulated maps, particularly the (triangulated) Platonics. When the operations in a sequence are commutative, the dual-pair will produce either non-distinguishable transforms or different transforms leading to a unique Stone-Wales SW rotated product.

The SW isomerization was performed on corazulenic supra-faces ($[n:(7(5c))_n]\text{Fw}$ or $[n:(7(5d))_n]\text{Fw}$), which are taken as the main Fw patterns in a covering; n is just the vertex degree in the original Platonic map. Direct ways to RO-transforms are also known.

Of particular interest is the SW rotation of the spokes of the n -gonal hub of $[n:(7(5d))_n]\text{Fw}$, leading to disjoint corazenic flowers $[n:(5,7)_{n/2}]\text{Fws}$. Note that any

supra-face or Fw has its own intersected/superposed “counterpart”, called here *co-Fw*. Of course, the attribute Fw and co-Fw are interchangeable. The covering by a sequence of operations is given in terms of supra-faces.

The five Platonic polyhedra and their symbols herein used are: *T* (tetrahedron), *O* (octahedron), *C* (cube), *D* (dodecahedron, and *I* (icosahedron). The dual pairs are: *T* & *T* (self-dual); *O* & *C* and *D* & *I*.

The symbol used for cages in the hereafter tables will include the actual nuclearity, the original cage and the map operation sequence (by its *m*-factor). When obtained by SW edge-rotation, the suffix RO is added.

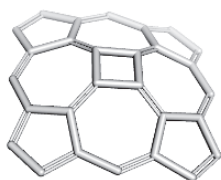
Figure 6-7 illustrates the most frequent azulenenic patterns appearing in (yet hypothetically) fullerenes. In comparison, two corannulenic flowers: Coronene = $[6 : 6_6]$ Fw and Sumanene = $[6 : (5, 6)_3]$ Fw, often coupled with the corazulenenic patterns, are given in Figure 6-8.

6.4.1. Covering by $[n : (7(5c))_n]$ Fw Patterns

The pattern $[n : (7(5c))_n]$ Fw shows the corazulenenic flower in an angular heptagon-pentagon $[7(5c)]$ arrangement. It is provided by the sequences: $^{80,96} Tr_s(Q(P_5(M)))$ or $Tr_s(Q(S_2(M)))$. Its SW transform is a sumanenic flower $[2n : (5, 6)_n]$ Fw.

The covering is given in terms of supra-faces and the multiplication factor *m* refers to the original map nuclearity. The size of the flowers' core is related to the size of

$[4:(7(5c))_4]$ Corazulene



$[4:(7(5d))_4]$ Corazulene

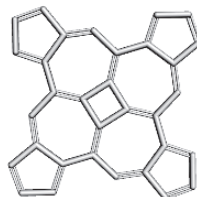


Figure 6-7. Corazulenenic patterns

Coronene = $[6:6_6]$ Fw



Sumanene = $[6:(5,6)_3]$ Fw



Figure 6-8. Corannulenic patterns

faces of the parent p (Platonic cage), dual d or their double size; to specify the above relatedness the following symbols are used: s_p , s_d , s_{dp} and s_{dd} , respectively. Details of the covering are given in the top of figures.

6.4.1.1. Sequence $Tr_s(Q(P_5(M)))$; $m = 22$.

Within this sequence, $P_5(O) = P_5(C)$ so that no distinction can be made between the transforms of the dual-pair objects. Figure 6-9 illustrates two cages covered by the above operation sequence (up to SW transforms). Out of the main flower, the corazulenic $[n : (7(5c))_n]$ Fw, hexagon-triple $[h\text{-triple}]$ co-Fw and hexagons can be evidenced.

Table 6-3 lists the energetic and structural data for the cages having $m = 22$. They are open closed or pseudo-closed π -shell cages (Table 6-3, column 6) and are less strained (column 5) than C_{60} . HOMA index of aromaticity (column 7) finds the corazulenic cages more aromatic than C_{60} . However, the ratio DF/Gap is in favour of C_{60} (with the lowest value – row 4, column 4). The rotated cages, derived from cube/octahedron, (Table 6-3, row 3, column 4) appear the most stable in this series.

According to Fowler and Pisanski,²⁶ the π -electronic shells of neutral graphitic cages are classified, function of their eigenvalue spectra, as: (i) *closed* (cl), when $x_{v/2} > 0 \geq x_{v/2+1}$; (ii) *pseudo-closed* (pscl), in case $x_{v/2} > x_{v/2+1} > 0$; (iii) *meta-closed* (mcl), with $0 \geq x_{v/2} > x_{v/2+1}$ and (iv) *open* (op), when the $v/2^{th}$ (HOMO) and $v/2 + 1^{th}$ (LUMO) molecular orbitals are degenerate: $x_{v/2} = x_{v/2+1}$.

Observe in Table 6-3, the co-Fws remain unchanged, under SW isomerization.

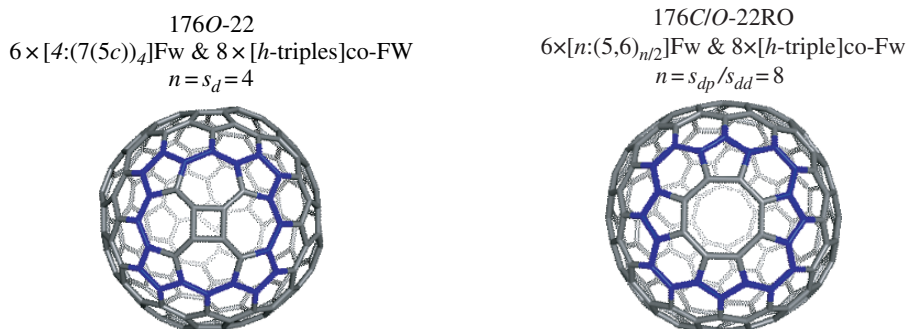


Figure 6-9. Corazulenic pattern $[4 : (7(5c))_4]$ Fw, designed by $Tr_s(Q(P_5(M)))$, and its SW transform $[8 : (5,6)_4]$ Fw; contour in dark/blue.

Table 6-3. Data for corazulenic $[n : (7(5c))_n]$ cages (of $m = 22$), designed by $Tr_s(Q(P_5(M)))$, and their SW isomers: heat of formation per atom, HF (kcal/mol); HOMO-LUMO GAP (eV); HF/Gap ($\times 100$; eV; PM3); strain energy per atom SE (kcal/mol; POAV1); total π -electron energy E_π (β -units; simple Hückel) and HOMA index of aromaticity. For comparison, fullerene C_{60} is included.

	Cage	Sym.	HF	Gap HF/Gap	SE	E_π shell	HOMA	HOMA- Fw	Fw
	1	2	3	4	5	6	7	8	9
1	88T- 22RO	T	11.847	4.051 12.690	4.457	1.549 op	0.316	0.287 0.370	$4 \times [6 : (5, 6)_3]$ $4 \times [h\text{-triple}] \text{co-Fw}$
2	176O- 22	O	11.033	3.556 13.463	2.865	1.536 cl	0.224	0.111 0.559	$6 \times [4 : (7(5c))_4]$ $8 \times [h\text{-triple}] \text{co-Fw}$
3	176C/O- 22RO	O	9.436	4.006 10.221	2.946	1.549 pscl	0.267	0.177 0.680	$6 \times [8 : (5, 6)_4]$ $8 \times [h\text{-triple}] \text{co-Fw}$
4	C_{60}	I_h	13.512	6.593 8.893	8.257	1.553 cl	0.169	0.251 0.169	$4 \times [5 : 6_5]$ $4 \times [6 : (5, 6)_3] \text{co-Fw}$

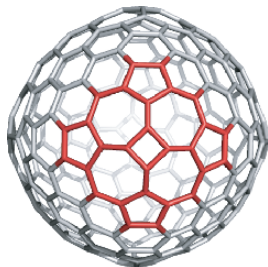
6.4.1.2. Sequence $Tr_s(Q(S_2(M)))$.

The multiplication factor is $m = 10d_0$ (with d_0 -the vertex degree), in the triangulated Platonic parent, or $m = 30$ in the trivalent dual. The main pattern, corazulenic $[n : (7(5c))_n] \text{Fw}$, $n = s_d$ changes by SW into sumanenic pattern $[n : (5, 6))_{n/2}] \text{Fw}$, $n = s_{dd}$ (Figure 6-10).

The sequence of map operations is non-commutative because of S_2 . This implies the clear difference between the dual-pair rotated transforms (Figure 6-11 and Table 6-4, rows 3 and 4). This is more evident for the corannulenic co-Fw which, in the 30RO-series, is Archimedean: $[(n : 6_n) \& s_{dd}] \text{DFw}$, $n = s_{dp}$. Observe the co-Fw remains unchanged, under the SW isomerization (Table 6-4, rows 2 and 3).

Remark, in Table 6-4, the highest aromatic character of 120T-30RO, (HOMA=0.402, row 1, column 7), in spite of the highest value of strain (4.792 kcal/mol

(a) 240O-30; $6 \times [4 : (7(5c))_4] \text{Fw}$



(b) 240O-30RO; $6 \times [8 : (5, 6)_4] \text{Fw}$

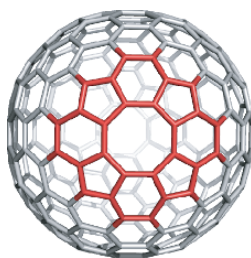


Figure 6-10. Corazulenic pattern $[n : (7(5c))_n] \text{Fw}$, $n = s_d$, (designed by $Tr_s(Q(S_2(M)))$ sequence) changes to sumanenic pattern $[2n : (5, 6))_n] \text{Fw}$, by SW.

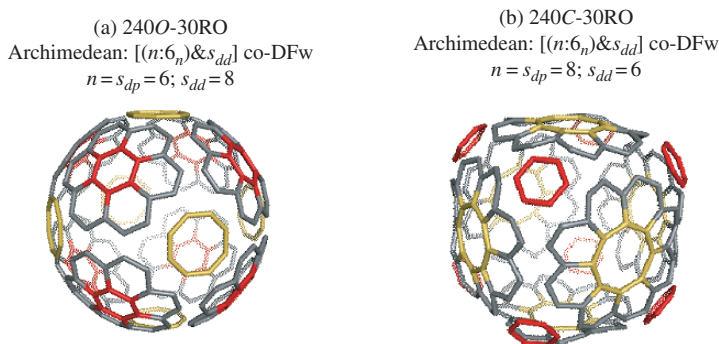


Figure 6-11. Difference between the transforms by $Tr_s(Q(S_2(M)))$ of the dual-pair octahedron (a) and cube (b) and finally SW rotated RO.

Table 6-4. Data for corazulenic $[n : (7(5c))_n]$ cages (of $m = 30$), designed by $Tr_s(Q(S_2(M)))$, and their SW isomers: heat of formation per atom, HF (kcal/mol); HOMO-LUMO GAP (eV); HF/Gap ($\times 100$; eV; PM3); strain energy per atom SE (kcal/mol; POAV1); total π -electron energy E_π (β -units; simple Hückel) and HOMA index of aromaticity.

	Cage	Sym.	HF	Gap HF/Gap	SE	E_π shell	HOMA	HOMA- Fw	Fw
	1	2	3	4	5	6	7	8	9
1	120T- 30RO	T_h	9.579	5.640 7.370	4.792	1.563 cl	0.402	0.365 0.502	$4 \times [6 : (5, 6))_3]$ $4 \times [6 : 6_6]$ co-DFw
2	240O- 30	O_h	9.371	4.783 8.502	2.357	1.545 cl	0.205	-0.022 0.645	$6 \times [4 : (7(5c))_4]$ $8 \times [6 : 6_6]$ co-Fw
3	240O- 30RO	O_h	7.283	5.273 5.993	2.107	1.558 cl	0.386	0.290 0.528 0.821	$6 \times [8 : (5, 6)_4]$ $8 \times [6 : 6_6]$ co-DFw $\& 6 \times s_{dd}; s_{dd} = 8$
4	240C- 30RO	O_h	12.960	6.175 9.107	4.285	1.561 cl	0.044	0.273 -0.086 0.392	$8 \times [6 : (5, 6)_3]$ $6 \times [8 : 6_8]$ co-DFw $\& 8 \times s_{dd}; s_{dd} = 6$

on the whole molecule, distributed as: $6.154/[6 : (5, 6))_3]$ Fw and $3.7324/[6:6_6]$ Fw. This is due to the coronene $[6:6_6]$ contribution but also to the presence of benzene ring (the core of sumanenic flower $[6 : (5, 6))_3]$ in an Archimedean covering (Figure 6-12).

6.4.2. Covering by $[n : (7(5d))_n]$ Fw, 3

Several sequences of map operations lead to the corazulenic $[n : (7(5d))_n]$ Fw, $n = s_d$ pattern. Its SW transform is a corazenic flower $[2n : (5, 7)_n]$ Fw.

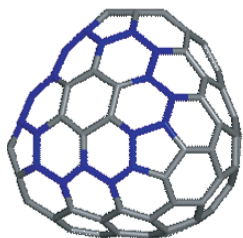
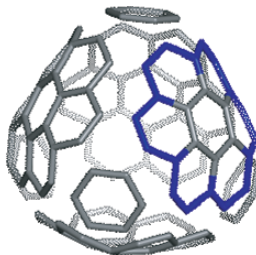
(a) 120*T*-30RO(b) Archimedean $[(n:6_n)&s_{dd}]$ co-DFw
 $n = s_{dp} = 6; s_{dd} = 6$ 

Figure 6-12. The most aromatic cage originating in a corazulenic $[4 : (7(5c))_4]$ fullerene derived from tetrahedron by $Tr_s(Q(S_2(M)))$; contour of Fws in dark/blue.

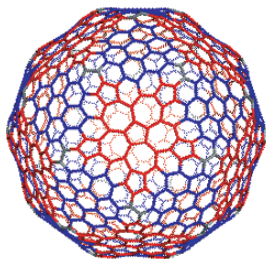
6.4.2.1. Sequence $Tr_s(S_1(S_2(M)))$.

The above sequence generates a corazulenic flower in the $[7(5d)]$ arrangement.⁸⁰ $S_1 = Capra$ induces chirality while truncation (of the selected vertices) provides a face-folding of seven in the final trivalent map. The multiplication factor is $m = 17d_0$ in the triangulated Platonic or $m = 51$ in the trivalent dual pair. Note that $S_1(S_2(M)) \neq S_2(S_1(M))$, in words, the operation sequence is non-commutative.

The tiling given by the above sequence is a mixture of corazulenic $[n : (7(5d))_n]$ Fw, $n = s_d$ and coronenic $[n : 6_n]$ co-Fw, $n = s_{dp}$ (Figures 6-13 and 6-14), separated by naphthalene and pyrene units.

Table 6-5 lists data on cages of this covering. They are pseudo-closed π -shells, except 408*O*-51 (entry 2), a corazulenic cage which shows a closed π -shells (column 6) and the highest aromaticity (column 7). The high value of HOMA index is due to the coronene flowers $[6:6_6]$ but the corazulenic $[4 : (7(5d))_4]$ flower is

1020*I*-51; $g=0$
 $12 \times [5:(7(5d))_5]$ Fw & $20 \times [6:6_6]$ co-Fw



1644($Op_{2a}(S_2(T))$)-51; $g=2$
 $12 \times [7:(7(5d))_7]$ Fw & $20 \times [6:6_6]$ co-Fw

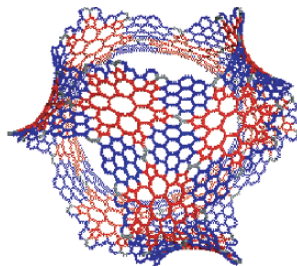


Figure 6-13. Covering by $Tr_s(S_1(S_2((M))))$ in two different embeddings.

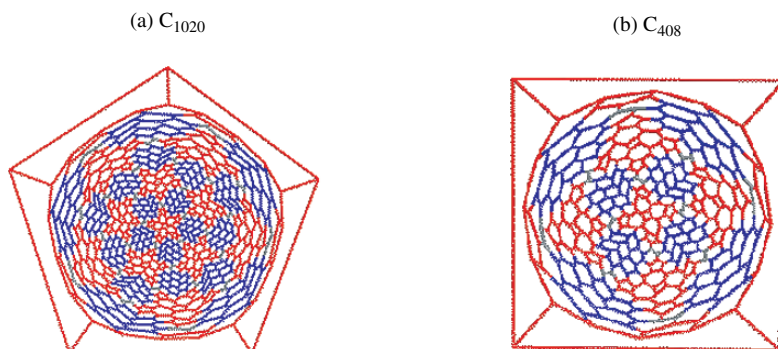


Figure 6-14. Corannulenic $[6 : 6_6]$ Fw and corazulenic $[n : (7(5d))_n]$ Fw patterns, designed by $Tr_s(S_1(S_2((M)))$, in the Schlegel projection: $n = 5$ (a) and $n = 4$ (b)).

more aromatic than in other cages (see the next tables), maybe a consequence of the size effect (?), also supported by the lowest HF value in this series.

In the RO-series, the covering is: $[n : (5, 7)_{n/2}]$ Fw, $n = s_{dd}$; $[n : 6_n]$ co-Fw, $n = s_{dp}$. The octahedron-derivative 408O-51RO is far more stable than that of its dual pair 408C-51RO (the last one not included in Table 6-5).

6.4.2.2. Sequence $Tr_s(S_{1f}(Q(M)))$.

In the above sequence, Q is the quadrupling map operation, S_{1f} represents the septupling operation performed so that the original faces of M remain untransformed and Tr_s is the truncation of selected vertices. The sequence leads to a Platonic disjoint corazulenic $[n : (7(5d))_n]$ DFw, $n = s_d$, chiral (by virtue of $S_1 = Ca_{2,1}$)

Table 6-5. Data for corazulenic $[n : (7(5d))_n]$ cages (of $m = 51$), designed by $Tr_s(S_1(S_2((M)))$, and their SW isomers: Structural, energetic and aromatic parameters: symmetry Sym, heat of formation per atom HF (kcal/mol); HOMO-LUMO GAP (eV); strain energy per atom SE (kcal/mol; POAV1); total π -electron energy E_π (β -units; simple Hückel) and HOMA index of aromaticity.

	Cage	Sym.	HF	Gap	SE	E_π shell	HOMA	HOMA- Fw	Fw
	1	2	3	4	5	6	7	8	9
1	204T-51RO	<i>T</i>	11.190	3.808	3.470	1.553 pscl	0.234	-0.074 0.313	$4 \times [6 : (5, 7)_3]$ $4 \times [6 : 6_6]$ co-Fw*
2	408O-51	<i>O</i>	7.532	3.330	1.466	1.556 cl	0.503	0.340 0.631	$6 \times [4 : (7(5d))_4]$ $8 \times [6 : 6_6]$ co-Fw*
3	408O-51RO	<i>O</i>	9.425	3.841	2.195	1.553 pscl	0.297	-0.121 0.562	$6 \times [8 : (5, 7)_4]$ $8 \times [6 : 6_6]$ co-Fw*

*there are also naphthalene and pyrene as co-Fws

covering; the co-Fw shows a sumanenic $[n : (5, 6)_{n/2}]$ Fw, pattern which forms an Archimedean $[n : (5, 6)_{n/2} \& s_d]$ co-DFw, $n = s_{dp}$ covering.⁸⁰

The sequence $(Q \& S_{1f}/Ca_{(2,1)}f \& Trs)$ is equivalent to the generalized¹⁴ “DAZU” operation and its multiplication factor is $m = 8d_0$ in the triangulated Platonic or $m = 24$ in the trivalent dual pair. Table 6-6 lists data for cages of $m = 24$.

Of particular interest⁹⁶ is here the SW rotation of the spokes of the n -gonal hub of $[n : (7(5d))_n]$ Fw. It leads to a Platonic covering by disjoint corazenic $[n : (5, 7)_{n/2}]$ Fw patterns. The rotation also changes the sumanenic flower to a corazenic one, so that both Fw and co-Fw are of corazenic type and both are disjoint. For a dual-pair, the corazenic $[n : (5, 7)_{n/2}]$ Fw and co-Fw are: $n = s_{dp}$ and $n = s_{dd}$, respectively.

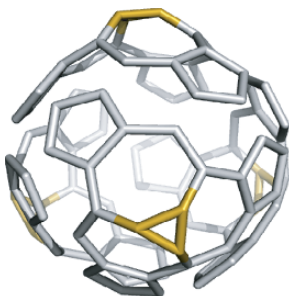
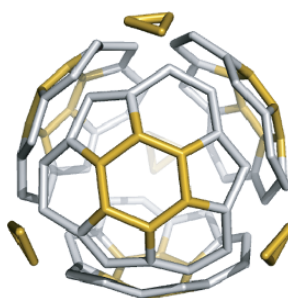
As an alternative tessellation, a Platonic anti-aromatic disjoint covering by pentalenes (*i.e.*, abutting pentagons) can be evidenced (see below). The tessellation by disjoint pentalenes represents a generalized^{26,96} perfect Clar structure, in the sense the faces composing the 2-factor represent pentalenic contours.

The covering of 96T-24 is a Platonic disjoint $[n : (7(5d))_n]$ DFw, $n = s_d = 3$ while the co-Fw forms an Archimedean disjoint $[n : (5, 6)_{n/2} \& s_d]$ co-DFw, $n = s_{dp} = 6$; $s_d = 3$ covering (Figure 6-15).

Tetrahedron is self-dual, so that the SW edge-rotation on 96T-24 provides only one RO-cage (Table 6-6, row 2). Moreover, identical Fw (coming out from the parent face) and co-Fw (accounting for the vertex degree of the parent, or the parent face of the dual) are obtained (row 2, column 9). Figure 6-16

Table 6-6. Data for corazulenic $[n : (7(5d))_n]$ cages (of $m = 24$), designed by $Tr_s(S_{1f}(Q(M)))$, and their SW isomers: heat of formation per atom, HF (kcal/mol); HOMO-LUMO GAP (eV); HF/Gap ($\times 100$; eV; PM3); strain energy per atom SE (kcal/mol; POAV1); total π -electron energy E_π (β -units; simple Hückel) and HOMA index of aromaticity.

Cage	Sym.	HF	Gap HF/Gap	SE	E_π shell	HOMA	HOMA- Fw	Fw
1	2	3	4	5	6	7	8	9
1 96T-24	<i>T</i>	16.040	4.580 15.197	6.338	1.545 mcl	0.190	0.054 0.091 0.567	$4 \times [3 : (7(5d))_3]$ DFw $4 \times [6 : (5, 6)_3]$ co-DFw $4 \times s_d$; $s_d = 3$
2 96T- 24RO	<i>T</i>	13.869	4.780 12.590	5.348	1.527 pscl	0.017	0.098 0.098 -0.285	$4 \times [6 : (5, 7)_3]$ DFw $4 \times [6 : (5, 7)_3]$ co-DFw $12 \times$ DPentalene
3 192O- 24	<i>O</i>	12.039	4.755 10.989	3.194	1.536 cl	0.173	0.041 0.267 0.249 -1.878	$6 \times [4 : (7(5d))_4]$ DFw $4 \times [6 : (5, 6)_3]$ co-Fw $4 \times [6 : (5, 6)_3]$ co-Fw $6 \times s_d$; $s_d = 4$
4 192C/O- 24RO	<i>O</i>	15.696	3.866 17.618	3.256	1.527 pscl	0.033	-0.154 0.292 -0.883	$6 \times [8 : (5, 7)_4]$ DFw $8 \times [6 : (5, 7)_3]$ co-DFw $24 \times$ DPentalene

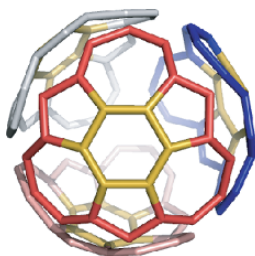
(a) 96T-24; Platonic $[n:(7(5d))_n]$ DFw, $n = s_d = 3$ (b) 96T-24; Archimedean $[n:(5,6)_{n/2} \& s_d]$ co-DFw, $n = s_{dp} = 6; s_d = 3$ Figure 6-15. Corazulenic pattern $[n : (7(5d))_n]$ DFw, $n = s_d$ and its co-Fw designed by $Tr_s(S_{1f}(Q(M)))$.

illustrates the cage 96T-24RO, with its disjoint corazenic flowers (6-16a) and the anti-aromatic disjoint pentalenes (6-16b).

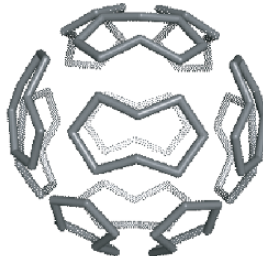
Between the two 96-cages, the RO-isomer appears more aromatic by the Kekulé structure count K criterion (1,149,200 for 96T-24RO vs 1,095,664 for 96T-24). The same ordering is given by the energetic criterion HF (which is lower for 96T-24RO, this being classified as more stable) but the reverse ordering is suggested by the total. π -electron energy E_π and total HOMA index (Table 6-6, rows 1 and 2, columns 6 and 7).

Closer to the K -criterion ordering is that given by local HOMA-Fw values which only account for the flowers (not for the connection between the disjoint supra-faces).

The tessellation by disjoint pentalenes represents a generalized^{26,96} perfect Clar structure, in the sense the faces composing the 2-factor represent pentalenic contours.

(a) 96T-24RO; Platonic $[n:(5,7)_{n/2}]$ DFw, $n = s_{dp}$ 

(b) 96T-24RO; Platonic disjoint pentalenes

Figure 6-16. Aromatic and anti-aromatic patterns: corazene (a) and pentalene (b), designed by $Tr_s(S_{1f}(Q(M)))$.

(a) 192C/O-24RO; Platonic $6 \times [8:(5,7)_4]$ DFw(b) 192C/O-24RO; Platonic $8 \times [6:(5,7)_3]$ co-DFw

Figure 6-17. Corazenic disjoint flowers $[n : (5,7)_{n/2}]$; $n = s_{dp}$ (a); $n = s_{dd}$ (b), designed by $Tr_s(S_{1f}(Q(M)))$.

The transforms of the dual-pair: octahedron (covered by $[4 : (7(5d))_4]$ Fw) and cube (with $[3 : (7(5d))_3]$ Fw pattern), by $(Q \& Ca_{(2,1)} \& Trs)$, provide, after SW edge-rotation, the only 192C/O-24RO cage (Table 6-6, row 4). Because of the trigonal faces, 192C-24 could not be optimized and consequently is missing in Table 6-6. Figure 6-17 illustrates the cage derived from C/O.

For corazene/isocoronene $[6:(5,7)_3]$, Fowler *et al.*⁹⁷ have recently predicted, in the ipsocentric⁹³ description, a single, unopposed, intense diatropic perimeter current arising from its four. π HOMO electrons; they qualified isocoronene as *super-aromatic*, on the magnetic criterion. By the energetic criterion, the coronene is, however, more stable/aromatic.

As a general trend, the corazulenic flowers are less aromatic than the corresponding co-Fws and the whole molecule is at least non-aromatic, with local manifestation of aromaticity/antiaromaticity (Table 6-6).

A special attention is further devoted to the most stable corazulenic cage of series 24: $C_{192} = 192O - 24$. It shows a Platonic, disjoint corazulenic $[4 : (7(5d))_4]$ DFw covering (Figure 6-18), which is a non-alternant, non-benzenoid pattern; the co-Fw forms an Archimedean $[n : (5,6)_{n/2} \& s_d]$ co-DFw, $n = s_{dp} = 6$; $s_d = 4$, sumanenic covering.

C_{192} is a generalized perfect Clar structure,⁸⁰ with the 2-factor designed as corazulenic $[4 : (7(5d))_4]$ disjoint flowers. The analysis by the geometric criterion enabled us to bring evidence for some of the dominant Kekulé valence structures.

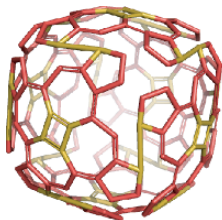
The four-fold symmetric structure, having the valence structure called⁸⁰ “Radialene” (*i.e.*, based on $[n]$ radialene substructures – Table 6-7, row 1) undergoes a Jahn-Teller⁹⁸ distortion to give a two-fold symmetry but more stable structure.

Among thousands of Kekulé valence structures, that called “Radialene”, has no Kekulé benzene KB rings, thus it was assigned as the anti-Fries⁹⁹ valence structure. The valence structure called “Triphenylene” (with triphenylene $[6 : (0,6)_3]$ Fw the main substructure – Figure 6-18) shows the maximum possible 32 KB rings, thus being identified as the Fries⁶⁵ valence structure (Table 6-7, row 2). Note the alternation of triphenylenic ($(3(0,3)^3)^{v/2}$) and triphenylenic ($(3(1,2)^3)^{v/2}$) units within the

sumanenic $[6:(5,6)_3]$ Fws, as shown by the local HOMA values and π -electron partition (Table 6-6, row 3, Table 6-7, row 2 and Figure 6-19).

The “Kekulé-Dewar” valence structure⁸⁰ (Table 6-7, row 3 and Figure 6-20) is a special one: the [5]radialenic subgraphs show only four equal length CC double bonds while the fifth is longer. As the “longer” bonds of two neighbor pentagons are located at the “*para*” 2,5-position of a 1,4-cyclohexadiene unit, it is tempting to consider the two opposite carbon atoms being joined by an “ineffective” bond, as in the Dewar valence structure of benzene. Thus, the whole valence structure consists of 8KB & 12DwB, disregarding the azulenic flowers. Our JSCHEM program⁵² enabled the separation between CC single and double bonds, at a threshold of 1.4005 angstroms, and drawing the valence structures. Note the high local HOMA values (high aromaticity) of the Kekulé KB and Dewar DwB in the Kekulé-Dewar valence structure.

(a) 192O-24; Platonic $6 \times [n:(7(5d))_n]$ DFw
 $n=s_d=4$



(b) 192O 24; Archimedean $[n:(5,6)_{n/2} \& s_d]$ lco-DFw
 $n=s_{dp}=6; s_d=4$

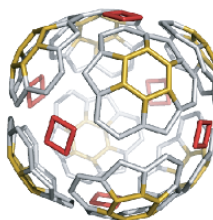


Figure 6-18. Covering by $Tr_s(S_{1f}(Q(M)))$, $M = O$: (a) corazulenic disjoint flowers $[n : (7(5d))_n]$ DFw (joined here only by Dewar “ineffective” bonds); (b) sumanenic disjoint flowers $[6 : (5,6)_3]$ DFw.

Table 6-7. Partition of π -electrons and subgraph count in 192O-24.

Valence Structure ^a	π -Electron partition ^b	Subgraph count	HOMA-subgraph
1	2	3	4
1 Radialene (anti-Fries)	$(0,5)^{sf} (2)^{sf} (2)^{sf/2} (0)^{v/3}$	\emptyset KB; $6 \times [4]$ Rad; $8 \times [6]$ Rad	0.173
2 Triphenylene (Fries)	$(1^{sf/2}) (2)^{sf} (3^{sf/2}) (3(0,3)^3)^{v/2}$ $(3(1,2)^3)^{v/2}$	32KB	0.463
3 Kekulé-Dewar	$(1,2,3)^{sf/2} (2)^{sf/2} (3,(1,2)^3)^v$	8KB+12DwB	0.670
4 Disjoint corazulene $[4 : (7(5d))_4]$ DFw	$(1^{sf/2}, (3,1)^{sf/2}, (4,1)^{sf/2}, 2s^{sf/2})^f (3,1,1,1)^v$	$6 \times [4 : (7(5d))_4]$	0.041

^a The valence structure is named by the main substructure, for which units count and HOMA value is given. ^b Partition is given for the whole covering; counting the electrons in the above partitions equals the multiplication m by the map operations: 192O-24; $m = 24$.

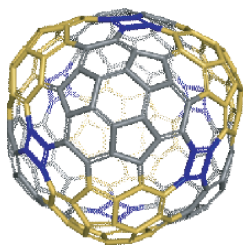
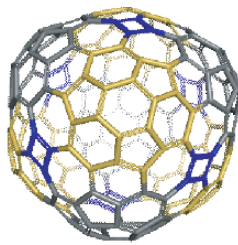
(a) Triphenylenic sumanene $[6:(5,6)_3]\text{Fw}$:
(3(0,3)₃) (gray)(b) Triphenylenic sumanene $[6:(5,6)_3]\text{Fw}$:
(3(1,2)₃)_{v/2} (yellow)

Figure 6-19. The “Triphenylenic-Kekulé” valence structure of 192O-24 with two distinct alternating $[6:(5,6)]\text{Fw}$ and their π -electron population.

The six disjoint corazulenic units $[4:(7(5d))_4]$ (Table 6-7, row 4; HOMA = 0.041) are complementary to the Fries substructure (HOMA = 0.463). More precisely, the Fries substructure is defined on all the vertices except the azulenic flower’s core. The combined overall HOMA value of 0.173 for 192O-24, is somewhere between non-aromatic and aromatic character.

In the ipsocentric description, we found¹⁰⁰ for corazulene (the hydrocarbon corresponding to the supra-face $[4:(7(5d))_4]\text{Fw}$, as appears in 192O-24) to show the magnetic properties of a circulene, with paired counter-rotating paratropic-hub and diatropic-rim currents (Figure 6-21). In comparison, the isomeric cornaphthalene shows strong local diatropic circulations in separated parts of the perimeter, being a clear support for the regio-selectivity of chemical reactions in such (yet hypothetical) molecules.

In view of evaluating the number of Kekulé valence structures, a criterion of aromaticity, we used¹⁰¹ a procedure based on the *divide et impera* strategy. Let G be any graph with $V(G)$ and $E(G)$ being the set of its vertices and edges, respectively. For each $V' \subseteq V(G)$, $G - V'$ denotes the graph obtained from G by deleting the vertices in V' and all edges adjacent to them. For each $E' \subseteq E$, we denote by $G - E'$ the graph obtained by deleting all the edges in E' . Denote by $K(G)$ the set of all Kekulé structures of G .

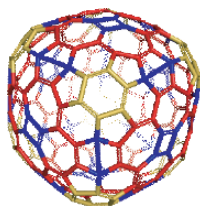
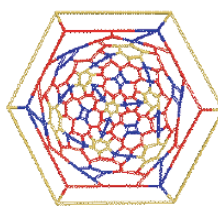
(a) 192O-24; $[4:(7(5d))_4]\text{DFw}$ & $[6:(5,6)_3]\text{DFw}$ (b) 192O-24; $[6:(5,6)_3]\text{DFw}$ 

Figure 6-20. The “Kekulé-Dewar” valence structure of 192O-24 in 3D (a) and Schlegel projection (b).

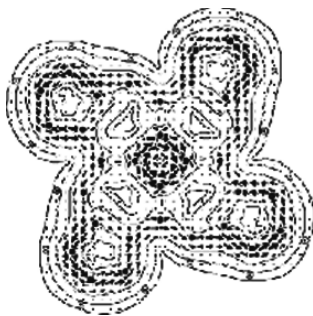


Figure 6-21. Total π current-density map of corazulene 192O-24

The number of Kekulé structure of C_{192} is equal to 1,771,875,132,416. To obtain this result, observe that, by cutting 16 edges, the graph in Figure 6-22 (*i.e.*, the Schlegel³⁵ projection of C_{192}) disintegrates in two components. Denote these edges $E_{cut} = \{e_1, \dots, e_{16}\}$; denote the “interior” component of $G - E_{cut}$ by G_1 and “exterior” component by G_2 . Write the vertices of G_1 $v_{1,1}, v_{1,2}, \dots, v_{1,96}$ and vertices of G_2 by $v_{2,1}, v_{2,2}, \dots, v_{2,96}$ in such a way that $e_i = (v_{1,i}, v_{2,i})$ for each $i = 1, \dots, 16$. Let X be any subset of E_{cut} . Denote $K = K(G)$ the set of all Kekulé (geometrical) structures of the molecule and its cardinality (*i.e.*, Kekulé structures count) $k = k(G) = |K|$. Denote K_X all the Kekulé structures having all the edges in X double and all edges in $E_{cut} - X$ single.

Clearly, K is a disjoint reunion: $K = \bigcup_{X \subseteq E_{cut}} K_X$ and whence $|K| = \sum_{X \subseteq E_{cut}} |K_X|$. Denote $V_1(X) = \{v_{1,i} : e_i \in X\}$ and $V_2(X) = \{v_{2,i} : e_i \in X\}$. It is immediate that $|K_X| = |K(G_1 - V_1(X))| \cdot |K(G_2 - V_2(X))|$ and next:

$$k(G) = \sum_{X \subseteq E_{cut}} \{k(G_1 - V_1(X)) \cdot k(G_2 - V_2(X))\} \quad (6.3)$$

Formula (6.3) is the ground formula of our algorithm. It is difficult to find all Kekulé structures of a graph with 192 vertices but in this way we have $2 \times 2^{16} = 131072$ times the number of Kekulé structures of graphs with at most 96 vertices. In fact, for half of them, we need not to count the Kekulé structures, because they have odd number of vertices and therefore the Kekulé structure count gives 0.

Evaluation of $|K(G_1 - V_1(X))|$ or $|K(G_2 - V_2(X))|$ is based on:

Lemma 6.1. *Let G be any graph, $v \in V(G)$ and u_1, \dots, u_k all the neighbors of v . Then:*
 $k(G) = k(G - v - u_1) + k(G - v - u_2) + \dots + k(G - v - u_k).$

The algorithm, developed by Vukičević,^{64,101,102} was used to find the Kekulé structure count of corazulenic $C_{240} = 240O-30$ fullerene: $K = 2,423,740,251,144,960$. The corannulenic fullerene C_{240} shows $K = 21,587,074,966,666,816$, which is one order of magnitude larger than that for the

corazulenic isomer. This suggests the corannulenic fullerene C_{240} is more aromatic and more stable than the corazulenic C_{240} . A lower HF value (6.584 vs 9.371), a lower ratio HF/Gap (5.587 vs 8.502) and a higher HOMA value (0.524 vs 0.205) – see also Tables 6-1 and 6-4) also support the above ordering. Of course, such huge numbers are useless and the researcher must find the far less number of equivalence classes of the geometrical Kekulé structures, as suggested Randić *et al.*⁶⁴

6.4.2.3. Sequence $Tr_s(Ca_{(3,2)c}(M))$.

In the above sequence, $Ca_{(3,2)c}$ represents the generalized operation $Ca_{(3,2)}$ with the faces of original map cut-off. It provides joint corazulenic flowers $[n : (7(5c))_n]$ Fw, $n = s_d$ which can be red $[n : (7(5d))_n]$ Fw as well; the co-Fw is a joint corazenic pattern $[n : (5, 7)_{n/2}]$ JFw (Figure 6-23). The joint is, however, not perfect (as in Capra Ca -transforms) but by means of the co-Fws core, thus being an Archimedean covering.

This is the only operation sequence that put together two corazulenic patterns, being in a mutual relation by SW. The multiplication factor is $m = 5d_0$ in the triangulated Platonic or $m = 15$ in the trivalent dual pair.⁹⁶

Rotating the spokes of the corazulenic flowers of 60T-15 results in 60T-15RO which is just C_{60} (Table 6-8, row 2). The transformed by $(Ca_{(3,2)c} \& Tr_s)$ of either octahedron $[4 : (7(5c))_4]$ Fw or cube $[3 : (7(5c))_3]$ Fw provide, after SW edge-rotation, one and the same 120C/O-15RO cage (Table 6-8, row 4). It is covered by sumanenes $[n : (5, 6)_{n/2}]$, both as Fw and co-Fw, in Archimedean coverings (Figure 6-24): $[n : (5, 6)_{n/2} \& s_{dp}]$ JFw; $n = s_{dd} = 8$; $s_{dp} = 6$ and $[n : (5, 6)_{n/2} \& s_{dd}]$ co-JFw, $n = s_{dp} = 6$; $s_{dd} = 8$.

Except 60T-15, which includes triangles, the other members of the series are of a high stability (Table 6-8, column 4), closed π -electron shells.

The HOMA index does not reflect properly the stability in this series or the aromaticity is not responsible here for the whole stability of a molecule (compare rows 2 and 4, columns 4 and 7).

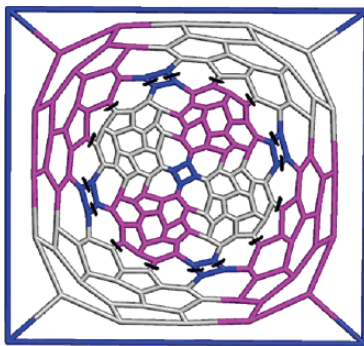


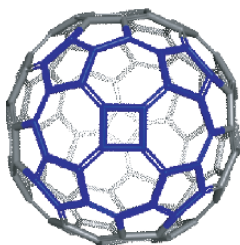
Figure 6-22. Divide et impera strategy in the case of 192O-24

The K -criterion is also in favor of $C_{60} = 60T-15RO$: 12,500 when compared with $60T-15$: 5,096. The same is true for the RO-cage derived from cube/octahedron: $120O-15RO$; 58,083,472, vs $120O-15$; 46,676,224. In comparison, $120T-30RO$; 136,861,056, supports the higher stability of this last 120-cage (designed by $Tr_s(Q(S_2(M)))$) vs the above isomers¹⁰³ (see also Table 6-4).

6.4.2.4. Sequence $Le(S_2(T))$

The sequence of the title (a non-commutative one) provides a disjoint sumanenic $[n : (5, 6)_{n/2}]DFw$; $n = s_{dd}$ pattern in a Platonic covering. The co-Fw forms an Archimedean joint of coronenic $[n : 6_n]Fw$, $n = s_{dp}$ and pentylenic $[p : (0, 5)_{p/2}]Fw$, $p = s_{dd}$ patterns. The tripentylene $[6 : (0, 5)_3]Fw$ can be viewed as an analogue of the triphenylene $[6 : (0, 6)_3]Fw$. Even no corazulenic covering is generated by the title sequence, the actual patterns are related to those designed by the above discussed sequences, this being the reason of including the current section.

(a) $120O-15$; $[n:(7(5c))_n \& s_{dp}]JFw$
 $n=s_d=4$; $s_{dp}=6$; Archimedean



(b) $120O-15$; $[n:(5,7)_{n/2} \& s_d]co-JFw$
 $n=s_{dp}=6$; $s_d=4$; Archimedean

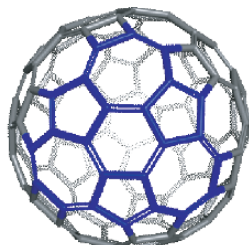
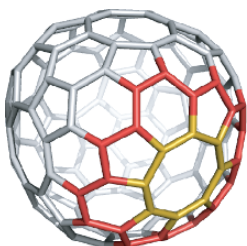


Figure 6-23. Two corazulenic flowers tessellating the $120O-15$ cage, designed by $Tr_s(Ca_{(3,2)c}(M))$.

(a) $120O-15RO$; $[n:(5,6)_{n/2} \& s_{dp}]JFw$
 $n=s_{dd}=8$; $s_{dp}=6$; Archimedean



(b) $120O-15RO$; $[n:(5,6)_{n/2} \& s_{dd}]co-JFw$
 $n=s_{dp}=6$; $s_{dd}=8$; Archimedean

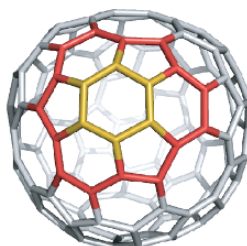


Figure 6-24. Two sumanenic patterns $[n : (5, 6)_{n/2}]Fw$; $n = 8$ (a) and $n = 6$ (b) in the SW edge-rotated $120O-15RO$ cage

Figures 6-25 and 6-26 illustrate the transformed by $Le(S_2(T))$ of tetrahedron and cube, respectively. Table 6-9 gives the energetic data and aromaticity in terms of HOMA index.

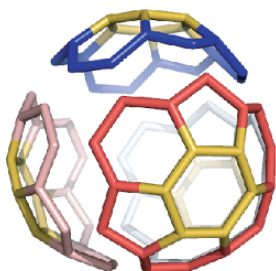
These cages are pretty stable structures, with the ratio HF/Gap lower than that of C_{60} . The most unstable appears the transform of cube 168C-21 (Table 6-9, row 3, columns 3 and 4), which is anti-aromatic, according to the negative global HOMA value. Quite strange is tripentylene, the most aromatic substructure, in terms of HOMA, while [8]coronene [(8:6₈)]Fw is the most anti-aromatic one, as expected.

E_π , calculated at Hückel level of theory (Table 6-9, column 6), does not fit neither with the PM3 data nor the HOMA results. The HOMO-LUMO gaps are well pronounced, as these cages show closed. π -shells.

Table 6-8. Data for corazulenic $[n : (7(5c))_n]$ cages (of $m = 15$), designed by $Tr_3(Ca_{(3,2)c}(M))$, and their SW isomers: heat of formation per atom, HF (kcal/mol); HOMO-LUMO GAP (eV); HF/Gap ($\times 100$; eV; PM3); strain energy per atom SE (kcal/mol; POAV1); total π -electron energy E_π (β -units; simple Hückel) and HOMA index of aromaticity.

Cage	Sym.	HF	Gap HF/Gap	SE	E_π shell	HOMA	HOMA- Fw	Fw
1	2	3	4	5	6	7	8	9
1 60T-15	T	21.350	5.360 17.284	9.716	1.525 cl	-0.090	-0.153 -0.026	$4 \times [3 : (7(5c))_3]$ JFw $4 \times [6 : (5, 7)_3]$ co-Fw
2 60T-15RO	I_h	13.512	6.593 8.893	8.257	1.553 cl	0.169	0.169 0.375	$4 \times [6 : (5, 6)_3]$ JFw $4 \times JR_6$ co-Fw
3 120O-15	O	13.717	5.007 11.888	4.057	1.514 cl	-0.073	-0.019 0.017	$6 \times [4 : (7(5c))_4]$ JFw $8 \times [6 : (5, 7)_3]$ co-Fw
4 120C/O-15RO	O	12.454	6.014 8.986	4.567	1.543 cl	-0.036	-0.054 0.116	$6 \times [8 : (5, 6)_4]$ JFw $8 \times [6 : (5, 6)_3]$ co-Fw

(a) 84T-21; [6:(5,6)₃]DFw
Platonic



(b) 84T-21; [(6:6₆)&(6:(0,5)₃)]co-JFw
Archimedean

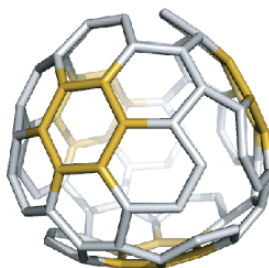


Figure 6-25. Disjoint sumanenic covering $[n : (5, 6))_{n/2}]DFw$, $n = s_{dd} = 6$ (a) and coronenic- pentylenic $[(6 : 6_6) \& (n : (0, 5))_{n/2}]co-JFws$, $n = s_{dd} = 6$ (b)

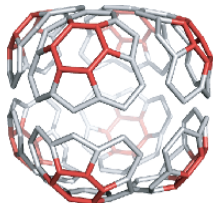
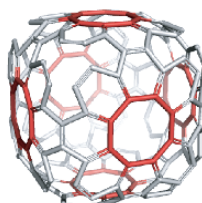
(a) 168C-21; [6;(5,6)₃]DFw
Platonic(b) 168C-21; [(8;6₈)&(6;(0,5)₃)]co-JFw
Archimedean

Figure 6-26. Platonic disjoint sumanenic covering $[n : (5, 6)]_{n/2}$ DFw; $n = s_{dd} = 6$ (a) and Archimedean joint of coronenic $[n : 6_n]$ Fw, $n = s_{dp} = 8$ and pentylenic $[p : (0, 5)]_{p/2}$ Fw, $p = s_{dd} = 6$ tessellation (b)

Table 6-9. Data for sumanenic $[n : (5, 6)]_{n/2}$ Fw; $n = s_{dd}$ cages (of $m = 21$) and their SW isomers: heat of formation per atom, HF (kcal/mol); HOMO-LUMO GAP (eV); HF/Gap ($\times 100$; eV; PM3); strain energy per atom SE (kcal/mol; POAV1); total π -electron energy E_π (β -units; simple Hückel) and HOMA index of aromaticity.

	Cage	Sym.	HF	Gap HF/Gap	SE	E _π shell	HOMA	HOMA- Fw	Fw
	1	2	3	4	5	6	7	8	9
1	84T- 21	<i>T</i>	11.795	6.234 8.213	6.334	1.559 cl	0.251	0.287 0.339 0.139	4 × [6 : (5, 6) ₃]DFw 4 × [(6 : 6 ₆)]co-JFw 4 × [(6 : (0, 5) ₃)]co-JFw
2	168O- 21	<i>O</i>	9.354	5.672 7.158	3.176	1.494 cl	0.245	0.223 0.491 −0.093	6 × [8 : (5, 6) ₄]DFw 8 × [(6 : 6 ₆)]co-JFw 6 × [(8 : (0, 5) ₄)]co-JFw
3	168C- 21	<i>O</i>	17.312	6.477 11.602	4.456	1.556 cl	−0.474	−0.009 −0.470 0.165	8 × [6 : (5, 6) ₃]DFw 6 × [(8 : 6 ₈)]co-JFw 8 × [(6 : (0, 5) ₃)]co-JFw

6.5. Retro Endo-Kroto Reaction

It is the place to mention another operation, which model the so-called Endo-Kroto¹⁰⁴ reaction (Figure 6-27), claimed in the mechanisms of fullerene growth. A C_2 unit is inserted into a hexagonal face, thus increasing the number of carbon atoms of a fullerene. In our case, more interesting is the “retro” operation, denoted *REK*, which leads to the smaller precursor.⁹⁶

Several cages having fused pentagons (i.e., pentalenes) can be looked for the *REK* operation: 204T-51RO (Table 6-5, row 1) leads to C_{180} (derived from $C_{20} = D$ by *Le&Le*; Table 6-1, row 2) and 300I-15 leads to C_{240} (derived from D by *Le*_(2,2)—Table 6-1, row 3). The products of *REK* operations above mentioned are included in the list of the most stable cages herein discussed. Other examples are given in Table 6-10; the



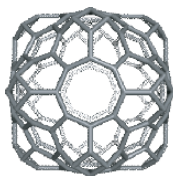
Figure 6-27. The Endo-Kroto growth operation.

name of these objects includes information on both the original cage and product by *REK*. These objects represent somewhat strained structures, with relatively high HF values. HOMA index classifies them as anti-aromatic or at most non-aromatic (Table 6-10, columns 7 and 8). They are, however, closed shells, with high HOMO-LUMO gap (column 4). The cage 192*O*_24*RO*_144*REK* (Figure 6-28) shows a tessellation equivalent to the “naphthylenic” covering embedded on the torus;¹⁰⁵ its $K = 70,556,640,625$.

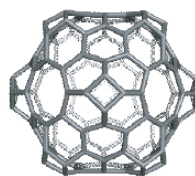
Table 6-10. Data for cages derived by the retro Endo-Kroto operation: heat of formation per atom, HF (kcal/mol); HOMO-LUMO GAP (eV); HF/Gap ($\times 100$; eV; PM3); strain energy per atom SE (kcal/mol; POAV1); total π -electron energy E_π (β -units; simple Hückel) and HOMA index of aromaticity.

Cage $6n$	Sym.	HF	Gap HF/Gap	SE	E_π	HOMA	HOMA -Fw	Fw
1	2	3	4	5	6	7	8	9
1 96 <i>T</i> _24 <i>RO</i> _72 <i>REK</i>	O_h	17.23	6.479 11.539	9.250	1.542 cl	0.039	0.117	$6 \times [4 : 6_4]\text{Fw}$
2 192 <i>O</i> _24 <i>RO</i> _144 <i>REK</i>	O_h	20.187	6.937 12.628	7.719	1.540 cl	-0.357	0.450 -0.229 -0.229 -0.235	$8 \times [R_6]$ $8 \times [6 : 6_6]\text{Fw}$ $6 \times [8 : 6_8]\text{Fw}$ $12 \times [4 : 6_4]\text{Fw}$
3 120 <i>O</i> _15_96 <i>REK</i>	O_h	14.152	5.970 10.287	7.405	1.550 cl	0.145	0.773 0.031	$16 \times [R_6]$ $6 \times [4 : 6_4]\text{DFw}$

(a) four-fold symmetry



(b) two-fold symmetry

Figure 6-28. Tessellation by retro Endo-Kroto operation: 192*O*_24*RO*_144*REK*

Conclusions

Sequences of classical or single generalized map operations were used to obtain corannulenic and corazulenic flowers as covering patterns for nanostructures.

The aromaticity of some cages tessellated by these chemically interesting supra-faces is discussed in terms of several criteria. The covering was given as π -electron partitions within Kekulé valence structures.

As a structural/geometric parameter of aromaticity, HOMA index enabled evaluation of local aromatic character of the discussed supra-faces and brought evidence for several dominant Kekulé valence structures.

Disjoint corannulenic flowers, in Platonic coverings, provided fully resonant graphs, associated to the most aromatic/stable structures herein discussed. Next stable cages were those having a disjoint corazulenic $[n : (7(5c))_n]$ Fw or $[n : (7(5d))_n]$ Fw coverings; these supra-faces were isomerized by the SW edge-rotations. Of particular interest was the SW rotation of $[n : (7(5d))_n]$ Fw, leading to disjoint corazulenic/isocoronenic flowers $[n : (5, 7)_{n/2}]$, predicted to show *super-aromatic* character, on the magnetic criterion.

New generalized perfect Clar structures, with the 2-factor designed as pentalenes or corazulenic $[4 : (7(5d))_4]$ disjoint flowers have been evidenced. Noticeable in this respect is the “Kekulé-Dewar” valence structure of the cage C_{192} .

Alternative co-Fw description revealed some Archimedean disjoint coverings, involved in the predicted good stability/aromaticity of some newly proposed cages.

Several operation sequences enabled joint flower coverings, with good stability and locally manifested aromatic (or anti-aromatic) character.

A retro Endo-Kroto operation was proposed to go back from cages tessellated with pentalenes (known as anti-aromatic, destabilizing patterns) to the more stable precursors.

All the herein described operations and their products are aimed to be helpful in the process of molecular structure elucidation and in guiding researchers in finding novel nano-structured materials.

References

1. T. Pisanski and M. Randić, in: *Geometry at work: a collection of papers showing applications of Geometry* (Gorini, C. A., Ed.) *Math. Assoc. Amer.*, 2000, **53**, 174–194.
2. A. J. Stone and D. J. Wales, *Chem. Phys. Lett.*, 1986, **128**, 501–503.
3. H. Ueno, S. Osawa, E. Osawa, and K. Takeuchi, *Fullerene Sci. Technol.*, 1998, **6**, 319–338.
4. Y. F. Zhao, Y. Lin, and B. I. Yakobson, *Phys. Rev. B*, 2003, **68**, 233403(1)-(4).
5. P. W. Fowler and J. I. Steer, *J. Chem. Soc., Chem. Commun.*, 1987, 1403–5.
6. M. V. Diudea, *Phys. Chem., Chem. Phys.*, 2004, **6**, 332–339.
7. P. W. Fowler G. Brinkmann and C. Justus, *J. Chem. Inf. Comput. Sci.*, 2003, **43**, 917–927.
8. J. E. Graver, *MATCH, Commun. Math. Comput. Chem.*, 2003, **48**, 189–196.
9. D. J. Klein, *Phys. Chem. Chem. Phys.*, 2002, **4**, 2099–2110.
10. G. Brinkmann, J. E. Graver and C. Justus, *J. Math. Chem.*, 2007 (in press).
11. F. Harary, *Graph Theory*, Addison-Wesley, Reading, MA, 1969.

12. J. L. Gross and T. W. Tucker, *Topological graph theory*, Dover Pubs, Dover, 2001.
13. L. Euler, *Novi Comment.Acad.Sci. I. Petropolitanae*, 1758, **4**, 109–160.
14. M. V. Diudea, M. Ştefu, P. E. John, and A. Graovac, *Croat.Chem.Acta*, 2006, **79**, 355–362
15. M. Ştefu and M. V. Diudea, *CageVersatile* 1.3, “Babes-Bolyai” University, 2003.
16. E. C. Kirby, in: *From Chemical Topology to Three - Dimensional Geometry*, (A. T. Balaban, Ed.), Plenum Press, New York, 1997, pp. 263–296.
17. M. Bühl and A. Hirsch, *Chem. Rev.*, 2001, **101**, 1153–1183.
18. M. Randić, *Chem. Rev.*, 2003, **103**, 3449–3605.
19. I. Gutman, M. Milun, and N. Trinajstić, *MATCH, Commun. Math. Comput.Chem.*, 1975, **1**, 171–175.
20. I. Gutman, M. Milun, and N. Trinajstić, *J. Am. Chem. Soc.*, 1977, **99**, 1692–1704.
21. J.-i. Aihara, *J. Am. Chem. Soc.*, 1976, **98**, 2750–2758.
22. R. C. Haddon, *J. Am. Chem. Soc.*, 1987, **109**, 1676–1685.
23. R. C. Haddon, *J. Am. Chem. Soc.*, 1990, **112**, 3385–3389.
24. R.C. Haddon, *J. Am. Chem. Soc.*, 1997, **119**, 1797–1798.
25. R.C. Haddon, *J. Am. Chem. Soc.*, 1998, **120**, 10494–10496
26. P. W. Fowler and T. Pisanski, *T. J. Chem. Soc. Faraday Trans.*, 1994, **90**, 2865–2871
27. M. Randić, *J. Chem. Inf. Comput. Sci.*, 2004, **44**, 365–372.
28. I. Gutman, D. Vukićević, A. Graovac, and M. Randić, *J. Chem. Inf. Comput. Sci.*, 2004, **44**, 296–299.
29. A. Miličević, S. Nikolić, and N. Trinajstić, *J. Chem. Inf. Comput. Sci.*, 2004, **44**, 415–421.
30. M. Randić and A. T. Balaban, *Polycyclic Arom. Comp.*, 2004, **24**, 173–193.
31. A. T. Balaban and M. Randić, *J. Chem. Inf. Comput. Sci.*, 2004, **44**, 50–59.
32. A. T. Balaban and M. Randić, *New J. Chem.* 2004, **28**, 800–806.
33. D. Vukicevic, M. Randić and A. T. Balaban, *J. Math. Chem.*, 2004, **36**, 271–279.
34. A. T. Balaban and M. Randić, *J. Chem. Inf. Comput. Sci.*, 2004, **44**, 1701–1707.
35. E. Clar, *Polycyclic Hydrocarbons*, Acad. Press, London, 1964.
36. E. Clar, *The Aromatic Sextet*, Wiley, New York, 1972.
37. N. Trinajstić, *Chemical Graph Theory*, CRC Press, Boca Raton, FL, 1992, p. 161, 187.
38. P. W. Fowler, D. J. Collins, and S. J. Austin, *J. Chem. Soc., Perkin Trans. 2*, 1993, 275–277.
39. S. J. Austin, P. W. Fowler, P. Hansen, D. E. Manolopoulos, and M. Zheng, *Chem. Phys. Lett.*, 1994, **228**, 478–484.
40. X. Liu, D. J. Klein, W. A. Seitz, and T. G. Schmalz, *J. Comp. Chem.*, 1991, **12**, 1265–1269
41. G. G. Cash, *J. Chem. Inf. Comput. Sci.*, 1998, **38**, 58–61
42. M. Randić, *Chem. Phys. Lett.*, 1976, **38**, 68–70.
43. M. Randić, *J. Am. Chem. Soc.*, 1977, **99**, 444–450.
44. M. Randić, *Tetrahedron*, 1977, **33**, 1905–1920.
45. M. Ozaki and A. Takahashi, *Chem. Phys. Lett.*, 1986, **127**, 242–244.
46. R. L. Disch and J. M. Schulman, *Chem. Phys. Lett.*, 1986, **125**, 465–466.
47. A. Julg and Ph. Francois, *Theor. Chim. Acta*, 1967, **7**, 249–261.
48. A. Julg, in: *Aromaticity, Pseudoaromaticity, Anti-Aromaticity* (E. D. Bergmann and B. Pullman, Eds.), Israel Acad. Sci. Human., Jerusalem, 1971, p 383.
49. C. W. Bird, *Tetrahedron*, 1985, **41**, 1409 - 1414.
50. T. M. Krygowski, *J. Chem. Inf. Comput. Sci.*, 1993, **33**, 70–78.
51. T. M. Krygowski and A. Ciesielski, *J. Chem. Inf. Comput. Sci.*, 1995, **35**, 1001–1003.
52. Cs. L. Nagy and M. V. Diudea, *JSCHEM* software, Babes-Bolyai University, Cluj, 2005
53. M. J. S. Dewar, *Angew. Chem., Int. Ed. Engl.*, 1971, **10**, 761–870.
54. K. Jug and A. M. Koester, *J. Phys. Org. Chem.* 1991, **4**, 163–169.
55. A.T. Balaban, D.C. Oniciu, and A.R. Katritzky, *Chem. Rev.*, 2004, **104**, 2777–2812
56. I. Lukovits, A. Graovac, E. Kalman, G. Kaptay, P. I. Nagy, S. Nikolić, N. Trinajstić, *J. Chem. Inf. Comput. Sci.*, 2003, **43**, 609–614.
57. I. Lukovits and D. Janežič, *J. Chem. Inf. Model.*, 2004, **44**, 410–414.
58. I. Lukovits, *J. Chem. Inf. Model.*, 2004, **44**, 1565–1570.
59. K. Salem, *MATCH, Commun. Math. Comput. Chem.*, 2005, **53**, 419–426.
60. K. Salem, *MATCH, Commun. Math. Comput. Chem.* 2005, **53**, 427–440.

61. H. Abeledo and G. Atkinson, in: *Discrete Mathematical Chemistry*, (P. Hansen, P. W. Fowler, and M. Zheng, Eds), DIMACS Series, in Discrete Mathematics and Theoretical Computer Science 51, Am. Math. Soc., Providence, RI, 2000, 1–8.
62. S. J. Cyvin, B. N. Cyvin and J. Brunvoll, *MATCH, Commun. Math. Comput. Chem.*, 1990, **25**, 105–113.
63. J. R. Dias, *J. Chem. Inf. Model.*, 2005, **45**, 562–571.
64. D. Vukièvić, H. W. Kroto and M. Randić, *Croat. Chem. Acta*, 2005, **78**, 223–234.
65. K. Fries, *J. Liebigs Ann. Chem.*, 1927, **454**, 121–324.
66. W.-Ch. Shiu, P. Ch. B. Lam, and H. Zhang, *Theochem*, 2000, **4**, 0210.
67. J. R. Dias, *J. Chem. Inf. Comput. Sci.*, 1999, **39**, 144–150.
68. S. J. Cyvin and I. Gutman, *Kekule Structures in Benzenoid Hydrocarbons*, (Lecture Notes in Chemistry 46) Springer-Verlag, Berlin, 1988.
69. J. R. Dias, *Thermochimica Acta*, 1987, **122**, 313–337.
70. J. R. Dias, *J. Chem. Inf. Comput. Sci.*, 1991, **31**, 89–96.
71. E. C. Kirby, *Fullerene Sci. Technol.*, 1994, **2**, 395–404.
72. E. C. Kirby, *MATCH, Commun. Math. Comput. Chem.*, 1996, **33**, 147–156.
73. E. C. Kirby, in: *Nanostructures-Novel Architecture*, (M. V. Diudea, Ed.), NOVA, New York, 2005, pp. 175–191.
74. S. Nikolić and N. Trinajstić, *Gazz, Chim. Ital.*, 1990, **120**, 685–689.
75. I. Gutman and S. Cyvin, *MATCH, Commun. Math. Comput. Chem.*, 1994, **30**, 93–102.
76. I. Gutman, S. J. Cyvin, V. Petrovic and A. Teodorovic, *Polycyclic Aromatic Compounds*, 1994, **4**, 183–189.
77. D. J. Klein and H. Zhu, in: *From Chemical Topology to Three - Dimensional Geometry*, (A. T. Balaban, Ed.), Plenum Press, New York, 1997, pp. 297–341.
78. V. Eberhard, *V. Zur Morphologie der Polyeder*, Leipzig, Teubner, 1891.
79. P. W. Fowler, *Chem. Phys. Lett.*, 1986, **131**, 444–450.
80. M. V. Diudea, *Phys. Chem., Chem. Phys.*, 2005, **7**, 3626–3633.
81. M. V. Diudea, *Forma* (Tokyo), 2004, **19** (3), 131–163.
82. M. V. Diudea, in: M. V. Diudea, Ed., *Nanostructures-Novel Architecture*, NOVA, New York, 2005, 203–242.
83. M. V. Diudea, in: M. V. Diudea, Ed., *Nanostructures-Novel Architecture*, NOVA, New York, 2005, 111–126.
84. H. Hosoya, Y. Tsukano, K. Nakada, S. Iwata, and U. Nagashima, *Croat. Chem. Acta*, 2004, **77**, 89–95.
85. H. Hosoya, Y. Tsukano, M. Ohuchi, and K. Nakada, in: *Computer Aided Innovation of New Materials II*, (M. Doyama, J. Kihara, M. Tanaka, and R. Yamamoto, Eds.), Elsevier, Amsterdam, 1993 pp. 155–158.
86. X. Liu, D. J. Klein, and T. G. Schmalz, *Fullerene Sci. Technol.*, 1994, **2**, 405–422.
87. E. E. B. Campbell, P. W. Fowler, D. Mitchell, and F. Zerbetto, *Chem. Phys. Lett.*, 1996, **250**, 544–548.
88. A. Ayuela, P. W. Fowler, D. Mitchell, R. Schmidt, G. Seifert, and F. Zerbetto, *J. Phys. Chem.*, 1996, **100**, 15634–15636.
89. E. Albertazzi, C. Domene, P. W. Fowler, T. Heine, G. Seifert, C. Van Alsenoy, and F. Zerbetto, *Phys. Chem. Chem. Phys.*, 1999, **1**, 2913–2918.
90. M. F. Dinca, S. Cigher, M. Stefu, F. Gherman, K. Miklos, Cs. L. Nagy, O. Ursu and M. V. Diudea, *Carpathian J. Math.*, 2004, **20**, 211–221.
91. E. Clar, U. Sanigok, M. Zander, *Tetrahedron*, 1968, **24**, 2817–2823
92. J. M. Schulman, and R. L. Disch, *J. Phys. Chem. A*, 1997, **101**, 9176–9179.
93. T. A. Keith and R. F. W. Bader, *Chem. Phys. Lett.*, 1993, **210**, 223–231.
94. P. Lazzeretti, in: *Progress in Nuclear Magnetic Resonance Spectroscopy*, (J. W. Emsley, J. Feeney, and L. H. Sutcliffe, Eds.) Elsevier, Amsterdam, 2000, **36**, 1–88.
95. A. Acocella, E. W. A. Havenith, E. Steiner, P. W. Fowler, and L. W. Jenneskens, *Chem. Phys. Lett.*, 2002, **363**, 64–72.
96. M. V. Diudea, A. E. Vizitiu, *J. Math. Chem.*, 2007 (in press).

97. A. Ciesielski, M. K. Cyranski, T. M. Krygowski, P. W. Fowler, and M. Lillington, *J. Org. Chem.* 2006, **71**, 6840–6845.
98. H. A. Jahn and E. Teller, *Proc. R. Soc. (London)*, 1937, **A161**, 220–235.
99. M. Randić and T. Pisanski, *Rep. Mol. Theory*, 1990, **1**, 107–114.
100. M. Lillington, P. W. Fowler and M. V. Diudea, *Polish J. Chem.*, 2007 (in press).
101. M. V. Diudea and D. Vukièević, *J. Nanosci. Nanotechnol.*, 2007, **7**, 1321–1328.
102. D. Vukièević and M. Randić, *Chem. Phys. Lett.*, 2005, **401**, 446–450.
103. S. Chigher and M. V. Diudea, *Kekule structure counter 1.1*, Babes-Bolyai” University, 2006.
104. M. Endo and H. W. Kroto, *J. Phys. Chem.*, 1992, **96**, 6941–6944.
105. M. V. Diudea, *Phys. Chem., Chem. Phys.*, 2002, **4**, 4740–4746.

Chapter 7

Triply Periodic Nanostructures

7.1. Introduction

Carbon allotropes, intensively studied in the last decade,^{1–5} consist of either finite or infinite entities, structured at molecular or intermolecular level, with sizes ranging from angstroms to nano- or up to micro-meters. Function of their (repeat) unit dimensionality, one can distinguishes:

- (i) *zero-dimensional* sp^2 -bonded objects, of (quasi) spherical shape, held together by van der Waals forces; this class includes the carbon fullerenes and related functionalized structures (eventually showing non-classical tessellation, lattice heteroatoms, endo-or exo-hedral metals and or chemical functional groups).
- (ii) *one-dimensional* sp^2 -bonded objects, of linear shape, either finite (capped), hemi-capped or open/infinite molecular structures; their tessellation is polyhex (by virtue of Euler theorem⁶), with caps tilted as in fullerenes.
- (iii) *two-dimensional* sp^2 -lattice of graphite, of hexagonal tiling, with cohesion ensured by van der Waals forces.
- (iv) *three-dimensional* sp^3 -lattice of diamond, with repeat units of tetrahedral symmetry, held together by covalences.
- (v) *three-dimensional* sp^2 -lattices of spongy carbon.

This last class of allotropes deserves more attention.

A three-dimensional, covalently bonded sp^2 -carbon network is necessarily conceivable to feel the gap between the above mentioned lower-dimensional allotropes and the diamond. Several theoretical conjectures have predicted the possibility of negatively curved graphite-like structures,^{7–12} as described by the infinite triply periodic minimal surfaces TPMSs. These hypothetical structures have been termed schwarzites, in the honor of H. A. Schwarz,^{13,14} who first investigated, in the early nineteen century, the differential geometry of this class of surfaces.

Total energy calculations, carried out with *ab initio* methods^{8,10} as well as with classical¹⁵ and tight-binding¹⁶ simulations, have shown that carbon schwarzites are energetically more favorable than fullerenes of comparable absolute Gaussian curvature.¹⁷ These data suggested that negatively curved carbon networks may appear during the fullerene and nanotube synthesis, at least as random (amorphous) schwarzites, if not in a periodic, crystalline form.

Porous carbon allotropes, synthesized by plasma-enhanced CVD, by Zaakhidov *et al.*,¹⁸ have various structures: diamond or inverse opal, depending on the synthesis conditions. Graphite inverse opals, obtained by surface templating, provide examples of both dielectric and metallic crystals. The Raman spectra of the inverse opal materials (tetrahedral and cubic, respectively) indicated the presence of sp^2 carbon. The synthesis of large amounts of carbon foam (obtained by using pulsed microplasma, in the presence of a metallorganic catalyst) was reported by Barborini *et al.*¹⁹ and Benedek *et al.*¹⁷ They brought clear evidences of a nanostructured 3D lattice, consisting entirely of covalently bonded sp^2 carbon. The simulated HRTEM images showed a spongy carbon with the topology of random schwarzites. The extremely high porosity (pores with diameters ranging from 50 to 600 nm)¹⁷ and low density of these nanoporous carbon materials suggested many possible applications, as thermal insulators, in catalysis, in gas and energy storage, in gas and liquid purification, in templating biomaterials and in electrochemistry, as well.

Carbon sponges are also useful in investigating negatively curved lattices. They seem to result by self-assembling of various repeat units, some of them encountered in 3D junctions of nanotubes.

7.2. Background on Surface Curvature

An embedding is a representation of a graph on a surface S such that no edge-crossing occurs.^{20,21} Two embeddings ε_1 and ε_2 are combinatorially equivalent if there is a one-to-one correspondence between their vertices v , edges e , and faces f , such that the incidence between their constitutive substructures is preserved.

A polyhedral lattice, embedded in an *orientable surface* S obeys the Euler's theorem:⁶

$$v - e + f = \chi(S) = 2(1 - g(s)) \quad (7.1)$$

where $\chi(S)$ is the Euler characteristic and g the genus (*i.e.*, the number of holes performed in a plastic sphere to make it homeomorphic to S). Positive/negative χ values indicate positive/negative curvature of a lattice embedded in S .

A surface is *orientable*, when it has two sides, or it is *non-orientable*, when it has only one side, like the Möbius strip.

The negative curvature can be induced in graphite (the reference, of zero curvature) by replacing hexagons by heptagons, or larger sized rings. Such nets form only open structures, in the opposite to those having pentagons or smaller rings, which bring positive curvature, and which form closed cages/polyhedra.

Curvature is the amount by which a geometric object deviates from the planarity. It is usually measured either as *Gaussian curvature* K or as *mean curvature* H . These are defined at each point on the surface as functions of the surface principal curvatures at the point:

$$K = \pm k_1 \cdot k_2 \quad (7.2)$$

$$H = \frac{1}{2} (k_1 + k_2) \quad (7.3)$$

To evaluate these at a given point of the surface, consider the intersection of the surface with a plane containing a fixed normal vector at the point. This intersection is a plane curve, having a curvature $k = 1/r$; if the plane is varied, this curvature will change, and there are two extreme values – the maximal and the minimal curvature, called the *principal curvatures*, k_1 and k_2 . Accordingly, the extreme directions are called principal directions. Usually, a curvature is taken positive if the curve turns in the same direction as the surface's chosen normal, otherwise it is negative.^{22–24}

A surface S is *flat* if $K(p) = 0$ and it is *minimal* if $H(p) = 0$, for every $p \in S$.

The integral of the Gaussian curvature over the whole surface is closely related to the Euler characteristic $\chi(S)$ (*Gauss-Bonnet* theorem) of the surface:^{22,25}

$$\int_S K dS = 2\pi\chi(S) \quad (7.4)$$

The above theorem relates the geometric curvature to the topology, as shown in eq 7.1 for an orientable surface. In case of a non-orientable surface, the Euler characteristic reads:

$$\chi(S) = 2 - n(S) \quad (7.5)$$

In the above relation, n is the number of *cross-caps* needed to be attached to the sphere to make it homeomorphic to that non-orientable surface.²⁶

If S is a topohedral surface in 3D, the count of vertices v , edges e and faces f , is given by the Euler relation (7.1). If $g = 0$, then (7.1) reads:

$$v - e + f = 2 \quad (7.6)$$

If a polyhedron has all degree-3 vertices, and each edge is shared by two faces, then:²⁷

$$3v = \sum_s s \cdot f_s = 2e; f = \sum_s f_s \quad (7.7)$$

where f_s is the number of s -gonal faces and (7.1) becomes:

$$(1/3) \sum_s s \cdot f_s - (1/2) \sum_s s \cdot f + \sum_s f_s = 2(1 - g) = \chi \quad (7.8)$$

$$\sum_s (6 - s) \cdot f_s = 12(1 - g) = 6\chi \quad (7.9)$$

Relation (7.9) gives the number of s -folded polygons for a surface of a given genus. Special cases are the *Platonic*- (with a single kind of polygons) and the *Archimedean*- (with two kinds of polygons) *tessellations*. If we consider polygons with $s = 3, 4 \dots 9$ sides, equation (7.9) reads:

$$3f_3 + 2f_4 + f_5 - f_7 - 2f_8 - 3f_9 = 12(1 - g) \quad (7.10)$$

In (7.10), $f_3, f_4 \dots f_9$ represent *defects* in the graphitic covering, leading to the curvature of the polyhedra; observe f_6 is not present (since hexagon produces zero Gaussian curvature), the number of hexagons being arbitrary. Archimedean fullerenes must always contain 12 f_5 ; thus f_6 comes out from (7.7):

$$\begin{aligned} 5 \cdot f_5 + 6 \cdot f_6 &= 60 + 6 \cdot f_6 = 3v \\ f_6 &= v/2 - 10 \end{aligned} \quad (7.11)$$

There is a theorem of *Descartes*^{22,23} stating that the overall angular defects (*i.e.*, disclinations) are proportional to the Euler's characteristic, if S is a topohedral surface in 3D:

$$\sum_p^s \phi_p = 2\pi\chi(S) \quad (7.12)$$

Mean curvature is closely related to the first variation of surface area. Surfaces everywhere having the mean curvature $H = 0$ are called *minimal surfaces* (*i.e.*, with minimal local area). The shapes taken by soap films are minimal surfaces. Unlike Gaussian curvature, the mean curvature depends on the embedding, for instance, a cylinder and a plane are locally isometric but the mean curvature of a plane is zero while that of a cylinder is nonzero.

7.3. Carbon Lattices Embedded in TPMSs

Triply periodic minimal surfaces TPMSs have, by definition, translational symmetries in three independent directions. They are saddle-shaped, everywhere except at certain *flat points*. A TPMS belongs to one of the crystallographic space groups as its symmetry group and, if it has no self-intersections, it partitions the space into two disjoint labyrinthine regions. Its topology is characterized by two interlacing networks, the *labyrinth graphs*.

A carbon lattice, having all sp^2 atoms, can be embedded in a TPMS. According to relations (7.1) and (7.4), a TPMS graphene will have a negative average Gauss curvature $\chi < 0$, (unlike fullerenes with $\chi > 0$, or open and toroidal tubulenes, with $\chi = 0$) and zero mean curvature $H = 0$, for every point belonging to the graphene net. It was conjectured that a covalent lattice, of all sp^2 carbon, embedded in a minimal periodic surface is energetically more favorable than fullerenes of comparable

Gaussian curvature.¹⁷ The generic name adopted for such carbon allotropes is *periodic schwarzites*.^{11,17}

Periodic schwarzites are generated by covalent connections of identical repeat units. The unit cell may contain one or more such units/elements. The centers of the elements can be viewed as the nodes of a corresponding dual lattice, *i.e.*, one of the two complementary labyrinths.

The dual lattice of the Four-connected diamond structure defines a class of cubic schwarzites, with two elements per unit cell (*i.e.*, *bielemental* schwarzites). They are tessellations of a D-type minimal surface. *Monoelemental* cubic schwarzites with a *sc*, or *bcc* or *fcc* dual lattice are also possible. P-type schwarzites have the structure of a simple monoelemental cubic lattice. They include a special class of structures known as polybenzenes.²⁸

Numerical computations of minimal surfaces may be done with several techniques. The classical method assumes knowledge of the Weierstrass integration formulas and does a numerical integration. Another method relies on the finite element theory and needs the calculation of partial differential equations with numerical techniques.²⁹

For visual representation, a minimal surface can simply be approximated by a trigonometric expression^{14,30,31} corresponding to the lowest-order terms of a Fourier expansion. For example, D- and P-type surfaces are well described in the (*x*, *y*, *z*) space by:

$$\text{D-type} : \cos(x) \cos(y) \cos(z) + \sin(x) \sin(y) \sin(z) = 1 \quad (7.13)$$

$$\text{P-type} : \cos(x) + \cos(y) + \cos(z) = 0 \quad (7.14)$$

Each (open) Platonic object is the zeroth element of an infinite series of larger schwarzites, obtained by inserting an arbitrary number of hexagons ($f_6 > 1$) in each unit. For example, the D-type schwarzites of Platonic-Archimedean tessellation (with only heptagons and hexagons) form a family of crystals with $2(28 + 2f_6)$ atoms in the unit cell. Figure 7-1 illustrates the zero members of the D- and P-type series of schwarzites, designed by (open) Ca/S_1 map operation as Platonic (7,3) coverings.

Isomeric forms of schwarzites are possible, by analogy to spherical fullerenes (see the next section).

The repeat units of schwarzites can be seen as *junctions of nanotubes*, of minimal length. Systematic search of unit cells of possible schwarzites, by the aid of map operations (see Chapter 5), will be presented in the next section and in the Atlas of junctions.

Some other surfaces with cubic symmetry have been described (named here by the Schoen's notation³²): IWP, FRD, OCTO, C(D), and G.²⁹

At the end of this section, we recall that random schwarzites have experimentally been obtained by supersonic deposition of carbon clusters in the presence of catalyst nanoparticles,¹⁷ and look like a porous spongy carbon. The numerical simulation

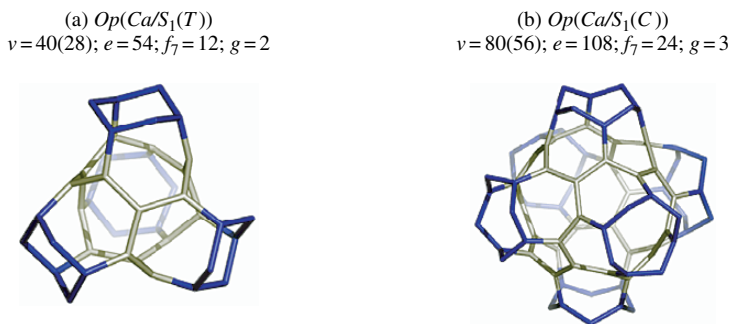


Figure 7-1. The first three members of the infinite families of D- (a) and P-type (b) schwarzites; the numbers in brackets account for the atoms in the repeat units.

of the TEM images brought evidence that random schwarzites grow in the form of a TPMS. These new structures consist of a fully covalent 3D lattice of sp^2 carbon.

Among the most prominent scientists who contributed to the development of TPMSs theory we enumerate: Schwartz,^{13,14} Neovius,³³ Schoen,³² Coxeter,³⁴ Fischer and Koch,³⁵ *etc.* The scientists of the last decade have added experimental evidences of the molecular realization of these fascinating structures.

7.4. Nanotube Junctions

The operation leading to open (repeat) units, as those encountered in schwarzites, is called Op_r (Chapter 5, eq 5.23) and is an E_r homeomorphic transformation of the parent edges. Most often $r = 1$ thus being omitted. The Op operation can be coupled to any map operation $\Omega(G)$ as $Op(\Omega(G))$ and performed in various ways to obtain either pro-chiral or achiral units.

Unit blocks provided by opening map transforms could model the junctions of carbon nanotubes; these are obtainable by “nano-welding” crossing tubes in an electron beam.³⁶

The genus of an open structure is calculable from (7.1). For the five Platonic solids, the genus of the corresponding $Op(G)$ is: 2 (Tetrahedron T); 3 (Cube C); 4 (Octahedron O); 6 (Dodecahedron D) and 10 (Icosahedron I). However, due to the dual parity, the transformed (open) structures (*e.g.*, nanotube junctions) belong to only three classes of symmetry: tetrahedral ($g = 2$); octahedral ($g = 3$) and icosahedral ($g = 6$).

To the above, a class of digonal symmetry ($g = 1$) and some of planar symmetry (of $g = 1.5, 2, 2.5, \dots$) have to be added.

Insertion of hexagons in the primary $Op(\Omega(G))$ junctions, in view of strain relief, can be achieved by a second map operation $\Omega_2(Op(\Omega_1(G)))$. Observe the

map operation preserves the genus of the parent structure and its class of symmetry. In the following, the main classes of junctions are presented.

7.4.1. Digonal Junctions

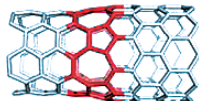
A digonal junction or simply a link between two nanotubes of same or different tessellation is the simplest junction (Figure 7-2a); observe the number of pentagons equals that of heptagons. Capping a nanotube by fullerene halves can also be considered as a digonal junction. Coalescence of spherical fullerenes to peanut-shaped periodic structures (Figure 7-2b) or a single torus realization (Figure 7-3 – see also Chapter 2) are also digonal junction objects. Conetori and DWT represent different types of toroidal structures (see Chapter 3). Bent tubes can be viewed as digonal junctions (Figure 7-4). Other examples are given in the Gallery.

The occurrence of such junctions in real synthesis of nanotubes, or in nano-welding under electron beam has been reported.³⁶ Shapes of bamboo, tapers, knees, *etc.* have been observed.^{37–40} Digonal junctions of Z&A nanotubes have been proposed as nano-diodes.⁴¹ Carbon tori is believed to be obtained experimentally.⁴²

7.4.2. Planar Junctions

Experimental synthesis of Y-type and T-type junctions have been reported.^{36,39,43–46} For such objects, non-integer g -values are calculated, from the Euler's theorem or as $g = \text{no. open faces}/2$; in case of Y-type junctions $g = 1.5$ (Figure 7-5).

(a) $J[(5,5)\&(10,0)]$
 $v = 140; e = 200; f_6 = 50; f_5 = 5; f_7 = 5; g = 1$



(b) $v(k\ 6^k\ (56)^k\ (65)^k\ 7^k - Z[2k,1] - r)$
 $k = 5; r = 4; v = 12kr = 240$

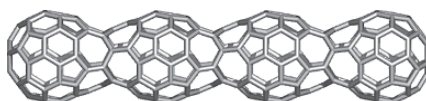


Figure 7-2. An A/Z-junction and a periodic kf_z -tubulene.

$T_{v((566)^{k/2}\ (665)^{k/2}\ 7 - Z[2k,0] - r)}; k = 6; r = 30; v = 8kr = 1440$

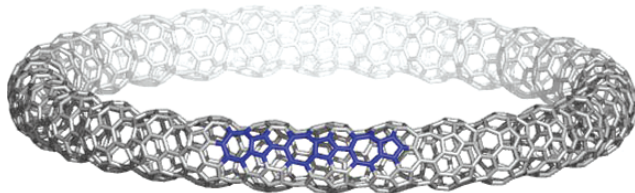
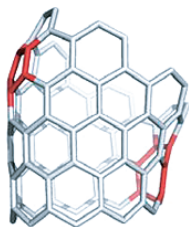


Figure 7-3. A toroidal embedding of the $((5,6,7)3)$ pattern.

(a) $K[TU(9,0)&TU(6,6)]$
 $v=87; e=120; f_6=31; f_5=1; f_7=1; g=1$



(b) $T(6 \times K[TU(5,5)&TU(5,5)])$
 $v=780; f_6=366; f_5=12; f_7=12; g=1$ SE = 2.629

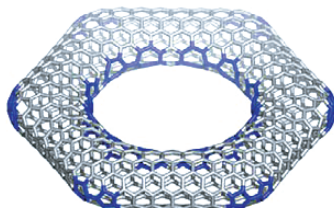
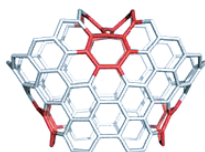


Figure 7-4. A knee and a torus made by knees.

(a) $Y[TU(9,0)&TU(6,6)]$
 $v=132; e=183; f_6=44; f_7=6; g=1.5$



(b) $Y[TU(9,0)&TU(6,6)]$
 $v=432; g=1.5$

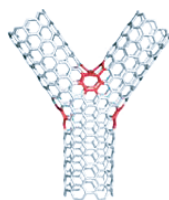
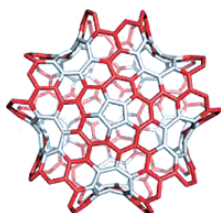


Figure 7-5. An Y-junction.

(a) $D_5[TU(4,8)]$
 $v=70; e=; f_6=90; f_5=2; f_8=10; g=2.5$



(b) $D_5[TU(4,8)]$
 $v=670; g=2.5$



Figure 7-6. A D_5 -junction.

Analogously, for a D_5 -type junction, a value of $g = 2.5$ is obtained (Figure 7-6). Observe the chirality of both the body and tubes of this junction, provided by the pro-chiral operation Capra. Also observe the parent faces are surrounded by their own hexagons, forming an Archimedean $[(5 : 6_5); (8 : 6_8)]$ JFW covering (the flower contours in black/red).

Such junctions have been inferred in construction of some nano-networks, with possible electronic applications.

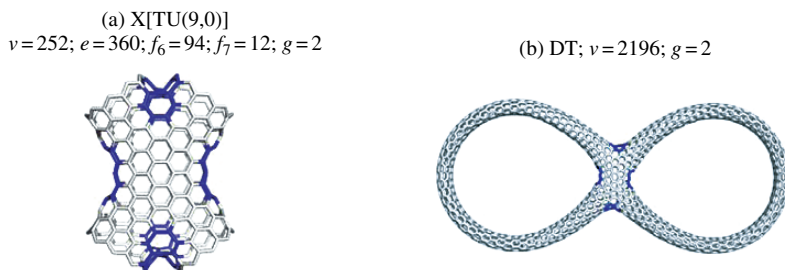


Figure 7-7. An X-junction and the corresponding double torus.

In case of $k = \text{even}$, the simplest junction is of X-type³⁶ (Figure 7-7) and if the tubes are pairwise closed, the objects represent tori of high genera. Other tori with planar junctions are presented in Figure 7-8. Bond currents in double tori as those in Figures 7-7 and 7-8 have been evaluated in terms of homology groups.⁴⁷ Conclusion of this study is the junction is the most important piece in deciding the electromagnetism of a carbon (multi) torus.

7.4.3. Tetrahedral Junctions

A systematic construction of multi tori can be based on the Platonic solids: they are operated by some map operations, *e.g.*, quadrupling Q , capra Ca , *etc.*, and next every original face opened and pairwise joined by appropriate nanotube segments. In this way, repeat units in possible infinite lattices or finite multi tori can be constructed. Figure 7-9 illustrates some double tori and the corresponding junctions.⁴⁸

Among various possible combinations of $\Omega_2(Op(\Omega_1(G)))$ we propose here a classification by the first map operation. This is the operation before opening and it dictates the type of “negative” face nf_s , *i.e.*, the polygon of size $s > 6$ which induces the negative curvature.

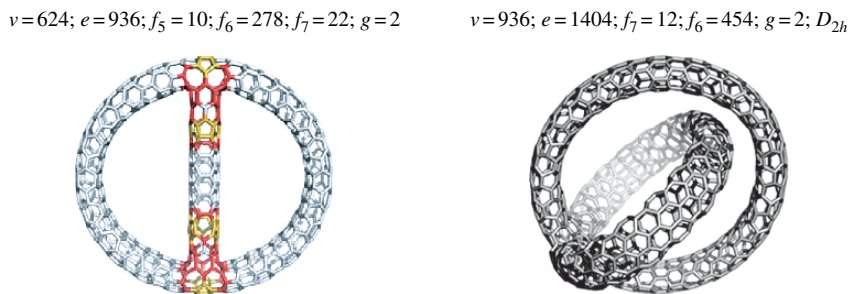
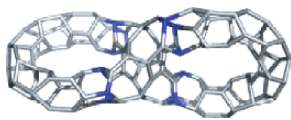
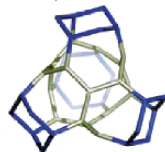


Figure 7-8. Double tori.

$DT(T); v=124; e=186; f_7=12; f_6=48; g=2$



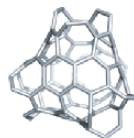
$Op(Ca_{2,1}(T)); TUV/A[3,0]$



$DT(T); v=480; e=720; f_6=226; f_7=12; g=2;$



$Le(Op(Ca(T))); TUV/A[3,3]$



$DT(T); v=1740; e=2610; f_6=856; f_7=12; g=2$



$Le_{221}(Op(Ca(T))); TUV/A[6,6]$

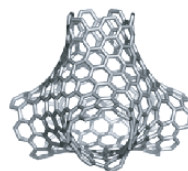
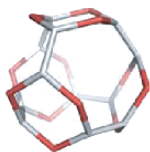


Figure 7-9. Double tori and the corresponding junctions.

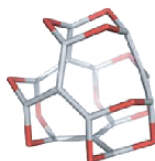
Let's now introduce the three basic (open) operations: leapfrog $Le_{1,1}$, quadrupling $Q_{2,0}$ and capra $Ca_{2,1}/S_1$ (more about these symbols the reader can find in Chapter 5). The objects in Figure 7-10 are transforms of the tetrahedron T .

In infinite lattice, the above units provide Platonic $(nf_s, 3)$ coverings. Observe the units provided by the S_1 (Figure 7-10) and S_2 (Figure 7-11) operations⁴⁹ are isomeric in infinite array (they all have 28 vertices but different embedding and chirality). The primary joining tube will of course be enlarged by applying the second map operation (see the Gallery), with the most important consequence the

(a) $Op(Le_{1,1}(T)); nf_9=4; Tu(3,0)$
 $v=24(12); e=30; f=4; g=2$



(b) $Op(Q_{2,0}(T)); nf_8=6; Tu(3,0)$
 $v=28(16); e=36; f=6; g=2$



(c) $Op(Ca_{2,1}/S_1(T)); nf_7=12; Tu(3,0)$
 $v=40(28); e=54; f=12; g=2$

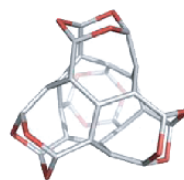
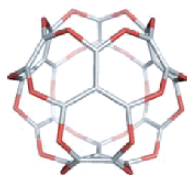


Figure 7-10. The main open repeat units.

(a) $Op_{11}(S_2(T))$; $nf_7 = 12$; $Tu(6,0)$
 $v = 52(28)$; $e = 66$; $f_7 = 12$; $g = 2$



(b) $Op_{24}(S_2(T))$; $nf_7 = 12$; $Tu(3,3)$
 $v = 52(28)$; $e = 66$; $f_7 = 12$; $g = 2$

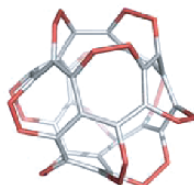
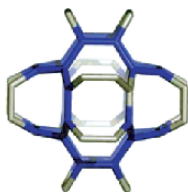


Figure 7-11. Isomeric repeat units with nf_7 , derived by S_2 operation.

(a) $E_{2d}(Q(C))$; $v = 56$; $e = 72$
 $f_8 = 12$; $g = 3$; $TU(2,2)$



(b) $TT(C)$; $v = 264$; $e = 396$; $f_8 = 12$; $f_6 = 116$; $g = 3$

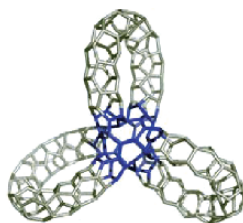


Figure 7-12. A core unit derived from cube C and its triple torus.

drop of strain energy; the evolving tube is given (in two integer symbols⁵⁰) in the top of the objects.

7.4.4. Octahedral Junctions

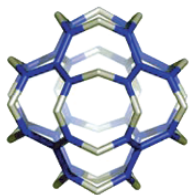
The objects in Figures 7-12 and 7-13 were inferred in the molecular realization of the Dyck graph⁵¹ (on 32 vertices of valence 3, 48 edges, 12 octagons, girth 6, diameter 5, and chromatic number 2, genus $g = 1$, with an embedding of the graph on the torus).^{52,53} They can work as octahedral junctions (*i.e.*, cores) in triple tori.⁴⁸

Similar objects can be obtained by (open) Capra of cube (Figure 7-14a; core in Figure 7-1b); when repeat the operation a more relaxed object is obtained⁴⁸ (Figure 7-14b).

The strain energy SE, in terms of the POAV1 theory,^{54–57} of such objects of high genera⁴⁸ is relaxed as the number of atoms increases. It is evident, when compare the structures in Figure 7-14 (320 atoms 2240 atoms), with a clear drop in their strain.

Out of triple tori, the junctions derived from cube by applying map operations (see the Gallery) can model octahedral junctions of nanotubes. They are involved in the realization of the schwarzites of P-type (see below).

(a) $E_1(Q(C)); v = 56; e = 72$
 $f_8 = 12; g = 3; TU(4,0)$



(b) $TT(C); v = 296; e = 444; f_8 = 12; f_6 = 132; g = 3$

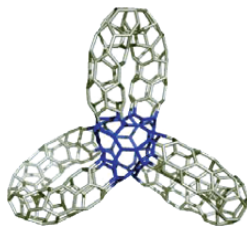
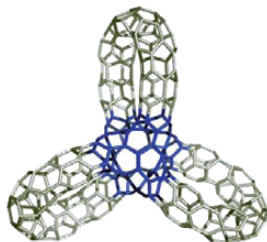


Figure 7-13. A core unit derived from cube and its triple torus.

(a) $TT(C); v = 320; e = 480; f_7 = 24; f_6 = 132; g = 3;$
 $SE = 9.29$



(b) $Ca_{2,1}(TT(C)); v = 2240; e = 3360; f_7 = 24;$
 $f_6 = 1092; g = 3; SE = 2.54$

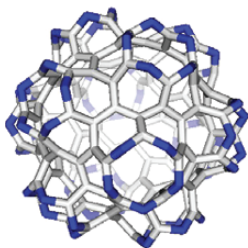


Figure 7-14. A triple torus ($g = 3$) and its core derived from the cube.

7.4.5. Icosahedral Junctions

When the opening operation is coupled to a composite operation like capra Ca , the transform of dodecahedron D can model an icosahedral junction, as illustrated in Figure 7-15, together with the corresponding multi-torus.⁴⁸

(a) $Op(Ca(D)); v = 200; e = 270; f_7 = 60; g = 6$



(b) $v = 3530; e = 5295; f_7 = 60; f_6 = 1695; g = 6$



Figure 7-15. An icosahedral junction and its multi-torus.

7.4.6. Structures of High Genera

Structures of high genera can be modeled, as above mentioned, by opening the Platonic solids, operated by appropriate map operations. Such units may form either infinite lattices of negative curvature or closed cages, showing porous structure.⁴⁸ Spongy carbons have been recently synthesized.¹⁷ Objects like those in Figure 7-16, of genus 2 and 3, respectively, can be built up by joining a conical domain lattice with each of the open faces of a junction unit and finally joining all the conical domains to each other. The core of the object in Figure 7-16b is the junction $Op(Ca_{2,1}/S_1(T))$ (Figure 7-10c).

The objects in Figure 7-17 are derived from the junctions in Figures 7-12a and 7-13a. They are isomers comprising either V/A or H/Z inner tubes. Observe their relatively low strain energy and the pretty stability of the object in Figure 7-17b, in terms of PM3 data.⁴⁸

The object in Figure 7-18 has the core the junction $Op(Ca(D))$ (Figure 7-15a).

Objects of high genera have also been modeled by Lenosky *et al.*,^{8,10} Terrones *et al.*,^{9,11} and more recently by Lijnen and Ceulemans.⁵⁸

Structures have been optimized at the Amber MM and PM3 (HyperChem) level of theory and the strain energy SE in POAV1 terms, by the JSChem software program.⁵⁹

(a) $v = 206; e = 309; f_3 = 12; f_6 = 72; f_9 = 2; g = 2$ (a) $v = 136; e = 204; f_6 = 40; f_7 = 24; g = 3$



Figure 7-16. Finite spongy carbons of trigonal and tetrahedral symmetry.

$g = 5; SE = 5.47$

$SE = 5.65; D_{2h}$
 $HF = 17.74 \text{ kcal/mol}; \text{Gap} = 4.56 \text{ eV}$



Figure 7-17. Finite spongy carbons of octahedral symmetry.

$$v = 1220; e = 1830; f_6 = 470; f_7 = 120; g = 11 \text{ (five fold)}$$

(three fold)

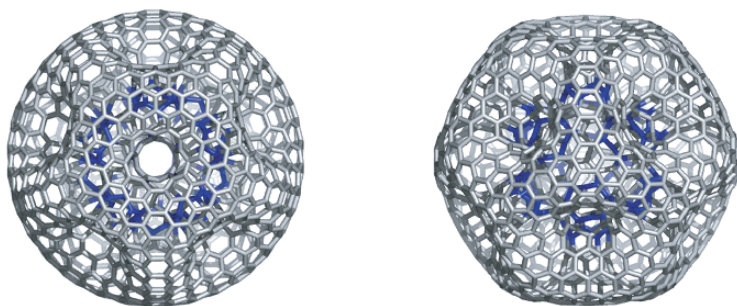


Figure 7-18. Finite spongy carbons of icosahedral symmetry.

7.5. Periodic Schwarzites

7.5.1. D- and FRD-Type Schwarzites

A spongy carbon allotrope, with all covalently bonded sp^2 atoms, which lattice can be embedded in a TPMS is called a TPMS-graphene or a *periodic schwarzite*,^{11,17,60,61} in the honor of H. A. Schwarz,^{13,14} who first investigated, in the early nineteen century, the differential geometry of such surfaces. The most frequently considered minimal surfaces in modeling schwarzites are of D-, FRD- and P-types.^{7,8,11,15,17,19,28,29,60,61}

Various repeat units of D-schwarzites can be designed by applying the map operations (Chapter 5).

Figures 7-19a,b illustrate the chiral pair of the S_1 -transformed tetrahedron: $Op(S_{1S}(T))$ and $Op(S_{1R}(T))$, put together by identifying their common open face, such as they appear (in an “intercalate” conformation) in the bi-elemental cell of an sp^2 diamond lattice, of a (7,3) Platonic tessellation²⁴ (Figures 7-19c,d). For diamond-like structures, the reader can find supplementary information in refs.60 and 61.

The building block $Op(S_1(T))$, (Figure 7-10c), as “eclipsed” bi-elemental cell, enabled construction of a supra-dodecahedron,^{52,53} a multi torus of genus 21, having a (7,3) Platonic tessellation (Figure 7-20a). Its core is given by $Op_{2a}(S_2(D))$ (Figure 7-20b). A similar structure can be built up starting from $Op_{2a}(S_2(T))$ (Figure 7-11b), while its core is $Op(S_1(D))$ (Figure 7-15a). Such supra-dodecahedra represent twin labyrinths interlaced in construction of the FRD-type surface; they could appear by a self-assembling process.²⁴ In the following, the assembling process is seen as a “map operation” and symbolized by “ $D(G)$ ”. Similarly, the core-structure is denoted by “ $C(G)$ ”.

Thus, the twin labyrinths can be achieved either starting from tetrahedral units or from dodecahedral ones. The twin labyrinths above presented can be written as $D(Op(S_1(T)));[Op_{2a}(S_2(D))]$ and $D(Op_{2a}(S_2(T)));[Op(S_1(D))]$, with the objects in

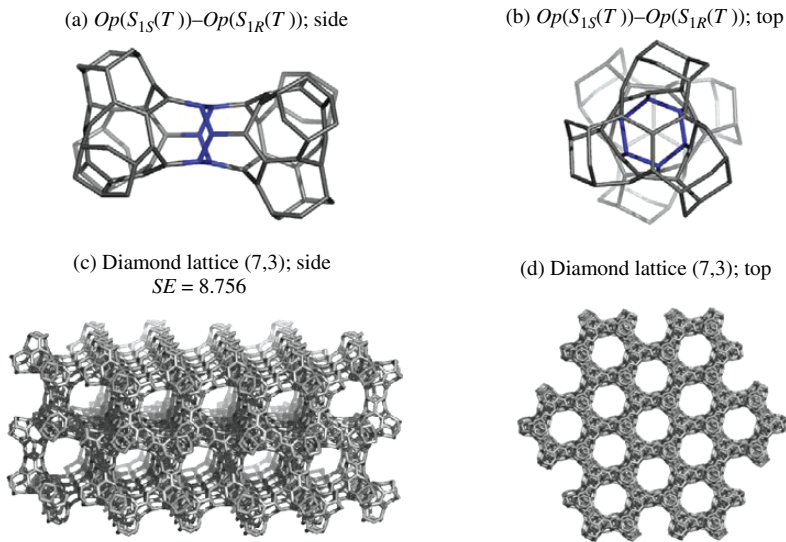


Figure 7-19. Repeat units and the sp^2 diamond (D-type surface) of Platonic (7,3) tessellation.

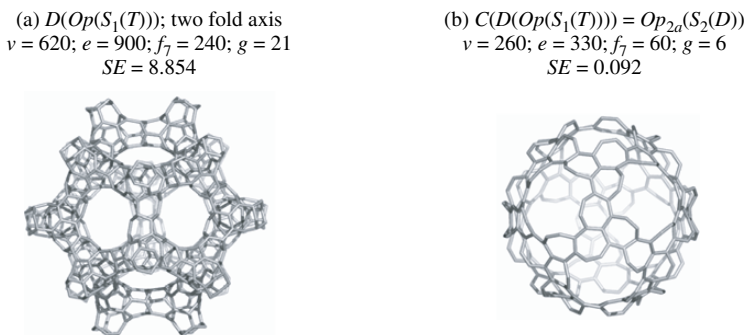


Figure 7-20. A supra-D structure of (7,3) Platonic tessellation, by S_1 , and its core.

the square brackets being the core of the supra-dodecahedra. The free boundary of the core changes from “armchair” (S_2) to “zigzag” (S_1) and *vice-versa*. This is just the expected complementarity of the objects derived by the twin (open) S_1/S_2 operations.

A supra-D structure can be further transformed in view of obtaining different Platonic or Archimedean tessellations. For example, the objects in Figure 7-21a are transformed by $Le_{2,2}$ -operation⁶² in: $Le_{2,2}((D(Op_{2a}(S_2(T))))[(Op(S_1(D)))]$). They show a Platonic, disjoint corannulenic^{52,53}[7:6⁷]DFw supra-covering (Figure 7-22). Supplementary information is given in the top of figures.

(a) $D(Op_{2a}(S_2(T)))$; two fold axis
 $v = 680$; $e = 960$; $f_7 = 240$; $g = 21$
 $SE = 2.097$

(b) $C(D(Op_{2a}(S_2(T)))) = Op(S_1(D))$
 $v = 200$; $e = 270$; $f_7 = 60$; $g = 6$
 $SE = 1.573$

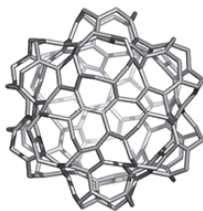
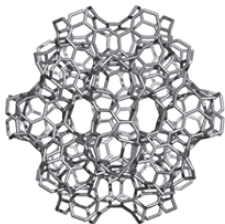


Figure 7-21. A supra-D structure of (7,3) Platonic tessellation, by S_2 , and its core.

(a) $Le_{2,2}(D(Op_{2a}(S_2(T))))$
 Platonic $60 \times [7:6^7]$ DFw
 $v = 6720$; $g = 21$; $SE = 0.318$

(b) $Le_{2,2}(C(D(Op_{2a}(S_2(T)))))$
 $= Le_{22}(Op(S_1(D)))$; Platonic $60 \times [7:6^7]$ DFw
 $v = 1680$; $e = 2400$; $f = 710$; $g = 6$

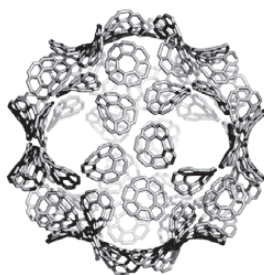
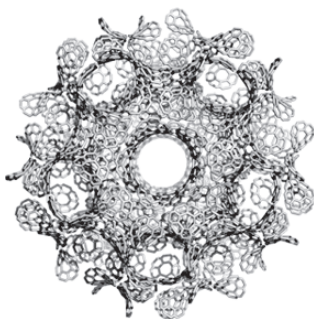


Figure 7-22. Supra-D structure (Figure 7-14a) transformed by $Le_{2,2}$ operation.

In another example, Ca/S_1 operation provides a Platonic covering of joined $[7:6^7]$ JFw tessellation in the $S_{1R}(D(Op_{2aS}(S_2(T)))[Op(S_{1S}(D))])$ embedding (Figure 7-23).

It is known that the curvature elastic⁶⁰ energy decreases in the series: sphere > cylinder > saddle > flat surface. The average strain energy SE values for C_{60} and a (6,6) nanotube are about 8.3 and 1.6 kcal/mol, respectively. In the open units of infinite lattices herein designed, the strain value drops up to 0.31 kcal/mol (see the top of figures), clearly supporting the above decreasing sequence of energy. It is expected that, as the number of atoms increases, the lattice becomes more and more relaxed. Thus, the energy gain from the repeat units to large structures will promote the self-assembling reaction.

Corannulenic disjoint covering is expected to give a particular magnetic response, due to the diamagnetic ring current of the flower periphery (see Chapter 6 and also refs.47 and 63)

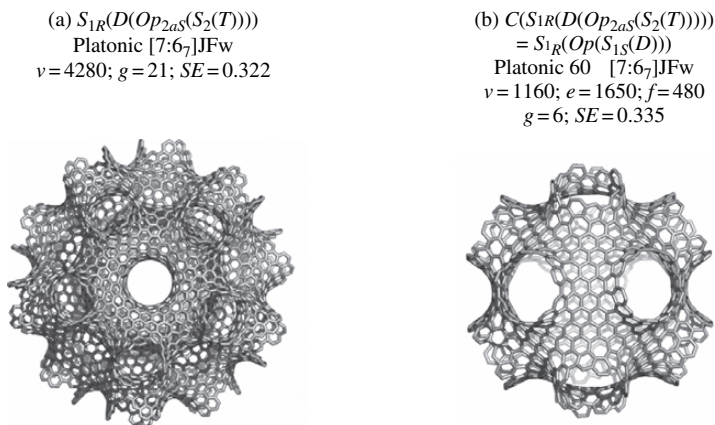


Figure 7-23. Supra-D structure (Figure 7-21a) transformed by S_1 operation.

A self-assembling process can be described for an open C_{60} structure. The repeat unit is $Le(Op(Ca(T)))$; $v = 84(60)$ and the common edges have to be identified in the process of building the supra-dodecahedron $D(Le(Op(Ca(T))))$; $[Op(Ca_{(3,2)C}(I))]$ (Figure 7-24).

Intermediate steps are presented in Figure 7-25.

The open embedding of the above supra-dodecahedron shows $g = 21$ while the closed one is $g = 11$ (cages of genus 11 have also been reported by Terrones and Terrones.⁶⁴). Observe the identical covering of the (quasi) spherical units to that of C_{60} , from which the open unit of $v = 60$ can be obtained by cutting off the edges sharing the pentagons and hexagons in the tetrahedral disposition. The above repeat unit $Le(Op(Ca(T)))$ ($v = 1 \times 60$, Figure 7-25) shows a joint triphenylenic

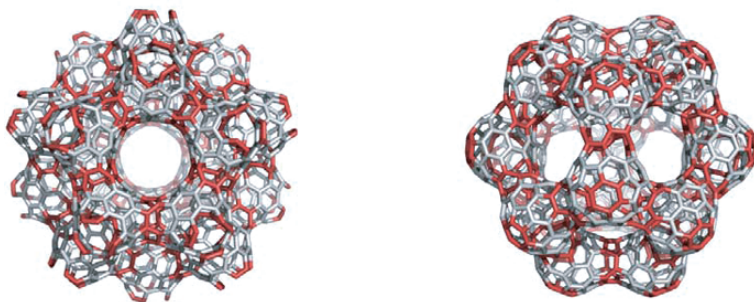
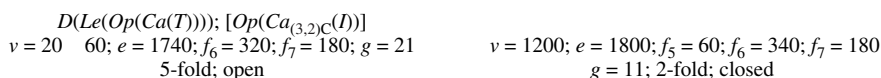


Figure 7-24. The supra-dodecahedron $D(Le(Op(Ca(T))))$; $[Op(Ca_{(3,2)C}(I))]$ in open and closed embedding.

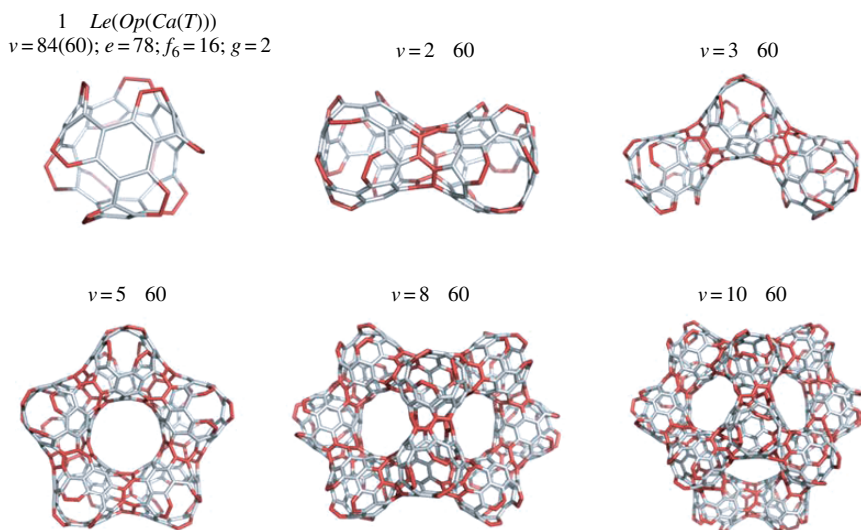


Figure 7-25. Intermediate steps in construction of supra-dodecahedron $D(Le(Op(Ca(T))))$; $[Op(Ca_{(3,2)C}(I))]$.

$[6:(0,6)_3]$ JFw covering, expected to show a high aromatic character and to contribute to the stability of the whole structure (see also Chapter 6).

The above supra-dodecahedron may evolve in a linear array, as shown in Figure 7-26. The core of these structures is described as $Op(Ca_{(3,2)C}(I))$ (Figure 7-26b), in an embedding of $g=6$. The dark/red lines are those shared by two structural units.

A simpler repeat unit is illustrated in Figure 7-27a. The pair $Op(Le(T))/Op(Le(I))$ provides a FRD-type surface²⁹ (space group $F_d 3m$) tessellated as $D(Op(Le(T)))[Op(Le(I))]$, (Figure 7-27c,d) with the same meaning of

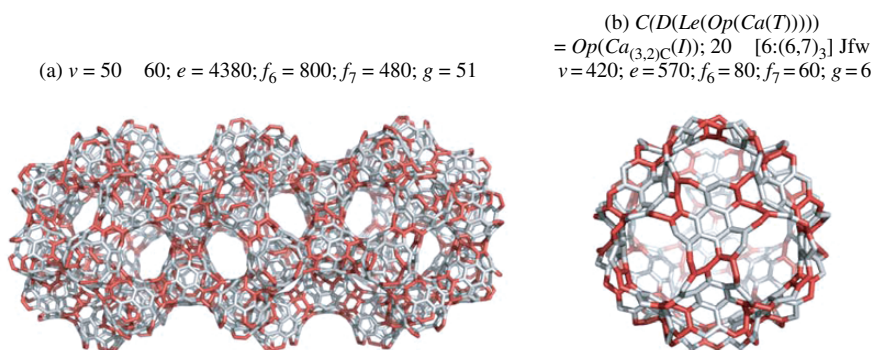


Figure 7-26. A linear array of $D(Le(Op(Ca(T))))$ and its core.

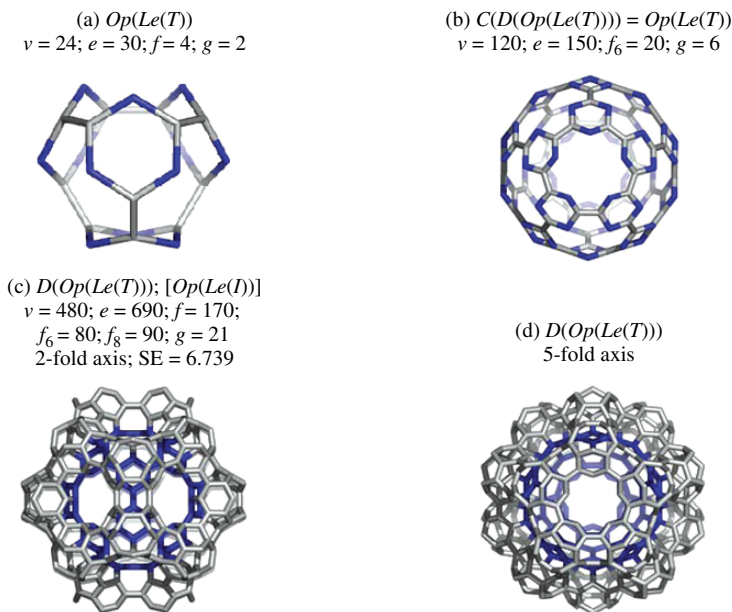


Figure 7-27. The supra-dodecahedron $D(Op(Le(T))); [Op(Le(I))]$ and its repeat units.

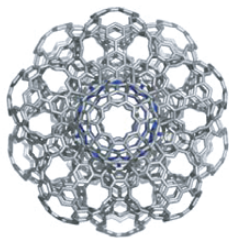
symbols as above. The tetrahedral unit is the smallest open unit $Op(Le(T))$ tiled by disjoint hexagons. The corresponding core is $Op(Le(I))$ (Figure 7-27b) and, as in the case of $C(D(Le(Op(Ca(T)))))$, the starting Platonic is the icosahedron.

By connecting $Op(Le(I))$ with other twelve identical objects results in an FRD-domain, of genus 66 (Figure 7-28a). It can be capped, to obtain the compact array A of 13 spheres²⁴ $A(Op(Le(I)))$ (Figure 7-28c,d). This array shows a core described as $D(Op(Le(T)))$, identical to the supra-dodecahedron illustrated in Figure 7-27c,d. This clearly demonstrates the complementariness of the units, derived from tetrahedron and dodecahedron, respectively, concerted in the construction of the FRD-type surface.

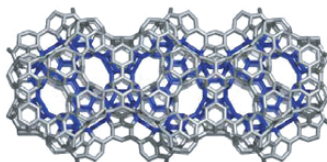
The unit $D(Op(Le(T)))$ may evolve in a linear array, as shown in Figure 7-28b.

Let's now start a construction by the object $D(Op(Le(T))); [Op(Le(I))]$. The steps (Figure 7-29) are essentially the same as those for the supra-dodecahedron $D(Le(Op(Ca(T))))$; $[Op(Ca_{(3,2)C}(I))]$ (Figure 7-27) but the repeat unit is just a supra-dodecahedron. Finally the array $A(D(Op(Le(T))))$; $[D(Op(Le(T)))]$ is obtained (Figure 7-30); its core is just the starting supra-dodecahedron. The unit of $v = 1200$ (Figure 7-29c) can be seen as the cap of structure with $v = 1920$ (Figure 7-29b), whose reunion (formally) leads to the target structure. The 13 spheres represented in Figure 7-28 are here surrounded by the tetrahedral units whose array generates the spherical parts of the twin labyrinth in an infinite lattice. The above array, as infinite embedding, shows $g = 131$.

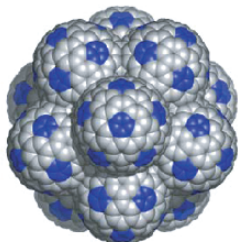
(a) FRD-type surface; $A(Op(Le(I)))$
 Infinite; $v = 1560$; $e = 2160$; $f = 470$
 $f_6 = 260$; $f_8 = 210$; $g = 66$; 5-fold axis; $SE = 3.72$



(a) Linear lattice of $D(Op(Le(T)))$
 Infinite; $v = 1200$; $e = 1740$; $f = 440$
 $f_6 = 200$; $f_8 = 240$; $g = 51$; $SE = 6.499$



(c) $A(Op(Le(I)))$
 Finite; $v = 1920$; $e = 2880$; $f = 902$
 $g = 30$; 5-fold axis; $SE = 3.73$



(d) 13 $Op(Le(I))$; 3-fold axis
 $g = 30$

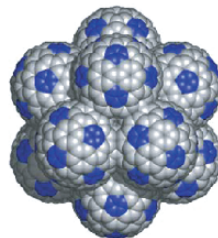
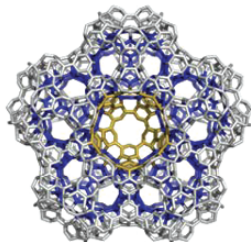


Figure 7-28. Spherical (a, c, d) and linear (b) evolution of $D(Op(Le(T)))$ unit.

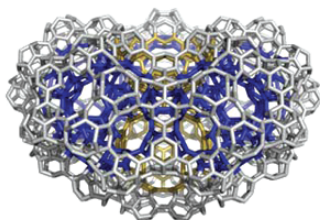
(a) $v = 1800$; 5-fold axis; top



(b) $v = 1920$; 5-fold axis;



(b') $v = 1920$; side



(c) $v = 1200$ (side)

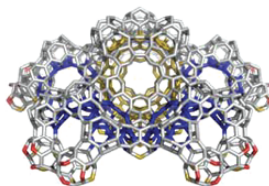


Figure 7-29. Steps in construction of the array $A(D(Op(Le(T))))$; $[D(Op(Le(T)))]$.

$$A(D(Op(Le(T)))); [D(Op(Le(T)))].$$

$v = 3120$; $e = 4590$; $f_6 = 520$; $f_8 = 690$; $f = 1210$; $g = 131$; 5-fold axis

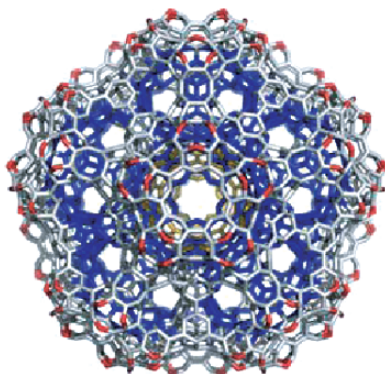


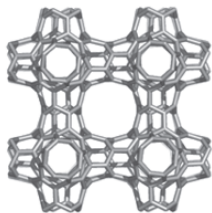
Figure 7-30. The array $A(D(Op(Le(T))))$; $[D(Op(Le(T)))]$.

Among several proposed synthetic routes for carbon schwarzites, two of them appear conceivable: one suggests the carbonization of foamed polymers, whereas the other infers the fullerenes as templates. Both routes ultimately converge to dual labyrinth structures, which could evolve from either a tetrahedral or a spherical (dodecahedral) repeat unit.

7.5.2. P-Type Schwarzites

The P-type surface shows the space group $P_n 3m$; a molecular realization, achieved by the two septupling map operations is exemplified in Figure 7-31. Observe the combination of the pro-chiral units, provided by these operations, in obtaining non-twisted (achiral) lattices of high genera. The pair lattice units are easily deduced as: $Op(S_1(C))/Op_{2a}(S_2(C))$, disregarding the chirality. The sequence $S_i(Op_n(S_i(M)))$

Lattice of $8 \times (Op(S_{1S}(C)) \& Op(S_{1R}(C)))$
 $v = 544$; $e = 768$; $f = 192$; $g = 17$; $SE = 2.127$



Lattice of $8 \times (Op_{2aR}(S_2(C)) \& Op_{2aR}(S_2(C)))$
 $v = 640$; $e = 864$; $f = 192$; $g = 17$; $SE = 0.857$

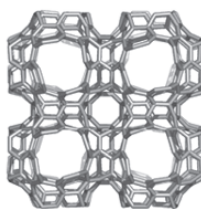


Figure 7-31. Platonic (7,3) tessellation of the P-type surface by the two septupling map operations.

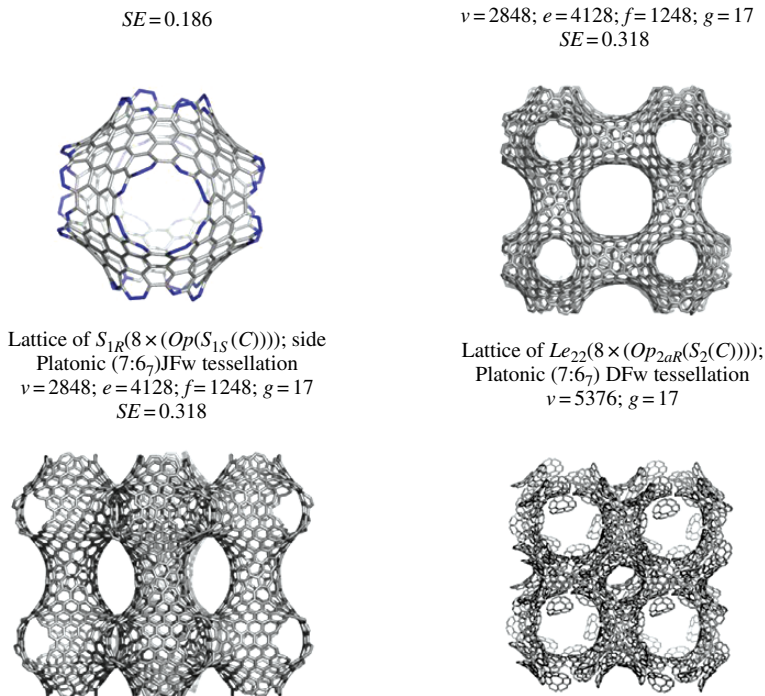


Figure 7-32. Transformed $S_1(G)$ coverings of the P-type surface.

or similar others, may provide variations of the P-surface covering (e.g., those shown in Figure 7-32).

Unit blocks provided by $Op(S_1(C))$ and $Op_{2a}(S_2(C))$ operations^{49,65} (Figures 7-31 and 7-32) could model the junctions of carbon nanotubes, obtainable by “nano-welding” crossing tubes in an electron beam.³⁶ The large hollows appearing in the above objects could explain the porosity of the spongy carbon materials.

Lattices of this type have been described in refs.7,8,9,15,24,28,66 Note that (7,3) tessellation is also called Klein tessellation, after F. Klein,^{67,68} whose graph is a representation of the automorphism of (heptakis) octahedral group.⁶⁹

All the presented structures have been computed by the original software program CageVersatile 1.5.⁷⁰

Conclusions

Spongy carbon nanostructures, also called schwarzites, recently synthesized, consist of highly connected covalent networks, periodic in the three dimensions of the Euclidean space. Triply periodic minimal surfaces TPMSs were claimed as the intimate structures of schwarzites.

A systematic construction of nanotube junctions was based on the Platonic solids, operated by some map operations, and next every original face opened. The eventual pairwise joining of the open faces by appropriate nanotube segments leads to multi-tori. If, instead of tubes, conical domains are used, it would result in some finite spongy carbons. The junctions can be self-assembled in networks (schwarzites) of high genera (and subsequently tessellated by some map operations). POAV1 strain energy calculations for structures of thousands atoms have shown that such structures are very relaxed and approach to the graphite sheet. Data support previous literature results indicating a decrease of energy in the series: sphere > cylinder > saddle > flat surface.

Calculations at various levels of theory have predicted extremely interesting properties (mechanical, thermal, electric, magnetic or theoretic ones) of spongy nanostructures.

Details of junctions herein discussed and other examples, classified by the operation before the opening, the are given in the Gallery, at the end of this book.

References

1. M. Endo, S. Iijima, M. S. Dresselhaus, *Carbon Nanotubes*, Pergamon, 1996.
2. P. W. Fowler, D. E. Manolopolous, *An atlas of fullerenes*, Clarendon Press, Oxford, 1995.
3. M. S. Dresselhaus, G. Dresselhaus, P. C. Eklund, *Science of fullerenes and carbon nanotubes*, Acad. Press, San Diego, 1996.
4. K. Tanaka, T. Yamabe, K. Fukui, *The science and technology of carbon nanotubes*, Elsevier, Amsterdam, 1999.
5. A. T. Balaban, (Ed.) *From Chemical Topology to three-dimensional Geometry*, Plenum Press, New York, 1997.
6. L. Euler, *Elementa doctrinae solidorum. Novi Comment. Acad. Sci. I. Petropolitanae*, 1758, **4**, 109–160.
7. A. L. Mackay, H. Terrones, *Nature*, 1991, **352**, 762.
8. T. Lenosky, X. Gonze, M. Teter, V. Elser, *Nature*, 1992, **355**, 333–335.
9. H. Terrones, A. L. Mackay, *Prog. Crystal Growth and Charact.*, 1997, **34**, 25–36.
10. S. J. Townsend, T. J. Lenosky, D. A. Muller, C. S. Nichols, V. V. Elser, *Phys. Rev. Lett.*, 1992, **69**, 921–924.
11. H. Terrones, A. L. Mackay, *Chem. Phys. Lett.*, 1993, **207**, 45–50.
12. L. N. Bourgeois, L. A. Bursill, *Phil. Mag. A*, 1997, **76**, 753–768.
13. H. A. Schwarz, Über Minimalflächen, *Monatsber. Berlin Akad.*, 1865.
14. H. A. Schwarz, *Gesammelte Matematische Abhandlungen*, Springer, Berlin, 1890.
15. D. Vanderbilt, J. Tersoff, *Phys. Rev. Lett.*, 1992, **68**, 511–513.
16. V. Rosato, M. Celino, G. Benedek, S. Gaito, *Phys. Rev. B*, 1999, **60**, 16928–16933.
17. G. Benedek, H. Vahedi-Tafreshi, E. Barborini, P. Piseri, P. Milani, C. Ducati, J. Robertson, *Diamond Relat. Mater.*, 2003, **12**, 768–773.
18. A. A. Zaakhidov; R. H. Baughman; Z. Iqbal; Ch. Cui; I. Khayrullin, S. O. Santos, J. Marti, V. G. Ralchenko, *Science*, 1998; **282**, 5390.
19. E. Barborini, P. Piseri, P. Milani, G. Benedek, C. Ducati, J. Robertson, *Appl. Phys. Lett.*, 2002, **81**, 3359–3361.
20. F. Harary, *Graph Theory*. Addison-Wesley, Reading, MA, 1969.
21. J. L. Gross, T. W. Tucker, *Topological graph theory*. Dover Pubs, Dover, 2001.
22. D. J. Klein, H. Zhu, in: A. T. Balaban, (Ed.), *From Chemical Topology to three-dimensional Geometry*. Plenum Press, New York, 1997, pp. 297–341.

23. D. J. Klein, in: D. Bonchev, D. H. Rouvray, (Eds.), *Chemical topology*. (Mathematical Chemistry Series) Gordon & Breach, Amsterdam, 1999, pp. 39–83.
24. Cs. L. Nagy, M. V. Diudea, in: M. V. Diudea, (Ed.), *Nanostructures-Novel Architecture*. NOVA, New York, 2005, 311–334.
25. O. Bonnet, *C. R. Acad. Sci. Paris*, 1853, **37**, 529–532.
26. D. J. Klein, *J. Chem. Inf. Comput. Sci.*, 1994, **34**, 453–459.
27. L. Euler, *Solutio Problematis ad Geometriam Situs Pertinentis. Comment. Acad. Sci. I. Petropolitanae*, 1736, **8**, 128–140.
28. M. O’Keeffe, G. B. Adams, O. F. Sankey, *Phys. Rev. Lett.*, 1992, **68**, 2325–2328.
29. H. Karcher, K. Polthier, *Phil. Trans. R. Soc. Lond. A*, 1996, **354**, 2077–2104.
30. D. Hoffman, *Nature*, 1996, **384**, 28–28.
31. R. Osserman, *A survey of minimal surfaces*, Dover, New York, 1986.
32. A. H. Schoen, *Infinite periodic minimal surfaces without self-intersections*, NASA Technical Report TN D-5541, Washington DC 1970.
33. E. R. Neovius, Bestimmung zweier speziellen Minimalflächen, *Akad. Abhandlungen*, Helsingfors 1883.
34. H. S. M. Coxeter, *Regular polytopes*, 3rd Edn, Dover Pubns, Dover, 1973.
35. W. Fischer, E. Koch, *Phil. Trans. R. Soc. London A*, 1996, **354**, 2105–2142.
36. M. Terrones, F. Banhart, N. Grobert, J.-C. Charlier, H. Terrones, P. M. Ajayan, *Phys. Rev. Lett.* 2002, **89**, 075505-1–075505-4.
37. C. J. Lee, J. Park, *Appl. Phys. Lett.*, 2000, **77**(21), 3397–3399.
38. V. Meunier, M. Buongiorno Nardelli, C. Roland, J. Bernholc, *Phys. Rev. B*, 2001, **64**, 195419-1–195419-7.
39. Z. Osváth, A. A. Koós, Z. E. Horváth, J. Gyulai, A. M. Benito, M. T. Martinez, W. Maser, L. P. Biró, *Mat. Sci. Eng.*, 2003, **C 23**, 561–564.
40. A. Fonseca, K. Hernadi, J. B. Nagy, Ph. Lambin, A. A. Lucas, *Synthetic Metals*, 1996, **77**, 235–242.
41. Z. Yao, H. W. Ch. Postma, L. Balents, C. Dekker, *Nature*, 1999, **402**, 273–276.
42. M. E. Lyn, J. He, B. Koplitz, *Applied Surface Science*, 2005, **246**, 44–47.
43. M. Menon, D. Srivastava, *Phys. Rev. Lett.*, 1997, **79**, 4453–4456.
44. A. N. Andriotis, M. Menon, D. Srivastava, L. Chernozatonskii, *Phys. Rev. Lett.*, 2001, **87**, 066802-1–066802-4.
45. A. N. Andriotis, M. Menon, D. Srivastava, L. Chernozatonskii, *Appl. Phys. Lett.*, 2001, **79**, 266–268.
46. W. Z. Li, J. G. Wen, Z. F. Ren, *Appl. Phys. Lett.*, 2001, **79**, 1879–1881.
47. E. Lijnen, A. Ceulemans, M. V. Diudea, *J. Math. Chem.*, 2007 (in press).
48. A. E. Vizitiu, M. V. Diudea, *Studia Univ. “Babes-Bolyai”*, 2006, **51**(1) 39–48.
49. M. V. Diudea, *J. Chem. Inf. Model.*, 2005, **45**, 1002–1009.
50. N. Hamada, S. Sawada, A. Oshiyama, *Phys. Rev. Lett.*, 1992, **68**, 1579.
51. W. Dyck, *Math. Ann.*, 1880, **17**, 510–516.
52. M. V. Diudea, *Forma* (Tokyo), 2004, **19**(3), 131–163.
53. M. V. Diudea, in: M. V. Diudea, (Ed.), *Nanostructures-Novel Architecture*, NOVA, New York, 2005, 203–242.
54. R. C. Haddon, *J. Am. Chem. Soc.*, 1987, **109**, 1676–1685.
55. R. C. Haddon, *J. Am. Chem. Soc.*, 1990, **112**, 3385–3389.
56. R. C. Haddon, *J. Am. Chem. Soc.*, 1997, **119**, 1797–1798.
57. R. C. Haddon, S.-Y. Chow, *J. Am. Chem. Soc.*, 1998, **120**, 10494–10496.
58. E. Lijnen, A. Ceulemans, *J. Chem. Inf. Model*, 2005, **45**(6), 1719–1726.
59. Cs. L. Nagy, M. V. Diudea, *JSChem software*, “Babes-Bolyai” Univ., Cluj, 2005.
60. F. Valencia, A. H. Romero, E. Hernández, M. Terrones, H. Terrones, *New J. Phys.*, 2003, **5**, 123.1–123.16.
61. H. Terrones, M. Terrones, *New J. Phys.*, 2003, **5**, 126.1–126.37.
62. M. V. Diudea, M. Stefu, P. E. John, A. Graovac, *Croat. Chem. Acta*, 2006, **79**, 355–362.

- 63. J.-A. Rodriguez-Manzo, F. Lopez-Urias, M. Terrones, H. Terrones, *Nano Lett.*, 2004, **4**, 2179–2183.
- 64. H. Terrones, M. Terrones, *Carbon* 1998, **36**, 725–730.
- 65. M. V. Diudea, *Studia Univ. “Babes-Bolyai”* 2003, **48**(2), 3–16.
- 66. Cs. L. Nagy, M. V. Diudea, *Studia Univ. “Babes-Bolyai”* 2003, **48**(2), 37–46.
- 67. F. Klein, *Vorlesungen über das Ikosaeder*. Teubner, Leipzig, 1884: Part I, Chapter II.
- 68. Klein, F. *Gesammelten Mathematischen Abhandlungen*. Springer Verlag, Berlin, 1923, vol. 3, pp. 90–136.
- 69. A. Ceulemans, R. B. King, S. A. Bovin, K. M. Rogers, A. Troisi, P. W. Fowler, *J. Math. Chem.* 1999, **26**, 101–123.
- 70. M. Stefu, M. V. Diudea, *CageVersatile* 1.5, Babes-Bolyai University, 2005.

Gallery of Carbon Nano Junctions and Derived Infinite Lattices

Abbreviations used:

T – tetrahedron

C – cube

D – dodecahedron

$Le_{1,1}$

$Le_{2,2}$

$Q_{2,0}$

$Q_{3,0}$

$Ca_{2,1}$

$Ca_{3,2}$

nf_s – negative face of size s

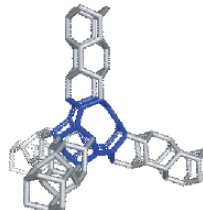
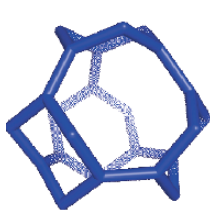
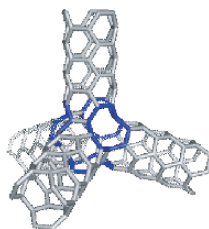
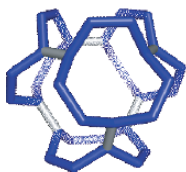
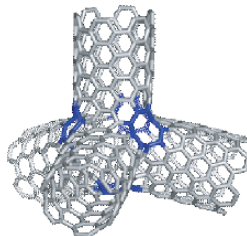
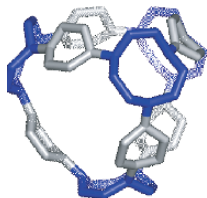
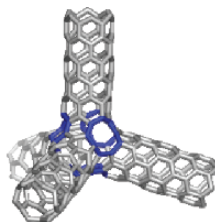
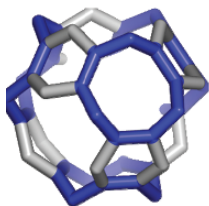
Op – open

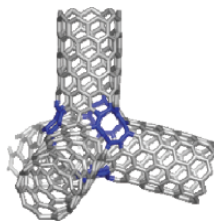
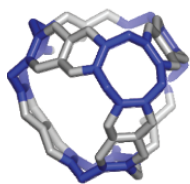
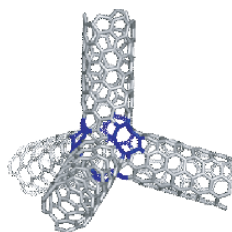
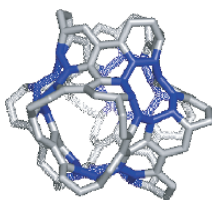
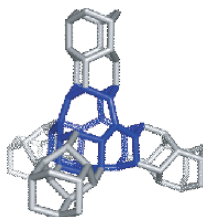
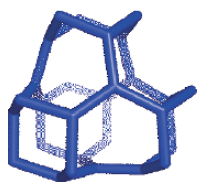
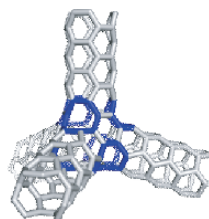
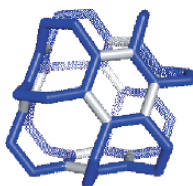
$Op_{1,1}$ – consecutive open

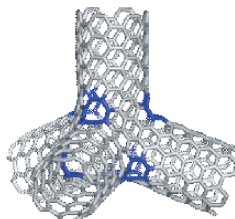
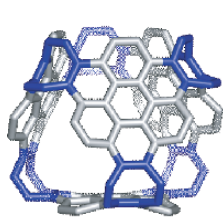
Op_{2a} – alternating open

A – array

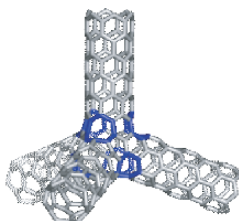
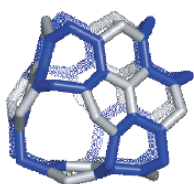
D – supra dodecahedron


 $Op(Le_{1,1}(T))\text{-TU}(3,0); v = 24$

 $Le_{1,1}(Op(Le_{1,1}(T)))\text{-TU}(3,3); v = 36$

 $Le_{2,2}(Op(Le_{1,1}(T)))\text{-TU}(6,6); v = 72$

 $Q_{2,0}(Op(Le_{1,1}(T)))\text{-TU}(6,0); v = 48$

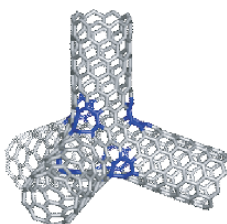
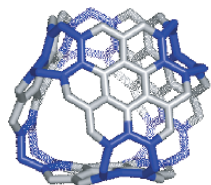

 $Q_{3,0}(Op(Le_{1,1}(T)))-TU(9,0); v=72$

 $Ca_{2,1}(Op(Le_{1,1}(T)))-TU(6,3); v=120$
 $Op(Q_{2,0}(T)); nf_8$

 $Op(Q_{2,0}(T))-TU(3,0); v=28$

 $Le_{1,1}(Op(Q_{2,0}(T)))-TU(3,3); v=48$



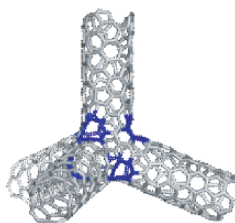
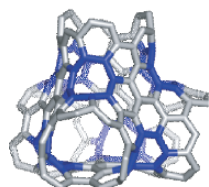
$$Le_{2,2}(Op(Q_{2,0}(T)))-TU(6,6) ; v = 120$$



$$Q_{2,0}(Op(Q_{2,0}(T)))-TU(6,0); v = 64$$

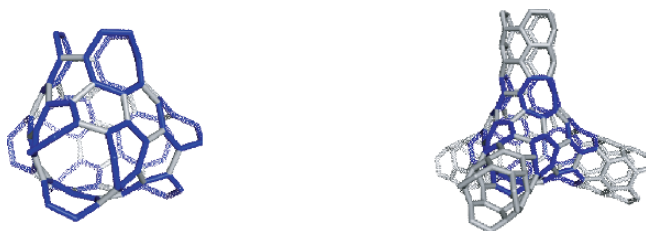


$$Q_{3,0}(Op(Q_{2,0}(T)))-TU(9,0); v = 180$$

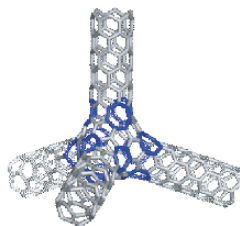
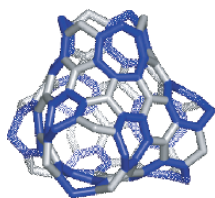


$$Ca_{2,1}(Op(Q_{2,0}(T)))-TU(6,3); v = 148$$

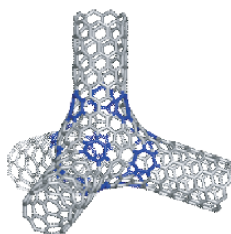
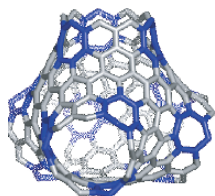

 $Ca_{3,2}(Op(Q_{2,0}(T)))-TU(9,6); v = 268$
 $Op(Ca_{2,1}(T)); nf_7$

 $Op(Ca_{2,1}(T))-TU(3,0); v = 40$

 $Le_{1,1}(Op(Ca_{2,1}(T)))-TU(3,3); v = 84$

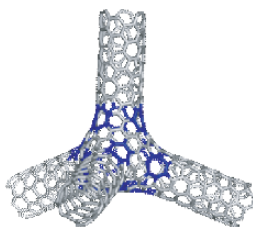
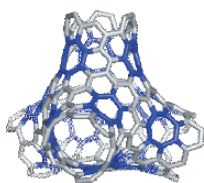
 $Le_{2,2}(Op(Ca_{2,1}(T)))-TU(6,6); v = 264$



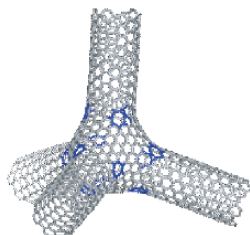
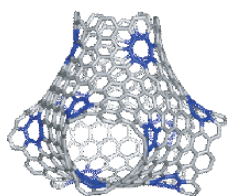
$$Q_{2,0}(Op(Ca_{2,1}(T)))-TU(6,0); v = 112$$



$$Q_{3,0}(Op(Ca_{2,1}(T)))-TU(9,0); v = 216$$



$$Ca_{2,1}(Op(Ca_{2,1}(T)))-TU(6,3); v = 160$$



$$Ca_{3,2}(Op(Ca_{2,1}(T)))-TU(9,6); v = 496$$

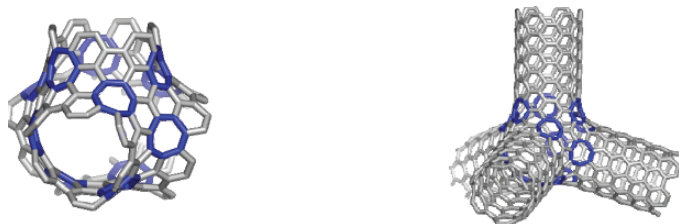
$$Op_{2a}(S_2(T)); nf_7$$



$$Op_{2a}(S_2(T))\text{-TU}(3,3); v=52$$



$$Le_{1,1}(Op_{2a}(S_2(T)))\text{-TU}(9,0); v=120$$



$$Q_{2,0}(Op_{2a}(S_2(T)))\text{-(6,6)}; v=184$$



$$Ca_{2,1}(Op_{2a}(S_2(T)))\text{-TU}(12,3)$$

$$Op_{1,1}(S_2(T)); nf_7$$



$$Op_1(S_2(T))\text{-TU}(6,0); v = 52$$



$$Le_{1,1}(Op_1(S_2(T)))\text{-TU}(6,6); v = 84$$

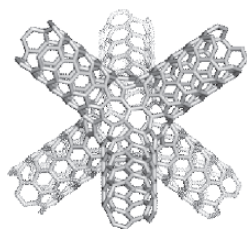


$$Q_{2,0}(Op_1(S_2(T)))\text{-TU}(12,0); v = 112$$

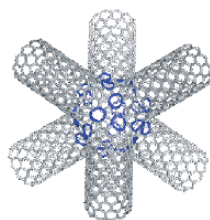
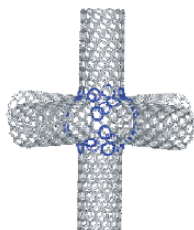
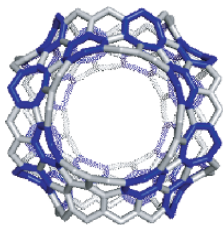


$$Ca_{2,1}(Op_1(S_2(T)))\text{-TU}(12,6); v = 268$$

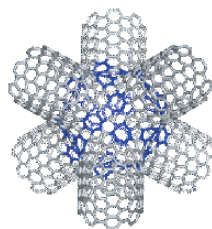
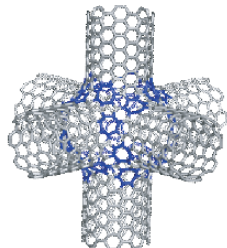
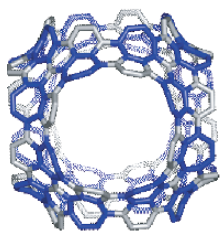
$$Op_{2a}(S_2(C)); nf_7$$



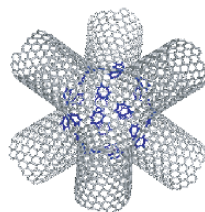
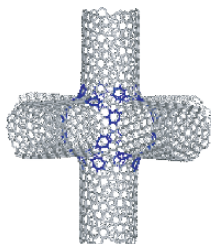
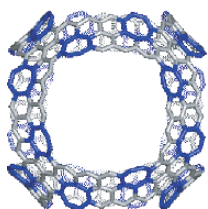
$$Op_{2a}(S_2(C))\text{-TU}(4,4); v = 104$$



$$Le_{1,1}(Op_{2a}(S_2(C)))\text{-TU}(12,0); v = 240$$

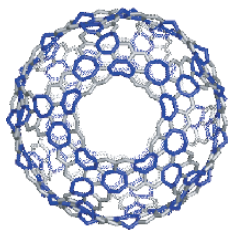


$$Q_{2,0}(Op_{2a}(S_2(C)))\text{-TU}(8,8); v = 368$$

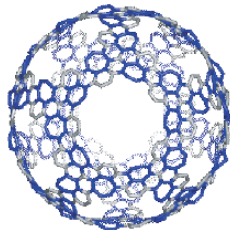


$$Ca_{2,1}(Op_{2a}(S_2(C)))\text{-TU}(16,4); v = 368$$

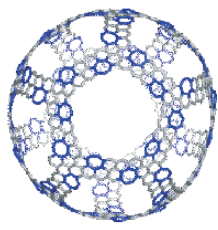
$Op_{2a}(S_2(D)); n f_7$



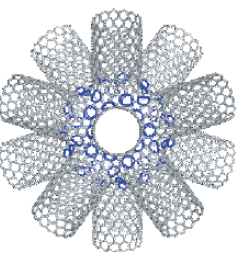
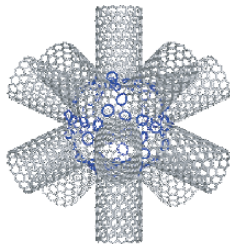
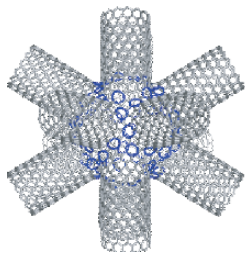
$Le_{1,1}(Op_{2a}(S_2(D)))-TU(15,0)$
 $v = 600$



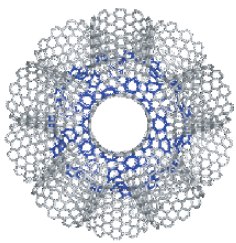
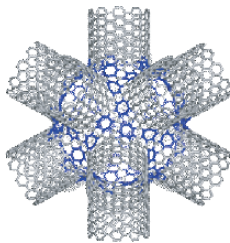
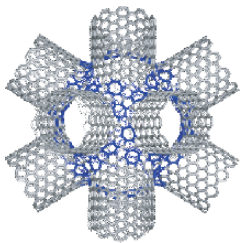
$Q_{2,0}(Op_{2a}(S_2(D)))-TU(10,10)$
 $v = 684$



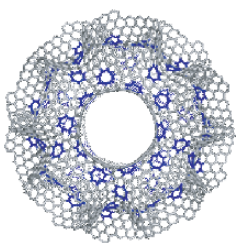
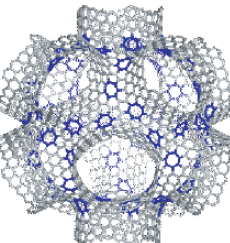
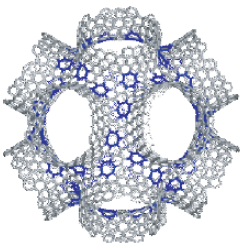
$Ca_{2,1}(Op_{2a}(S_2(D)))-TU(20,5)$
 $v = 918$



$Le_{1,1}(Op_{2a}(S_2(D)))-TU(15,0)$

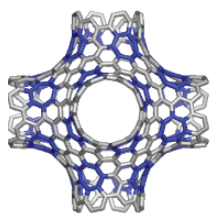
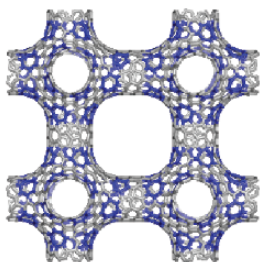
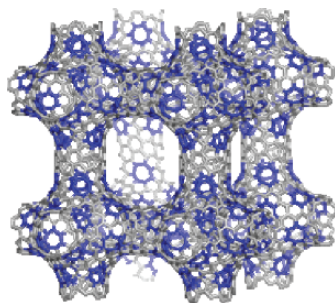
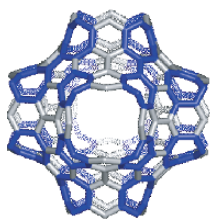
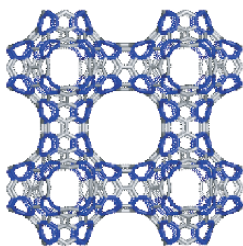
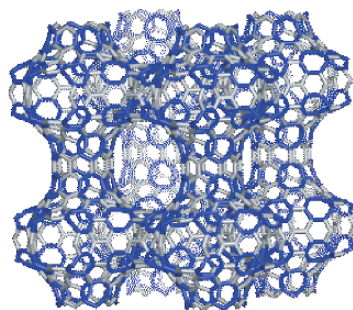
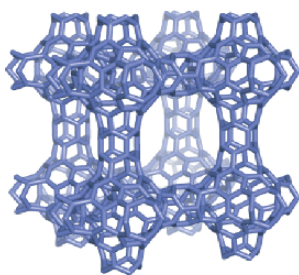
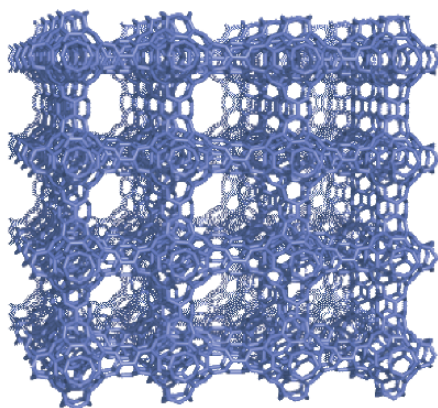


$Q_{2,0}(Op_{2a}(S_2(D)))-TU(10,10)$

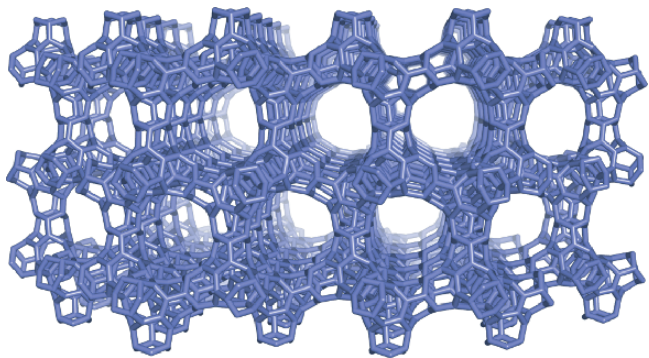


$Ca_{2,1}(Op_{2a}(S_2(D)))-TU(20,5)$

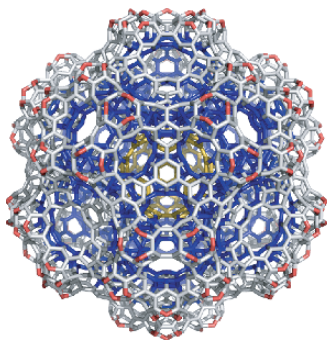
P-type networks


 $Ca_{2,1}R(Op(Ca_{2,1}S(C)))$

 $4 \times Ca_{2,1}R(Op(Ca_{2,1}S(C)))$

 $8 \times Ca_{2,1}R(Op(Ca_{2,1}S(C)))$

 $Op(Le_{1,1}(Le_{1,1}(Le_{1,1}(C))))$

 $4 \times Op(Le_{1,1}(Le_{1,1}(Le_{1,1}(C))))$

 $8 \times Op(Le_{1,1}(Le_{1,1}(Le_{1,1}(C))))$

 $4 \times Op(Le_{1,1}(Le_{1,1}(C)))$

 $16 \times Op(Le_{1,1}(Le_{1,1}(C)))$

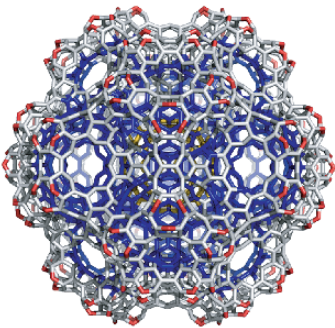
D- and FRD-type networks



$126 \times Op(Ca_{2,1}(T)); v = 3816$



$v = 3120 - 3; 3\text{-fold axis}$



$v = 3120 - 2; 2\text{-fold axis}$

$A(D(Op(Le(T)))); [D(Op_1(Le_{1,1}(T)))]$

Index

- ¹³C NMR spectroscopy(spectra) 2,3
- achiral tubes 22
- Archimedes 117
- armchair cylinders 21
- armchair nanotubes 20, 23, 25, 28, 51, 52, 65, 100
- armchair tubes 31, 65, 67, 99
- aromaticity 46, 48, 64, 137–139, 144, 145, 147–152, 154–156, 158, 160–163
- capped armchair nanotubes 25, 28
- capped nanotubes 1, 23, 28
- capped zig(-)zag nanotubes 26, 31
- capra/sextupling 135
- carbon allotropes 8, 35, 167, 168, 171, 180
- carbon lattices 51, 170
- chamfering 120, 121
- chamfering/quadrupling 135
- characteristic polynomial 43, 45, 46, 77
- chiral tubes 22, 23
- CI index 99, 103, 104
- Clar representation 138
- Clar theory 140, 141
- closed nanotubes 1, 19, 23
- Cluj matrices 75, 82, 84
- Cluj polynomials 82, 83, 85, 86
- coalescence in peapods 8
- coalescence reactions 1, 7
- cone angle 61
- conetori 60, 61, 63, 64, 173
- continuous transformation of origin of current
 - density - diamagnetic zero (CTOCD-DZ) 44
- continuous transformation of origin of current
 - density (CTOCD) 145
- corannulenic cages 140, 143, 144
- corazulenic cages 145, 150, 154
- counting polynomials 69, 77, 79, 83, 111
- cutting procedures 92, 94, 135
- cylinder rule 21
- detour w index 72
- diagonal junctions 173
- diameter doubling 5, 65–67
- disjoint corannulenic DFw structure 44, 141
- distance degree sequence (DDS) 79, 90, 91
- distinct topological objects 40, 45
- distinct walled tori(torus) DWT 51–61, 67, 173
- D-type schwarzites 171, 180
- dualization Du 116–120, 135, 143, 144
- DWNT 8, 9, 15, 51, 54, 61, 67
- DWT precursors 51
- electronic criterion 138
- energetic criterion 138, 153, 154
- Euler formula 115
- Euler's theorem 32, 35, 137, 167, 168, 173
- external cone 63, 64
- external V/A-tube 61, 62
- factorization procedure 101
- Fadeev, D.K. 77

- finite-length carbon nanotubes 19
 flowers 44, 141–143, 145, 146, 150,
 153–155, 158, 159, 163
 Frame, J.S. 77
 FRD-type schwarzites 180
 FT-IR 3
 fullerene dimers 1
 fullerene fusion 1, 5
- generalized operations 128–130, 135,
 141, 158
 geometrical Kekulé structures 138, 158
 Goldberg list 135
 graph theory 22, 44, 69, 140
 graphite zone-folding procedure 35
- Hadamard matrix 74, 75
 Haeckelite structure 9
 half-buckminsterfullerene 61, 139
 Harary, F. 71, 77
 harmonic oscillator model of aromaticity
 (HOMA) 139, 144, 145, 147–153, 155,
 156, 158, 160–163
 HF formation 14, 29, 31, 107, 110, 138
 high genera 175, 177, 179, 187, 189
 high genera structures 179
 High-resolution transmission electron
 microscopy (HRTEM) 8, 65, 168
 HOMA index of aromaticity, *see* harmonic
 oscillator model of aromaticity
 HOMO-LUMO gap 29–32, 43, 45, 138, 142,
 144, 148, 149, 151, 152, 160–162
 Hosoya, H. 77, 79, 111
 Hosoya polynomial 79, 89–94
 Hückel theory 20, 21, 31, 77, 143
 hyper-detour index 72
 hyper-Wiener index 71, 72
 H/Z tube 41
- icosahedral junctions 178
 identical polyhex toroidal graphs 45
 internal H/Z-tube 61–63
 isomerization routes 130
- joint corannulenic JFw pattern 141
 junctions of nanotubes/nanotube junctions 168,
 171, 172, 177, 189
- KCN 2
 Kekulé structure 2, 10, 22, 44, 46, 57, 77,
 138–140, 145, 153, 154, 156–158, 163
- Kekulé-Dewar valence structure 155, 156, 163
 Klein tessellation 188
- labyrinth graphs 170
 layer matrices 78, 79, 107
 layer/shell matrices 78, 79, 82
 Le Verrier 77
 leapfrog Le 44, 58, 106, 107, 117–120, 122, 130,
 138, 140–144, 159–161, 176, 183–187, 204
 leapfrog rule 21
 leapfrog structures 22
 leapfrog transformation 22, 118
 LUMO 20, 21, 29–32, 43, 45, 125, 138, 142,
 144, 147–149, 151, 152, 160–162
- magnetic criterion 139, 154, 163
 MALDI-TOF 3
 medial Me 86, 116–118, 143, 144
 memory element 8
 Miliç, L. 77
 minimal surfaces 167, 170, 171, 180, 188
 molecular mechanics procedure 37, 41
- nanopeapods 7, 8, 14, 16, 51, 61, 66
 nanostructure building 9
 nanostructures 1, 23, 69, 89, 98, 111, 115, 130,
 135, 138, 163, 167, 188, 189
 nanostructures, aromaticity 137–163
 nanotube caps 22–25, 28
 numerical Kekulé valence structure 138
- octahedral junctions 177
 omega polynomials 40, 86, 87, 98, 100–104, 106,
 107, 111
 omega-derived descriptors 107
 omega-type polynomials 86, 88
 one-dimensional sp²-bonded objects 167
 operations on maps 58, 86
- pentagon fusions 107
 pentagon/octagon/pentagon (POP) triplets 51
 perfect clar DWTs 57
 periodic fullerenes 1–33
 periodic schwarzites 171, 180
 planar junctions 173, 175
 Platonic polyhedral 116, 146
 POAV1 theory 41, 47, 138, 177
 Poincaré, H. 116
 Polygonal Pn capping 117
 polyhex tori 35–48, 54, 92, 93, 101–103, 106,
 126, 140–142

- polynomial coefficients 78, 90
 polynomials 69, 77, 82, 83, 85–89, 92, 101, 111
 polynomials, counting 69–111
 POP-DWTs 53–60
 P-type schwarzites 171, 187
 pyramidalization angle 41
- QSPR studies 107
 quadrupling Q 120, 121, 175
 quasi-orthogonal cut (qoc) strip 86, 87
- radialene 139, 142, 144, 154, 155
 Raman spectroscopy(spectra) 2, 5, 9, 19, 168
 resonance energy 46–48, 77, 138, 145
 retro endo-kroto reaction 161
 rules of Valencia 45, 46
- Sachs graph 77
 Schlegel projection 100, 151, 156, 157
 Schlegel representation 98, 104
 semiempirical calculations 5, 11, 54, 57, 67, 110
 septupling operations 112, 123, 125, 126, 143, 151
 septupling operations, on maps 187
 septupling operations, molecular realization 126, 135
 shell matrices 78, 80
 short closed nanotubes 1
 simple Huckel theory 20, 21, 31, 143
 single-walled carbon nanotube (SWNT) 1, 8, 19, 65, 67, 143
 snub Sn 117, 118
 Spialter, L. 77
 spectral theory 43
 square tiled tori 36
 stellation 58, 117, 119
 Stone-Wales bond flipping 7, 12
 Stone-Wales SW bond rotations 7, 67
 Stone-Wales transformation 1, 7, 12, 13, 15, 16, 65, 146, 147
 strain energy calculations 9, 28, 33, 41, 47, 189
 structural/geometric criterion 139
 surface curvature 168
- TEM 15, 16, 67, 172
 Tessellation 40, 115, 119–121, 141, 143, 152, 153, 161, 162, 167, 170, 171, 173, 180–182, 187, 188
 tetrahedral junctions 175
 three-dimensional sp²-lattice of diamond 167
 three-dimensional sp²-lattice of spongy carbon 167
 topological effect on molecular orbitals (TEMO) 77
 topological index 71, 77, 84, 87
 topological resonance energy TRE 77, 145
 toroidal nanostructures 89
 toroidal structures 51–67, 127, 173
 totally resonant sextet (TRS) 44, 58, 140
 TPMSs 167, 170, 172, 180, 188
 Triangulation 117, 119
 triply periodic nanostructures 167–191
 truncation Tr 116, 117, 119–122, 141, 146–148, 150, 151, 158, 159
 tubular nanostructures 23, 98, 111, 130, 135
 tubulenes 5–7, 10, 12–16, 26, 27, 31, 33, 67, 134, 170, 173
 twisted/chiral tori 37, 101
 two-dimensional sp²-lattice of graphite 167
- unsymmetric Cluj distance detour (UCJDE) 76, 81, 82
 unsymmetric Cluj distance matrix (UCJDI) 76, 81, 82, 84
 unsymmetric Szeged matrices (USZ) 73
 UV-VIS 3
- Wiener 77
 Wiener Index 79, 84, 92–94, 96, 98
 Wiener numbers 92
- X-ray analysis 2
- zero-dimensional sp²-bonded objects 167
 zigzag closed nanotubes 23
 zig-zag cylinders 21
 zig-zag tubes 22, 23, 66, 67, 99, 100

Developments in Fullerene Science

Series Editor:

Tibor Braun, *Institute of Inorganic and Analytical Chemistry,
L. Eötvös University, Budapest, Hungary*

1. T. Braun (ed.): *Nuclear and Radiation Chemical Approaches to Fullerenes Science*. 2000 ISBN 978-0-7923-6524-2
2. B. Tumanskii and O. Kalina: *Radical Reactions of Fullerenes and their Derivatives*. 2001 ISBN 978-1-4020-0716-5
3. T. Akasaka and S. Nagase (eds.): *Endofullerenes. A New Family of Carbon Clusters*. 2002 ISBN 975-1-4020-0982-2
4. D. M. Guldi and N. Martin (eds.): *Fullerenes: From Synthesis to Optoelectronic Properties*. 2003 ISBN 978-1-4020-0983-9
5. E. E. Campbell: *Fullerene Collision Reactions*. 2004 ISBN 978-1-4020-1250-6
6. F. J. M. Rietmeijer (ed.): *Natural Fullerenes and Related Structures of Elemental Carbon*. 2006 ISBN 978-1-4020-4134-1
7. M. V. Diudea and C. L. Nagy: *Periodic Nanostructures*. 2007 ISBN 978-1-4020-6019-9